energies

Special Issue Reprint

# Heat Transfer Performance and Influencing Factors of Waste Management

Edited by
Hongting Ma and Shuo Ma

mdpi.com/journal/energies

MDPI

# Heat Transfer Performance and Influencing Factors of Waste Management

# Heat Transfer Performance and Influencing Factors of Waste Management

Guest Editors

**Hongting Ma**
**Shuo Ma**

MDPI

Basel • Beijing • Wuhan • Barcelona • Belgrade • Novi Sad • Cluj • Manchester

*Guest Editors*

Hongting Ma
School of Environmental Science and Engineering
Tianjin University
Tianjin
China

Shuo Ma
School of Energy and Safety Engineering
Tianjin Chengjian University
Tianjin
China

*Editorial Office*
MDPI AG
Grosspeteranlage 5
4052 Basel, Switzerland

This is a reprint of the Special Issue, published open access by the journal *Energies* (ISSN 1996-1073), freely accessible at: https://www.mdpi.com/journal/energies/special_issues/PH25GEGF2K.

For citation purposes, cite each article independently as indicated on the article page online and as indicated below:

Lastname, A.A.; Lastname, B.B. Article Title. *Journal Name* **Year**, *Volume Number*, Page Range.

**ISBN 978-3-7258-9081-1 (Hbk)**
**ISBN 978-3-7258-9082-8 (PDF)**
**https://doi.org/10.3390/books978-3-7258-9082-8**

© 2026 by the authors. Articles in this reprint are Open Access and distributed under the Creative Commons Attribution (CC BY) license. The reprint as a whole is distributed by MDPI under the terms and conditions of the Creative Commons Attribution-NonCommercial-NoDerivs (CC BY-NC-ND) license (https://creativecommons.org/licenses/by-nc-nd/4.0/).

# Contents

**Hongting Ma, Yang Bai, Shuo Ma and Zhipeng Zhou**
Heat Transfer Performance and Influencing Factors of Waste Tires During Pyrolysis in a Horizontal Rotary Furnace
Reprinted from: *Energies* **2025**, *18*, 4028, https://doi.org/10.3390/en18154028 . . . . . **1**

**Chen Xu, Yizhou Wang, Xinrong Zhang, Wenyi Li and Jieru Li**
Numerical Simulation of Pool Boiling on Novel Microstructured Heated Surface
Reprinted from: *Energies* **2025**, *18*, 4830, https://doi.org/10.3390/en18184830 . . . . . **21**

**Xin Xu, Jiaxin Zheng, Licheng Sun, Xiting Long, Tianyi Gao, Biao Li, et al.**
Numerical Analysis of Bismuth Telluride-Based Thermoelectric Device Performance in Lunar Extreme Cold Environments
Reprinted from: *Energies* **2025**, *18*, 5224, https://doi.org/10.3390/en18195224 . . . . . **36**

**Bin Wu, Lei Ren, Renyi Wen, Chenrui Yang and Daren Zheng**
Advances in the Aerothermal Performance Enhancement of Turbine Blade Tip Configurations
Reprinted from: *Energies* **2025**, *18*, 5930, https://doi.org/10.3390/en18225930 . . . . . **52**

**Qinyi Zhang, Yi Feng, Chunxiao Zhu, Jiaxin Zheng, Xin Xu, Min Du, et al.**
Numerical Analysis of Heat Transfer Process and Mechanisms for High-Temperature Air Flowing Across Staggered Lined Fine Tubes
Reprinted from: *Energies* **2026**, *19*, 796, https://doi.org/10.3390/en19030796 . . . . . **81**

**Yang Yu, Jing Wang, Xinyue Li, Jinyu Zhao, Shuman Wang, Fei Ma, et al.**
Dynamic Thermal Resistance-Capacity Modeling and Thermal Short-Circuit Analysis: A Study on Natural Convection in a Direct-Expansion $CO_2$ Downhole Heat Exchanger
Reprinted from: *Energies* **2026**, *19*, 2015, https://doi.org/10.3390/en19092015 . . . . . **105**

**Yanling Chen, Zhongyun Tian, Mingzhi Kong, Lei Sun, Lizhi Zhou, Wujun Wang and Mengyao Liu**
A Study on the Thermal Management Performance of Server-Oriented Memory Liquid Cooling Solutions
Reprinted from: *Energies* **2026**, *19*, 2150, https://doi.org/10.3390/en19092150 . . . . . **132**

**Xuyan Xu, Tao Zhang, Dongming Li, Wanchun Sun, Zhijiang Wu and Yansheng Xu**
A Dual-Factor Defrosting Model for Air-Source Heat Pumps Considering Ambient Temperature and Compressor Frequency
Reprinted from: *Energies* **2026**, *19*, 2787, https://doi.org/10.3390/en19122787 . . . . . **148**

*energies*

MDPI

*Article*

# Heat Transfer Performance and Influencing Factors of Waste Tires During Pyrolysis in a Horizontal Rotary Furnace

**Hongting Ma [1], Yang Bai [1], Shuo Ma [2,*] and Zhipeng Zhou [1]**

[1] School of Environmental Science and Engineering, Tianjin University, Tianjin 300350, China; mht116@tju.edu.cn (H.M.); baiyang@hnic.com.cn (Y.B.); 1022214046@tju.edu.cn (Z.Z.)
[2] School of Energy and Safety Engineering, Tianjin Chengjian University, Tianjin 300384, China
* Correspondence: ms0305@tju.edu.cn; Tel.: +86-022-2308-5107

**Abstract**

Pyrolysis technology currently serves as a significant method for recycling and reducing waste tires. In this paper, in order to improve the heat transfer efficiency during the pyrolysis of waste tires in a horizontal rotary furnace and the yield of pyrolysis oil, the effect laws of tire particle size, rotary furnace rotation speed, enhanced heat transfer materials, and adding spiral fins on heat transfer performance and pyrolysis product distribution were studied, respectively. The innovation lies in two aspects: first, aiming at the problems of slow heat transfer and low pyrolysis efficiency in horizontal rotary furnaces, we identified technical measures through experiments to enhance heat transfer, thereby accelerating pyrolysis and reducing energy consumption; second, with the goal of increasing high-value pyrolysis oil yield, we determined optimal operating parameters to improve economic and sustainability outcomes. The results showed that powdered particles of waste tires were heated more evenly during the pyrolysis process, which increased the overall heat transfer coefficient and the proportion of liquid products. When the rotational speed of the rotary pyrolysis furnace exceeded 2 rpm, there was sufficient contact between the material and the furnace wall, which was beneficial to the improvement of heat transfer performance. Adding heat transfer enhancement materials such as carborundum and white alundum could improve the heat transfer performance between the pyrolysis furnace and the material. Notably, a rotational speed of 3 rpm and carborundum were used as a heat transfer enhancement material with powdered waste tire particles during the pyrolysis process; the overall heat transfer coefficient was the highest, which was 16.89 W/(m$^2$·K), and the proportion of pyrolysis oil products was 46.1%. When spiral fins were installed, the comprehensive heat transfer coefficient was increased from 12.78 W/(m$^2$·K) to 16.32 W/(m$^2$·K). The experimental results show that by increasing the speed of the pyrolysis furnace, adding heat transfer enhancing materials with high thermal conductivity to waste tires, and appropriate particle size, the heat transfer performance and pyrolysis rate can be improved, and energy consumption can be reduced.

**Keywords:** waste tires; pyrolysis oil; horizontal rotary furnace; heat transfer coefficient

## 1. Introduction

With the rapid development of domestic transportation and the automotive industry, waste tire generation has surged. As one of the world's largest tire producers (contributing over 30% of global output), China faces pressing challenges in waste tire management—their non-degradability, polluting incineration, and the country's rubber resource shortage

underscore the urgency of high-value utilization. Globally, approximately 1.5 billion waste tires are generated yearly, with China as a top producer. These non-biodegradable tires (due to thermomechanical properties) pose risks: illegal dumping/accumulation may cause uncontrolled combustion, releasing toxins like polycyclic aromatic hydrocarbons. In China, underdeveloped collection systems lead to reliance on landfills/incineration, worsening pollution. Globally, developing nations face backward technologies; developed ones (e.g., the EU, 70–90% recycling) still have residual pollution from incineration [1].

Current waste tire disposal has five limited methods: crumb rubber for roads (toxin leaching), physical-chemical recycling (only for slightly worn tires), incineration/gasification (pollutant emissions), building fillers (structural risks), and landfills (land waste, fire risks). Pyrolysis, by contrast, produces gas (fuel after desulfurization), liquid ($C_6$–$C_{24}$ hydrocarbons including 25 wt.% limonene), and solid (activatable carbon black) with broad uses. Yet challenges remain: liquid sulfur (1.0–1.75 wt.%), high pretreatment costs, pyrocondensate's high unsaturated hydrocarbons (iodine value 67.8 $gI_2$/100 g), and sulfur (1.59 wt.%) requiring further processing [2]. Pyrolysis stands out among treatment methods for its small scale, low investment, controllable processes, high-value products (carbon black, combustible gas, pyrolysis oil), and reduced emissions, making it a focus of research [3–7].

Tires consist of natural rubber, synthetic rubber, steel wire, carbon black, and additives. Their pyrolysis involves three key stages: evaporation and decomposition of low-boiling water and additives at 200 °C; onset of rubber pyrolysis with product generation at 300 °C; and near-completion of the reaction at 500 °C [8–10]. During this process, aromatics and saturated hydrocarbons from rubber decomposition undergo cracking (macromolecules breaking into small molecules to form pyrolysis gas, gasoline, diesel, and heavy-oil fractions), while deep cracking leads to polycyclic aromatic condensation in heavy oil, forming coke [3,11].

Waste tire pyrolysis is endothermic, with the pyrolysis degree dependent on external heating and internal heat transfer [12–14]. Influencing factors include reaction conditions (temperature, heating rate), raw material properties (composition, particle size), and reactor structure [13]. Kar et al. found a maximum oil yield of 60.02 wt.% in a fixed bed reactor at a heating rate of 10 °C/min and 425 °C [15]. Galvagno et al. used a pilot-scale rotary kiln (0.4 m diameter, 3 rpm rotation speed) and reported a maximum oil yield of 38.12 wt.% at 550 °C [16].

However, critical gaps exist in current research. Most studies focus on pyrolysis processes and products, with little attention to heat transfer performance and its influencing factors in horizontal rotary furnaces—despite heat transfer directly affecting reaction rate, energy consumption, product distribution, and the technology's practical application.

Horizontal rotary furnaces are widely adopted in industry for their adaptability to raw materials, scalability for continuous operation, and operational flexibility. Yet, their large-volume cylinders cause uneven heat distribution, low heat transfer efficiency, and high energy consumption. Compounding this, pyrolysis in such furnaces involves complex interactions: material mixing, heat/mass transfer between materials and the reactor, and intricate chemical reactions.

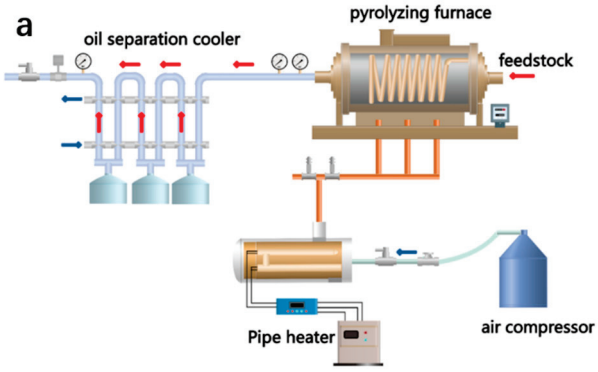
This study addressed these challenges by experimentally analyzing how key factors—waste tire particle size, furnace rotational speed, heat-transfer-enhancing materials, and spiral fins on the pyrolysis chamber outer wall—influence material temperature, heat transfer coefficients, and product distribution. The goal is to identify optimal pyrolysis conditions and heat transfer enhancement measures, thereby improving heat transfer and pyrolysis efficiency and boosting the economic value of products.

The innovation of this article lies in (1) addressing the problems of slow heat transfer rate and low pyrolysis efficiency during the pyrolysis of waste tires in a horizontal rotary furnace, with technical measures being determined through experiments to improve heat transfer performance, thereby accelerating pyrolysis speed and reducing pyrolysis energy consumption; (2) with the goal of increasing the yield of high-value pyrolysis oil, the optimal operating parameters for the pyrolysis process of waste tires were determined through experiments to improve the economy and sustainability of waste tire pyrolysis. Under the conditions of this experiment, when the particle size of waste tires is 1.0–2.3 cm, the rotation speed is 1.5 revolutions per minute, and the enhanced heat transfer material is diamond sand, the yield of pyrolysis oil is the best, and the economy of pyrolysis is the best.

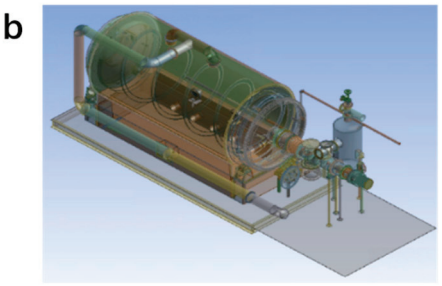
## 2. Materials and Methods

### *2.1. Experimental System*

To investigate the heat and mass transfer characteristics and influencing factors during the pyrolysis process of waste tires in a horizontal rotary furnace, an experimental system was designed and constructed, as depicted in Figure 1.




(a) Schematic diagram of experimental system




(b) Three dimensional simulation diagram of rotary pyrolysis furnace




(c) Physical image of the experimental system

**Figure 1.** Diagram of horizontal pyrolysis experimental device for waste tires.

The length of the pyrolysis furnace is 1.1 m, the inner diameter of the cylinder is 0.414 m, the outer diameter is 0.426 m, and the outer surface area is 1.47 $m^2$.

The system predominantly consisted of a horizontal rotary pyrolysis furnace, pipeline heater, air compressor, oil separation cooler, temperature measurement system, and pyrolysis product collection system. For this experiment, specialized pipeline heating furnaces and air compressors were employed to provide high-temperature gas, achieving a peak temperature of 800 °C. The oil-separating cooler was constructed as a double-pipe heat exchanger, with cooling water circulating through the outer pipe and the volatile gas generated in the pyrolysis furnace passing through the inner pipe. Upon cooling, the

gas and oil were efficiently separated. The temperature monitoring system incorporated wireless temperature sensors, enabling real-time tracking of temperature variation within the materials in the furnace and the high-temperature air.

In this study, three horizontal heat-resistant stainless steel sleeves were installed in the pyrolysis chamber, with one horizontal heat-resistant sleeve installed near the bottom of the pyrolysis chamber to come into contact with the waste tire particle layer throughout the pyrolysis process. Five K-type thermocouples were arranged on each sleeve to measure the temperature distribution of different sizes of waste tire particle layers, as shown in Figure 2. All numbers in the picture are in millimeters.

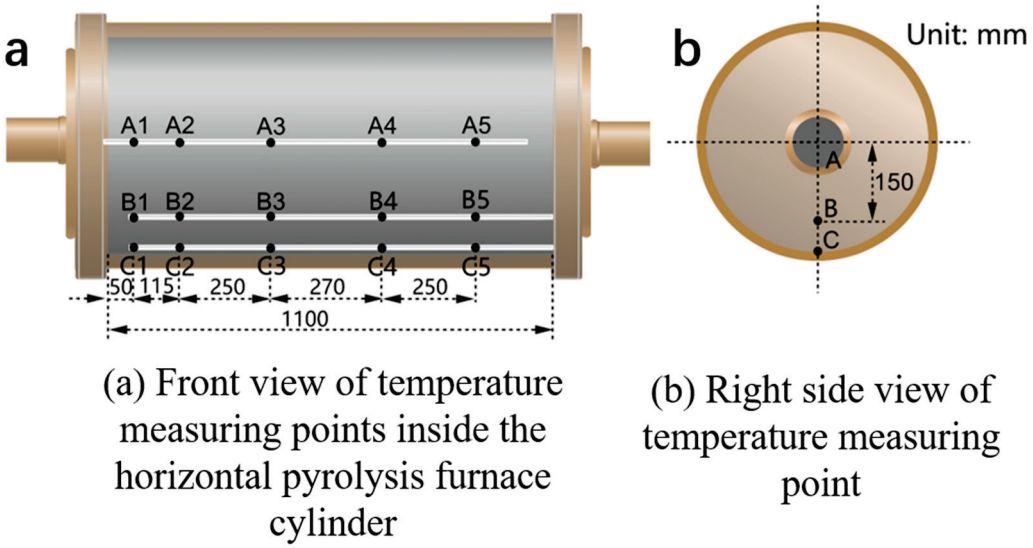



**Figure 2.** Schematic diagram of temperature measuring point in the inner cylinder of horizontal pyrolysis furnace.

### *2.2. Experimental Materials and Conditions*

The waste tires used in this experiment are car tires, which are mainly used for transportation vehicles such as passenger cars and commercial vehicles. They are the main type of waste tires. The experiments were carried out on four kinds of particle sizes: powder, fine, medium, and coarse. The corresponding density and particle size were presented in Table 1 below.

**Table 1.** Density and particle size of different particle types.

| Particle Type | Density (kg/m$^3$) | Size (cm) |
|---|---|---|
| Powder | 414 | <0.1 |
| Fine | 470 | 0.3~2.1 |
| Medium | 446 | 1.0~2.3 |
| Coarse | 421 | 2.0~3.0 |

The experimental conditions were as follows: the hot gas flow rate was 24 m$^3$/h, the pyrolysis final temperature was 470 °C, the pyrolysis furnace speed $n$ = 1~3 rpm, the experimental material mass was 10 kg, and the addition amount of heat transfer enhancement material was 5 kg.

Due to the fact that the waste tires had been crushed into small particles with a diameter of less than 3 mm before the experiment, and the metal cords were sorted out, the pyrolysis products did not contain metal cords.

*2.3. Method for Calculating the Heat Transfer Coefficient of a Rotary Furnace*

The heat transfer process during the pyrolysis of waste tires in a rotary pyrolysis furnace consists of three parts: the convection heat transfer between the high-temperature gas and the outer wall surface of the inner cylinder of rotary pyrolysis furnace, the heat conduction of the cylinder body in rotary pyrolysis furnace, and the heat transfer between the inner wall surface of the inner cylinder of rotary pyrolysis furnace and waste tire particles [16–18].

(1) The convective heat transfer coefficient between the high-temperature gas and the outer wall of the inner cylinder in a rotary pyrolysis furnace.

The convective heat transfer coefficient $\alpha_{aw,\lambda}$ between high-temperature gas and the outer wall of the rotary pyrolysis furnace can be calculated by the energy balance calculation formula as follows:

$$\alpha_{aw,\lambda} \cdot A_{aw} \cdot \Delta T = Q_1 + Q_2 + Q_3 + Q_4, \quad (1)$$

$$Q_1 = M_r \cdot C_{p,r} \cdot \frac{dT_{r,m}}{dt}, \quad (2)$$

$$Q_2 = M_s \cdot C_{p,s} \cdot \frac{dT_{s,m}}{dt}, \quad (3)$$

$$Q_3 = M_o \cdot C_{p,o} \cdot \frac{dT_{o,m}}{dt}, \quad (4)$$

where $Q_1$ is the heat absorbed by the inner cylinder, W. $Q_2$ is the heat taken away by the material in the inner cylinder, W. $Q_3$ is the heat taken away by oil and gas during pyrolysis, W. $Q_4$ is the various heat losses through the brick masonry of the base of the outer cylinder, the insulation layer of the outer cylinder, the two end faces of the inner cylinder, the rolling ring, the gear ring, and the furnace door. It is initially set as 20% of the total energy from the high-temperature gas, based on experience, W. $A_{\mathrm{aw}}$ is the outer wall area of the inner cylinder of the rotary pyrolysis furnace, $m^2$. $t$ is the pyrolysis time, s. $M_{\mathrm{r}}$ is the inner tube mass of the rotary pyrolysis furnace, kg. $T_{\mathrm{r,m}}$ is the average temperature of the inner cylinder of the rotary pyrolysis furnace, °C. $C_{\mathrm{p,r}}$ is the heat capacity of the inner cylinder of the rotary pyrolysis furnace at constant pressure, J/kg·K. $M_{\mathrm{s}}$ is the mass of waste tire involved in the pyrolysis reaction, kg. $T_{\mathrm{s,m}}$ is the average temperature of the waste tire involved in the pyrolysis reaction, °C. $C_{\mathrm{p,s}}$ is the heat capacity of waste tire material at constant pressure, J/kg·K. $M_{\mathrm{o}}$ is the mass of oil and gas produced by pyrolysis, kg. $T_{\mathrm{o,m}}$ is the average temperature of oil and gas produced by pyrolysis, °C. $C_{\mathrm{p,o}}$ is the heat capacity of oil and gas produced by pyrolysis at constant pressure, J/kg·K.

(2) Thermal conductivity of the inner cylinder

The inner cylinder is made of 304 steel, and the thermal conductivity is 16.3 W/(m·K) at 100 °C and 21.5 W/(m·K) at 500 °C. The thermal conductivity kt is calculated by interpolation according to the arithmetic average of the temperature of the inner wall and the outer wall of the inner cylinder.

(3) The apparent heat transfer coefficient between the inner surface of the inner cylinder of the pyrolysis furnace and the material

The apparent heat transfer coefficient between the inner wall and the material in the inner cylinder of the rotary pyrolysis furnace is a crucial parameter for describing the heat transfer efficiency, which is defined as the ratio of the heat transferred through the inner wall per unit area in a unit time to the temperature difference between the inner wall and the material. In order to determine the apparent heat transfer coefficient, it is considered that the pyrolysis chamber is energy balanced, assuming that the total energy from the wall is transferred to the material bed and absorbed by the material. Given that

the thermal resistance of waste tire substantially surpasses that of the thermal resistance of the contact gap between the material bed and the wall, the impact of the contact gap between the material bed and the wall on the apparent heat transfer coefficient is ignored. The apparent heat transfer coefficient between the wall and the material is calculated by the energy balance formula as follows [19]:

$$\alpha_{ws,\lambda} \cdot A_{w,s} \cdot (T_w - T_{s,m}) = M_s \cdot C_{p,s} \cdot \frac{dT_{s,m}}{dt}, \quad (5)$$

where $A_{ws}$ is the contact area between cylinder wall and material bed in the rotary pyrolysis furnace, which is related to filling degree, $m^2$. $T_w$ is the temperature of cylinder wall in the rotary pyrolysis furnace, °C.

The variation of apparent heat transfer coefficient between the wall and the material can be obtained according to the temperature distribution data measured in the experiment over time.

(4) The comprehensive heat transfer coefficient of rotary pyrolysis furnace

After calculating the convection heat transfer coefficient between high-temperature gas and the outer wall of the inner cylinder of the rotary pyrolysis furnace, the thermal conductivity coefficient of the cylinder in the rotary pyrolysis furnace, and the apparent heat transfer coefficient between the inner wall of the inner cylinder of the rotary pyrolysis furnace and waste tire particles, the comprehensive heat transfer coefficient $K$ of the rotary pyrolysis furnace was calculated according to the following formula:

$$K = 1 / \left( \frac{1}{\alpha_{aw,\lambda}} + \frac{k_t A_{aw}}{\delta} + \frac{1}{\alpha_{ws,\lambda}} \right) \quad (6)$$

where $\delta$ is the thickness of the inner cylinder of the rotary pyrolysis furnace, m.

## 3. Results and Discussion

### *3.1. Effect of Waste Tire Particle Size on Heat Transfer Performance and the Distribution of Pyrolysis Products*

There was a certain impact of particle size on the material temperature distribution, heat transfer performance, and pyrolysis reaction rate during the pyrolysis process. Therefore, pyrolysis experiments were carried out using waste tires with particle sizes of powdered, fine, medium, and coarse, respectively. The temperature changes of the materials and the composition of the pyrolysis products during the pyrolysis process were measured, and the influence of tire particle size on heat transfer performance and product distribution was analyzed.

Figure 3 shows the variation in temperature with time during the pyrolysis process of waste tires with four particle sizes of powdered, fine, medium, and coarse.

The experimental results showed that the temperature variation trends for waste tires of different particle sizes during the pyrolysis process were basically the same. The maximum temperature disparity between material layers of different particle sizes was noted as 12.1 °C.

In the initial stage (0~2 h), there was little effect of particle size on the temperature change of the materials, and the heating rate was about 3.01 °C/min. It indicated that the heating process of the materials at this stage was mainly affected by the overall heating conditions, rather than the particle size.

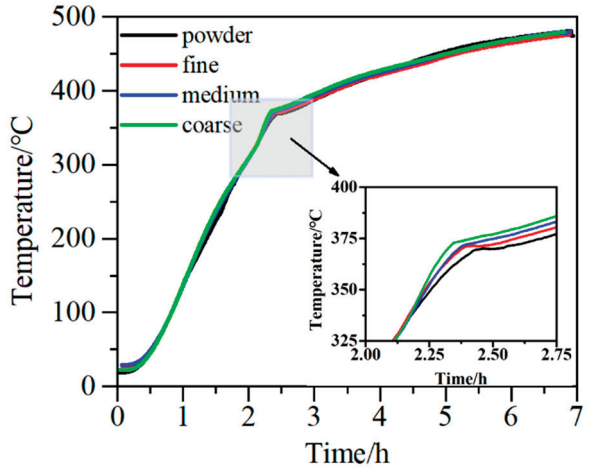



**Figure 3.** The temperature of waste tires with different particle sizes varies with the pyrolysis time.

Upon reaching an approximate temperature of 340 °C in the material layer, the waste tires proceed into the pyrolysis stage, and the change rate of temperature begins to exhibit variations among different particle sizes. Especially in the period from 2.25 to 2.75 h, the heating rate decreased with decreasing particle size. It was attributed to the fact that pyrolysis is an endothermic reaction. Smaller particles possess a larger specific surface area, which enhances the contact with the inner surface of the pyrolysis chamber. It facilitated the heat transfer effect, enabling the particles to absorb more heat within the same time, and the pyrolysis reaction rate was faster. However, the majority of the absorbed heat was utilized for the pyrolysis reaction, which resulted in a relatively low heating rate. In contrast, larger particles resulted in nonuniform heat transfer; their pyrolysis reaction rate was slower, less heat was absorbed and mainly used for temperature rise, and their temperature rising rate was obviously higher than that of small particle tires. When the temperatures of the material layers of the four types of particles (powdered, fine, medium, and coarse) rose to 373.1 °C, 371.5 °C, 370.6 °C, and 369.4 °C, the heating rate decreased significantly. It indicated that the materials began to rapidly pyrolyze, accompanied by significant heat adsorption, resulting in a marked decrease in the heating rate.

As the pyrolysis progresses, the temperature variations of the material layers with different sizes gradually became uniform, and the heating rate decreased to approximately 0.56 °C/min. When the temperature of the material layer reached 400 °C, the pyrolysis reaction basically came to an end. The remaining solid residue mainly consisted of inorganic substances such as carbon black and fibers, and their particle size effect became negligible. Notably, the temperatures of tires with different particle sizes were very close, with a maximum temperature difference of only 3.9 °C.

To intuitively illustrate the heat transfer rate during the pyrolysis process, the measured temperature distribution data were used to calculate the apparent heat transfer coefficients of waste tire particles with different particle sizes. The results were shown in Figure 4.

As can be seen from Figure 4a, the apparent heat transfer coefficients corresponding to different particle sizes exhibited a bimodal distribution as temperature altered during the pyrolysis process. In the initial stage, the first peak appeared at approximately 130 °C, followed by a second peak around 370 °C. When the temperature was higher than 400 °C, the apparent heat transfer coefficient dropped rapidly to a relatively lower value and subsequently decreased slowly.

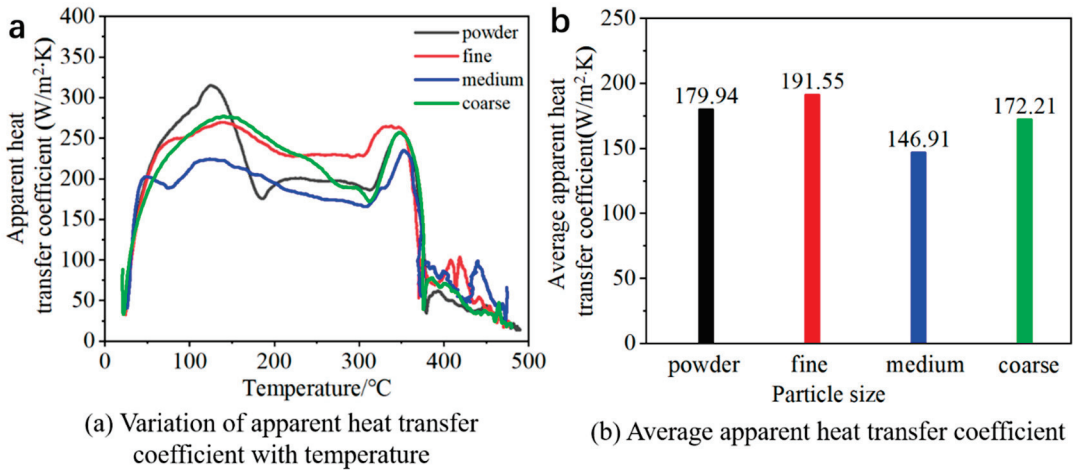



**Figure 4.** Heat transfer performance between the inner wall of the pyrolysis furnace and the material during the pyrolysis of waste tires with different particle sizes.

The main reasons for the above-mentioned phenomenon can be attributed to the following. In the initial stage of pyrolysis, the waste tire particles retained their original appearance, and they were not deformed by heat. The gaps between the particles resulted in poor thermal conductivity, making it difficult to transfer heat to the interior of the material. Therefore, the external temperature of materials rose quickly, leading to a large temperature gradient between the interior and exterior. Moreover, given that evaporation is an endothermic process, the evaporation of water and low-boiling-point additives in materials requires absorbing substantial heat. Consequently, the heating rate was slow, leading to an increase in the temperature gradient of the tire. In addition, with the increase in temperature, more water vapor was generated. The disturbance of water vapor would strengthen the heat transfer effect, so the apparent heat transfer coefficient increased rapidly, reaching an extremum at about 130 °C.

As the temperature continued to rise, the waste tires appeared to be partially softened and agglomerated. The closer contact between the particles resulted in a more uniform heating, leading to a reduced temperature gradient. Therefore, the apparent heat transfer coefficient decreased to some extent.

When the temperature of the materials rose to around 340 °C, waste tires began to undergo pyrolysis reaction. However, the pyrolysis reaction process requires absorbing a large amount of heat, which increases the temperature gradient inside the materials and promotes the transfer of heat from the wall surface to the interior of the materials. Meanwhile, the gas and liquid products generated during the pyrolysis increase the specific surface area and fluidity of the materials, further improving the heat transfer performance. In addition, with the increase in temperature, the radiation heat transfer between the surface of the pyrolysis chamber and the materials was enhanced, resulting in an increase in the apparent heat transfer coefficient. As the pyrolysis reaction proceeded, the temperature in the material bed gradually reached a state of equilibrium, and the temperature gradient stabilized with minimal variation.

When the temperature reached about 400 °C, the pyrolysis process essentially ended. The majority of the organic substances in the materials had been decomposed, and the remaining solid residue exhibited poor thermal conductivity, so the apparent heat transfer coefficient decreased.

Upon analyzing the data from the entire pyrolysis process, the average apparent heat transfer coefficients corresponding to different particle sizes were obtained, as illustrated in Figure 4b. It can be seen that the average apparent heat transfer coefficient of fine

particle waste tires was the largest with 191.55 W/(m$^2$·K), and the average apparent heat transfer coefficient of powder, medium, and coarse particles was 179.94 W/(m$^2$·K), 146.91 W/(m$^2$·K), and 172.21 W/(m$^2$·K), respectively.

The main reason for the highest average apparent heat transfer coefficient corresponding to fine particle waste tires is that the average apparent heat transfer coefficient is related to the contact area between the waste tire particles and the surface inside the pyrolysis chamber, as well as the contact thermal resistance between the particles. When the quality of experimental materials is the same, the smaller the particle size, the higher the packing density of the material layer, and the lower the contact thermal resistance between particles, which has a positive effect on heat transfer. However, the decrease in particle size reduces the contact area between the material and the surface inside the pyrolysis chamber, which has an adverse effect on heat transfer. Under the combined action of these two factors, the comprehensive heat transfer effect of fine particulate materials reaches its optimum, and the average apparent heat transfer coefficient reaches its maximum value.

During the pyrolysis process, the comprehensive heat transfer coefficient between the inner wall of the pyrolysis furnace and the material when using waste tires with different particle sizes is shown in Figure 5.

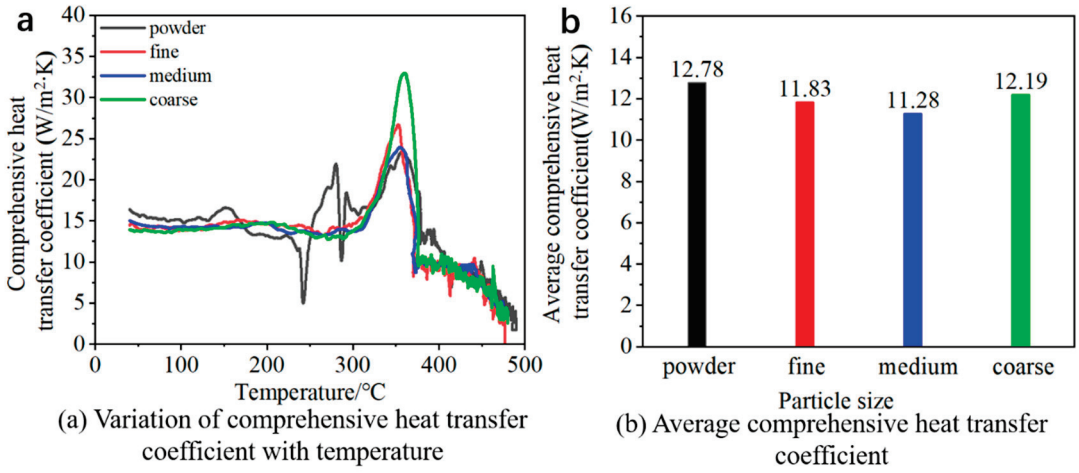



**Figure 5.** Comprehensive heat transfer performance during pyrolysis of waste tires with different particle sizes.

The heat transfer coefficient increased slightly in the initial stage of pyrolysis. However, upon transitioning into the pyrolysis process, the heat transfer coefficient increased rapidly and reached its maximum value near 380 °C, which corresponded to the temperature at which the maximum thermogravimetric rate of waste tire occurred. Subsequently, a significant decrease in the yield of pyrolysis gas was observed due to the deceleration of the pyrolysis rate, and the comprehensive heat transfer coefficient dropped rapidly as well. When the pyrolysis temperature exceeded 400 °C, the pyrolysis process basically completed, with the comprehensive heat transfer coefficient maintaining a low level and gradually decreasing.

As can be seen from Figure 5b, the average comprehensive heat transfer coefficients for the four particle sizes were 12.78 W/(m$^2$·K), 11.83 W/(m$^2$·K), 11.28 W/(m$^2$·K), and 12.19 W/(m$^2$·K), respectively. Contrary to the average apparent heat transfer coefficient, the average comprehensive heat transfer coefficient of the pyrolysis furnace is the highest when the waste tire particles are powder. This is mainly because the small particles with lower mass are more readily carried by the flow in the high-temperature gas. Thus, the degree of turbulence of the gas was increased, and the mixing and momentum exchange inside the gas were enhanced. The enhanced turbulence effect can effectively break the thermal

boundary layer, thereby accelerating the rate of heat transfer. As a result, the convective heat transfer coefficient was increased, thus increasing the average comprehensive heat transfer coefficient.

During the pyrolysis of waste tire particles in a horizontal rotary furnace, liquid, gaseous, and solid products are generated, and the pyrolysis products of tires with different particle sizes were collected and analyzed, as shown in Figure 6.

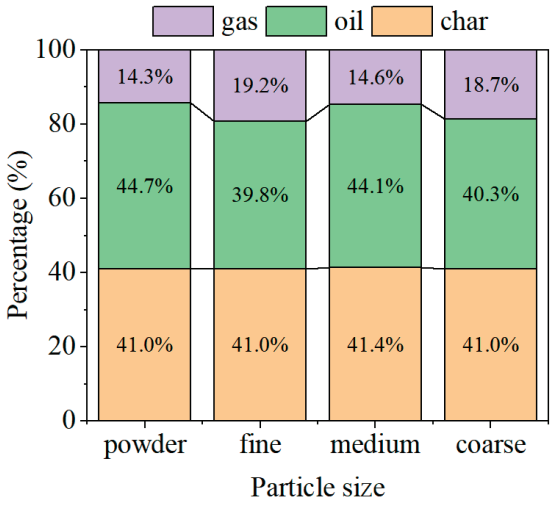



**Figure 6.** Effect of particle size of waste tire on distribution of pyrolysis products.

The waste tires used in the experiment were relatively clean, and the content of metals, quartz sand, or white corundum in the carbon black was very low, so other impurities were not considered when weighing the pyrolysis solid product.

As illustrated in Figure 6, the mass of solid products remaining after the pyrolysis of tires with different particle sizes was essentially the same, approximately 41%. However, the proportions of liquid and gaseous products were different. The yield of liquid products from powdered and medium tire particles was relatively high, reaching 44.7% and 44.1%, respectively. It might be because smaller particles possess a larger specific surface area, enabling them to absorb heat more uniformly. Consequently, the pyrolysis reaction was facilitated to proceed more thoroughly, generating more liquid products. In particular, powdered particles experienced a more uniform heating process, and their pyrolysis process reached thermal equilibrium rapidly. It prevented secondary cracking of liquid products caused by local overheating, consequently resulting in a higher yield of liquid products [20].

For fine and coarse particles of waste tires, the yields of liquid products were low (39.8% and 40.3%), and gaseous products were relatively high (19.2% and 18.8%, respectively), but the reasons were different. Fine particles, with a relatively broad size range, nonuniform particle sizes, and high bulk density, lead to significant local overheating. As a result, liquid products were further decomposed into gaseous products under high temperature conditions. For coarse particles, the low bulk density with high porosity resulted in poor heat transfer performance, which led to a significant temperature gradient. Owing to the low thermal conduction efficiency, the pyrolysis reaction was incomplete; some of the raw materials failed to be fully converted into liquid products and instead directly volatilized into gaseous substances, leading to an increase in the proportion of gaseous products [21,22].

Under the same final pyrolysis temperature, the yield of pyrolysis oil is mainly related to the heating rate of waste tires. The key factors affecting the heating rate include particle size, contact heat transfer between particles, and heat transfer process between particles and the surface inside the pyrolysis chamber. According to the experimental results of this

article, it is possible that the heating rates of powdered particles and medium particles in the pyrolysis chamber are relatively high and close, so the pyrolysis oil yield is also relatively close.

### *3.2. Effect of Rotational Speed on Heat Transfer Performance and the Distribution of Pyrolysis Products*

The rotational speed of the rotary pyrolysis furnace can affect the pyrolysis efficiency of waste tires and thus influence the degree of pyrolysis. Therefore, we explored the variation of the average temperature of the materials in the pyrolysis chamber over time at different rotational speeds, as shown in Figure 7.

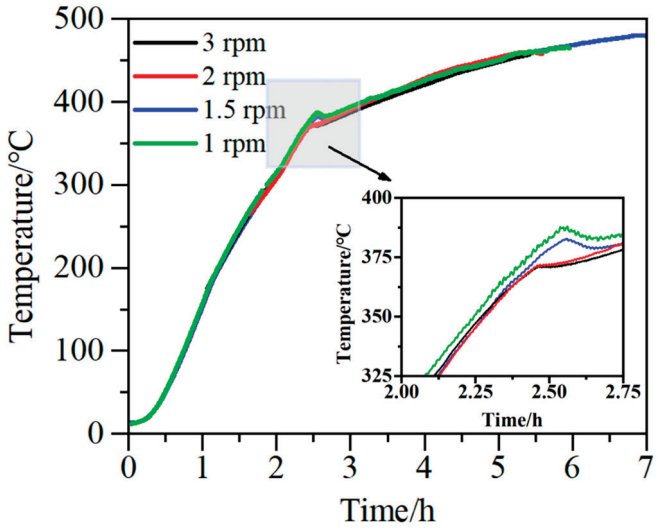



**Figure 7.** The temperature of waste tires with different pyrolysis furnace speeds.

From Figure 7, the temperature variation trends of waste tires in the pyrolysis chamber were basically consistent at different speeds. Within 2.25 h after the beginning of heating, the rotational speed had almost no effect on the temperature of the materials. After that, the influence of the rotational speed gradually appeared. When the temperature of the material layer rose to around 340 °C, the waste tires began to pyrolyze, which was an endothermic reaction. The heating rate decreased, and the influence of the rotational speed on the temperature of the materials appeared different. Within the 2.25 to 2.75 h, the temperature of the materials corresponding to a higher rotational speed was slightly lower than that of a lower rotational speed, with a maximum temperature difference of 16.2 °C. It was because as the rotational speed increased, the contact between the materials and the pyrolysis chamber wall became more sufficient. More heat was transferred from the outside of the pyrolysis chamber, and the temperature distribution within the materials was more uniform. The materials absorbed more heat during the pyrolysis reaction, resulting in a slower increase in the materials' temperature.

When the temperature of the material layer reached 400 °C, the pyrolysis reaction was almost finished. The fewer remaining components, the less the influence of the rotational speed on the temperature of the materials, which gradually becomes consistent.

To illustrate the influence of the rotational speed of the pyrolysis furnace on heat transfer performance, the apparent heat transfer coefficients between the inner wall of the inner cylinder of the rotary pyrolysis furnace and the material at the rotational speeds of 1 rpm, 1.5 rpm, 2 rpm, and 3 rpm were calculated, respectively, as shown in Figure 8.

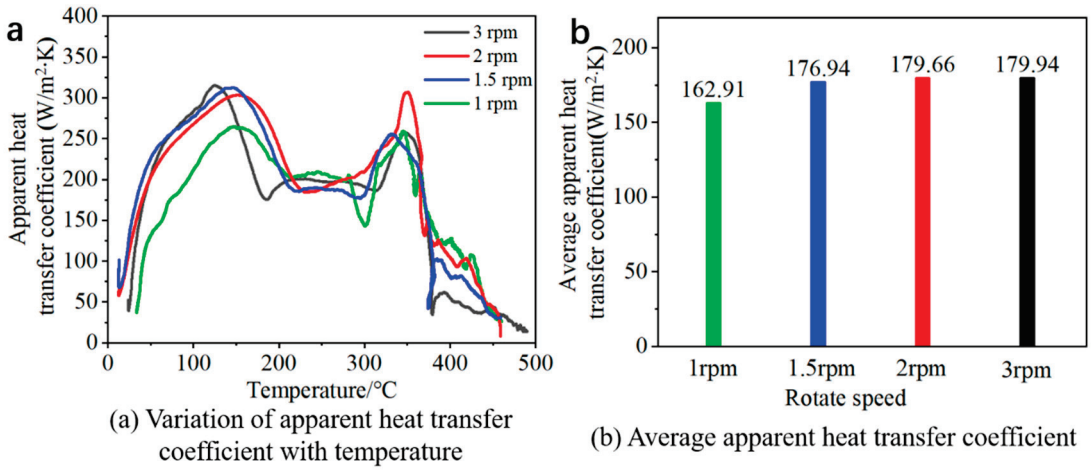



**Figure 8.** Heat transfer performance between the inner wall of the inner cylinder and the material in the pyrolysis furnace at different speeds.

As can be seen from Figure 8a, the apparent heat transfer coefficient between the pyrolysis furnace and the materials at different stages presented different trends during the pyrolysis process. At the beginning, it was increased with the rise of temperature, reached a maximum value at 135 °C, and then decreased, entering a plateau period. When the temperature reached 340 °C, there was a notable increase in the apparent heat transfer coefficient with the increase in temperature. It subsequently reached a maximum value at 370 °C, before undergoing a decrease.

As shown in Figure 8b, the apparent heat transfer coefficients at the four rotational speeds of 1 rpm, 1.5 rpm, 2 rpm, and 3 rpm were 162.91 W/(m$^2$·K), 176.94 W/(m$^2$·K), 179.66 W/(m$^2$·K), and 179.94 W/(m$^2$·K), respectively. As the rotational speed increased, the heat transfer coefficient also increased. When the rotational speed increased to 2 rpm, the heat transfer coefficient almost no longer changed. The increased rotational speed ensured a more sufficient contact between the materials and the chamber wall, enabling the apparent heat transfer coefficient between the inner wall of the pyrolysis furnace and the materials to reach a relatively higher value [23,24].

The instantaneous comprehensive heat transfer coefficient of the horizontal rotary pyrolysis furnace and temperature, as well as the average comprehensive heat transfer coefficient, when the rotational speeds of the horizontal rotary pyrolysis furnace were 1 rpm, 1.5 rpm, 2 rpm, and 3 rpm, respectively, are shown in Figure 9.

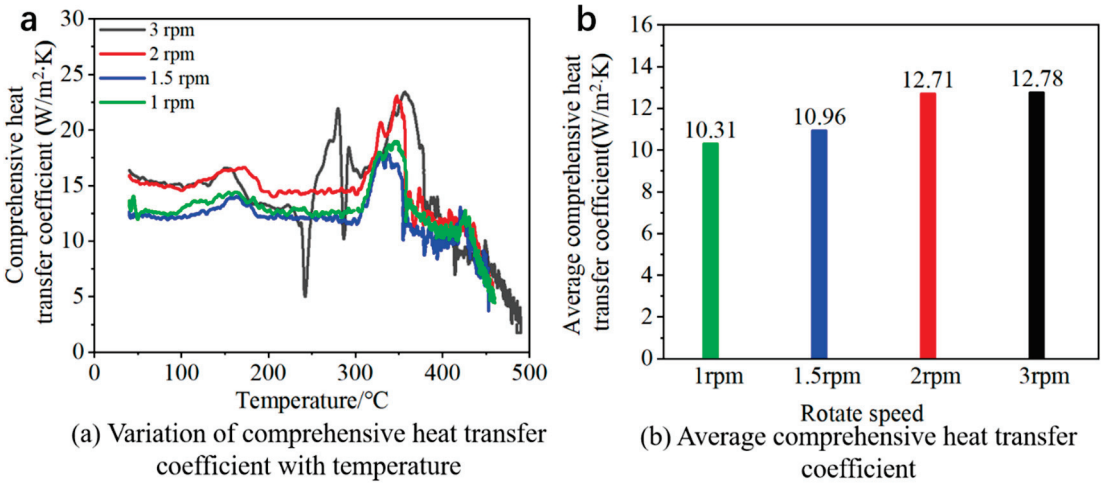



**Figure 9.** Comprehensive heat transfer performance of pyrolysis furnaces at different rotational speeds.

As shown in Figure 9a, the variation trends of the instantaneous comprehensive heat transfer coefficient at different rotational speeds with temperature during the pyrolysis process exhibited almost unanimously, all presenting a bimodal pattern. The first peak appeared at about 180 °C, followed by a second peak at around 370 °C. Thereafter, a dramatic decrease was observed after 400 °C, eventually leading to a slow change. The main factor contributing to this transformation was the evaporation of water in the initial and the accelerated pyrolysis occurring in the subsequent stage.

For Figure 9b, the average comprehensive heat transfer coefficients of the rotary pyrolysis furnace with the rotational speeds of 1 rpm, 1.5 rpm, 2 rpm, and 3 rpm were 10.31 W/(m$^2$·K), 10.96 W/(m$^2$·K), 12.71 W/(m$^2$·K), and 12.78 W/(m$^2$·K), respectively. It indicated that the average comprehensive heat transfer coefficient increased as the rotational speed increased accordingly. The acceleration of the rotational speed resulted in an increase in both the frequency and intensity of the materials being agitated in the pyrolysis furnace. The contact between the materials became more sufficient, and there were more heat transfer paths, enabling heat to be transferred more easily within the materials. A higher rotational speed made the gas boundary layer on the surface of the materials thinner, reducing the resistance to heat transfer. Thus, the heat exchange between the high-temperature gas and the materials became easier, and the heat transfer performance was enhanced.

In order to analyze the influence of the rotational speed of the horizontal pyrolysis furnace on the distribution of pyrolysis products, the mass of solid, liquid, and gaseous products during the pyrolysis of waste tires at different rotational speeds was collected and analyzed. The results were shown in Figure 10.

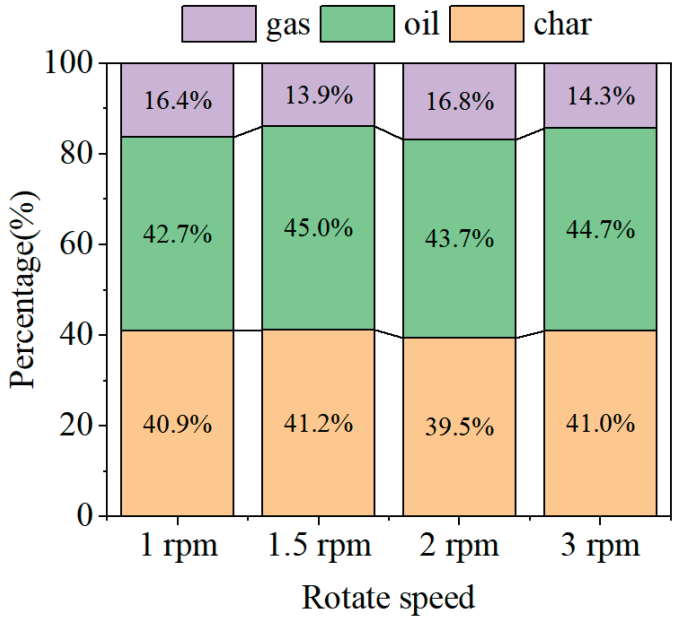



**Figure 10.** Effect of pyrolysis furnace rotation speed on the distribution of pyrolysis products.

As depicted in Figure 10, the mass of solid products remained relatively consistent at different rotational speeds, with the maximum relative deviation being only 4.1%. When the rotational speed exceeded 1.5 rpm, there was a slight increase in liquid products and a corresponding decrease in gaseous products. This phenomenon can be attributed to the higher rotational speeds, which reduced the residence time of pyrolysis oil in the high-temperature environment, thereby inhibiting further pyrolysis into gaseous products.

### *3.3. Effect of Heat Transfer Enhancement Materials on Heat Transfer Performance and the Distribution of Pyrolysis Products*

To further enhance the heat transfer efficiency during the pyrolysis process, three materials, including carborundum, quartz sand, or white alundum, were chosen as enhanced heat transfer materials incorporated into waste tires. The variation of the material temperature over time is shown in Figure 11.

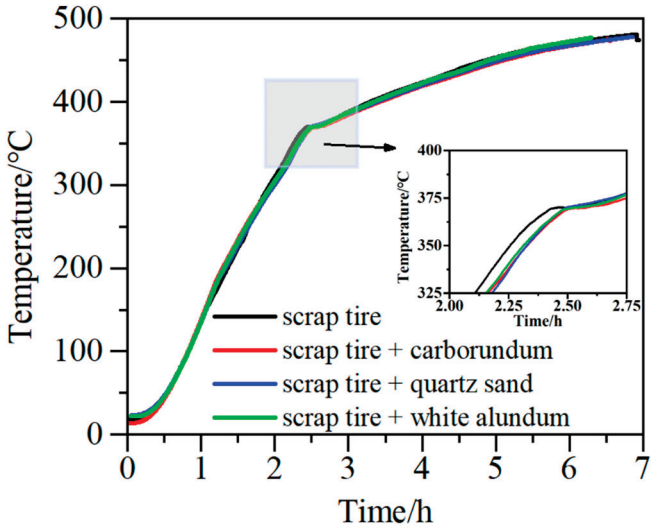



**Figure 11.** The temperature of waste tires over time when adding different enhanced heat transfer materials.

As illustrated in Figure 11, the temperature of waste tires mixed with different enhanced heat transfer materials showed a trend of rapid increase at the beginning, followed by a slower increase. In the first 2 h of the pyrolysis process, prior to the commencement of the pyrolysis reaction, the heating rate of waste tires alone and those with different materials added was around 3.0 °C/min. When the pyrolysis reaction began, the heating rate for mixtures containing heat transfer enhancement materials and waste tires decreased slightly. It was attributed to the enhanced heat transfer materials that improve the heat transfer efficiency, which was beneficial for waste tires to absorb heat for the pyrolysis reaction. When the temperature reached approximately 370 °C, the pyrolysis reaction became vigorous and required substantial heat adsorption, resulting in a marked decrease in the heating rate.

According to the measured material temperature, the apparent heat transfer coefficient between the material and the inner surface of the pyrolysis furnace after adding different enhanced heat transfer materials can be obtained through calculation, as depicted in Figure 12.

As can be seen from Figure 12a, it was evident that the variation trends of the apparent heat transfer coefficients of waste tires alone and mixtures with enhanced heat transfer materials were fundamentally identical, both showing a bimodal pattern. During the pyrolysis process, the first peak appeared at around 130 °C in the initial stage, and the second peak occurred at about 370 °C.

By analyzing the instantaneous apparent heat transfer coefficient in Figure 12a, the average apparent heat transfer coefficients for the pyrolysis of waste tire alone and mixtures with carborundum, quartz sand, and white alundum were determined, respectively. As shown in Figure 12b, the values were 179.94 W/(m$^2$·K), 205.68 W/(m$^2$·K), 169.35 W/(m$^2$·K), and 202.33 W/(m$^2$·K), respectively.

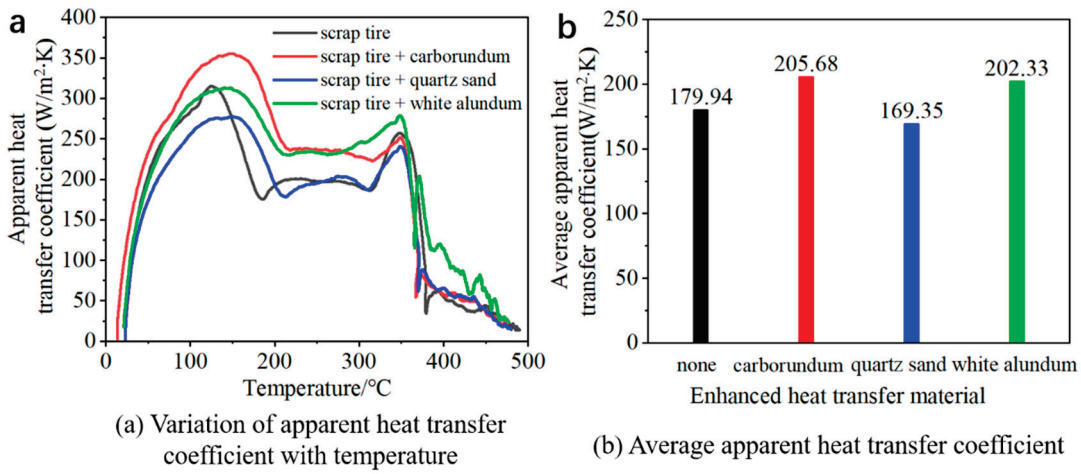



**Figure 12.** Heat transfer performance between the inner wall of the pyrolysis furnace and materials with different heat transfer enhancement materials.

The heat transfer performance can be significantly enhanced after incorporating carborundum and white alundum, while the effect of quartz sand was not obvious. The main reasons were as follows. On the one hand, the thermal conductivity of carborundum is 135.6 W/(m·K), and that of white alundum is 20~30 W/(m·K), which are both significantly higher than that of quartz sand, which is 1~10 W/(m·K). Materials with high thermal conductivity establish more efficient heat conduction paths within the material, enabling faster heat transfer and improving heat transfer efficiency during the thermal exchange process. On the other hand, the coefficient of thermal expansion also significantly influenced the heat transfer efficiency. The coefficients of thermal expansion of carborundum, white alundum, and quartz sand are 4~5 $\times$ $10^{-6}$/°C, 8~9 $\times$ $10^{-6}$/°C, and 5.5 $\times$ $10^{-7}$/°C, respectively. Appropriate expansion enhanced the contact area and tightness between the enhanced heat transfer materials and the surrounding medium (such as pyrolysis gas or heated materials), facilitating the heat transfer [25–32].

Additionally, the heat transfer performance was also influenced by the density of enhanced heat transfer materials. During the process of heat conduction, heat was transferred through the vibration of atoms and molecules or the movement of free electrons. The densities of carborundum, white alundum, and quartz sand are 3.06~3.20 g/cm$^3$, 3.95~4.00 g/cm$^3$, and 2.65 g/cm$^3$, respectively. Materials with higher density typically feature more closely packed atoms or molecules, forming a tightly connected "heat transfer chain" that enables more efficient heat transfer within the material.

The comprehensive heat transfer coefficients after adding three enhanced heat transfer materials of carborundum, quartz sand, and white alundum are shown in Figure 13.

It can be observed that the comprehensive heat transfer coefficients for the pyrolysis of waste tires alone and with the addition of carborundum, quartz sand, and white alundum were 12.78 W/(m$^2$·K), 13.53 W/(m$^2$·K), 12.69 W/(m$^2$·K), and 13.20 W/(m$^2$·K), respectively. Among them, carborundum exhibited the best heat transfer enhancement effect, followed by white alundum, with quartz sand being the least effective.

Compared with the particle size of waste tires and the rotation speed of the pyrolysis furnace, the enhanced heat transfer materials with the most significant impact on heat transfer performance could effectively improve pyrolysis efficiency and reduce energy consumption.

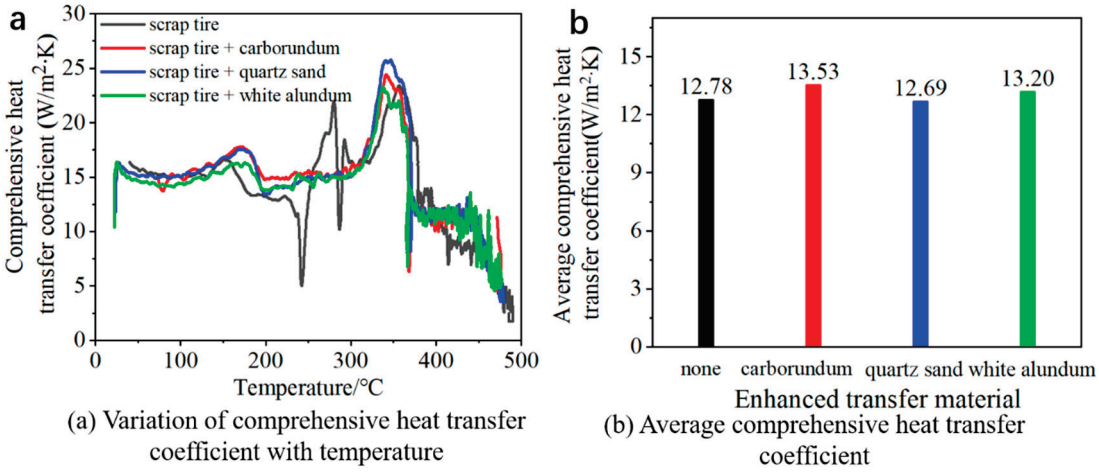



**Figure 13.** Comprehensive heat transfer performance after adding different enhanced heat transfer materials.

The mass of solid, liquid, and gaseous products of waste tire pyrolysis after mixing with different enhanced heat transfer materials was collected and analyzed. The distribution of pyrolysis products is shown in Figure 14.

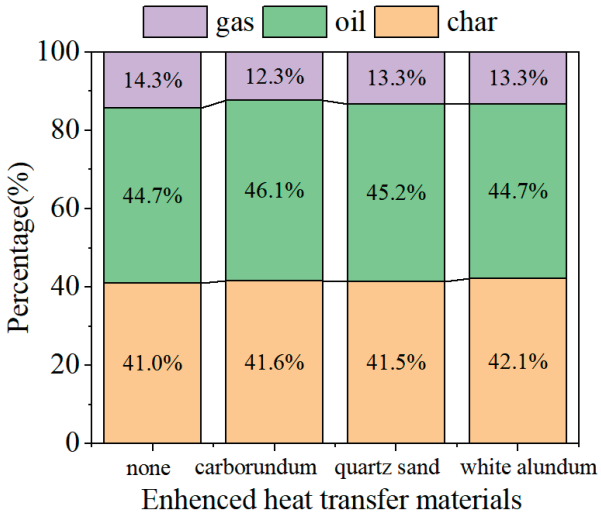



**Figure 14.** Effect of enhanced heat transfer materials on the distribution of pyrolysis products.

The results indicated that adding enhanced heat transfer materials had minimal impact on the solid products in the pyrolysis products, maintaining it at approximately 41%. After adding carborundum and quartz sand, the proportion of liquid products increased from 44.7% to 46.1% and 45.2%, respectively, while the proportion of gaseous products decreased from 14.3% to 12.3% and 13.3%. In contrast, adding white alundum had little effect on the liquid product fraction but slightly reduced the gaseous product fraction from 14.3% to 13.3%.

### *3.4. Effect of Installing Spiral Fins on Heat Transfer Performance*

Owing to the superior heat transfer performance and space-saving characteristics, spiral finned tubes were prevalently employed in heat exchange equipment. To enhance heat transfer efficiency, spiral fins were installed in this study, and the variation trends of material temperature with time were monitored, as shown in Figure 15.

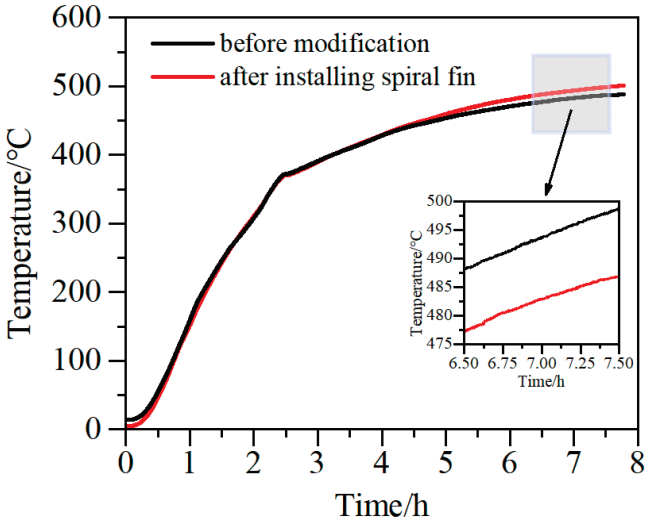



**Figure 15.** The temperature of waste tires over time when installing spiral fins.

As can be seen from Figure 15, the general trend of material temperature variation during the pyrolysis process of waste tires remained consistent before and after installation of spiral fins on the outer wall of the inner cylinder. The maximum temperature difference of the material layer after pyrolysis, before and after installing spiral fins on the outer wall of the inner cylinder, was 11.2 °C. The results showed that the influence of spiral fins on the final temperature of the material layer was limited.

The apparent heat transfer coefficients between the materials and the inner surface of the pyrolysis furnace, before and after installing spiral fins, were calculated based on the measured material temperatures, as shown in Figure 16.

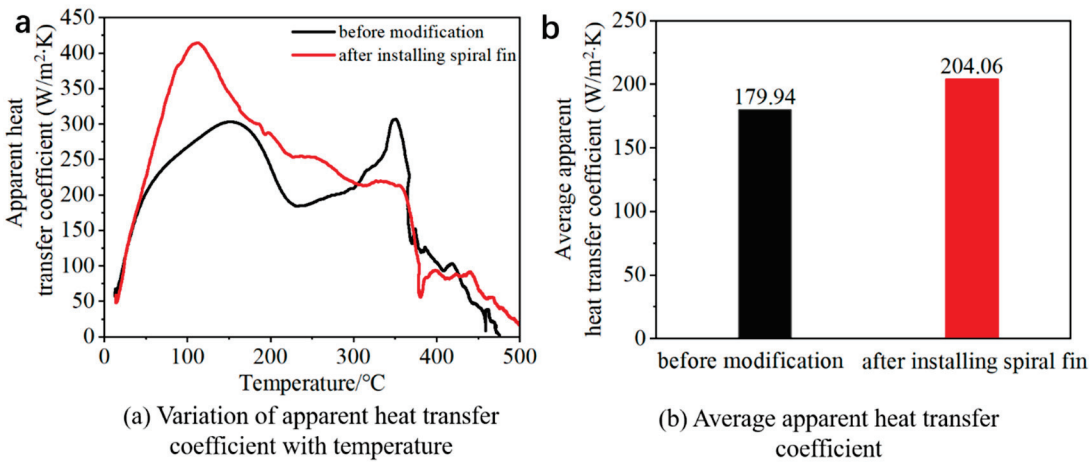
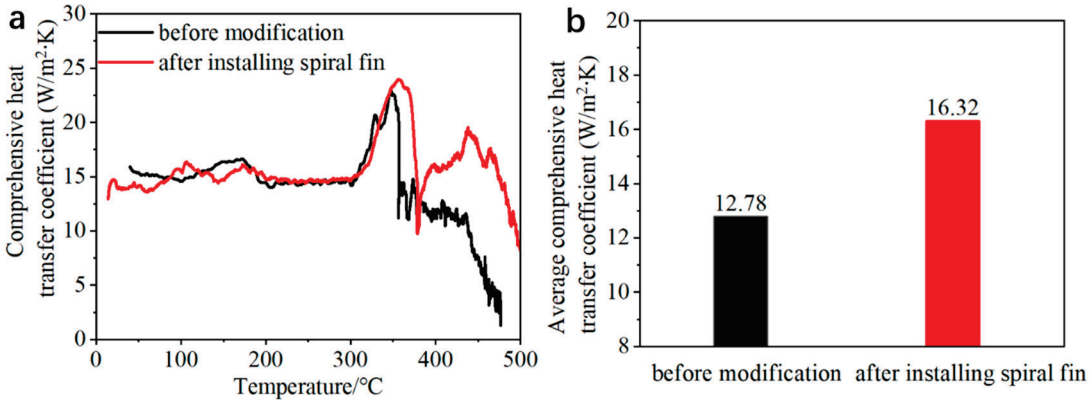



**Figure 16.** The apparent heat transfer coefficient between the inner wall of the inner.

After installing spiral fins on the outer wall of the inner cylinder of the rotary pyrolysis furnace, the maximum value of the apparent heat transfer coefficient in the water evaporation stage was higher than that before the modification. Subsequently, it decreased as the temperature increased, with a sharp decline observed at 370 °C. As shown in Figure 16b, the average apparent heat transfer coefficients before and after the modification were 179.94 W/(m$^2$·K) and 204.06 W/(m$^2$·K), with an increase of 13.60%, demonstrating that installation of spiral fins on the outer wall of the inner cylinder can significantly enhance heat transfer.

The comprehensive heat transfer coefficients before and after installation of spiral fins are shown in Figure 17.




(a) Variation of comprehensive heat transfer coefficient with temperature

(b) Average comprehensive heat transfer coefficient

**Figure 17.** Comprehensive heat transfer performance of the rotary pyrolysis furnace before and after modification.

## 4. Conclusions

In this study, the effects of tire particle size, rotary furnace rotation speed, addition of enhanced heat transfer materials, installation of spiral fins on the transfer performance, and distribution of pyrolysis products were investigated experimentally, and the following conclusions were drawn:

(1) During the process of waste tire pyrolysis, the use of powder particles ensured uniform heating, achieving the maximum comprehensive heat transfer coefficient of 12.78 W/(m$^2$·K) and the highest liquid products of 44.7%. However, the fine particles resulted in localized overheating, leading to deeper cracking and increased gaseous products.

(2) At a rotational speed of 3 rpm for the rotary pyrolysis furnace, there was sufficient contact between material and kiln wall, achieving the maximum comprehensive heat transfer coefficient 12.78 W/(m$^2$·K). The liquid product proportion was highest at rotational speeds of 1.5 rpm and 3 rpm, accounting for 45.0% and 44.7%, respectively.

(3) Adding carborundum or white alundum was beneficial for improving the heat transfer performance and heat transfer uniformity during the pyrolysis process, enhancing the pyrolysis efficiency, and reducing energy consumption, with comprehensive heat transfer coefficients of 13.53 W/(m$^2$·K) and 13.20 W/(m$^2$·K). Among them, there was a positive effect on the enhancement of the proportion of liquid product by adding carborundum, which increased to 46.1%.

(4) Compared with the unmodified pyrolysis chamber, the heat transfer enhancement effect was very obvious after the installation of spiral fins, and the comprehensive heat transfer coefficient was increased by 27.7% from 12.78 W/(m$^2$·K) to 16.32 W/(m$^2$·K).

(5) The operating parameters with the best heat transfer performance and the highest pyrolysis oil yield were obtained through this study, but these conclusions were obtained on small-scale experimental equipment and need to be verified through engineering practice before they can be promoted and applied.

**Author Contributions:** Writing—original draft preparation, H.M. and Y.B.; methodology, H.M.; validation, Y.B. and S.M.; writing—review and editing, S.M.; project administration, Y.B.; investigation, Z.Z. All authors have read and agreed to the published version of the manuscript.

**Funding:** This work is supported by the National Key Research and Development Program of China (No. 2022YFC3902300).

**Data Availability Statement:** The original contributions presented in this study are included in the article. Further inquiries can be directed to the corresponding author.

**Conflicts of Interest:** The authors declare no conflicts of interest.

## References

1. Hrynyshyn, K.; Skorokhoda, V.; Chervinskyy, T. Study on the composition and properties of pyrolysis 598pyrocondensate of used tires. *Chem. Chem. Technol.* **2022**, *16*, 159–163. [CrossRef]
2. Pyshyev, S.; Lypko, Y.; Demchuk, Y.; Kukhar, O.; Korchak, B.; Pochapska, I.; Zhytnetskyi, I. Characteristics and applications of waste tire pyrolysis products: A review. *Chem. Chem. Technol.* **2024**, *18*, 244–257. [CrossRef]
3. Adhikari, B.; Maiti, S. Reclamation and recycling of waste rubber. *Prog. Polym. Sci.* **2000**, *25*, 909–948. [CrossRef]
4. Xia, Y.; Yang, Y.; Zhu, C.; Ouyang, S.; Wang, J.; Li, L. Kinetic and thermodynamic characteristics in scrap tyres pyrolysis process and components analysis of pyrolysis oil. *Low-Carbon Chem. Chem. Eng.* **2023**, *48*, 36–44.
5. Qin, L.; Wang, L. Reaction kinetic analysis of waste tire pyrolysis catalyzed by WUST10. *Environ. Prot. Chem. Ind.* **2021**, *41*, 452–457.
6. Chang, Q.; Jin, L.; Feng, Z.X.; Li, A.; Shen, K. Research on the Control and Management of Atmospheric Pollutants in Waste Tire Pyrolysis Projects. *Fluid Meas. Control.* **2024**, *5*, 52–55.
7. Gao, N.; Wang, F.; Quan, C.; Santamaria, L.; Lopez, G.; Williams, P.T. Tire pyrolysis char: Processes, properties, upgrading and applications. *Prog. Energy Combust. Sci.* **2022**, *93*, 101022. [CrossRef]
8. Yang, Q.; Yu, S.; Zhong, H.; Liu, T.; Yao, E.; Zhang, Y.; Zou, H.; Du, W. Gas products generation mechanism during co-pyrolysis of styrene-butadiene rubber and natural rubber. *J. Hazard. Mater.* **2021**, *401*, 123302. [CrossRef]
9. Han, J.; Li, W.; Liu, D.; Qin, L.; Chen, W.; Xing, F. Pyrolysis characteristic and mechanism of waste tyre: A thermogravimetry-mass spectrometry analysis. *J. Anal. Appl. Pyrolysis* **2018**, *129*, 1–5. [CrossRef]
10. Kan, T.; Strezov, V.; Evans, T. Fuel production from pyrolysis of natural and synthetic rubbers. *Fuel* **2017**, *191*, 403–410. [CrossRef]
11. Zhang, H.L.; Fan, X.X.; Liu, Y.F. Experimental study on pyrolysis of blocky tires in a fixed-bed reactor. *Renew. Energy Resour.* **2015**, *33*, 149–153.
12. Caponero, J.; Tenório, J.A.S.; Levendis, Y.A.; Carlson, J.B. Emissions of batch combustion of waste tire chips: The afterburner effect. *Energy Fuels* **2003**, *17*, 225–239. [CrossRef]
13. Ziadat, A.H.; Sood, E. An environmental impact assessment of the open burning of scrap tires. *J. Appl. Polym. Sci.* **2014**, *14*, 2695–2703. [CrossRef]
14. Labaki, M.; Jeguirim, M. Thermochemical conversion of waste tyres—A review. *Environ. Sci. Pollut. Res.* **2017**, *24*, 9962–9992. [CrossRef]
15. Yan, D. *Study on the Utilization of Pyrolytic Products from Pyrolysis of Used Tyre in a Pilot-Scale Rotary Kiln and the Mechanism and Kinetic Model of Rubber Pyrolysis*; University of Zhejiang: Hangzhou, China, 2006.
16. Kar, Y. Catalytic pyrolysis of car tire waste using expanded perlite. *Waste Manag.* **2011**, *31*, 1772–1782. [CrossRef]
17. Galvagno, S.; Casu, S.; Casabianca, T.; Cornacchia, G. Pyrolysis process for the treatment of scrap tyres: Preliminary experimental results. *Waste Manag.* **2002**, *22*, 917–923. [CrossRef]
18. Yin, Z.J.; Zhang, H.; Han, T. Simulation of particle flow on an elliptical vibrating screen using the discrete element method. *Powder Technol.* **2016**, *302*, 443–454. [CrossRef]
19. Zhu, H.P.; Yu, A.B. A theoretical analysis of the force models in discrete element method. *Powder Technol.* **2006**, *161*, 122–129. [CrossRef]
20. Zhao, Y.; Yang, S.L.; Zhang, L.Q.; Chew, J.W. Understanding the varying discharge rates of lognormal particle size distributions from a hopper using the Discrete Element Method. *Powder Technol.* **2019**, *342*, 356–370. [CrossRef]
21. Tchapda, A.H.; Pisupati, S.V. A review of thermal co-conversion of coal and biomass/waste. *Energies* **2014**, *7*, 1098–1148. [CrossRef]
22. Undri, A.; Rosi, L.; Frediani, M.; Frediani, P. Upgraded fuel from microwave assisted pyrolysis of waste tire. *Fuel* **2014**, *115*, 600–608. [CrossRef]
23. Beaumontt, O.; Schwob, Y. Influence of physical and chemical parameters on wood pyrolysis. *Ind. Eng. Chem. Res. Des. Dev.* **1984**, *23*, 637–641. [CrossRef]
24. Oyedun, A.; Lam, K.L.; Fittkau, M.; Hui, C.W. Optimisation of particle size in waste tyre pyrolysis. *Fuel* **2012**, *95*, 417–424. [CrossRef]
25. Kaminsky, W.; Mennerich, C.; Zhang, Z. Feedstock recycling of synthetic and natural rubber by pyrolysis in a fluidized bed. *J. Anal. Appl. Pyrolysis* **2009**, *85*, 334–337. [CrossRef]

26. Raj, R.E.; Kennedy, Z.R.; Pillai, B.C. Optimization of process parameters in flash pyrolysis of waste tyres to liquid and gaseous fuel in a fluidized bed reactor. *Energy Convers. Manag.* **2013**, *67*, 145–151. [CrossRef]
27. Cheng, Z.; Liang, J.; Kawamura, K.; Zhou, H.; Asamura, H.; Uratani, H.; Tiwari, J.; Graham, S.; Ohno, Y.; Nagai, Y.; et al. High thermal conductivity in wafer-scale cubic silicon carbide crystals. *Nat. Commun.* **2022**, *13*, 7201. [CrossRef]
28. Xia, J.; Qin, Y.; Wei, X.; Li, L.; Li, M.; Kong, X.; Xiong, S.; Cai, T.; Dai, W.; Lin, C.-T.; et al. Enhanced Thermal Conductivity of Polymer Composite by Adding Fishbone-like Silicon Carbide. *Nanomaterials* **2021**, *11*, 2891. [CrossRef]
29. AbdulKarim-Talaq, M.; Hassan, K.T.; Hameed, D.A. Improvement of thermal conductivity of novel asymmetric dimeric coumarin liquid crystal by doping with boron nitride and aluminium oxide nanoparticles. *Mater. Chem. Phys.* **2023**, *297*, 127367. [CrossRef]
30. Kedzierski, M.A.; Brignoli, R.; Quine, K.T.; Brown, J.S. Viscosity, density, and thermal conductivity of aluminum oxide and zinc oxide nanolubricants. *Int. J. Refrig.* **2017**, *74*, 3–11. [CrossRef]
31. Liu, L.; Cai, G.; Liu, X.; Liu, S.; Puppala, A.J. Evaluation of thermal-mechanical properties of quartz sand-bentonite-carbon fiber mixtures as the borehole backfilling material in ground source heat pump. *Energy Build.* **2019**, *202*, 109407. [CrossRef]
32. Ju, Z.; Lu, S.; Guo, K.; Liu, X. Changes in the thermal conductivity of soil with different salts. *J. Soils Sediments* **2023**, *23*, 3376–3383. [CrossRef]


**Disclaimer/Publisher's Note:** The statements, opinions and data contained in all publications are solely those of the individual author(s) and contributor(s) and not of MDPI and/or the editor(s). MDPI and/or the editor(s) disclaim responsibility for any injury to people or property resulting from any ideas, methods, instructions or products referred to in the content.

energies

MDPI

*Article*

# Numerical Simulation of Pool Boiling on Novel Microstructured Heated Surface

**Chen Xu [1] Yizhou Wang [1,*], Xinrong Zhang [1,*], Wenyi Li [2] and Jieru Li [2]**

[1] School of Mechanics and Engineering Science, Peking University, Beijing 100871, China; xchester@pku.edu.cn
[2] Peking University Ordos Research Institute of Energy, Ordos 017000, China
* Correspondence: pku_wyz@stu.pku.edu.cn (Y.W.); xrzhang@pku.edu.cn (X.Z.); Tel.: +86-010-62755052 (X.Z.)

**Abstract**

Improving the pool boiling heat transfer by changing the properties of the heating surface has been experimentally studied by many researchers. In this paper, two novel microstructured surfaces with open channels were simulated and investigated. The two microstructured surfaces had different cavity positions and different groove widths of open channels. At the same time, a pool boiling experiment on the plain-heated surface was carried out to verify the reliability and accuracy of the CFD model. The results showed the relationship between the heat flux and wall superheat. Moreover, the bubble dynamic behaviors of different surfaces were obtained. It was found that both microstructured surfaces could enhance the pool boiling heat transfer coefficient (HTC) and critical heat flux (CHF). Enlarging the length of the groove gap can not only increase the heat transfer area, but also increase the bubble nucleation rate. However, constantly increasing the groove width will cause the horizontal coalescence of bubbles on the heating surface at low heat flux. When the negative effect of bubble coalescence is higher than the enhancement effect, the boiling heat transfer capacity of the heating surface will decrease unless the heat flux is high enough to delay bubble coalescence.

**Keywords:** open-channel microstructured surface; CFD simulation; bubble departure frequency and diameter; heat transfer coefficient; critical heat flux

## 1. Introduction

The miniaturization trend of mechanical and electronic components is the driving force behind the widespread attention to compact passive phase change heat transfer, which aims to obtain better HTC in smaller heated surfaces and effectively prevent the equipment from exceeding the CHF at the same time. Pool boiling is the preferred method to meet this requirement. Many researchers have studied how to improve the pool boiling heat transfer performance including changing the properties of the working medium [1], adding nanoparticles [2], machining the heating surface [3], and so on. With the advancement of high-power electronics and special scenarios (e.g., space exploration, natural gas liquefaction), pool boiling heat transfer has become crucial for thermal management, and novel microstructured heated surfaces (micro/nano composite gradient porous, micropillar arrays, grooved/spline-patterned) have significantly enhanced its performance by optimizing the vapor-liquid dynamics [4–6].

However, the conclusions of these methods in the experiment are not uniform, and there is still some dispute regarding the effectiveness of these methods in improving the heat performance of pool boiling. Among them, the microstructure surface can not only

analyze the pool boiling heat transfer performance from the perspective of heat transfer, but also reveal some heat transfer laws from the perspective of bubble dynamics. Therefore, it is an effective means to achieve the goal of enhanced heat transfer, whether from the study of the microstructure or macro phenomena.

Mehralizadeh et al. [7] regarded three methods to improve the boiling heat transfer by changing the heating surface: (1) the surface textures, (2) surface characteristics, and (3) surface structures. The modification of these parts had a significant effect on the bubble dynamics, HTC, and CHF in the evaluation of the boiling process. Since first reported in the study by Nakayama et al. [8–10], open micro-channel surfaces have better heat transfer performance. A large number of existing studies in the broader literature have examined microstructured heated surfaces. Kim et al. [11] designed a set of experiments on microstructured heated surfaces where the experimental results showed that the HTC and CHF of the microstructure surface were not only higher than that of the smooth surface, but were also closely related to the gap size of the microstructure. The smaller gap size improved the heating surface roughness, which improved the surface capillary wicking rate. The experimental data of Chu et al. [12] also supported this view. It is considered that the roughness of the modified heating surface and the amplification of capillary force are the reasons for the enhancement of CHF on the microstructure surface

Zhang et al. [13] conducted a series of boiling experiments using an alumina sponge-like nanoporous surface as the heated surface. The results showed that the heat transfer effect was significantly enhanced due to the significant increase in active nucleation sites. Dong et al. [14] conducted experiments on horizontal heated surfaces with microstructures and found that the microstructure surface had a higher HTC, especially the microstructure with a smaller size. The large-size microstructure surface could only increase the heating surface area to improve the HTC, while the small-size microstructure could significantly increase the density of the bubble nucleation center. Mitrovic et al. [15] developed a cylindrically shaped type of microstructure and used it in pool boiling experiments with the refrigerant R141b at atmospheric pressure. They also concluded that the bubble nucleation density on the surface of microstructure increased significantly. Kong et al. [16] used six different kinds of micro-pin-finned surfaces for experiments. The results showed that the CHF of the microstructure surface could reach 120% of that of the smooth surface. This is because the micro-pin-finned region could not only form a large number of nucleation points, but also the growth, aggregation, and merging of bubbles were more active.

On the other hand, in addition to using pin-fin surfaces, Bian et al. [17] also used grooves and cubed microstructure surfaces for experimental research. The experimental results showed that the microstructure surface of grooves and cubes was obviously helpful for heat transfer enhancement. However, compared with the smooth plane, the effect of pin-fin surfaces on improving thermal efficiency was not ideal.

The last decades have seen a growing interest trend toward open channels embedded on heated surfaces. Kandlikar et al. [18–20] conducted a series of tests using open microchannel surfaces and believed that this efficient surface allows the liquid to quickly fill the nucleation positions of bubbles to enhance heat transfer. At the same time, the study found that surfaces with deeper and wider microchannels showed the best effect on enhancing heat transfer. Das et al. [21,22] also used several structural surfaces with different open channels to explore their enhancement effect on boiling heat transfer. Nucleate boiling heat transfer was found to be much more apparently augmented because the open channel provided more discrete bubble nucleation sites for the heated surface than the increase in the heated surface area. However, the research results of Kim et al. [23] showed that the CHF of the microstructure is determined by both the bubble separation frequency and the

rewetting ability of the heated surface. The increase in surface liquid flow resistance caused by microstructure could degrade the value of CHF.

Several kinds of research have been proposed for microstructured surfaces, some focusing on the enhancement of HTC, and others on CHF values. Although the reasons for the change in boiling heat transfer characteristics caused by the microstructure surface are different in the literature, it is certain that they are related to the change in bubble dynamics. Furthermore, how specific microstructural parameters, such as cavity positions and the groove widths of open channels, quantitatively affect pool boiling heat transfer has not been clearly clarified, making it difficult to guide the precise design of high-performance heating surfaces. This study therefore focused on these parameters to reveal their intrinsic influence mechanisms, aiming to offer practical references for improving the efficiency of pool boiling systems.

As organizing and characterizing the boiling performances and bubble dynamics reflected on the various micro-scale structured surface were of interest, simple simulations and analysis were introduced in this study. Based on the CFD method, the two-dimensional simulation of the microstructure heating surface was carried out by using the commercial software FLUENT to clearly show the boiling performance and bubble dynamics. Two novel types of open-channel microstructure heated surfaces had different positions of easily nucleated points. At the same time, by changing the groove width of the open channel, the main influence of the bubble dynamics affecting the boiling performance on the microstructured surfaces was studied. Furthermore, the pool boiling experiment was conducted to validate the simulation results, and the bubble dynamic behaviors on the smooth surface were observed using a high-speed experimental system.

## 2. Simulation Model

In the present study, a square liquid area was conducted to investigate pool boiling on a microstructured surface, as shown in Figure 1. Surface 1 and surface 2 had the same heating area but different nucleation sites. However, the different lengths of the groove width will change the heating area. In the process of the numerical simulation, water was used as the boiling working medium. The boiling process involves two phases: liquid water and water vapor. It was assumed that liquid water and water vapor are incompressible fluids with constant physical properties under saturation temperature and pressure. The open channels with two different structures were evenly distributed on the surface of the heating surface, the hydrophilicity and hydrophobicity of the whole wall were consistent, and it was assumed that the physical parameters did not change with temperature. The parameters of the microstructure are listed in Table 1. The groove was set as the groove length, which was the only variable.

**Table 1.** Parameters of the microstructured open channels.

| Items | Category | Groove Length |
|---|---|---|
| Case 1 | Surface 1 | 300 μm<br>500 μm<br>700 μm |
| Case 2 | Surface 2 | 300 μm<br>500 μm<br>700 μm |

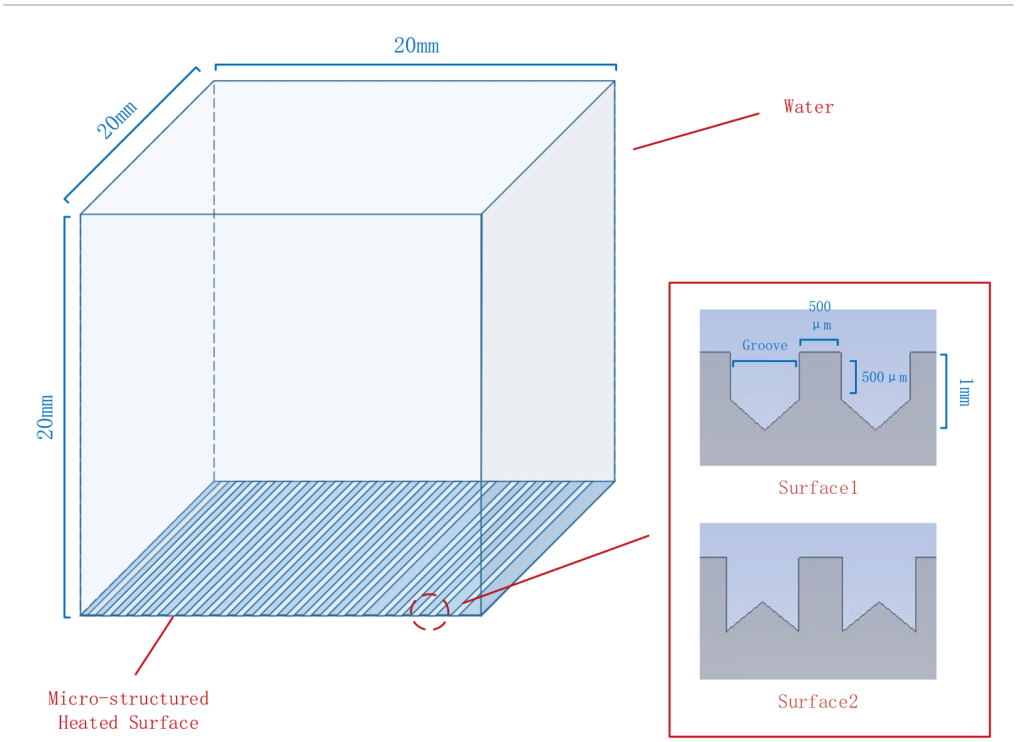



**Figure 1.** Macroscale model of the computational domain.

### *2.1. Governing Equation and Multi-Phase Flow Model*

The VOF model was used to simulate the multi-phase pool boiling process. Studies using VOF to simulate phase transition are well-documented [24–26]; it is also well-acknowledged that VOF makes the calculation of phase transition easier by defining the motion of all phases and tracking the position of interfaces accordingly. The fluid volume fraction in the mesh is defined as $\alpha_l$, so the specific phase of the control volume can be defined easily by $\alpha_l$.

$$\begin{cases} \alpha_l = 0 & Vapor \\ 0 < \alpha_l < 1 & Mixture \\ \alpha_l = 1 & Water \end{cases} \tag{1}$$

The relevant conservation equations of mass, momentum, and energy with the source terms are as follows [27]:

Continuity equation:

$$\frac{\partial}{\partial u}(\alpha_l \rho_l) + \nabla \cdot \left(\alpha_l \rho_l \vec{u}\right) = S_M \tag{2}$$

where $\rho_l$ and $u$ are the density and velocity of the primary phase (liquid phase), respectively, and the volume fraction for the secondary phase (v) can be calculated using Equation (3). $S_M$ is the mass source term that can be chosen as the Lee model in FLUENT, which is used to transport the mass from one phase to another during the evaporation and condensation processes.

$$\alpha_l + \alpha_v = 1 \tag{3}$$

Momentum equation:

$$\frac{\partial}{\partial u}\left(\rho \vec{u}\right) + \nabla \cdot \left(\rho \vec{u} \vec{u}\right) = -\nabla p + \rho \vec{g} + \nabla \cdot \left[\mu\left(\nabla \vec{u} + \nabla \vec{u}^T\right) - \frac{2}{3}\mu \nabla \cdot u\delta\right] + S_F \tag{4}$$

where $\rho$ and $\mu$ represent the density and viscosity of the mixture, respectively, and $\delta$ is the surface tension coefficient. The thermophysical properties (density, viscosity, and surface tension) of deionized water are temperature-dependent in the simulation. This dependency is realized through a UDF coupled with the heat transfer source term. $S_F$ is the continuum surface force (CSF) acting on the interface between two phases and is used in FLUENT as implicit body force. According to the VOF model, the value of $\rho$ and $\mu$ only depend on the volume fraction of the phase via the following equations:

$$\rho = \alpha_l \rho_l + \alpha_v \rho_v \tag{5}$$

$$\mu = \alpha_l \mu_l + \alpha_v \mu_v \tag{6}$$

Energy equation:

$$\frac{\partial}{\partial u}(\rho E) + \nabla \cdot \left[ \vec{u}(\rho E + p) \right] = -\nabla \cdot \left( k_{eff} \nabla T \right) + S_E \tag{7}$$

where $E$ (energy), $k_{eff}$ (thermal conductivity), and $T$ (temperature) are the average variables:

$$k_{eff} = \alpha_l k_l + \alpha_v k_v \tag{8}$$

$$E = \frac{\sum_{i=l}^{v} \alpha_i \rho_i C_{p_i}}{\sum_{i=l}^{v} \alpha_i \rho_i} \cdot (T - T_{sat}) \tag{9}$$

where $C_{pi}$ is the specific heat of the phase. $S_E$ is the energy source term, which can be calculated from the mass source term.

The numerical simulation was operated under atmosphere pressure. Next, we assumed that the heat transfer applied from the heated surface was only used for the vapor generation, and all of the walls were adiabatic conditions except the heated wall. The numerical model settings and parameters are listed in Table 2.

**Table 2.** Numerical simulation parameters.

| Elements | Setting | Elements | Setting |
|---|---|---|---|
| Model | 2D Transient | Mass transfer | Evaporation-Condensation (Lee) |
| Multi-phase model | VOF | Pressure-velocity coupling | Simple |
| Surface tension force | 0.059 | Pressure | PRESTO! |
| Viscous model | Laminar | Momentum and energy | Second Order Upwind |

### *2.2. Grid Independence Test*

In order to ensure the precision of the model and verify the reliability, three different accuracies were used to obtain the calculation results of different grids under the same working conditions to test the independence of the grid. Under the boundary condition of 10 kW/m$^2$ heat flux, the grid test was carried out on the smooth plane, Surface 1, with a 500 μm groove width, and Surface 2 with a 500 μm groove width. The results are listed in Table 3. It was found that the differences among the wall superheat under different grid numbers were not greater than 3%. Therefore, the grid systems with numbers 161,036, 165,257, and 167,680 were adopted for computation.

**Table 3.** Grid independence test.

| Heat Flux (kW/m$^2$) | Items | Grid Number | Wall Grid Spacing (μm) | Wall Superheat |
|---|---|---|---|---|
| 10 | Smooth plane | 43,552 | 100 | 4.88 |
| | | 161,036 | 80 | 4.9 |
| | | 638,159 | 50 | 4.85 |
| | Surface 1 | 41,860 | 100 | 3.89 |
| | | 165,257 | 80 | 4.01 |
| | | 653,106 | 50 | 3.92 |
| | Surface 2 | 42,133 | 100 | 4.1 |
| | | 167,680 | 80 | 4.15 |
| | | 668,232 | 50 | 4.07 |

## 3. Experiment Setup

### *3.1. Experimental Description and Uncertainty*

In order to further verify the accuracy of the simulation, a set of pool boiling experimental equipment, as shown in Figure 2, was used to collect the pool boiling experimental data of the smooth plane. The experimental setup consisted of four main parts: power control system, working fluid boiling system, data acquisition system, and heating copper column device. The power control system included an AC power supply. The input heat load controlled by the voltage regulator passes through the voltage regulator and the input value is clearly displayed on the power meter. After heating, the data acquisition system collects the relevant experimental data. The real-time temperature data displayed by the temperature sensor through the digital display controller are recorded by the computer. At the same time, the dynamic changes of bubbles during boiling are recorded by the high-speed camera. The working fluid boiling system was composed of a $10 \times 10 \times 10$ cm$^3$ square container made of high borosilicate glass, and the glass reflection cover above the container was connected with a condensation pipe, a preheating heating rod, and a temperature sensor. The dimensions of the heating rod are shown in Figure 3. Observation ports were reserved on both sides of the container, and under the container was a $2 \times 2$ cm$^2$ smooth heated plane, which was also the top of the red copper heating column. In addition, the whole device was wrapped with thermal insulation materials, and Teflon plates were installed at the connection with the boiling vessel to increase the sealing and thermal insulation.

The uncertainty in this study was mainly caused by thermocouples with an accuracy of 0.1 K. This negligible change in the data acquisition system used was considered as no uncertainty. The uncertainty of the nucleate pool boiling heat transfer coefficient is calculated as [28]:

$$\varepsilon\% = \frac{\Delta h}{h} = \sqrt{\left(\frac{\Delta q}{q}\right)^2 + \left(\frac{\Delta T_W}{T_W - T_{sat}}\right)^2 + \left(\frac{\Delta T_{sat}}{T_W - T_{sat}}\right)^2} \quad (10)$$

The maximum uncertainty in the boiling heat transfer coefficient in this research was in the range of 3.7–8.6%.

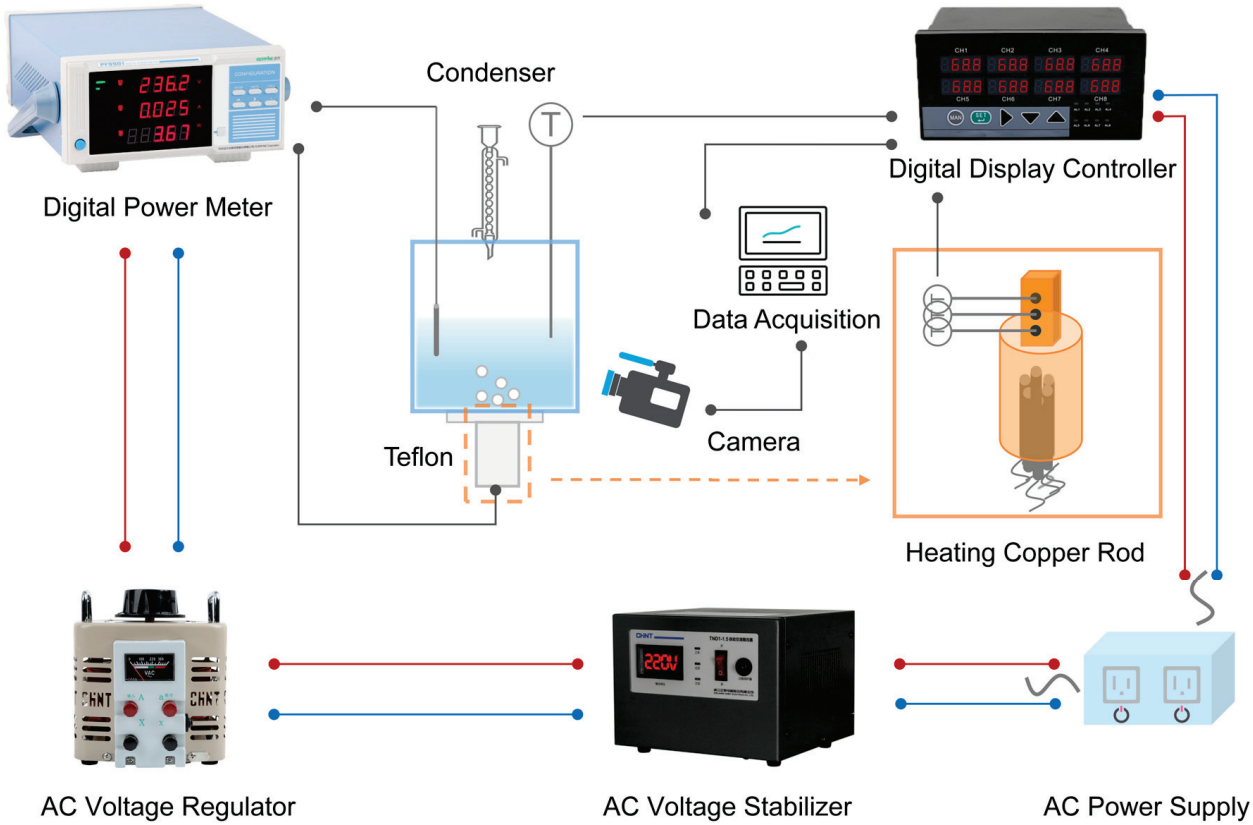



**Figure 2.** Experimental apparatus.




**Figure 3.** The heating copper column device.

### *3.2. Simulation Validation*

In addition, the simulation and experimental results of the plain surface were compared with the Rohsenow curve in Figure 4, which was plotted with Rohsenow's equation [29]. It can be seen from the graph that the simulation results were in good agreement with the experimental data and Rohsenow curve, which proves the accuracy and reliability of the research method in this paper. Figure 5 showed the differences between experimental and simulation boiling curves for plan and microstructured surfaces.

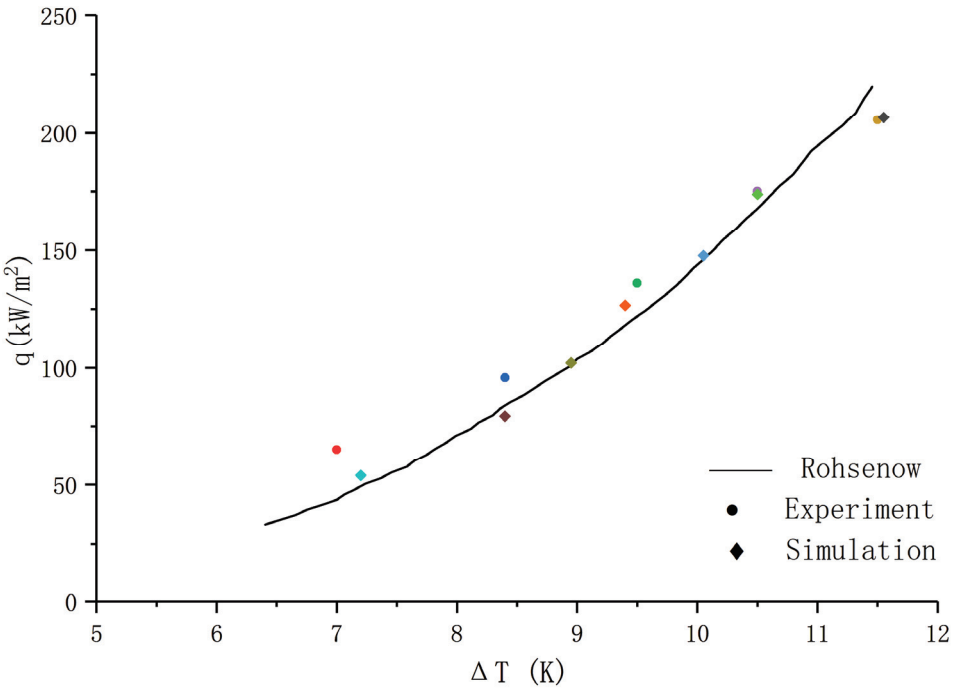



**Figure 4.** Validation of the simulation results with the experimental results and Rohsenow curve.

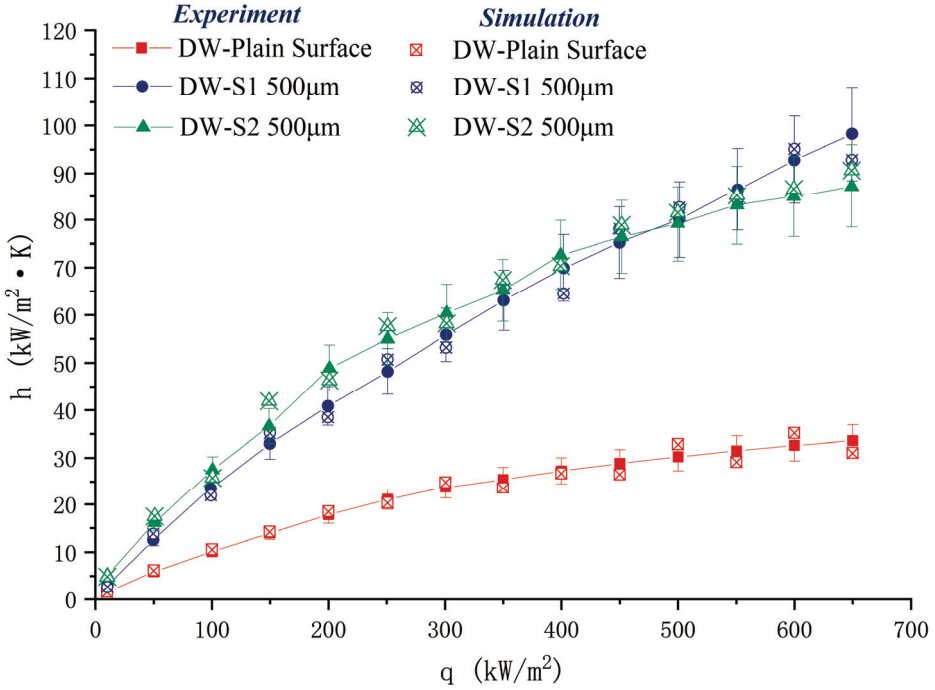



**Figure 5.** Validation of the simulation results with the experimental results for the microstructured surfaces.

## 4. Results and Discussion

### *4.1. Pool Boiling Characteristics*

In order to study the effect of the microstructure surface on the boiling performance, a pool boiling simulation was carried out on microstructure heated surfaces with different structures under the same boundary conditions. These results were then compared with the smooth heated surface. Moreover, the groove width of the open channel was changed to further explore the influence of the microstructure on the bubble dynamics during boiling.

Figure 6 shows the pool boiling curve related to the heat flux and wall superheat to characterize the boiling heat transfer performance of the heated surface. From the figure, it can be concluded that the superheat of all microstructure surfaces was lower than that of the smooth surfaces under the same heat flux. This is because microstructures expand the heat area, reduce the nucleation energy, and boost liquid replenishment via capillarity. Especially at high heat flux, the enhancement of nucleate boiling in the microstructure surface was more obvious than that on the smooth plain surface. The microstructure surfaces could dissipate more heat than the plain surface for the same superheat. This is why the microstructured surfaces also had a higher CHF. When ΔT approached 25 K (Figure 6), q growth slowed as the surfaces entered late nucleate boiling—smooth surfaces lacked liquid replenishment, while microstructured ones faced a reduced effective area, though still outperformed the smooth surfaces.

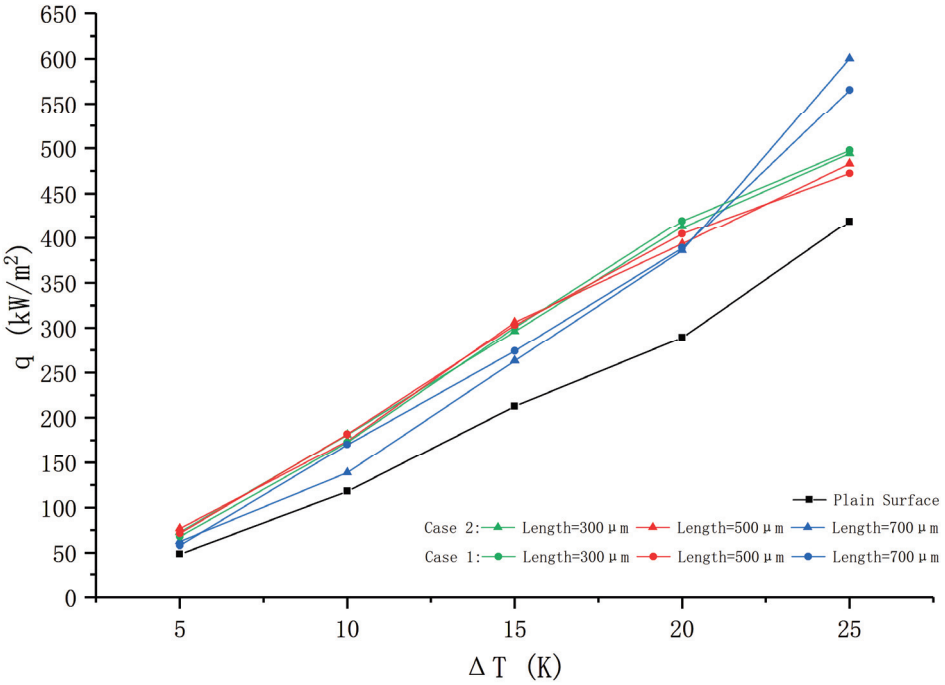



**Figure 6.** Pool boiling curve (heat flux versus wall superheat).

The HTC curve in Figure 7 showed the same boiling characteristics, which further confirmed the improvement effect of the microstructured surface on heat transfer performance. It can be seen from the figure that the boiling curve trend of each microstructured surface is complex. In general, the improvement in the nucleate boiling heat transfer performance on the heating surface of the open channel with the 500 μm groove width was stronger than that with 700 μm. The 500 μm grooves balanced nucleation promotion and coalescence suppression, while the 700 μm ones caused excessive merging, lowering the HTC. With regard to the microstructured surfaces with the same groove width, surface 1 had a better heat transfer improvement effect than surface 2 under the 500 μm length, and this improvement was consistent with the change in heat load. However, the promotion advantage of the two microstructure surfaces to HTC varied with the change in heat flux when the groove width was 300 μm or 700 μm. Figures 6 and 7 are linear because q is roughly proportional to ΔT in the narrow nucleate boiling range, thus HTC stays nearly constant.

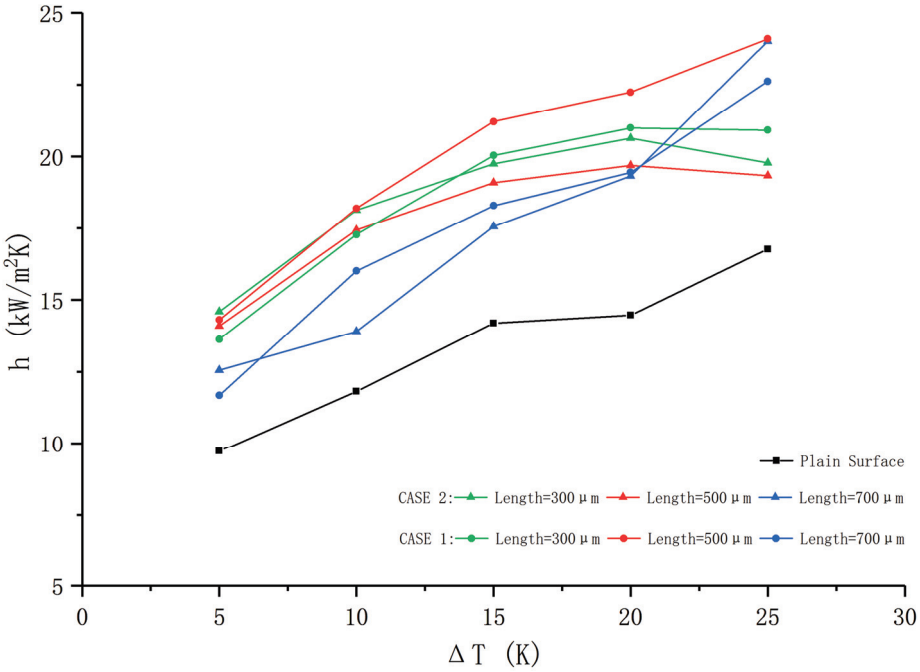
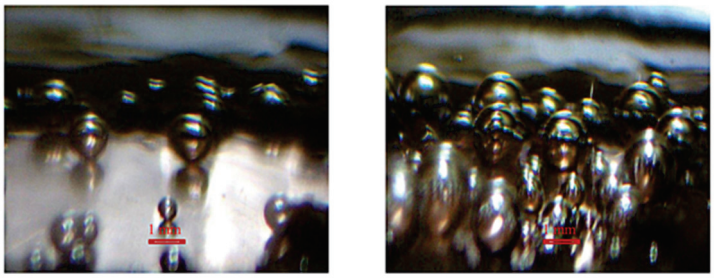



**Figure 7.** Pool boiling curve (heat transfer coefficient versus wall superheat).

Therefore, the enhancement of heat transfer affected by the microstructured surface cannot simply be attributed to the expansion of the heat transfer area. Especially with the rise in heat flux, the heat transfer difference between various heated surfaces sharply increases. The change in bubble behaviors on the plain surface under different heat fluxes is shown in Figure 8, which was photographed by a high-speed camera. It can be seen from the figure that the change in heat flux had a significant impact on the bubble dynamics of the heated surface. With the increase in heat flux, the heated surface had a lot more bubble nucleation points, a smaller bubble diameter, and faster separation frequency. The results of the plain surface boiling experiments showed that the key factor influencing the enhancement effect of pool boiling may be the change in bubble dynamics on the heated surface.



(**a**) 25 kW/m² (**b**) 75 kW/m²

**Figure 8.** Boiling experiment on the plain surface.

*4.2. Bubble Nucleation and Growth*

Figure 9 shows the bubble behavior of grooves with different widths on surface 1 during nucleate boiling. As can be seen from Figure 8, the number of bubble nucleation points increased linearly with the increase in length. This is because the increase in groove length increases the heat transfer area. When boiling occurs, there are more single nucleation points of bubbles. However, it is not simply that the more nucleation points, the better the heat transfer effect.

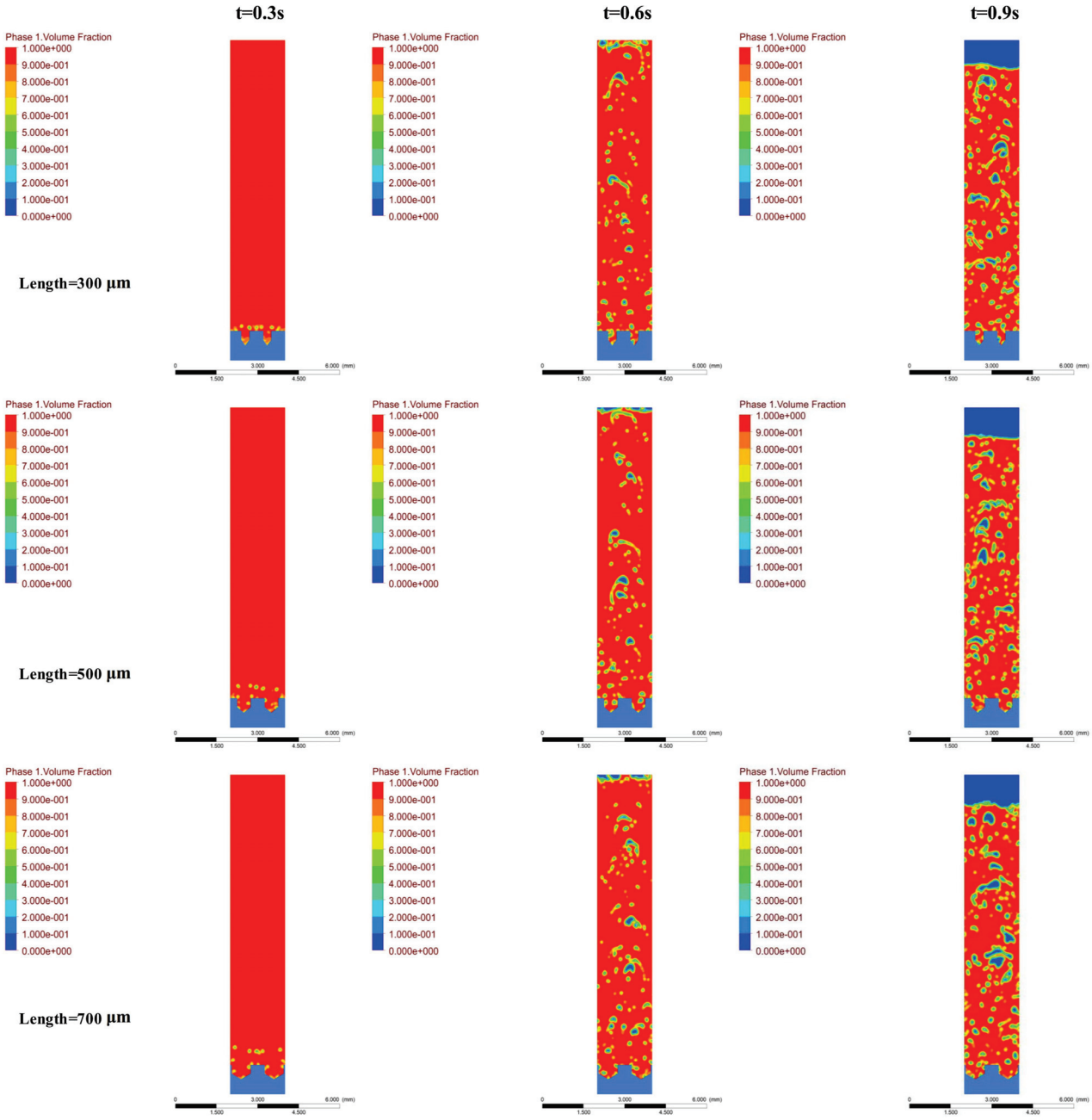



**Figure 9.** 2D view of bubble behaviors on surface 1 with different groove lengths.

When the length increased from 300 μm to 500 μm, the bubble density increased significantly, while when the length continued to increase to 700 μm, the bubble density decreased. It can be found that when the length was 300 μm, although the microstructured surface generated more nucleation sites compared with the plain, the bubbles in the upper half of the groove hindered the generation of bubbles at the bottom due to the narrow gap of the grooves. When the length increased to 500 μm, the number of bubble nucleation points further increased. At the same time, the disturbance between bubbles was decreased, which introduced the frequency of bubble departure acceleration. Therefore, the bubble density was higher and the HTC was better.

However, when the length further increased to 700 μm, the bubbles began to gather laterally due to the large space and formed with a larger diameter before the departure. Therefore, the bubble separation frequency became slower, the bubble diameter became larger, and the heat transfer effect became weaker. The heat transfer effect would then be enhanced

when the buoyancy of bubbles is large enough at a higher heat flux to reduce the transverse aggregation of bubbles. This also verifies the boiling curve results shown in Figures 6 and 7.

In theory, surface 2 has more cavities to produce more bubble nucleation points compared with surface 1. However, it can be seen from Figure 10 that the bubble density decreased and the bubble separation diameter was larger with the increase in groove length. As shown in Figure 10, the cavity structure did increase the number of bubble nucleation points at the beginning of boiling, but the bubbles also emerged to coalesce during their growth process.

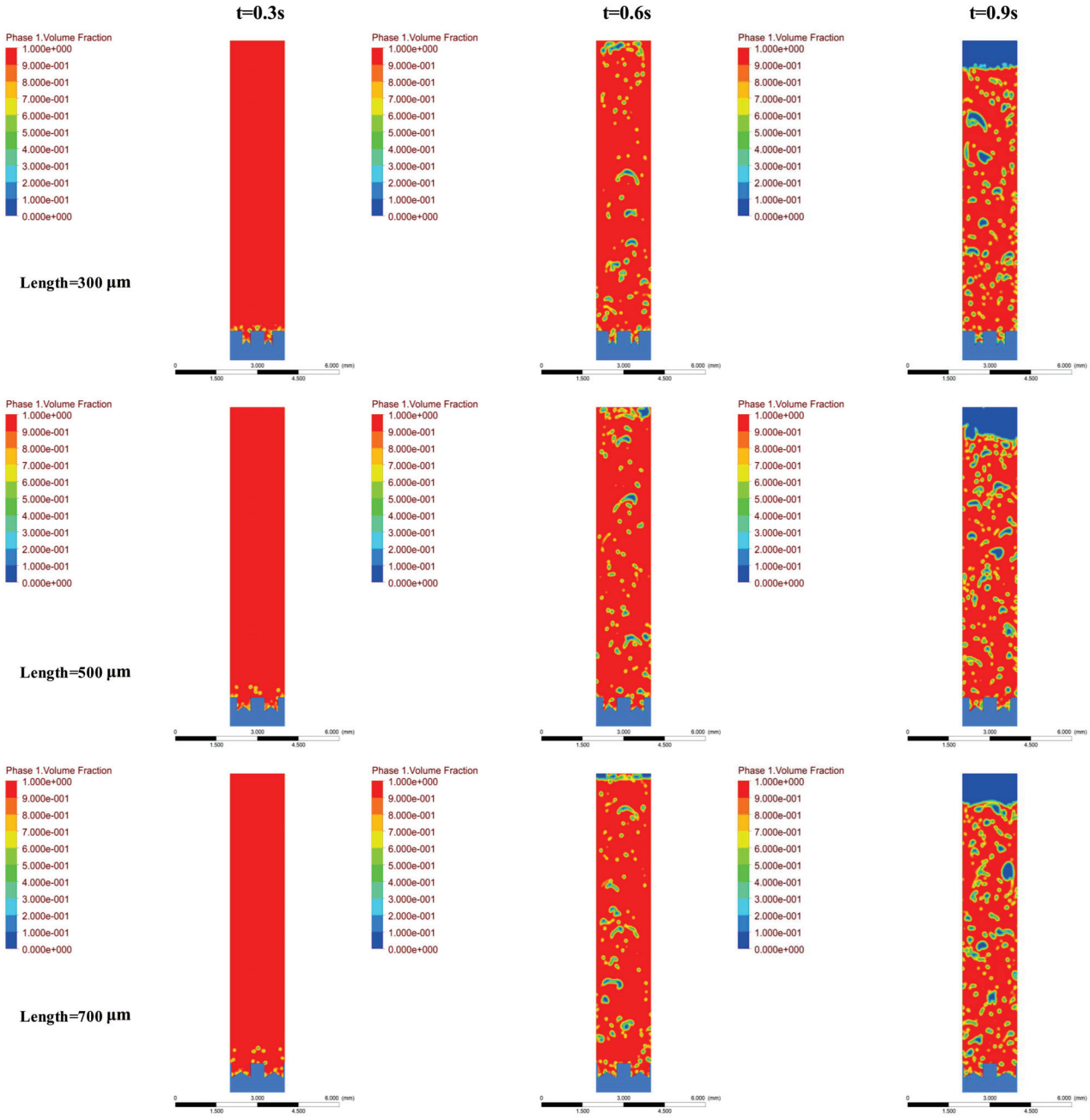



**Figure 10.** 2D view of bubble behaviors on surface 2 with different groove widths.

The coalescence process of bubbles reduces the bubble departure rate. When the length was 500 μm, the heat transfer effect of increasing the nucleation points was stronger than the negative effect of reducing the bubble departure frequency, so the heat transfer had the best efficiency. With the growing length of the groove gap, the bubble diameter kept being larger, and the heat transfer effect was reduced for the decreased bubble departure frequency. This negative effect can only be offset at high heat flux.

## 5. Conclusions

In conclusion, pool boiling heat transfer is a complex phenomenon, and the accurate simulation of this process can be difficult. The proposed CFD model was validated with the Rohsenow curve and available experimental data, and further validation is still necessary over more complex operating conditions. The purpose of this paper was to show the bubble dynamic behaviors on novel open-microchannel surfaces through simulation. The simulation and experimental investigation led to the following conclusions:

- The boiling effect of each microstructured surface was better than that of the plain heated surface, which was due to the increase in the heat transfer area of open channels. Furthermore, the structure of surface 1 had a better HTC than surface 2 because the bubble dynamics play a more important role in nucleate boiling.
- A larger length of groove can increase the bubble nucleation rate to further improve the boiling effect, which could obviously be observed in the simulation results. At the same time, an enhanced groove gap can lead to bubbles emerging with bigger diameters.
- At low heat fluxes, constantly increasing the width of the groove will obtain a descending HTC by facilitating bubble coalescence and decreasing the bubble departure frequency. Additionally, the structure of the open channel will also affect the growth and separation process of the bubbles, since bubbles were more likely to coalesce on surface 2 than on surface 1. Thus, the microstructured surfaces had a greater HTC and CHF at high fluxes when the bubble release frequency was higher, and the merging of bubbles was delayed.

**Author Contributions:** Conceptualization, C.X. and Y.W.; Methodology, C.X. and X.Z.; Software, C.X.; Validation, C.X., Y.W. and X.Z.; Formal analysis, C.X.; Writing—original draft preparation, C.X.; Writing—review and editing, Y.W. and X.Z.; Visualization, C.X.; Supervision, W.L. and J.L.; Funding acquisition, X.Z. All authors have read and agreed to the published version of the manuscript.

**Funding:** This research was funded by the Inner Mongolia Autonomous Region Science and Technology Major Project, Technology Research and Application of Wind Photovoltaic Storage Cooling Heating Electricity Zero Carbon Airport Construction.

**Data Availability Statement:** Data is contained within the article.

**Conflicts of Interest:** The authors declare no conflicts of interest.

## Abbreviations

| | |
|---|---|
| $S_M$ | Mass source term, kg/m$^3$·s |
| $S_F$ | Continuum surface force, kg/m$^2$·s$^2$ |
| E | Energy, J/kg |
| $k_{eff}$ | Thermal conductivity, W/m·K |
| T | Temperature, K |
| $S_E$ | Energy source term, J/m$^3$·s |
| $C_{pi}$ | Specific heat, J/kg·K |
| Greek symbols | |
| $\alpha_l$ | Liquid volume fraction |
| $\alpha_v$ | Vapor volume fraction |
| $\delta$ | Surface tension coefficient, N/m |
| $\mu$ | Dynamic viscosity, Pa·s |
| $\rho_l$ | Density of the liquid phase, kg/m$^3$ |
| Subscripts | |
| l | Liquid |
| Sat | Saturation |
| v | Vapor |
| W | Wall |

## References


1. Najim, A.; Pise, S. Boiling heat transfer enhancement with surfactant on the tip of a submerged hypodermic needle as nucleation site. *Appl. Therm. Eng.* **2016**, *103*, 989–995. [CrossRef]
2. Choi, S.U.S.; Eastman, J.A. *Enhancing Thermal Conductivity of Fluids with Nanoparticles*; ASME International Mechanical Engineering Congress & Exposition: San Francisco, CA, USA, 1995; Volume 11.
3. Moita, A.S.; Teodori, E.; Moreira, A.L.N. Influence of surface topography in the boiling mechanisms. *Int. J. Heat. Fluid. Flow.* **2015**, *52*, 50–63. [CrossRef]
4. Guan, S.Y.; Zhang, Z.H.; Wu, R.; Zhao, C.Y. Boiling heat transfer via micro-nano composite gradient and grooved porous structures: Liquid film and vapor dynamics insights. *Int. J. Heat Mass Transf.* **2025**, *254*, 127655. [CrossRef]
5. Ma, B.; Zhao, Z.; Li, W.; Zhang, R.; Ma, X. Investigation of bubble behavior on micro-structured surfaces in pool boiling with data-driven integrated experimental and numerical method. *Int. J. Heat Mass Transf.* **2025**, *254*, 127673. [CrossRef]
6. Singh, P.K.; Rahul, N.; Sen, D.; Maity, S. Enhanced pool boiling heat transfer via micro/nano-engineered copper surfaces: A study of machining techniques. *Int. J. Heat Mass Transf.* **2025**, *254*, 127700. [CrossRef]
7. Mehralizadeh, A.; Reza Shabanian, S.; Bakeri, G. Effect of modified surfaces on bubble dynamics and pool boiling heat transfer enhancement: A review. *Therm. Sci. Eng. Prog.* **2020**, *15*, 100451. [CrossRef]
8. Nakayama, W.; Daikoku, T.; Kuwahara, H.; Nakajima, T. Dynamic Model of Enhanced Boiling Heat Transfer on Porous Surfaces—Part I: Experimental Investigation. *J. Heat. Transf.* **1980**, *102*, 445–450. [CrossRef]
9. Ramaswamy, C.; Joshi, Y.; Nakayama, W.; Johnson, W.B. High-speed visualization of boiling from an enhanced structure. *Int. J. Heat. Mass. Transf.* **2002**, *45*, 4761–4771. [CrossRef]
10. Ramaswamy, C.; Joshi, Y.; Nakayama, W.; Johnson, W.B. Effects of varying geometrical parameters on boiling from microfabricated enhanced structures. *ASME J. Heat. Transf.* **2003**, *125*, 103–109. [CrossRef]
11. Kim, S.H.; Lee, G.C.; Kang, J.Y.; Moriyama, K.; Kim, M.H.; Park, H.S. Boiling heat transfer and critical heat flux evaluation of the pool boiling on micro structured surface. *Int. J. Heat. Mass. Transf.* **2015**, *91*, 1140–1147. [CrossRef]
12. Chu, K.-H.; Enright, R.; Wang, E.N. Structured surfaces for enhanced pool boiling heat transfer. *Appl. Phys. Lett.* **2012**, *100*, 241603. [CrossRef]
13. Zhang, B.J.; Park, J.; Kim, K.J. Augmented boiling heat transfer on the wetting-modified three dimensionally-interconnected alumina nano porous surfaces in aqueous polymeric surfactants. *Int. J. Heat. Mass. Transf.* **2013**, *63*, 224–232. [CrossRef]
14. Dong, L.; Quan, X.; Cheng, P. An experimental investigation of enhanced pool boiling heat transfer from surfaces with micro/nano-structures. *Int. J. Heat. Mass. Transf.* **2014**, *71*, 189–196. [CrossRef]
15. Mitrovic, J.; Hartmann, F. A new microstructure for pool boiling. *Superlattices Microstruct.* **2004**, *35*, 617–628. [CrossRef]
16. Kong, X.; Zhang, Y.; Wei, J. Experimental study of pool boiling heat transfer on novel bistructured surfaces based on micro-pin-finned structure. *Exp. Therm. Fluid. Sci.* **2018**, *91*, 9–19. [CrossRef]
17. Bian, H.; Kurwitz, C.; Sun, Z.; Cheng, K.; Chen, K. Enhanced nucleate boiling on 3D-printed micro-porous structured surface. *Appl. Therm. Eng.* **2018**, *141*, 422–434. [CrossRef]
18. Cooke, D.; Kandlikar, S.G. Effect of open microchannel geometry on pool boiling enhancement. *Int. J. Heat. Mass. Transf.* **2012**, *55*, 1004–1013. [CrossRef]
19. Jaikumar, A.; Kandlikar, S.G. Enhanced pool boiling heat transfer mechanisms for selectively sintered open microchannels. *Int. J. Heat. Mass. Transf.* **2015**, *88*, 652–661. [CrossRef]
20. Cooke, D.; Kandlikar, S.G. Pool Boiling Heat Transfer and Bubble Dynamics Over Plain and Enhanced Microchannels. *J. Heat. Transf.* **2011**, *133*, 052902. Available online: http://heattransfer.asmedigitalcollection.asme.org/ (accessed on 28 January 2016). [CrossRef]
21. Das, A.K.; Das, P.K.; Saha, P. Performance of different structured surfaces in nucleate pool boiling. *Appl. Therm. Eng.* **2009**, *29*, 3643–3653. [CrossRef]
22. Das, A.K.; Das, P.K.; Saha, P. Some investigations on the enhancement of boiling heat transfer from planer surface embedded with continuous open tunnels. *Exp. Therm. Fluid. Sci.* **2010**, *34*, 1422–1431. [CrossRef]
23. Kim, D.E.; Yu, D.I.; Park, S.C.; Kwak, H.J.; Ahn, H.S. Critical heat flux triggering mechanism on micro-structured surfaces: Coalesced bubble departure frequency and liquid furnishing capability. *Int. J. Heat. Mass. Transf.* **2015**, *91*, 1237–1247. [CrossRef]
24. Fadhl, B.; Wrobel, L.C.; Jouhara, H. CFD modelling of a two-phase closed thermosyphon charged with R134a and R404a. *Appl. Therm. Eng.* **2015**, *78*, 482–490. [CrossRef]
25. De Schepper, S.C.K.; Heynderickx, G.J.; Marin, G.B. Modeling the evaporation of a hydrocarbon feedstock in the convection section of a steam cracker. *Comput. Chem. Eng.* **2009**, *33*, 122–132. [CrossRef]
26. Alizadehdakhel, A.; Rahimi, M.; Alsairafi, A.A. CFD modeling of flow and heat transfer in a thermosyphon. *Int. Commun. Heat. Mass. Transf.* **2010**, *37*, 312–318. [CrossRef]
27. Alammar, A.A.; Al-Dadah, R.K.; Mahmoud, S.M. Numerical investigation of effect of fill ratio and inclination angle on a thermosiphon heat pipe thermal performance. *Appl. Therm. Eng.* **2016**, *108*, 1055–1065. [CrossRef]

28. Peng, H.; Ding, G.; Hu, H.; Jiang, W. Effect of nanoparticle size on nucleate pool boiling heat transfer of refrigerant/oil mixture with nanoparticles. *Int. J. Heat. Mass. Transf.* **2011**, *54*, 1839–1850. [CrossRef]
29. Norouzipour, A.; Abdollahi, A.; Afrand, M. Experimental study of the optimum size of silica nanoparticles on the pool boiling heat transfer coefficient of silicon oxide/deionized water nanofluid. *Powder Technol.* **2019**, *345*, 728–738. [CrossRef]

**Disclaimer/Publisher's Note:** The statements, opinions and data contained in all publications are solely those of the individual author(s) and contributor(s) and not of MDPI and/or the editor(s). MDPI and/or the editor(s) disclaim responsibility for any injury to people or property resulting from any ideas, methods, instructions or products referred to in the content.

energies

MDPI

*Article*

# Numerical Analysis of Bismuth Telluride-Based Thermoelectric Device Performance in Lunar Extreme Cold Environments

**Xin Xu [1], Jiaxin Zheng [1], Licheng Sun [1,2,*], Xiting Long [2,*], Tianyi Gao [1], Biao Li [1,2], Qinyi Zhang [1], Cunbao Li [2], Jun Wang [2], Zhengyu Mo [1], Min Du [1] and Heping Xie [1,2]**

[1] State Key Laboratory of Intelligent Construction and Healthy Operation and Maintenance of Deep Underground Engineering, College of Water Resource & Hydropower, Sichuan University, Chengdu 610065, China
[2] Guangdong Provincial Key Laboratory of Deep Earth Sciences and Geothermal Energy Exploitation and Utilization, Institute of Deep Earth Sciences and Green Energy, College of Civil and Transportation Engineering, Shenzhen University, Shenzhen 518060, China
* Correspondence: sunlicheng@scu.edu.cn (L.S.); longxiting@szu.edu.cn (X.L.)

**Abstract**

As lunar exploration missions advance, the need for safe and sustainable in situ energy systems has become increasingly critical. This study investigates the thermoelectric performance of $Bi_2Te_3$-based thermoelectric materials under the natural temperature variations on the lunar surface, aiming to illustrate the potential of thermoelectric generation technology in power supply for a crewed moon base. A numerical approach was employed to assess the energy conversion behavior and optimize the geometric design of a thermoelectric module couple consisting of a P-leg and N-leg. The results indicate that $Bi_2Te_3$-based modules exhibit promising functionality under cryogenic conditions, highlighting their potential as an in situ power source during the long lunar night. Furthermore, geometric optimization was shown to significantly enhance the overall thermoelectric performance. The present study illustrates that TEG technology offers a viable pathway toward reliable energy generation in extreme lunar environments, supporting future mission sustainability.

**Keywords:** $Bi_2Te_3$-based thermoelectric material; TEG technology; lunar environment; power supply; thermoelectric performance; cryogenic

## 1. Introduction

The establishment of a permanent lunar human outpost has grown into a widely shared international aspiration [1–3]. Through the Artemis program, the United States aims to achieve a crewed lunar landing by 2026, with plans to subsequently establish a sustainable human presence on the Moon's surface [2,4]. Meanwhile, China has outlined an ambitious lunar exploration road-map, targeting its first crewed Moon landing in 2029 as part of the International Lunar Research Station (ILRS) in collaboration with Russia and other partners [5]. A permanent moon base seems within range. However, key technological advancements for lightweight, reliable, and cost-effective energy generation are imperative [4], to support the transmission of information, satellite navigation, life maintenance, resource exploitation and other essential energy supplies [6,7]. Since each lunar day and night lasts approximately 14.77 Earth days [7], the traditional approach of using solar panels with batteries faces a major limitation due to massive energy storage demands [8]. Thermoelectric generators (TEGs) offer a promising power generation solution for lunar bases [9]. Their operation relies on the thermoelectric effect, enabling the direct conversion

of thermal energy into electricity. Unlike conventional heat engine cycles, TEGs contain no moving parts or kinetic components, resulting in superior reliability, operational stability, and structural robustness [7,9–11]. These attributes provide TEGs with distinct advantages for use in the challenging lunar environment [12].

Cold energy harvesting by thermoelectric generator module (TEM) provides a full chain utilization of the whole temperature zone, and has the characteristics of feasibility and large-scale utilization [13,14]. Furthermore, the efficiency of cold energy conversion with TEG is better than that of waste heat conversion [15]. During the lunar night, the surface temperature of the Moon drops to approximately 90 K, whereas the thermal conductivity of lunar regolith is extremely low, with a value of only ~0.01 W/(m·K), at depths greater than ~0.4 m, the regolith maintains a nearly constant temperature of around 250 K [16–18]. This creates a natural source of cold energy with a gradient of approximately 160 K between the surface and the deeper regolith layer [19,20]. If this inherent cold energy can be effectively harnessed for electricity generation, it could largely overcome the power supply challenges faced by equipment during the extended lunar night [21]. Thermoelectric generator (TEG) technology has emerged as a promising method for generating power from the cold energy available during the lunar night, despite challenges such as low thermoelectric conversion efficiency and a shortage of high-performance thermoelectric materials (TMs) suitable for cryogenic environments [22].

Published papers on TE module performance at the temperature gradient from room temperature to cryogenic temperature are scarcely available [23,24]. The maximum conversion efficiency of 1.76% at the temperature range of 200–300 K was measured for TE module with N-type BiSb-based and P-type MgAgSb-based materials [14]. Lobunets [14] reported a maximum power output around 25 W and conversion efficiency of 8.85% for a single thermoelectric module consisting of 263 $Bi_2Te_3$-based P-N couples. This represents the highest performance documented in published studies to date for a TEM under cryogenic temperature conditions. Kambe et al. [23] reported a maximum power output of 8.6 W from a TEM with dimension of 40 × 35 × 1 $mm^3$, fabricated using conventional BiTe materials, under a temperature difference of 210 K and the hot-side temperature of 298 K. Sidorenko et al. [25] studied thermoelectric properties of $Bi_{0.91}Sb_{0.09}$ extruded crystals and single crystals were studied over the entire temperature range of 77–200 K, with an averaged value of thermoelectric figure of merit (*ZT)* around 0.6. Using improved extrusion technology for bismuth antimony tellurides, new extruded TEMs were developed with increased thermoelectric figure of merit around 0.7–0.8 [26]. When doped appropriately, the material $CsBi_4Te_6$ exhibits a high thermoelectric figure of merit below room temperature ($ZT_{max}$ = 0.8 at 225 K) [27]. Enhanced cryogenic thermoelectric *ZT* with an average value as high as 0.8 from 180 to 300 K was obtained for $Bi_{0.5}Sb_{1.5}Te_3$ by carrier optimization [28].

The integration of TEGs with in situ resource utilization (ISRU) systems offers a promising solution for providing continuous power during the lunar night [7]. However, harnessing the abundant cold energy of the lunar environment for power generation remains a significant challenge in establishing a crewed lunar base [29]. Previous reviews on TMs indicate a notable research gap in the application of TEGs for cold energy utilization. This study focuses on the heat-to-electricity conversion performance of BiTe-based thermoelectric materials under lunar conditions. Numerical simulations using COMSOL Multiphysics 6.2 are employed to analyze the thermoelectric behavior of BiTe-based materials throughout the entire lunar diurnal cycle. Based on these simulations, the potential of TEG technology for lunar in situ energy utilization is comprehensively evaluated.

## 2. Methodology

### *2.1. Geometric TEM Model*

A typical TEM consists of multiple P-type and N-type semiconductor couples connected electrically in series and thermally in parallel, all encapsulated between two highly thermally conductive ceramic plates. In this study, a single couple is analyzed for simplicity, neglecting the influence of the connecting adhesives. The geometric configuration of the thermoelectric couple is illustrated in Figure 1a, with the corresponding computational mesh presented in Figure 1b. Both the P-type and N-type legs exhibit identical geometric dimensions. A detailed summary of the dimensional parameters and thermoelectric properties for each leg is provided in Table 1. Both the P-leg and the N-leg are identical, with dimensions of $1.7 \times 1.7 \times 1.8$ mm$^3$, which are the same with that of Luo et al. [30] for validation of the present numerical method. The P-leg and N-leg are connected by a 0.2 mm wide copper interconnecting plate.

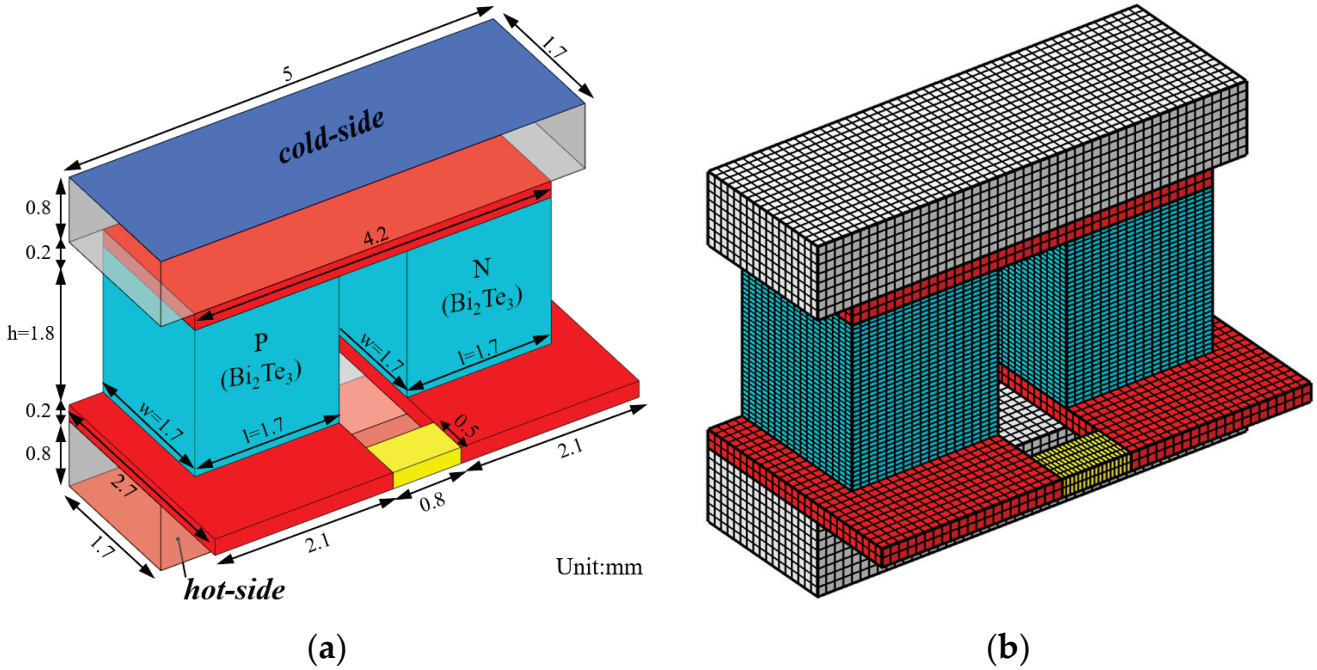



**Figure 1.** Schematic of a 3D thermoelectric couple model: (**a**) geometric configuration; (**b**) computational mesh.

**Table 1.** P-leg and N-leg specifications used in the present study.

| Items | Value | Units |
|---|---|---|
| **P-leg** | | |
| Cross-section area | $w \times l$ | mm$^2$ |
| Height | $h$ | mm |
| Seebeck coefficient | $1.52 \times 10^{-4} - 5.8 \times 10^{-8}$T + $1.65 \times 10^{-9}$T$^2$ − $2.7 \times 10^{-12}$T$^3$ (<300 K) | V/K |
| | $(3.5874 \times 10^{-6}$T$^3$ − $6.37 \times 10^{-3}$T$^2$ + 3.3976T − 367.8679$)/10^6$ (>300 K) | V/K |

**Table 1.** *Cont.*

| Items | Value | Units |
|---|---|---|
| Electrical conductivity | $277660 - 819T + 0.67T^2$ (<300 K) | S/m |
| | $10^5/(-9.218 \times 10^{-8}T^3 + 1.1856 \times 10^{-4}T^2 - 0.04623T + 6.2083)$ (>300 K) | S/m |
| Thermal conductivity | $3.748 - 0.01449T + 2 \times 10^{-5}T^2$ (<300 K) | W/(m·K) |
| | $3.4352 \times 10^{-8}T^3 - 2.4638 \times 10^{-5}T^2 + 6.08 \times 10^{-3}T + 1.5035$ (>300 K) | W/(m·K) |
| **N-leg** | | |
| Cross-section area | $w \times l$ | $mm^2$ |
| Height | $h$ | mm |
| Seebeck coefficient | $-1.52 \times 10^{-4} + 5.8 \times 10^{-8}T - 1.65 \times 10^{-9}T^2 + 2.7 \times 10^{-12}T^3$ (<300 K) | V/K |
| | $(2.6555 \times 10^{-6}T^3 - 2.54 \times 10^{-3}T^2 + 0.6364T - 198.6904)/10^6$ (>300 K) | V/K |
| Electrical conductivity | $277660 - 819T + 0.67T^2$ (<300 K) | S/m |
| | $10^5/(1.2802 \times 10^{-8}\ T^3 - 1.634 \times 10^{-5}\ T^2 + 8.69 \times 10^{-3}T - 1.1129)$ (>300 K) | S/m |
| Thermal conductivity | $3.748 - 0.01449T + 2 \times 10^{-5}T^2$ (<300 K) | W/(m·K) |
| | $2.3892 \times 10^{-8}T^3 - 3.0422 \times 10^{-5}T^2 + 0.0152T - 0.013$ (>300 K) | W/(m·K) |
| **Copper conductor** | | |
| Cross-section area (lunar surface) | $4.2 \times 1.7$ | $mm^2$ |
| Cross-section area (subsurface regolith) | $2.1 \times 1.7$ | $mm^2$ |
| Height | 0.2 | mm |
| Electrical conductivity | 57,142,857 | S/m |
| Thermal conductivity | 399 | W/(m·K) |
| Density | 8960 | $kg/m^3$ |
| **$Al_2O_3$ ceramic plates** | | |
| Cross-section area | $5 \times 1.7$ | $mm^2$ |
| Height | 0.8 | mm |
| Thermal conductivity | 18 | W/(m·K) |

### *2.2. Properties of TE Materials*

Table 1 summarizes the geometric and material properties of the thermoelectric (TE) couple. For clarity, the Seebeck coefficient, electrical conductivity, thermal conductivity, and figure of merit ($ZT$) of the thermoelectric materials within the temperature range of 300–500 K are presented in Figure 2. It should be noted that the $ZT$ value of the P-leg material exhibits a decreasing trend above 350 K, primarily due to an increase in thermal conductivity and a decrease in electrical conductivity. In contrast, the $ZT$ value of the N-leg material decreases gradually with temperature. Both materials demonstrate relatively high $ZT$ values at lower temperatures, which enhances their performance under cryogenic conditions.

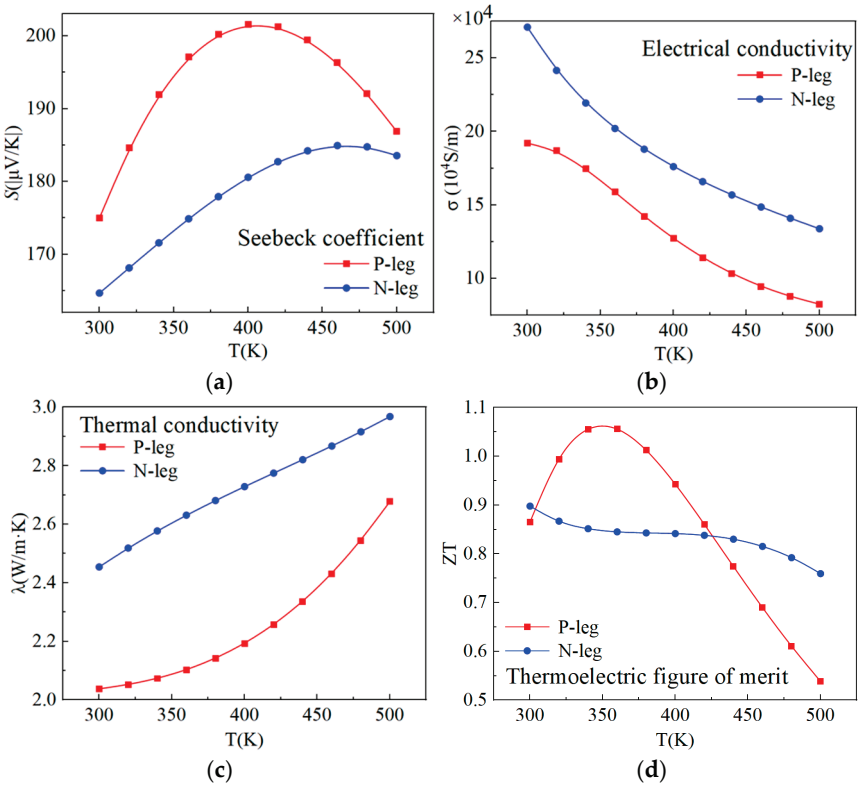



**Figure 2.** Thermoelectric properties of the TMs: (**a**) Seebeck coefficient; (**b**) Electrical conductivity; (**c**) Thermal conductivity; (**d**) Thermoelectric figure of merit.

### *2.3. Governing Equations*

The conservation equations and physical laws of TEGs are as follows [30]:

$$\nabla \cdot (\lambda_{\mathrm{P}}(\mathrm{T})\nabla \mathrm{T_P}) = -\rho_{\mathrm{P}}(\mathrm{T})\bar{\mathrm{J}}^2 + \nabla\alpha_{\mathrm{P}}(\mathrm{T})\bar{\mathrm{J}}\mathrm{T_P} \quad (1)$$

$$\nabla \cdot (\lambda_{\mathrm{N}}(\mathrm{T})\nabla \mathrm{T_N}) = -\rho_{\mathrm{N}}(\mathrm{T})\bar{\mathrm{J}}^2 + \nabla\alpha_{\mathrm{N}}(\mathrm{T})\bar{\mathrm{J}}\mathrm{T_N} \quad (2)$$

where $\bar{J}$ and $\alpha$ represent the current density vector and Seebeck coefficient, respectively. The local current density is given by

$$\bar{\mathrm{J}} = -\nabla \mathrm{V} + \alpha\nabla(\mathrm{T}) \quad (3)$$

The power output of the TEG is

$$P = I^2 R_L \quad (4)$$

where $R_L$ is the load resistance. The current, $I$, is given by the Ohm's Law:

$$\mathrm{I} = \frac{\alpha(\mathrm{T_h} - \mathrm{T_c})}{\mathrm{R_L} + \mathrm{R}} \quad (5)$$

The thermoelectric conversion efficiency of the TEG is

$$\eta = \frac{I^2 R_L}{Q_h} \quad (6)$$

The maximum power output ($P_{max}$) and maximum conversion efficiency ($\eta_{max}$) can be obtained by altering the load resistance [30].

### *2.4. Computational Setup*

The physics interfaces and corresponding settings employed in the simulation are summarized in Table 2, which includes the Heat Transfer interface with initial temperature, fixed temperature boundaries, and thermal insulation conditions; the Electric Current interface incorporating initial current and electrical insulation settings; and the Multiphysics couplings for thermoelectric effects and electromagnetic heating. The numerical solutions are obtained using the Finite Element Method (FEM).

**Table 2.** Numerical calculation scheme.

| Physics Interface | Description | Settings |
|---|---|---|
| Heat Transfer | Initial condition | $T_0$ = 293.15 K |
| | Fixed temperature | hot-side = constant temperature<br>cold-side = constant temperature |
| | Thermal insulation | load resistance, all other external surfaces |
| Electric current | Initial condition | $I_0$ = 0 |
| | Electric insulation | $Al_2O_3$ ceramic plates, all external surfaces |
| Multiphysics coupling | Thermoelectric effect | P-leg, N-leg |
| | Electromagnetic heating | P-leg, N-leg, Copper conductor |
| - | Numerical method | Finite Element Method (FEM) |

Due to the very slow temperature variation throughout the lunar diurnal cycle, transient processes have a negligible influence on thermoelectric performance. Therefore, the entire cycle was discretized into multiple time segments, each assumed to have a constant temperature. The overall performance of the thermoelectric unit over the full cycle is approximated by evaluating its behavior within each individual segment. Accordingly, all simulations in this study were carried out under steady-state assumptions, and transient effects were neglected.

### *2.5. Grid Independence Validation*

As shown in Figure 1b, a structured grid consisting predominantly of hexahedral elements is employed for the TEG couple. A grid independence study was conducted to determine the suitable mesh size for numerical simulations. The steady-state output performance of the TEG couple under different mesh sizes was evaluated, with the load resistance set to 0.01 Ω; the corresponding results are presented in Table 3. When the mesh size is reduced to 0.1 mm, the relative error in output power drops to 0.02%, indicating sufficient numerical accuracy. Accordingly, a mesh size of 0.1 mm was selected for all subsequent simulations to balance computational efficiency and model precision.

**Table 3.** Steady-state output performance of a TEG couple with different mesh numbers.

| Mesh Size (mm) | Mesh Number | Output Voltage (mV) | Output Power (W) | Error of Output Power |
|---|---|---|---|---|
| 0.2 | 5343 | 35.6720 | 0.1241 | 0.06% |
| 0.15 | 14392 | 35.6680 | 0.1241 | 0.03% |
| 0.1 | 38274 | 35.6660 | 0.1241 | 0.02% |
| 0.08 | 82525 | 35.6650 | 0.1240 | 0.01% |

## 3. Simulation Results

### *3.1. Model Verification*

Figure 3a presents the numerical simulation results of the output power for a single TEM couple under a hot-side temperature of $T_h$ = 500 K, a cold-side temperature of $T_c$ = 300 K, and varying external load resistances. The corresponding results from Luo et al. [30] are also included for comparison. The maximum prediction error relative to Luo et al.'s data is less than 0.7%, indicating high accuracy of the current numerical approach. Figure 3b displays the temperature and electrical potential contours from both the present study and Ref. [30], which exhibit strong agreement and further validate the correctness of the present methodology.

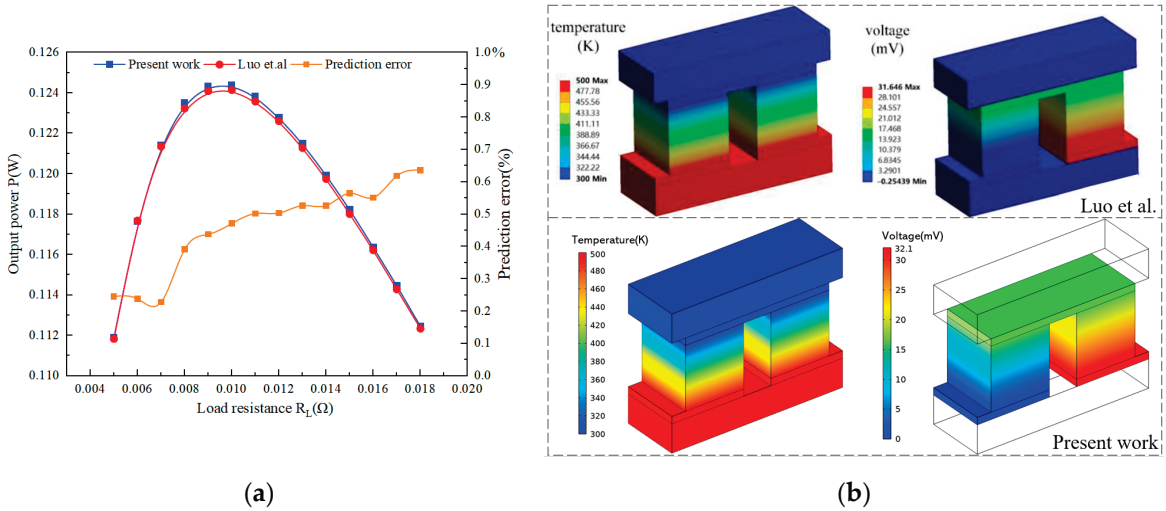



**Figure 3.** Comparison of the numerical results of present work and [30]: (**a**) output power; (**b**) temperature and electrical potential contours.

### *3.2. Thermoelectric Performance of a Single TEM Couple*

Figure 4 illustrates the thermoelectric performance of the TEM couple under various cryogenic temperature gradients. The cold side of the ceramic plate is held constant at 90 K, representing the minimum temperature encountered on the lunar surface. The hot side temperature varies from 248 K (corresponding to the stable temperature layer of lunar regolith) to 400 K.

Figure 4a shows the performance under the maximum temperature difference of 158 K during the lunar night. The maximum output power and thermoelectric conversion efficiency under these conditions are 0.08 W and 3.76%, respectively. As the hot side temperature increases to 300 K, resulting in a temperature difference of 210 K, the thermoelectric performance shows significant improvement: the maximum output power rises by 75%, reaching 0.14 W, and the conversion efficiency increases by 37.3%, reaching 5.17%. This enhancement is attributed to the rise in the dimensionless figure of merit (ZT) with increasing temperature. When the hot side temperature reaches 400 K, the output power and efficiency further increase to 0.28 W and 7.48%, respectively. The external load resistance corresponding to the maximum power and efficiency remains. The load resistances corresponding to both maximum power and efficiency varies slightly with the increase in hot-side temperature.

Figure 5 shows the output power and electrical potential as functions of electric current under the temperature differences presented in Figure 4. The output power exhibits a linear relationship with the current. As the hot-side temperature increases from 248 K to 400 K, the current at which maximum power output occurs rises from 3 A to 4.8 A, while the corresponding open-circuit electrical potential increases from approximately 36 mV to 72 mV.

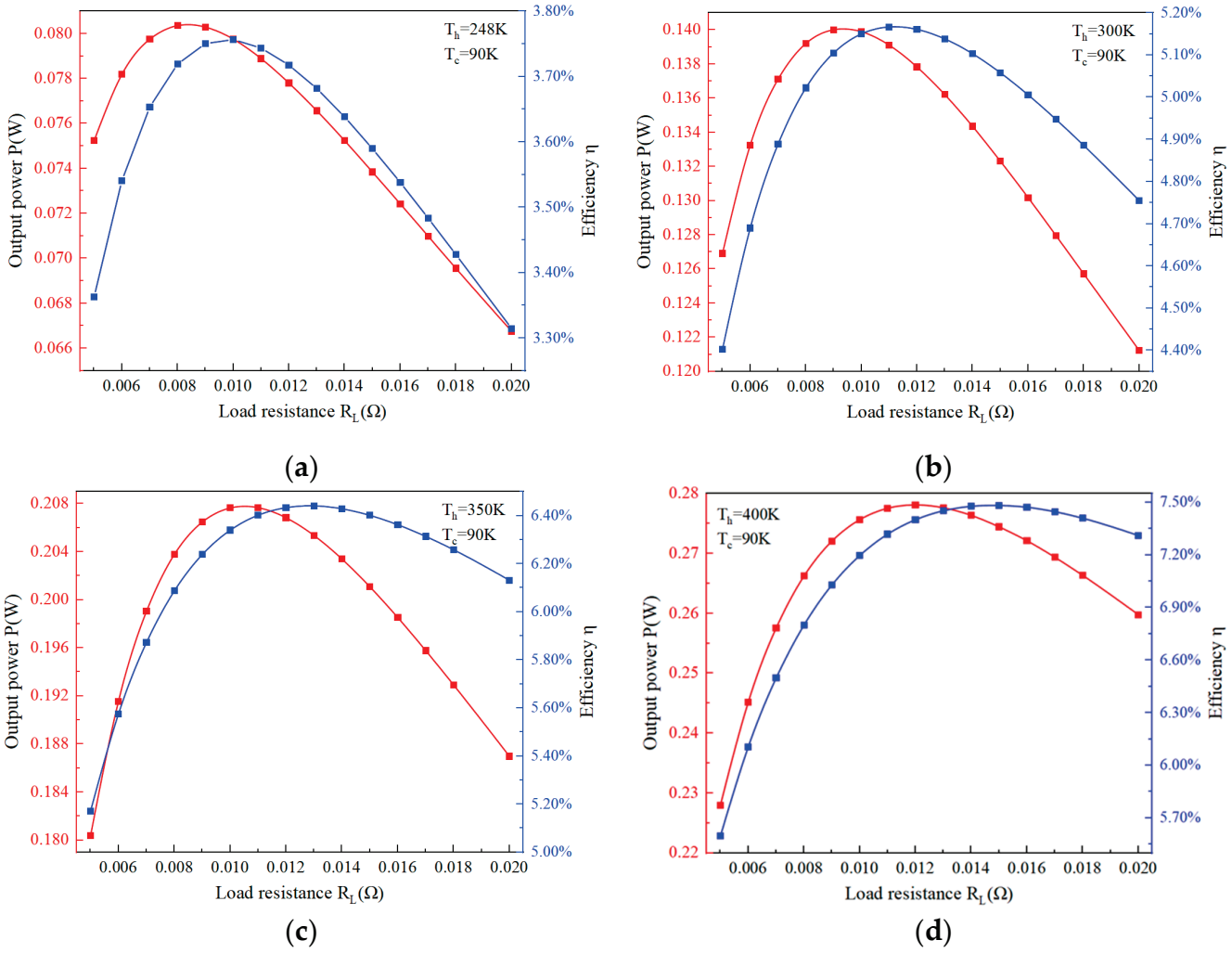



**Figure 4.** Performance of a single couple under constant $T_c$ = 90 K and varying $T_h$: (**a**) $T_h$ = 248 K; (**b**) $T_h$ = 300 K; (**c**) $T_h$ = 350 K; (**d**) $T_h$ = 400 K.

Figure 6 illustrates the maximum output power and thermoelectric conversion efficiency of a single TEM couple under conditions of constant hot-side temperature and varying cold-side temperature. Both parameters decrease as the cold-side temperature increases, owing to the corresponding reduction in temperature difference. Nonetheless, the couple retains its power generation capability across a broad range of temperature gradients. This feature provides TEG technology with a notable advantage over other energy conversion methods for in situ energy utilization on the Moon, as it can effectively exploit the natural temperature variations present in the lunar environment.

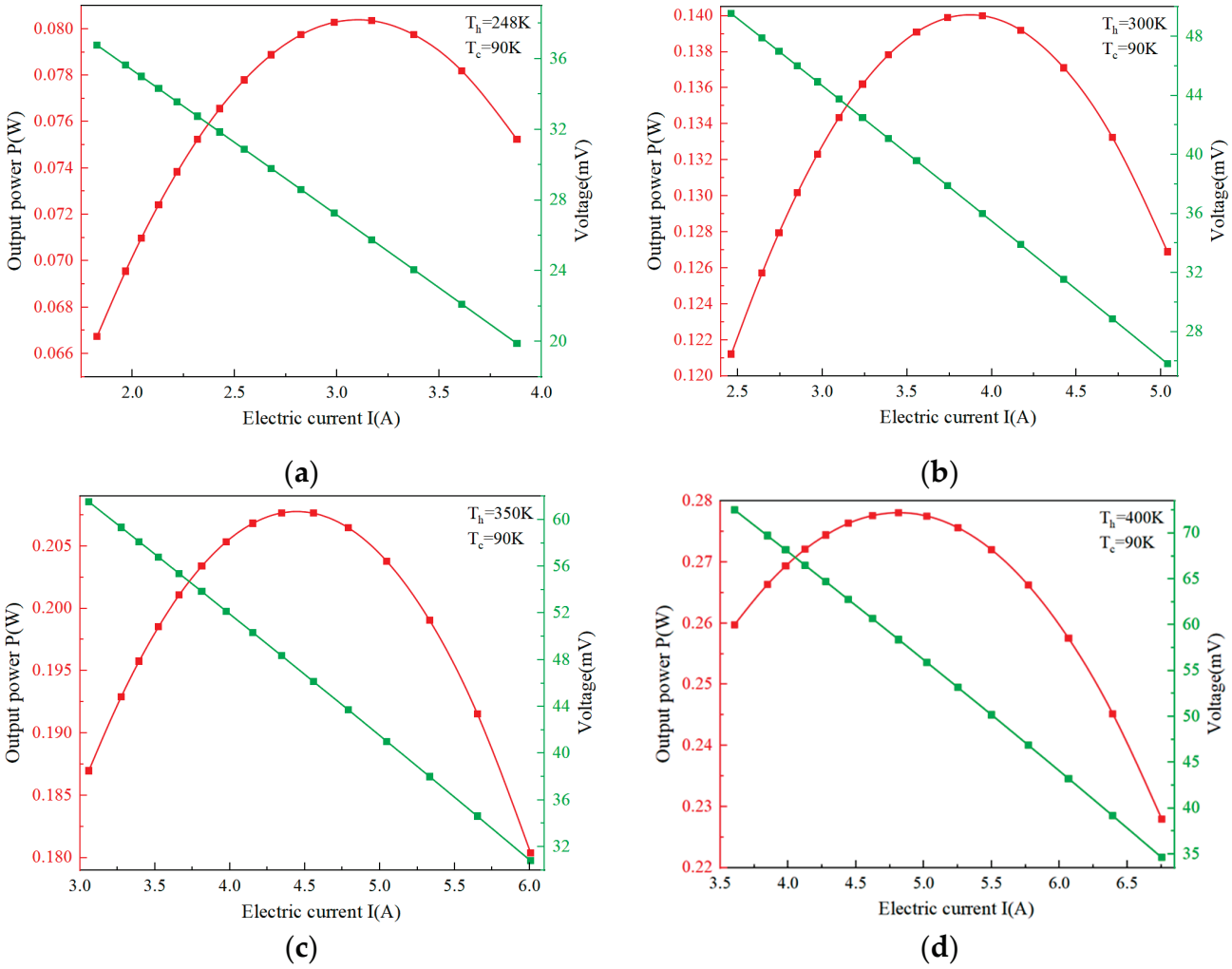



**Figure 5.** I-A and I-W curves of a single couple under constant $T_c$ = 90 K and varying $T_h$: (**a**) $T_h$ = 248 K; (**b**) $T_h$ = 300 K; (**c**) $T_h$ = 350 K; (**d**) $T_h$ = 400 K.

During the lunar night, if energy storage devices are employed to maintain an elevated hot-side temperature, the thermoelectric performance can be enhanced significantly. As the hot-side temperature increases from 248 K to 400 K, both the maximum output power and thermoelectric conversion efficiency of a single TEM couple double, demonstrating considerable application potential for TEG technology under lunar conditions. The highest output power reaches 0.278 W, implying that a TEM comprising 200 couples could theoretically achieve a maximum output power of 55.6 W at $T_h$ = 400 K and $T_c$ = 90 K.

As shown in Figures 4 and 6, both the output power and thermoelectric conversion efficiency remain below 10%, which represents a major limitation of TEG technology in the lunar environment—a challenge also observed under conventional conditions. This performance constraint is primarily due to the relatively low *ZT* values (0.4–0.6) at cryogenic temperatures. The key to improving performance lies in enhancing the ZT value through the optimization of thermoelectric materials and fabrication techniques. Achieving a *ZT* value greater than 1 would significantly increase the applicability of TEG for power generation on the Moon.

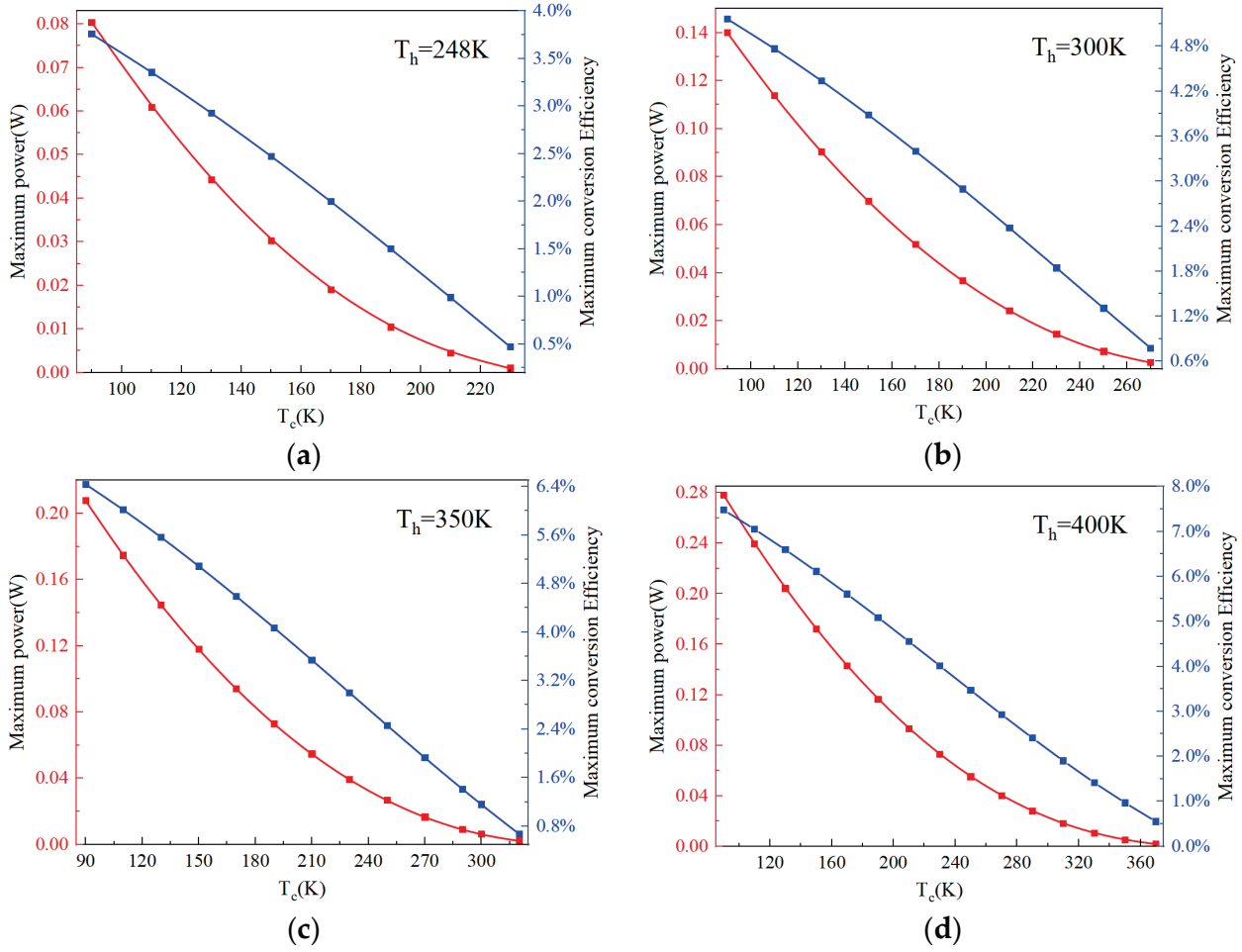



**Figure 6.** Maximum output power and thermoelectric conversion efficiency of a single couple under constant $T_h$ and varying $T_c$ from 90 K to 210 K. (**a**) $T_h$ = 248 K; (**b**) $T_h$ = 300 K; (**c**) $T_h$ = 350 K; (**d**) $T_h$ = 400 K.

### *3.3. Geometry Optimization*

An analysis was conducted to examine the influence of geometric dimensions on the thermoelectric performance of a thermoelectric module (TEM) couple. The cross-sectional areas of both the P-type and N-type legs were varied from 1.0 × 1.0 mm$^2$ to 2.0 × 2.0 mm$^2$, while the leg height was adjusted between 1.5 mm and 2.0 mm. The numerical methodology and mesh generation for the computational domain were consistent with the approach described in Section 3.2 for a TEM couple with leg dimensions of 1.7 × 1.7 × 1.8 mm$^3$.

As shown in Figure 7, under a constant temperature difference, increasing the cross-sectional area of the legs leads to a rise in the maximum output power. However, both the maximum thermoelectric conversion efficiency and the maximum power flux (defined as the maximum output power per unit cross-sectional area) decrease slightly. This decline is attributed to the corresponding increase in the electrical resistance of the couple. Consequently, the cross-sectional area has only a minor effect on the overall performance of the TEM couple from the perspective of power capacity. It should be noted that the results presented in Figure 7 were obtained under a constant temperature difference across the legs—a condition that may be difficult to achieve in practice. In real applications, a reduction in cross-sectional area could alter the temperature gradient along the legs, which in turn may significantly affect the thermoelectric performance.

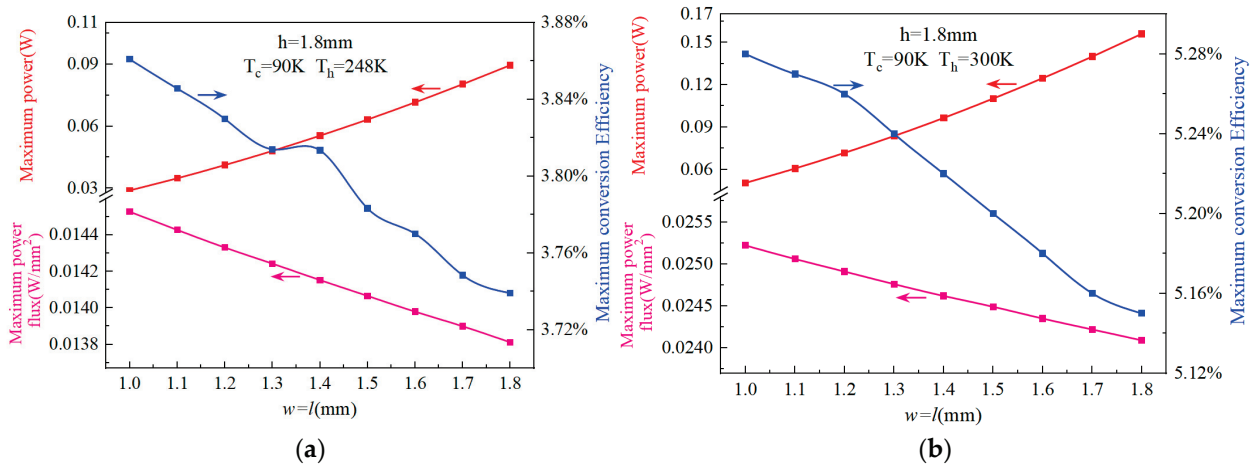



**Figure 7.** Effect of cross-sectional area on thermoelectric performance of a single couple under constant $T_h$ and $T_c$. (**a**) $T_h$ = 248 K, $T_c$ = 90 K; (**b**) $T_h$ = 300 K.

Figure 8 shows the simulated results of the maximum output power and maximum thermoelectric conversion efficiency of a TEM couple as functions of leg height under a constant temperature difference. In response to increasing leg height, the maximum output power and conversion efficiency demonstrate opposite behaviors; the former diminishes concurrently as the latter is enhanced. This behavior occurs because greater leg height reduces heat flux through the module, yet the output power declines only marginally. Consequently, as shown in Figure 8a, the overall conversion efficiency improves, rising from 3.73% to 3.82% as the leg height increases from 1.5 mm to 2.0 mm under constant temperature difference.

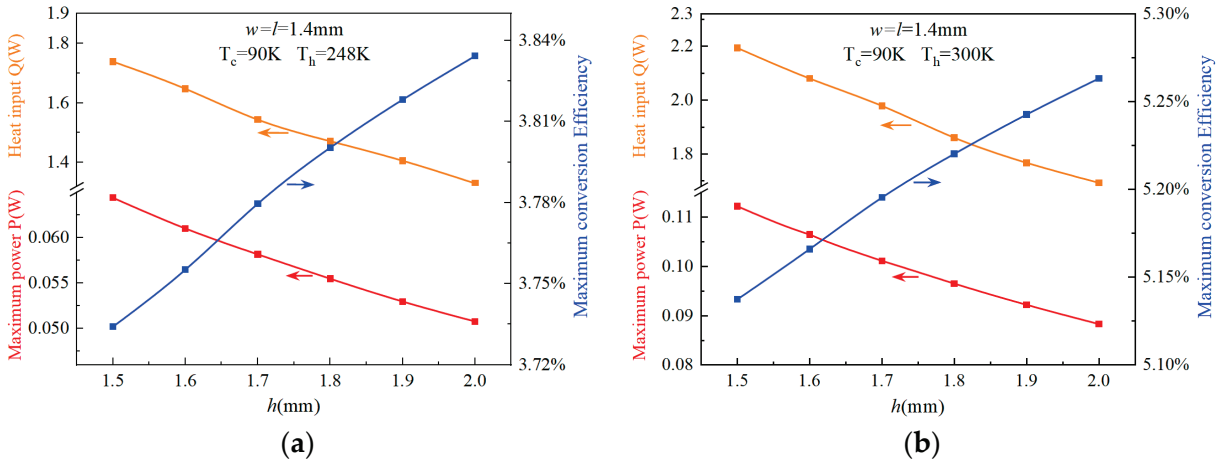



**Figure 8.** Effect of the leg height on thermoelectric performance of a single couple under constant $T_h$ and $T_c$. (**a**) $T_h$ = 248 K, $T_c$ = 90 K; (**b**) $T_h$ = 300 K. The arrows indicate the corresponding coordinate axis of the curve.

As indicated in Figure 8, when the hot side temperature increases from 248 K to 300 K, a significant improvement in performance is observed. The maximum output power rises from 0.064 W to 0.112 W for the leg height of 1.5 mm, while the maximum conversion efficiency increases from 3.83% to 5.26% for the leg height of 2.0 mm. This enhancement in output power is attributed to the increased heat flux resulting from the larger temperature difference. These results suggest that integrating an energy storage system to raise the hot side temperature during the lunar night could be an effective way to improve TEM performance.

### *3.4. Performance of a TEM Couple over a Lunar Diurnal Cycle*

The lunar surface experiences extreme diurnal temperature variations, ranging from approximately 90 K to 400 K. These fluctuations, combined with the relatively stable temperature of the subsurface regolith layer, cause significant changes in the thermoelectric performance of a thermoelectric module (TEM). To assess the feasibility of thermoelectric generator (TEG) technology for lunar power systems under realistic conditions, the performance of a TEM couple was simulated over a full diurnal cycle based on the methodology in Section 3.3. The couple uses P-type and N-type legs with the same dimensions of $1.4 \times 1.4 \times 1.6$ mm$^3$. This geometry offers an optimized balance between thermoelectric efficiency and mechanical durability.

Figure 9 illustrates the thermoelectric performance of the TEM couple over a diurnal cycle equivalent to approximately 30 Earth days. Under the natural temperature gradient of the lunar environment and the influence of the isothermal regolith layer, the couple demonstrates relatively strong performance, particularly during the lunar night, where it operates stably and maintains high thermoelectric conversion efficiency and power output. Around 75% and 70% of the diurnal cycle, the efficiency exceeds 3.0% and the maximum output power surpasses 0.03 W, respectively. Figure 10 presents the cumulative electrical energy generated over one full diurnal cycle, totaling 28 W·h. This result implies that a TEM comprising 200 such couples would produce approximately 5.6 kW·h of electricity, a very considerable output for a TEM device measuring $40 \times 40 \times 4$ mm$^3$. If an energy storage device is employed, raising the temperature of the isothermal layer to 400 K, the accumulated energy output of the couple and the TEM can be significantly increased, reaching 60 W·h and 12 kW·h, respectively.

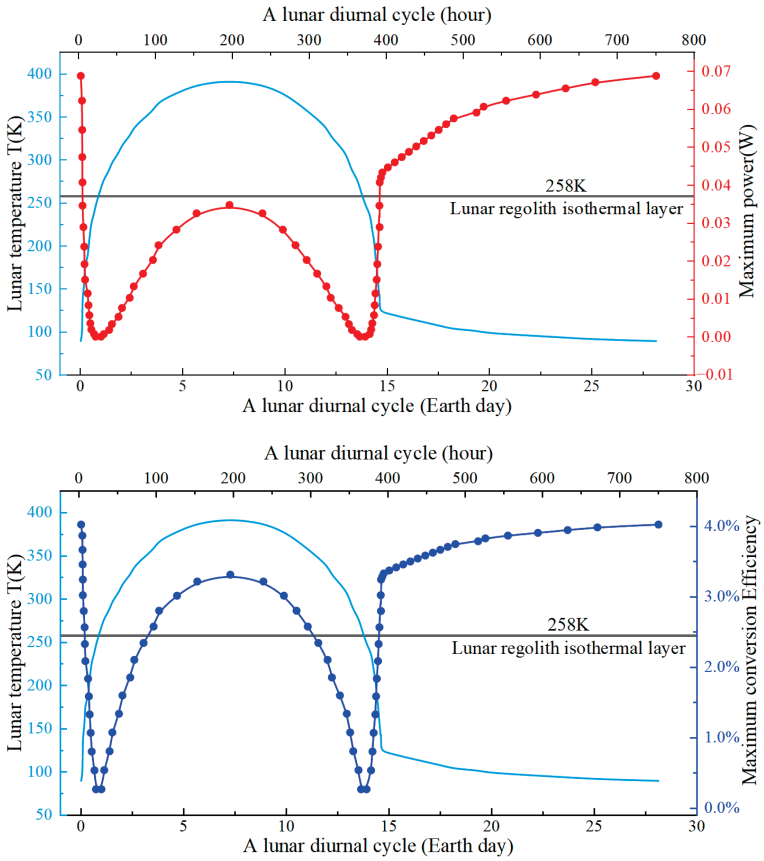



**Figure 9.** Maximum output power and conversion efficiency of a single couple over a diurnal lunar cycle. The light blue line represents the lunar surface temperature.

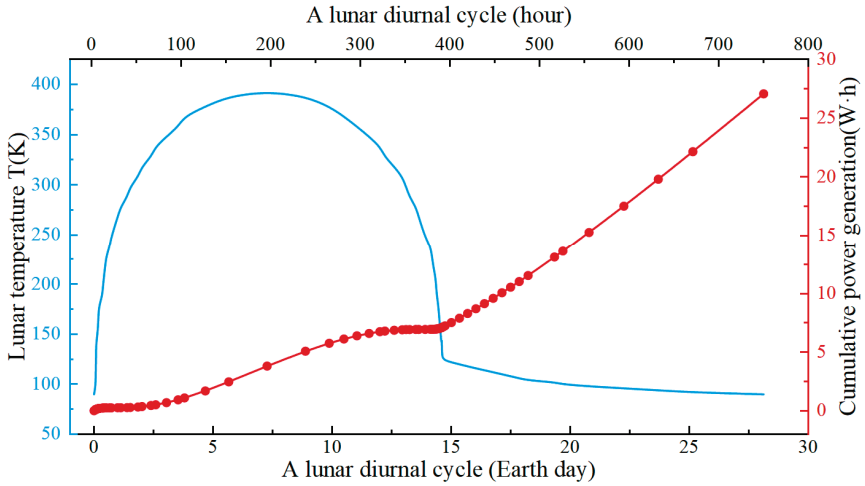



**Figure 10.** Cumulative output power of a single couple over a diurnal lunar cycle. The light blue line represents the lunar surface temperature.

## 4. Discussion

The simulation results presented in Section 3 demonstrate that TEG technology exhibits significant application advantages for in situ power generation on the lunar surface. The natural temperature difference between the lunar regolith isothermal layer and the environment provides an essential prerequisite for the implementation of TEG technology. Especially during the lunar night, the temperature difference between the isothermal layer and the lunar surface environment exceeds 150 K for almost the entire period, which ensures stable and highly efficient operation of the TEG system. Moreover, power supply during the lunar night phase is particularly challenging: photovoltaic technology ceases to operate entirely, and relying solely on energy storage to meet power demands throughout the approximately 15-Earth-day-long lunar night is practically infeasible. The strong performance of TEGs during the lunar night effectively compensates for the limitations of photovoltaics. When combined with photovoltaic power generation during the lunar daytime, TEG technology offers a viable solution for continuous and reliable energy supply over the entire day-night cycle on the lunar surface.

At present, the primary bottleneck for applying TEG technology to lunar power supply remains the thermoelectric materials (TEMs). Their thermoelectric performance in low-temperature ranges is inferior to that in other temperature zones. Enhancing the thermoelectric properties of these materials under the extremely cold conditions on the lunar surface is therefore crucial. Based on this, another key technical challenge is the development of highly efficient heat exchange technologies suitable for the extreme environmental conditions on the Moon. Such technologies would enable TEG systems or devices to maintain the largest possible temperature difference across the TEM, while minimizing thermal resistance in every heat transfer pathway within the system.

Additionally, the modification of lunar regolith has emerged as another critical focus. Upon processing the lunar regolith to enhance its thermal conductivity, it can serve as a high-quality heat source during the lunar night, thereby significantly enhancing the performance of TEG systems.

## 5. Conclusions

With the accelerating progress of lunar exploration, a safe and sustainable power and energy supply has become one of the key technologies in this highly complex scientific endeavor. In this study, the performance of $Bi_2Te_3$-based thermoelectric materials is numerically evaluated under natural lunar temperature differential conditions. The main conclusions are summarized as follows:

(1) $Bi_2Te_3$-based thermoelectric materials demonstrate significant potential for in situ power generation under cryogenic temperature conditions by utilizing local resources. This approach could offer a viable power supply solution during the extended lunar night.

(2) Taking a thermoelectric couple consisting of a P-type leg and an N-type leg, each with dimensions of $1.7 \times 1.7 \times 1.8$ mm$^3$, as an example, it can achieve a maximum output power ranging from 0.08 W to 0.278 W under temperature differences between 158 K and 310 K. The corresponding maximum thermoelectric conversion efficiency reaches values from 3.76% to 7.45%.

(3) Effect of the geometry size of a TE couple on its thermoelectric performance was conducted, based on which a couple using P-type and N-type legs with the same dimensions of $1.4 \times 1.4 \times 1.6$ mm$^3$ was selected for evaluation the performance of the couple under natural temperature difference on the moon over a diurnal lunar cycle.

(4) The couple exhibits a good potential for power supply. The average maximum output power over a diurnal lunar cycle reaches 0.039 W and accumulated electric energy production reaches 28 W·h. A TEM comprising such 200 TE couples can produce 5.6 kW·h of electricity.

By examining the electricity generation potential of a fundamental thermoelectric module (TEM) unit under lunar surface conditions, this work conceptually validates the application of TEGs in utilizing natural temperature differences for power production. Nonetheless, scaling up TEG technology still faces multiple practical engineering hurdles, including system design, integration methods, heat transfer enhancement, and in situ thermal storage modification. These aspects require further in-depth research and development in subsequent studies.

**Author Contributions:** Conceptualization, L.S., X.L. and H.X.; methodology, X.X. and J.W.; software, X.X. and T.G.; validation, B.L. and Q.Z.; formal analysis, C.L. and J.W.; investigation, X.X. and J.Z.; resources, J.Z.; data curation, L.S. and Z.M.; writing—original draft preparation, X.X.; writing—review and editing, L.S. and M.D.; visualization, X.X.; supervision, L.S., X.L. and H.X.; project administration, X.L. and H.X. All authors have read and agreed to the published version of the manuscript.

**Funding:** This research was funded by THE NATIONAL SCIENCE AND TECHNOLOGY MAJOR PROJECT, 2025ZD1009905 and by THE NATIONAL NATURAL SCIENCE FOUNDATION OF CHINA, 52422403&12075160, and by THE NATIONAL KEY R&D PROGRAM OF CHINA, 2021YFB1507403), and by THE NATURAL SCIENCE FOUNDATION OF SICHUAN PROVINCE, 2025ZNSFSC0445.

**Data Availability Statement:** The original contributions presented in this study are included in the article. Further inquiries can be directed to the corresponding authors.

**Acknowledgments:** During the preparation of this manuscript/study, the authors used DeepSeek for the purposes of generating text. The authors have reviewed and edited the output and take full responsibility for the content of this publication.

**Conflicts of Interest:** The authors declare no conflicts of interest. The funders had no role in the design of the study.

## Abbreviations

The following abbreviations are used in this manuscript:

| | |
|---|---|
| ISRU | In situ resource utilization |
| ILRS | International Lunar Research Station |
| TEG | Thermoelectric Generation |
| TEM | Thermoelectric Module |
| TM | Thermoelectric Material |

## References


1. Zhang, P.; Dai, W.; Niu, R.; Zhang, G.; Liu, G.; Liu, X.; Bo, Z.; Wang, Z.; Zheng, H.; Liu, C.; et al. Overview of the lunar in situ resource utilization techniques for future lunar missions. *Space Sci. Technol.* **2023**, *3*, 37. [CrossRef]
2. Marrone, M.; Pasqualin, L.; Ferro, C.G. Lunar power sources: An opportunity to experiment. *Aerospace* **2025**, *12*, 58. [CrossRef]
3. Peng, Q.; Wang, P.; Xing, L. Perspectives on China's Manned Lunar Scientific Research and Test Station. *Adv. Astronaut. Sci. Technol.* **2024**, *7*, 51–64. [CrossRef]
4. Cuervo-Ortiz, J.M.; Palomares, J.C.G.; Ozen, S.; Härtel, M.; Sarisozen, S.; Dittwald, A.; Kourkafas, G.; Castro-Méndez, A.-F.; Peña-Camargo, F.; Seid, B.A.; et al. Moon Photovoltaics Utilizing Lunar Regolith and Halide Perovskites. *Device* **2025**, *3*, 100747. [CrossRef]
5. Pei, Z.; Wang, Q. Strategic Concept of Resource Utilization Development Route of the International Lunar Research Station. *J. Astronaut. Sci.* **2024**, *45*, 625–637. (In Chinese) [CrossRef]
6. Lei, S.; Guoqing, Z.; Yaohui, W.; Chang, W.; Bo, L. A Review of the Construction of the Supporting Energy System for the Lunar Base. *Front. Astron. Space Sci.* **2025**, *12*, 1609140. [CrossRef]
7. Qi, S.; Wang, J.; Liu, X.; Xia, C.; Li, X.; Shao, W.; Wang, Z. Experimental and Simulation Investigation of Lunar Energy Storage and Conversion Thermoelectric System Based on In-Situ Resource Utilization. *Appl. Therm. Eng.* **2024**, *254*, 123854. [CrossRef]
8. Palos, M.F.; Serra, P.; Fereres, S.; Stephenson, K.; González-Cinca, R. Lunar ISRU Energy Storage and Electricity Generation. *Acta Astronaut.* **2020**, *170*, 412–420. [CrossRef]
9. Kim, S.; Lim, H.; Kim, B.-J.; Kim, T.; Park, S.-H.; Jeong, J.-W. Simulation of a Thermoelectric Power Generation System with Multiple Heat Storage for Lunar Habitat. *Acta Astronaut.* **2025**, *236*, 616–626. [CrossRef]
10. Liu, Z.; Cheng, K.; Wang, Z.; Wang, Y.; Ha, C.; Qin, J. Performance Analysis of the Heat Pipe-Based Thermoelectric Generator (HP-TEG) Energy System Using in-Situ Resource for Heat Storage Applied to the Early-Period Lunar Base. *Appl. Therm. Eng.* **2023**, *218*, 119303. [CrossRef]
11. Mazzetti, A.; Gianotti Pret, M.; Pinarello, G.; Celotti, L.; Piskacev, M.; Cowley, A. Heat to Electricity Conversion Systems for Moon Exploration Scenarios: A Review of Space and Ground Technologies. *Acta Astronaut.* **2019**, *156*, 162–186. [CrossRef]
12. Palaporn, D.; Tanusilp, S.; Sun, Y.; Pinitsoontorn, S.; Kurosaki, K. Thermoelectric Materials for Space Explorations. *Mater. Adv.* **2024**, *5*, 5351–5364. [CrossRef]
13. Chen, J.-L.; Liao, Y.; Zhou, Q.; Liang, J.; Miao, L.; Zhu, Y.; Wang, S.; He, W.; Nishiate, H.; Lee, C.-H.; et al. Realizing High Conversion Efficiency in Shallow Cryogenic Thermoelectric Module Based on N-Type BiSb and p-Type MgAgSb Materials. *Mater. Today Phys.* **2022**, *28*, 100855. [CrossRef]
14. Lobunets, Y. Thermoelectric Generator for Utilizing Cold Energy of Cryogen Liquids. *J. Electron. Mater.* **2019**, *48*, 5491–5496. [CrossRef]
15. Sun, W.; Hu, P.; Chen, Z.; Jia, L. Performance of Cryogenic Thermoelectric Generators in LNG Cold Energy Utilization. *Energy Convers. Manag.* **2005**, *46*, 789–796. [CrossRef]
16. Vasavada, A.R.; Bandfield, J.L.; Greenhagen, B.T.; Hayne, P.O.; Siegler, M.A.; Williams, J.-P.; Paige, D.A. Lunar Equatorial Surface Temperatures and Regolith Properties from the Diviner Lunar Radiometer Experiment. *J. Geophys. Res. Planets* **2012**, *117*, E00H18. [CrossRef]
17. Zhong, Z.; Yan, J.; Xiao, Z. Lunar Regolith Temperature Variation in the Rümker Region Based on the Real-Time Illumination. *Remote Sens.* **2020**, *12*, 731. [CrossRef]
18. Xiao, X.; Yu, S.; Huang, J.; Zhang, H.; Zhang, Y.; Xiao, L. Thermophysical Properties of the Regolith on the Lunar Far Side Revealed by the in Situ Temperature Probing of the Chang'E-4 Mission. *Natl. Sci. Rev.* **2022**, *9*, nwac175. [CrossRef]
19. Malla, R.B.; Brown, K.M. Determination of Temperature Variation on Lunar Surface and Subsurface for Habitat Analysis and Design. *Acta Astronaut.* **2015**, *107*, 196–207. [CrossRef]
20. Martinez, A.; Siegler, M.A. A Global Thermal Conductivity Model for Lunar Regolith at Low Temperatures. *J. Geophys. Res. Planets* **2021**, *126*, e2021JE006829. [CrossRef]

21. Horvath, T.; Hayne, P.O.; Paige, D.A. Thermal and Illumination Environments of Lunar Pits and Caves: Models and Observations from the Diviner Lunar Radiometer Experiment. *Geophys. Res. Lett.* **2022**, *49*, e2022GL099710. [CrossRef]
22. Daniarta, S.; Błasiak, P.; Kolasiński, P.; Imre, A.R. Sustainability by Means of Cold Energy Utilisation-to-Power Conversion: A Review. *Renew. Sustain. Energy Rev.* **2024**, *205*, 114833. [CrossRef]
23. Kambe, M.; Morita, R.; Omoto, K.; Koji, Y.; Yoshida, T.; Noishiki, K. Thermoelectric Module Performance in Cryogenic Temperature. *J. Power Energy Syst.* **2010**, *4*, 12–26. [CrossRef]
24. Zulkepli, N.; Yunas, J.; Mohamed, M.A.; Hamzah, A.A. Review of Thermoelectric Generators at Low Operating Temperatures: Working Principles and Materials. *Micromachines* **2021**, *12*, 734. [CrossRef]
25. Sidorenko, N.; Parashchuk, T.; Maksymuk, M.; Dashevsky, Z. Development of Cryogenic Cooler Based on n-Type Bi-Sb Thermoelectric and HTSC. *Cryogenics* **2020**, *112*, 103197. [CrossRef]
26. Lavrentev, M.G.; Drabkin, I.A.; Ershova, L.B.; Volkov, M.P. Improved Extruded Thermoelectric Materials. *J. Electron. Mater.* **2020**, *49*, 2937–2942. [CrossRef]
27. Chung, D.Y.; Hogan, T.; Brazis, P.; Rocci-Lane, M.; Kannewurf, C.; Bastea, M.; Uher, C.; Kanatzidis, M.G. $CsBi_4Te_6$: A High-Performance Thermoelectric Material for Low-Temperature Applications. *Science* **2000**, *287*, 1024–1027. [CrossRef] [PubMed]
28. Wang, X.; Chen, Z.; Zhang, S.; Zhang, X.; Zhou, R.; Li, W.; Luo, J.; Pei, Y. Enhanced Cryogenic Thermoelectric Cooling of $Bi_{0.5}Sb_{1.5}Te_3$ by Carrier Optimization. *InfoMat* **2025**, *7*, e12663. [CrossRef]
29. Woods-Robinson, R.; Siegler, M.A.; Paige, D.A. A Model for the Thermophysical Properties of Lunar Regolith at Low Temperatures. *J. Geophys. Res. Planets* **2019**, *124*, 1989–2011. [CrossRef]
30. Luo, D.; Wang, R.; Yu, W.; Zhou, W. Parametric Study of Asymmetric Thermoelectric Devices for Power Generation. *Int. J. Energy Res.* **2020**, *44*, 6950–6963. [CrossRef]


**Disclaimer/Publisher's Note:** The statements, opinions and data contained in all publications are solely those of the individual author(s) and contributor(s) and not of MDPI and/or the editor(s). MDPI and/or the editor(s) disclaim responsibility for any injury to people or property resulting from any ideas, methods, instructions or products referred to in the content.

energies

MDPI

*Review*

# Advances in the Aerothermal Performance Enhancement of Turbine Blade Tip Configurations

**Bin Wu, Lei Ren, Renyi Wen, Chenrui Yang and Daren Zheng ***

Key Laboratory of Aircraft Environment Control and Life Support, MIIT, Nanjing University of Aeronautics and Astronautics, Nanjing 210016, China
* Correspondence: zhengdareng@gmail.com

**Abstract**

A clearance necessarily exists between the blade tip and the casing in turbines. A leakage flow, formed by the accelerated gas through the tip clearance, is a major cause of turbine stage efficiency loss. Severe heat loads on the blade tip surface also result from a leakage flow, a primary cause of blade damage. Although the understanding of leakage flow mechanisms is mature after years of research, the continuous rise in turbine inlet temperature, pursuing higher engine thrust, requires more effective cooling methods for the blade tip region. This paper presents a review of research on three fundamental tip structures (flat tip, squealer tip, and winglet tip) to explain their design concepts, analyze their respective flow mechanisms as well as heat transfer characteristics, and introduce various modified designs. Various film cooling arrangements applied to these tip structures are examined to identify effective strategies that strengthen the advantages of structural optimization. In view of engineering applications, this paper reviews research on unsteady wake interactions as the aforementioned framework, hoping to provide readers a more comprehensive understanding.

**Keywords:** turbine blade tip; leakage flow; tip cooling performance; unsteady wake interaction; machine learning for blade design

## 1. Introduction

Gas turbines play a critical role in advanced turbine engines to generate thrust. Modern turbines mainly adopt the axial-flow configuration with multiple stages. Each stage includes a stator mounted on the casing and a rotor mounted on a shaft. The gas, under the guidance of the stator, impinges on the rotor at an incidence angle, forcing the rotor to rotate to generate mechanical energy, which is used to drive the compressor and other components to process the next working cycle. The rotating shaft may experience radial displacement, and the blade exposed to the high-temperature gas will experience spanwise deformation. This leads to an increased possibility of rubbing between blade tips and casing. Maintaining an adequate clearance between them is essential to ensure the safety of these moving and static components. However, partial gas flows through the gap because of the pressure difference between two sides of the blade, which is the leakage flow. The leakage flow contributes to significant efficiency loss, approximately one-third [1,2].

Quantities of research were conducted to clarify the leakage flow mechanism and the associated loss. Not only were experiments conducted using advanced facilities and technologies, but numerical simulation generally became a widely used method as computational codes and commercial software made significant progress. Studies [3–5] comparing

computational data with experimental results verified the reliability of the numerical simulation. The combined studies based on experimental and numerical approaches helped researchers better understand the flow pattern and heat transfer characteristics, significantly contributing to the development of the cooling system design for turbine blades.

The efficiency penalty of tip loss measured by Booth et al. [6] showed that a 1% additional tip clearance gives 1.5% additional loss. Moore and Tilton [7] further validated the flow patterns involving a vena contracta and described them using a simple two-dimensional model at the foundation of Rains' research [8]. Based on the above model, a modified equation between the contraction coefficient and the discharge coefficient theory was derived by Heyes et al. [9]. Measurements on velocity field and pressure distribution of leakage flow in clearance were conducted by Sjolande et al. [10] and Yaras et al. [11], and the detail structures were obtained. Bindon [12] explained the formation of leakage flow loss dominated by separation bubbles. Dishart and Moore [13] and Yaras and Sjolander [14] investigated the leakage loss under different clearance conditions, and the aforementioned theories about discharge coefficient and separation bubble were referenced, providing a more accurate method for loss prediction.

Achieving higher efficiency must be established on the foundation that the turbine blade can operate normally. The main reason for blade damage, even failure, is the severe heat load. The temperature of the leakage flow significantly exceeds the material limit, and the turbine inlet temperature increases with the engine development to obtain more powerful thrust. As a consequence, a thorough understanding of heat transfer characteristics and the development of an effective cooling system are the essential parts of the turbine blade design. Given the complex three-dimensional flow field within the tip gap that creates nonuniform heat transfer coefficient distributions with localized peak magnitudes on the tip, the acquisition of detailed heat transfer coefficient profiles becomes not only a prerequisite for blade tip cooling design but also a critical criterion for solution effectiveness validation. Historically, modification of tip geometry to mitigate leakage flow or alter flow field distribution has always been a normal strategy for reducing heat transfer coefficients in tip region. A detailed review of structure design will be presented in a later section. Film cooling is one of the common cooling methods to protect blades from extremely high heat load. Coolant flow generated within the compressor and transferred through the blade's internal cooling channel is ejected from the film cooling hole to protect the local surface from high temperature gas over-tip leakage, effectively reducing the localized heat transfer coefficient. Research focusing on enhancing film cooling effectiveness has been widely conducted and will be reviewed in detail in the subsequent section.

This paper provides a review based on different tip geometries to explain their design concepts, analyze their respective flow field characteristics as well as heat transfer characteristics, and introduce various optimized designs. Different combinations of film cooling configurations and various blade tip structures are systematically reviewed, with the aim of exploring efficient solutions where structural optimization and cooling strategies mutually enhance advantages of each other. Not only steady conditions but unsteady conditions are also taken into consideration to gain deeper insights into the effects of wake interaction.

## 2. Flat Tip

A flat tip is the simplest and most basic of all the blade tip structures. It acts as both the primary research subject and the essential comparison standard for subsequent investigations. Figure 1 shows the basic flow pattern of over-tip leakage for an unshrouded flat tip. The leakage flow is driven by the pressure gradient through the tip clearance. After exiting the clearance, the leakage flow mixes with the mainstream flow, forming a leakage vortex and generating significant mixing losses. Figure 1b illustrates the simple model of

tip clearance flow on the plane normal to the camber line of a flat tip. After the leakage flow accelerates into the gap from the pressure side, the abrupt narrowing of the passage induces a vena contracta phenomenon. Additionally, a separation bubble exists near the pressure side on the tip. Depending on the blade thickness (accurately the ratio of clearance height to blade thickness), the leakage flow exhibits differences in flow attachment or not, downstream of the separation bubble. Yaras et al. [11] found that the separation bubble occupied a larger proportion as the tip clearance increased, while the discharge coefficient showed a decreasing trend with increasing tip clearance, indicating that the effective flow area was reduced by the separation bubble. The experimental results of Heyes et al. [9] were in agreement with the conclusion of Yaras et al. [11] and indicated that the discharge coefficient should be decreased to achieve a reduction in the all over losses. Moore et al. and Bindon et al. [15,16] concluded that the vena contracta significantly contributed to the localized high heat transfer coefficients and the burnout of the blade pressure side.

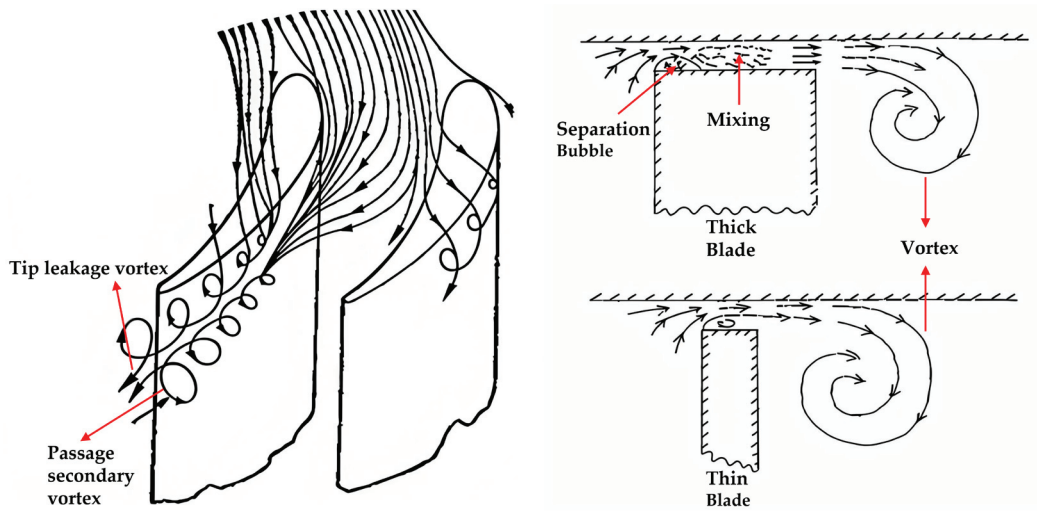



**Figure 1.** Schematic diagram of leakage flow for a subsonic flat tip. (**a**) Schematic diagram of the basic form of over tip leakage; (**b**) schematic diagram of the gap flow [1,17].

Research by Mayle and Metzger [18] on simulated two-dimensional heat transfer revealed that the leakage flow and the relative blade-to-endwall motion were the primary factors influencing blade tip heat transfer. Local heat fluxes on the flat tip from leading edge to approximately thirty percent chords were obtained by Metzger et al. [19] at two different clearances. Nearly the entirety of heat transfer coefficients on a flat tip were measured by Bunker and Ameri [20]. In the study combining the experimental and numerical methods of Ameri and Bunker [21], an accurate model was built for computation according to the details of the experimental rig. Good agreement was achieved in the comparison of the experimental results and the numerical data. The combined research not only obtained detailed heat transfer coefficients on part of the flat tip but also validated the reliability of the numerical method and the k-ω turbulence model.

Azad et al. [22] measured detailed heat transfer coefficients and static pressure distributions on a blade tip with the GE-E3 profile in a five-bladed stationary liner cascade through the transient liquid crystal technique. They also considered the influence of the tip clearance and the turbulence intensity. The high heat transfer region exhibited a high degree of consistency with the leakage flow path, and the flow path of the leakage flow was changed towards the leading-edge suction side by the decreased tip gap. The decreased tip gap reduced both the leakage flow rate and the associated heat transfer coefficient, while the increased turbulence intensity enhanced the heat transfer where the leakage flow

passed through. Yang et al. [23] performed a numerical simulation of the flow and heat transfer in the GE-E3 tip region to validate their model against the experimental data of Azad et al. [22], with good agreement achieved. Calculation results from several different turbulence models were compared to evaluate the effect of different turbulence models. These turbulence models all showed qualitatively consistent results and were quantitatively different from those of the experiment, while the RNG k-ε yielded the best consistency. Effect of tip clearance for the flat tip was included in many studies [24,25], and the general conclusion was that higher clearances compared to lower ones resulted in a higher heat transfer coefficient when other variables were controlled.

Sealing geometries such as ribs, trip strips, pins, and so on were set on a flat tip surface in order to block leakage flow in tip clearance. Rational sealing configuration arrangements can optimize the flow field and reduce the leakage flow rate. On the contrary, improper arrangements may induce more severe flow separation and increase loss. Therefore, investigations on such sealing configuration arrangements were conducted to verify the value of the designs. Saxena et al. [26] investigated the effect on reduction of the leakage flow and heat transfer by several configurations like trip strips and pin fins, as shown in Figure 2. The trip strips perpendicular to the leakage flow direction exhibited the lowest leakage flow rate and the highest overall heat transfer coefficient reduction.

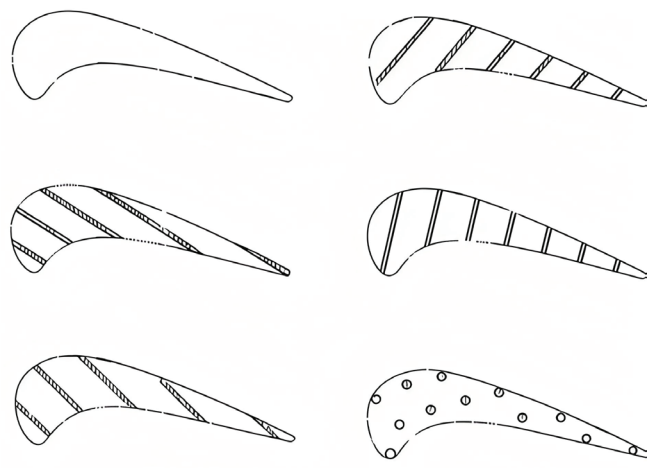


**Figure 2.** Schematic diagram of tips from research of Saxna et al. [26].

Kwak et al. [27] studied the film cooling effectiveness on the first-stage blade tip of an aircraft engine turbine (GE-E3). There were 13 film cooling holes along the camber and on the pressure side. Two arrangements were studied (ejection only from the tip and from both the tip as well as the pressure side). Three tip gap clearances and three blowing ratios were the controlled variables. Higher film cooling effectiveness was obtained with the larger tip gap. The increasing blowing ratio resulted in an increase in film cooling effectiveness. Compared with injection from the tip hole only, injection from both the tip and pressure side holes provided lower heat transfer coefficients and better film cooling effectiveness.

Under typical engine operating conditions, the blade tip flow is primarily transonic. The transonic flow is accompanied by complex phenomena such as shock wave generation, flow separation, and reattachment variations, which significantly influence heat transfer on a blade tip. Following extensive exploration of characteristics of blade tip heat transfer under subsonic conditions, researchers began to pay increased attention to investigating heat transfer performance on transonic blade tips. A primary issue was whether the conventional pressure-driven wisdom still maintained its applicability under transonic conditions, serving as the basis for research as it did in subsonic conditions. Zhang and He [28] carried out a study for conditions ranging from subsonic to transonic. Different

flow patterns were observed between subsonic and transonic conditions. The contour of the Mach number along a plane for subsonic and transonic tip flow is shown in Figure 3. From the results, a large portion of the tip region experiencing transonic flow was observed to be choked, which was also reported by Shyam et al. [29]. The choking limited the overall leakage flow rate. The influence from the suction side was also mitigated, which resulted in the pressure difference between the pressure and suction sides not being the dominant influence of the leakage flow rate. The choking was believed to be advantageous for designing a high-load blade due to its suppression of leakage flow. Wheeler et al. [30] used a CFD code to compare the nature of heat transfer on the blade tip in subsonic and transonic conditions; significant differences were observed. These transonic flow features included the form of the shock wave and the halving of the length of the separation bubble, which were in agreement with the study of Zhang and He [28]. The shortening of the separation bubble was due to the supersonic acceleration of the mainstream flow passing over the separation zone, which generated a stronger pressure gradient that forced the separated flow to reattach. These phenomena resulted in lower turbulence production. The weakened turbulent mixing in the transonic tip region was responsible for the reduction in heat load, in contrast to the low-speed condition. High-speed flow was less dominated by turbulent dissipation compared with low-speed flow, leading to less differences in the choice of turbulence model. Zhang et al. [31] accurately described the high-speed nature of the blade tip. The flow over the first 30% of the axial chord was subsonic and the leading-edge region exhibited higher heat transfer compared to the downstream transonic area. The multiple and repeated heat transfer variations in the form of stripes were first observed in the supersonic part of the tip. The inner link between these stripes and the patterns of shock wave initiation and reflection was explained. Additionally, the influence of clearances on heat transfer of a transonic blade tip was studied by Zhang et al. and Anto et al. [32,33], among others.

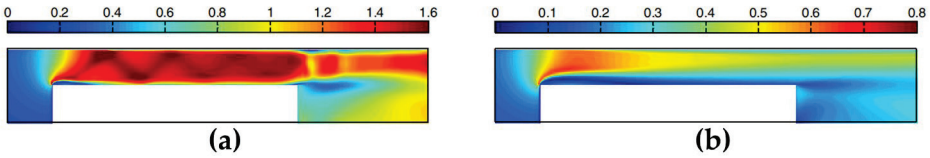



**Figure 3.** Mach number contours along an axial cut plane from research by Zhang and He. (**a**) Subsonic tip flow, exit Mach number of 1.01; (**b**) transonic tip flow, exit Mach number of 0.37 [28].

After reviewing the preceding article, we can find that the understanding of the flat tip demonstrates a spiral progression. The principles of driven pressure difference, vena contracta, and pressure bubble theory have guided the design for reducing blade loss. Recognizing the need to ensure blade protection while enhancing efficiency, research on blade cooling has gained significant attention. After substantial advancements in subsonic blade studies, subsequent research into transonic blades has further filled the knowledge gaps. The flat tip, as the most conventional blade tip profile, frequently serves as a contrast for evaluating the performance of more complex tip designs. Consequently, its characteristics will be discussed further in the subsequent sections where relevant comparative studies are presented.

## 3. Squealer Tip

It is known that a smaller tip clearance brings lower losses and lower heat load, but it will increase the risk of the blade tip rubbing into the casing, accordingly. The contradiction can be effectively solved by using a squealer tip. The squealer tip is characterized by a recessed cavity on a flat tip. The thin wall surrounding the cavity is the squealer rim

that serves as a sacrificial feature. Even if rubbing occurs, only part of the rim will be damaged without compromising the integrity of the main blade body. Therefore, the effective tip clearance is decreased by decreasing the gap between the rim top and the casing. In addition, the cavity functions as a labyrinth seal to resist leakage flow [34]. From the oil flow visualization shown in Figure 4, the flow in the flat tip gap maintains a predominantly axial flow direction, while the flow within the cavity exhibits a component of streamwise velocity [35], demonstrating a lower velocity in the cavity. The leakage flow rate was verified to be reduced by using squealer tips [9]. Mischo et al. [36] predicted three-dimensional flow through a squealer tip, as shown in Figure 5. The complex flow in the cavity of a squealer was characterized by three dominant vortices. The cavity vortex, formed by the separation and roll-up of the rim boundary layers along the cavity bottom corners, extended across both the pressure side and the front suction side. The scraping vortex was generated by the casing boundary layer fluid interacting with leakage flow. The corner vortex developed when jets from the leading edge of pressure side impinged on the suction-side corner.

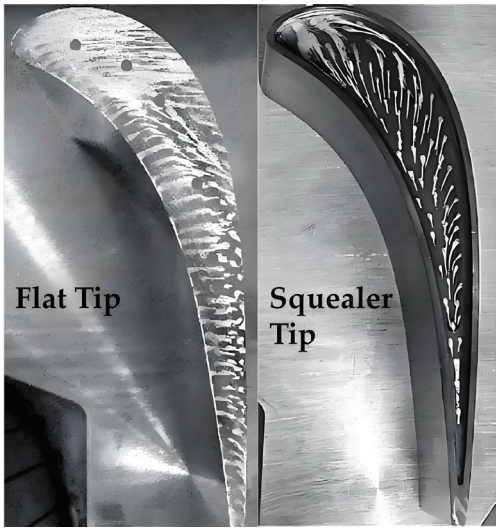



**Figure 4.** Flow visualization of flat and squealer tip [35].

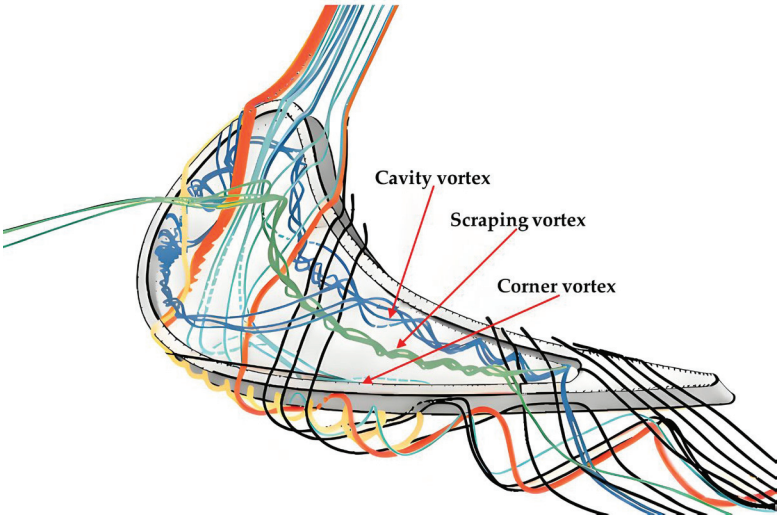



**Figure 5.** Three-dimensional CFD predicted flow field in a squealer tip [36].

Numerous studies conducted with different methods have demonstrated a reduced overall heat transfer coefficient relative to flat tips [4,37–40]. Metzger et al. [37] and Chyu

et al. [4] used two-dimensional tip models to study the heat transfer on squealer tips with varying cavity depth-to-width and tip gap-to-width ratios, and an optimal ratio was obtained. Azad et al. [38] and Kwak et al. [39] measured the all-coverage heat transfer coefficient distribution on the three-dimensional squealer tip, as shown in Figure 6. Yang et al. [40] performed a numerical simulation with boundary conditions consistent with reference [38]. The location of the high heat transfer coefficient on the cavity floor compared with that on the flat tip was found to shift toward the suction side and axially toward the leading edge. However, the rim surface showed higher heat transfer coefficients than the cavity floor, particularly at the trailing edge and the suction side, where the values exceeded those of the corresponding flat tip, while the pressure-side rim was observed to have comparable heat transfer to the flat tip [4,37,38]. Although the numerical predictions by Ameri et al. [41] indicated that the cavity bottom showed higher heat transfer than the flat tip, the predictions for the rim region maintained qualitative consistency with experimental results. In addition, the leading edge at the cavity floor was observed to exhibit a heat transfer peak because of the flow impingement [39,41]. The flow impingement can be recognized clearly in Figure 4, where the dots appear smeared. The squealer tip provided a pronounced reduction in heat transfer coefficients on the shroud compared to the flat tip. However, the reductions for the tip region of two blade sides were comparably not remarkable [39].

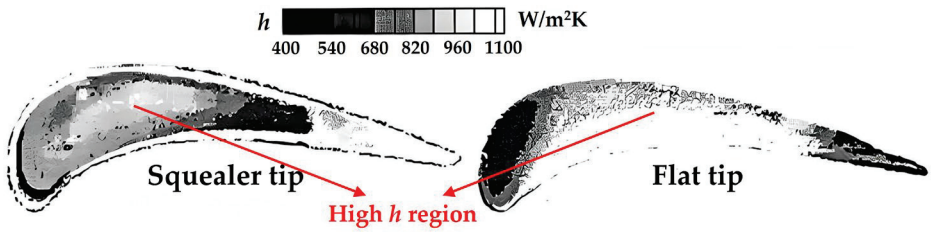



**Figure 6.** Heat transfer coefficient on squealer tip and flat tip measured by Azad et al. [38].

The width and depth (equivalent to cavity depth) of the squealer rim, typical characteristics of the squealer tip, are fundamental design parameters whose effects should be well understood. Yang et al. [42] and Lee et al. [43] both separately studied five cavity depths. The similar conclusion they reached was that as the cavity depth increased, there existed an optimum value for reducing leakage flow. When the cavity depth exceeded the value, no additional reduction could be obtained. (Especially, Yang et al. [42] identified a 3% cavity depth-to-blade span ratio, while Lee et al. [43] found a 2.75% rim height-to-axial chord length ratio.) On the other hand, heat transfer coefficients exhibited a monotonically decreasing trend as the groove depth increased. Wang et al. [44] and Li et al. [45] investigated different rim widths under subsonic and transonic conditions, respectively. An increased rim width led to a reduction in the heat load on the cavity floor. Each of their smallest widths (0.58% of axial chord in reference [44] and 0.8% of blade height in reference [45]) presented maximum aerodynamic efficiency and the lowest heat transfer coefficient, respectively. The tip clearance influence on the squealer tip was similar to that on the flat tip. Three different tip clearances were studied by Azad et al. [38], and five different tip clearances were taken into consideration by Yang et al. [42]. A larger gap yielded a higher overall heat transfer coefficient, which was attributed to the increased leakage flow rate.

As most of the studies mentioned above were conducted under the condition that the blades were stationary relative to the casing, the validity requires further validation. Experiments by Metzger et al. [37] and Chyu et al. [4] introduced a moving shroud surface aimed at investigating the influence of relative motion and verified the effectiveness of

a stationary model in the tip heat transfer investigation. The influence of rotation on the blade tip leakage flow and heat transfer was numerically simulated by Yang et al. [46]. The three simulated rotation conditions included the rotating blade with a stationary shroud, the stationary blade with a rotating shroud, and the stationary blade with a stationary shroud. The main influencing factor of the rotation was the relative motion of the endwall, while the influence of the Coriolis and centrifugal forces played a limited role.

The film cooling effectiveness distribution on the squealer tip was measured by Kwak et al. [47], as shown in Figure 7. The higher blowing ratio could lead to a decreased average heat transfer coefficient. The overall film cooling effectiveness could be enhanced with the increasing blowing ratio but showed no consistent trend across tip gap clearance. Notice should be focused on the fact that, compared with the flat tip, the squealer tip presented higher film cooling effectiveness. He et al. [48] conducted a numerical study on film cooling and heat transfer on the squealer tip investigated in reference [47], with the validation agreeing well with the experimental results. The computational results regarding the effect of tip clearance and blowing ratio remain qualitatively consistent with experimental results. Higher film cooling effectiveness was obtained with coolant injection from both the tip and pressure side holes instead of only injecting from the tip holes. These could be attributed to the blockage of the leakage flow, combined with an expanded region of coolant coverage on the suction side resulting from pressure-side injection. Li et al. [49] studied the effect of tip clearance and cavity depth on pressure loss and cooling effectiveness under a staged environment. They reported that when the cavity depth was increased, the decrease in the leakage flow rate and the enlargement of the cavity vortex occurred simultaneously, resulting in an improvement at first and then deterioration of aerodynamic performance. As the depth increased at a fixed tip clearance, the separation line shifted from the pressure side toward the suction side, altering its position relative to the holes. They suggested that positioning holes on separation lines could enhance cooling effectiveness. Ma et al. [50,51] revealed the interaction between the coolant and leakage flow. The critical flow structure was a counter-rotating vortex pair (CRVP). The CRVP, characterized by its asymmetric strength with a dominant left leg, resulted from the impingement of the coolant on the casing. Strips of high heat transfer coefficient were identified at the upstream subsonic part in the cavity, as shown in Figure 8, because the strength difference induced the leakage flow to move to the cavity floor. At the trailing-edge transonic region, the leakage flow with relatively high momentum was less affected by the cooling flow. An interesting finding was that a reduction in heat flux was observed in regions unreached by injected coolant, confirming that the upstream propagation of the interaction between the coolant and the leakage flow resulted in a reduction in the local heat transfer coefficient.

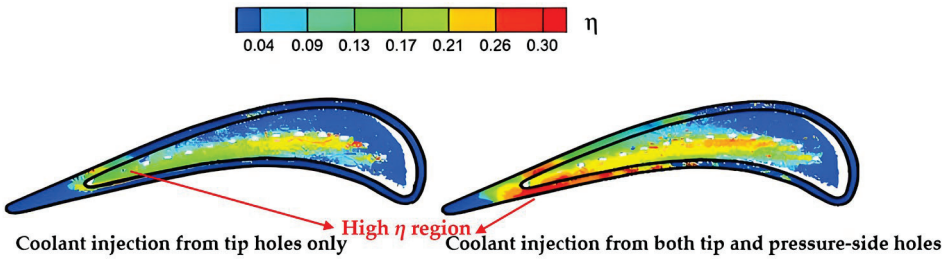



**Figure 7.** The detailed film cooling effectiveness on the squealer tip by Kwak et al. [47].

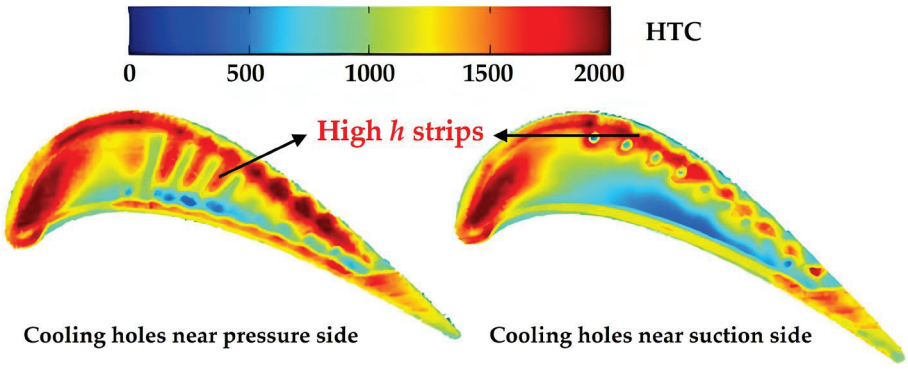



**Figure 8.** Contour of HTC for nine cooling holes by Ma et al. [50].

Adjusting the location and quantity of squealer rims was a common approach to modify the squealer tip structure. Azad et al. [52] and Kwak et al. [53,54] studied squealer tips with different rim arrangements. Measurements were conducted on the tip, shroud, and the near-tip regions. The high heat transfer region was related to the reattachment of the leakage flow downstream from the squealer rim. Therefore, different rim arrangements altered the leakage flow path, resulting in significant differences in heat transfer distribution, as shown in Figure 9. The suction-side squealer tip showed the best performance in reducing the heat transfer coefficient. Additionally, the high heat transfer region observed along the suction side corresponded to the leakage vortices developing from the tip or the squealer rim.

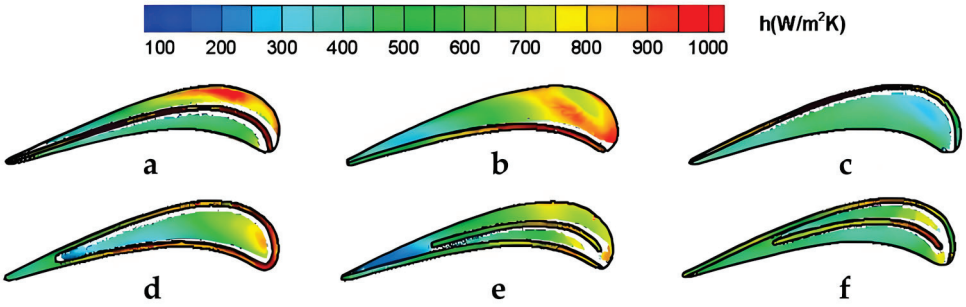



**Figure 9.** Heat transfer coefficient on squealer tips with different arrangements by Kwak et al. (**a**) The camber line; (**b**): the pressure side; (**c**) the suction side; (**d**) the pressure and suction sides; (**e**) the camber line and the pressure side; (**f**) the camber line and the suction side [53].

Mischo et al. [36] designed an improved squealer tip with nonuniform rim width; the three-dimensional schematic diagram with a cavity flow is shown in Figure 10. Comparing it with the cavity flow of the conventional squealer tip, which is shown in Figure 5, the new design eliminated the suction-side leading edge recirculation zone by optimized profiling, suppressing the cavity vortex. The jet from the pressure-side leading edge was able to spread to the entire cavity floor without localized impingement on the suction-side corner, eliminating the extreme heat region. The scraping vortex broke away from the constraint of the casing and mixed with the pressure-side jet, reducing aerodynamic losses. The improved design simultaneously enhanced total efficiency by 0.38% and reduced the Nusselt number by 7% compared with the conventional squealer tip.

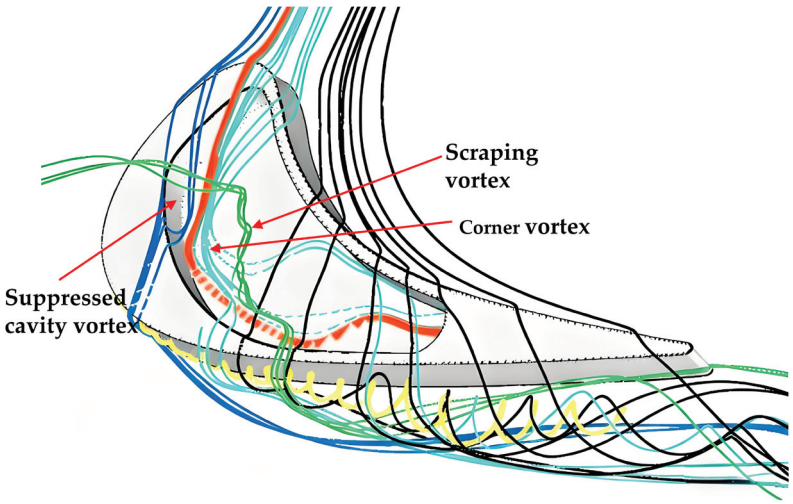



**Figure 10.** Schematic diagram of flow field for an improved squealer tip [36].

The influence of the partial loss of squealer rim material on turbine blade heat transfer was studied by Bunker and Bailey [55]. Their findings were out of expectation that material loss of the pressure-side rim in the mid-chord region could reduce tip heat transfer, which could be considered an inspiration for the design of partial squealer rims. Camci et al. [56,57] selected an optimal tip structure from several partial squealer tips according to their aerodynamic characteristics. The schematic diagram of these partial squealer rims is shown in Figure 11. The performance of leakage flow reduction and stage efficiency enhancement by suction-side partial squealers performed better than pressure-side partial squealers. Mhetras et al. [58] and Gao et al. [59] investigated the film cooling effectiveness of a partial squealer tip with the pressure side trailing-edge cut. The effects of varying squealer cavity depth, blowing ratios, and coolant injection arrangements were also considered. They concluded that the pressure-side cutback squealer tip provided enhanced cooling effectiveness in the trailing edge compared to the conventional full squealer. Naik et al. [60] compared film cooling effectiveness between a full and a partial squealer tip. The partial squealer tip provided enhanced film cooling at the trailing edge but reduced effectiveness near the leading edge. Lu et al. [61] evaluated two partial squealer tip configurations, featuring a cutback on the pressure-side rim and suction-side rim, respectively. The pressure-side cutback squealer tip suffered a strong impinging leakage flow, leading to an increased heat transfer coefficient near the trailing edge compared with the suction-side cutback design. Due to wiping effect of the high-pressure leakage flow which swept the coolant away from the tip surface, the intended cooling areas could not be covered effectively. Thus, the pressure-side cutback played an inefficient role. In contrast, the suction side cutback effectively enhanced film cooling effectiveness because of the sheltering effect of the pressure-side rim, as the coolant maintains sustained coverage above the cavity floor to the trailing edge.

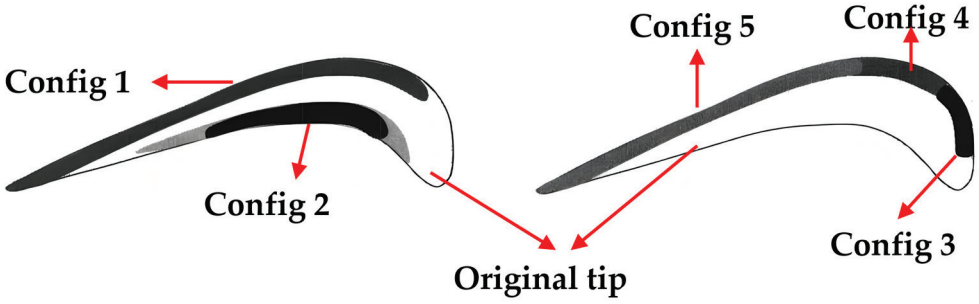



**Figure 11.** Schematic diagram of partial squealer tips designed by Camci et al. [56].

Jeong et al. [62] designed partial cavity tips. In previous studies, a "sweet point" was observed at the flat tip leading edge, and a low heat transfer coefficient could be found at the cavity trailing edge at the squealer tip. Therefore, the partial cavity tips were designed to combine their respective advantages. As shown in Figure 12, these tips featured a flat surface near the leading edge and a cavity extending from mid-chord to the trailing edge. The lowest heat transfer coefficient was achieved by the partial cavity with the cavity extending from the 10% chord, while the highest film cooling effectiveness was yielded by the conventional squealer tip for its uniform coolant distribution and recirculation. Li et al. [63] further studied the influence of a partial cavity on squealer tips with the PW-E3 turbine blade profile. Computational models were obtained by filling the front partial areas of the cavity tip geometry. The size of the pressure-side corner vortex showed a trend of initially increasing and then decreasing as the filling areas increased, and the heat transfer coefficient showed a consistent trend. They suggested that the weakening pressure-side corner vortex correlated with reduced blade tip heat transfer. Enhancing the scraping vortex and suppressing the suction-side corner vortex contributed to a decrease in leakage flow. Du et al. [64] added ribs on the foundation of the partial cavity tip to investigate whether the designs could optimize the heat transfer characteristics. The suction-side rib configuration and the lateral ribs configuration did enhance the aerothermal performance compared to the flat tip. A 27.4% reduction in averaged Nusselt number on the tip surface and a 16.3% decrease in leakage flow were achieved by the suction-side ribbed configuration. The lateral ribs configuration showed an averaged Nusselt number reduction of 27.2% on the tip surface and a 17.3% decrease in leakage flow.

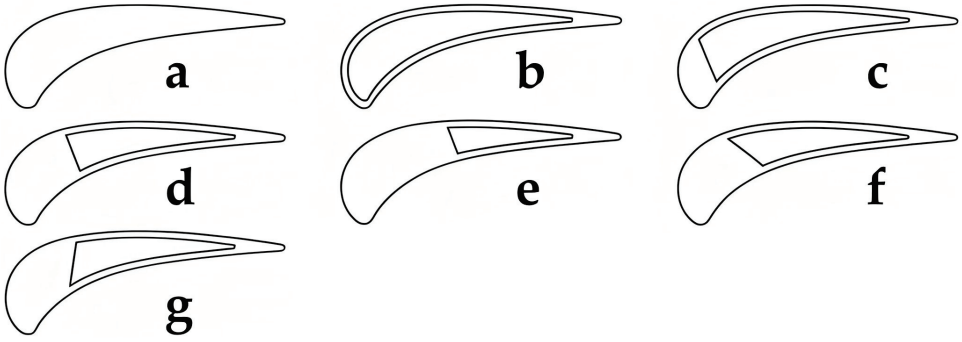



**Figure 12.** Schematic diagram of partial cavity tips designed by Jeong et al. [62].

Cernat al. [65] designed a multi-cavity squealer-like tip, with its geometry presented in Figure 13. The multi-cavity squealer-like tip took the partial squealer design with an island closed rim presented in the middle of the outer squealer cavity. The multi-cavity squealer-like tip could limit mid-chord leakage by dual sealing and improve efficiency by 3% over the flat tip. However, a higher heat flux in the casing region was observed due to frequent impacts between the multi-cavity and the casing.

Park et al. [66] performed experimental and numerical studies into multi-cavity blade tips, which were obtained by separating the cavity with ribs. Du et al. [67] investigated the aerothermal performance of multi-cavity squealer tips. Four ribs were specified as perpendicular to the camber line with equal spacing, dividing the cavity into five small cavities. In addition, according to the number of ribs arranged in the cavity, four cases were distinguished and studied. The rib design was intended to weaken the high heat at the cavity floor due to the reattachment flow. They concluded that the multi-cavity squealer tip showed a lower heat transfer because the reattachment flow was truncated by the ribs. However, regions near the ribs worked more similar to a flat tip, especially the trailing edge. The multi-cavity tip exhibited a higher total pressure loss than the single

cavity. Consequently, the five-cavity tip demonstrated the lowest overall heat transfer coefficient but the highest total pressure loss among all configurations. Jiang et al. [68] further optimized the multi-cavity squealer tips. They replaced ribs in five cavity tips with half-ribs of different numbers and locations. The four-rib tip, with half-ribs connected to the pressure side, not only could truncate the reattachment line but also could prevent the deficiency of the trailing-edge aerothermal characteristics from being similar to the flat tip. Therefore, the four-rib tip obtained optimal comprehensive aerothermal performance. Studies on such squealers with ribs in the cavity were also conducted by Park et al. [69], Huang et al. [70], and Bi et al. [71]. Typically, film cooling on similar multi-cavity tips was investigated by Bi et al. [71]. They concluded that although ribs placed mid-chord downstream hindered coolant coverage by altering leakage flow paths, those ribs placed upstream effectively blocked the separation region at the cavity bottom, thereby improving coolant coverage. The multi-cavity tip with two ribs positioned at 10% and 25% chord exhibited optimum performance, demonstrating a superior balance of reducing the leakage flow and heat transfer coefficient while enhancing film cooling effectiveness. Specifically, compared to the uncooled ribless one, this configuration achieved a 24.96% reduction in the averaged heat transfer coefficient and an 18.82% decrease in the leakage flow mass rate.




**Figure 13.** Geometry of the multi-cavity squealer like tip by Cernat et al. [65].

In summary, the traditional squealer tip configuration demonstrated significant advantages compared to flat tips, including reducing the leakage flow rate, reducing the heat transfer coefficient, and enhancing the film cooling effectiveness. Building on this foundation, researchers have further explored structural modifications on squealer tips to achieve improved aerothermal performance. Initial broad parametric studies investigated critical squealer rim geometry parameters, such as width and height. Subsequent efforts focused on targeted structural designs based on detailed analysis of flow field and heat transfer characteristics, followed by experimental validation. Through advancing design methodologies and increasingly mature research approaches, researchers have made substantial achievements in enhancing tip cooling performance through optimized squealer tip structures. Table 1 summarizes the features and advantages of the squealer tip and its modified designs.

**Table 1.** Features and advantages of the squealer tip and its modified designs.

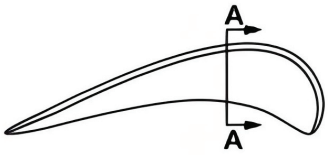
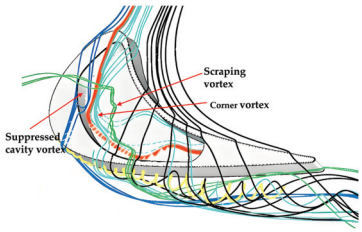
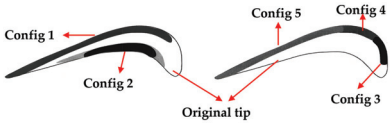
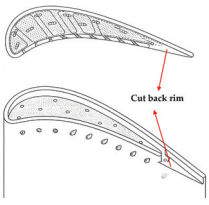
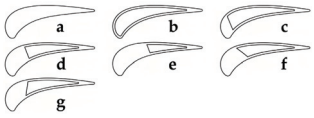
| Tip Configurations | Schematic Diagram | Results |
| --- | --- | --- |
| Conventional squealer tip [4,37–40] |  | Lower overall heat transfer coefficient than flat tip. [4,37–40]<br>High heat transfer region on cavity floor moved toward the suction side and the leading edge compared to flat tip. [38,40]<br>High heat transfer region on squealer rims increased particularly at the trailing edge and the suction side compared to flat tip [4,37,38]. |
| Squealer with different cavity depths [42,43] | | Existing an optimum cavity depth for leakage flow reduction. (3% cavity depth-to-blade span ratio 42, 2.75% rim height-to-axial chord length ratio [43]).<br>Depth increased; heat transfer coefficient decreased. |
| Squealer tip with different rim widths [44,45] | | Existing optimum rim width for aerodynamic efficiency (0.58% of axial chord) [44].<br>Existing optimum rim width for total heat transfer coefficient (0.8% of blade height) [45]. |
| Squealer tip with cooling holes [47–49] |  | Higher overall film cooling effectiveness than flat tip [47,48].<br>Depth increased, leakage flow reduction initially increased and then decreased [49].<br>Film holes located on the separation line could be beneficial for film cooling effectiveness [49]. |
| Squealer tip with different rim arrangements [53,54] |  | Flow reattachment downstream from the squealer rim results in a high heat transfer region.<br>Suction-side squealer showed highest reduction in heat transfer coefficient. |
| Squealer tip with nonuniform rim width [36] |  | Optimizing the flow structure compared to conventional squealer tip.<br>Result of 0.38% total efficiency enhancement and 7% Nusselt number reduction. |
| Partial squealer tip [56,57] |  | Suction-side partial squealers showed higher stage efficiency enhancement than pressure side. |
| Partial squealer tip (pressure side trailing edge cut) with cooling holes [58–60] |  | Higher film cooling effectiveness in trailing-edge region compared to full squealer tip [58,59].<br>Lower film cooling effectiveness in the leading-edge region compared to full squealer tip [60]. |
| Partial squealer tips with cooling holes [61] | | Suction-side cut back showed better film cooling effectiveness compared to pressure-side cutback. |
| Partial cavity tips [62] |  | Tip with cavity from 10% chord showed the lowest heat transfer coefficient.<br>Conventional squealer tip showed the highest cooling effectiveness. |

**Table 1.** *Cont.*

| Tip Configurations | Schematic Diagram | Results |
| --- | --- | --- |
| Partial cavity tips [63] |  | Filling area increased, heat transfer coefficient initially increased and then decreased. |
| Partial cavity tips with ribs [64] | | Suction-side ribbed configuration (SRT) showed 27.4% reduction in the averaged Nusselt number and 16.3% decrease in leakage flow compared to flat tip.<br>Lateral ribs configuration (SLCT) showed 27.2% reduction in averaged Nusselt number and 17.3% decrease in leakage flow compared to flat tip. |
| Partial squealer design with an island closed rim [65] |  | Lower leakage flow, 3% higher efficiency, and higher heat flux compared to flat tip. |
| Multi-cavity tip [67] | | Four-rib configuration showed weakened high heat region by reattachment flow, lower heat transfer, and higher pressure loss compared to conventional squealer tip.<br>Two leading-edge full-ribs and two trailing-edge half-ribs configurations showed the most comprehensive aerothermal performance. |
| Multi-cavity tip with two ribs at 10% and 25% chord [71] | | Result of 24.96% averaged heat transfer coefficient reduction and 18.82% decrease in leakage flow rate compared to conventional uncooled squealer tip. |

## 4. Winglet Tip

A "winglet" is originally designed for installation at the tips of airplane wings to weaken wingtip vortices and decrease induced drag. The concept of the winglet used in turbine blade tips is a very short extension by extending a tip platform in a tangential direction, as Dey and Camci [72] explained. The concept of the winglet was involved in research by Booth et al. [6]. They intended it to reduce the inlet pressure drop, thus decreasing the pressure difference. The use of the winglet reduced the discharge coefficient by 9% compared to a flat tip, which demonstrated the effect of winglet design in leakage suppression and improving turbine efficiency. Willinger et al. [73] used a simplified model to simulate and predict the discharge coefficient of the winglet tip. Despite a 5% discrepancy from the experimental data of Booth et al. [6], the prediction still demonstrated the effect of reducing leakage flow by the winglet tip. Dey and Camci [72] investigated the use of the pressure-side winglet and suction-side winglet on an axial flow turbine blade tip to reduce the leakage flow with comparison to the flat tip. The pressure-side winglet tip was demonstrated to be an effective design to reduce the jet leaking into the suction side, while the suction-side winglet did not present its effectiveness. Kang and Seo [74,75] studied a flat tip with a full-coverage overhang with the influence of different tip clearances. Mass/heat transfer on the tip and bottom surface of the overhang were analyzed. The mass/heat transfer rate on the bottom surface of the winglet showed a liner negative correlation trend with the tip clearance. The original surface region of the flat tip on the winglet tip was verified to suffer less thermal load than the flat tip, while the overhang region showed higher heat load than the flat tip surface.

Harvey et al. [76] validated the effectiveness of reducing leakage flow on the unshrouded tip by a new winglet tip design. As shown in Figure 14, there are two winglets with an aerofoil shape at the blade tip, forming a channel and indirectly doubling the number of rotor tips. The prediction indicated that the turbine stage efficiency was improved by 1.2–1.8 percent and the tip loss exchange rate was reduced by 30 percent. Harvey et al. [17] and Willer et al. [77] conducted further investigations on the winglet tip described in reference [76] to consider its partial application value. They proposed that the unshrouded blades with winglets could not replace current full shroud blades in aircraft engines at that time, although the significant effectiveness in reducing leakage flow loss by the winglet was equivalent to a two-fin shrouded tip. For a replacement to be viable, the winglet tip would not only need to perform better than the current design (which has two fins and two fences) but also undergo further improvement. O'Dowd et al. [78] and Zhou et al. [79] investigated the aerothermal performance of a transonic winglet tip. The geometry resembled the winglet design presented by Harvey [76], as seen in Figure 15. The average heat load on the winglet tip was nearly 2.7 times higher than that on a flat tip. This was not a surprising result because the primary design purpose of the winglet was to reduce leakage flow, with cooling achieved through introducing cooling holes on the surface. Zhou et al. [80] and O'Dowd et al. [81] further studied the aerothermal performance of the cooled winglet tip at low-speed and transonic conditions, respectively. The combined effects of relative endwall motion and reduced tip clearance were investigated. Endwall motion reduced the leakage mass flow but increased scraping vortex loss, contributing to a net 15% decrease in tip leakage loss and a 31% reduction in winglet tip heat flux, driven by a 14% lower Nusselt number and 9% higher cooling effectiveness. Smaller tip clearances improved film cooling effectiveness through superior coolant coverage. The winglet tip was also used in a study on wall thermal conditions conducted by Zhang and He [82]. They proposed a challenge to the conventional assumption that the leakage flow characteristics were not influenced by the wall thermal boundary conditions at transonic conditions. The computational results demonstrated that there was a strong two-way interaction between aerodynamics and heat transfer under transonic conditions, and the newly proposed nonlinear correction method obtained a simulation accuracy close to the conjugate heat transfer, improving significantly over the traditional linear method.

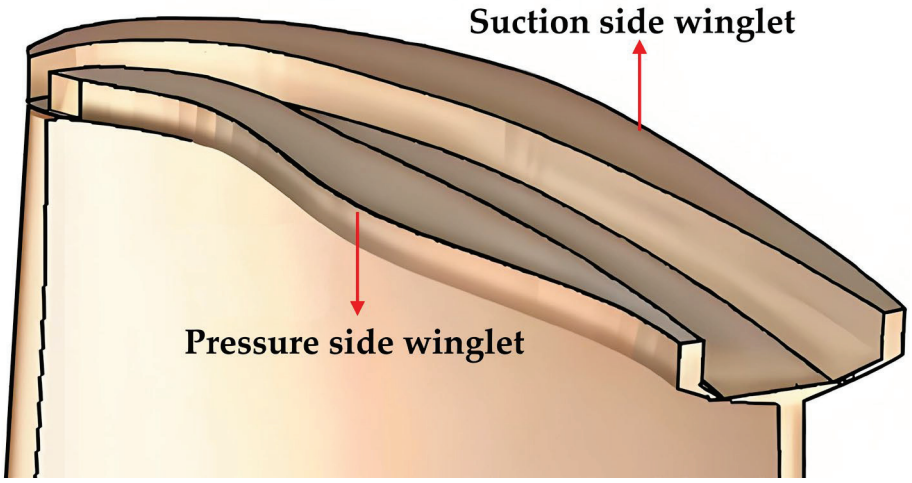



**Figure 14.** Geometry of the winglet presented by Harvey et al. [76].

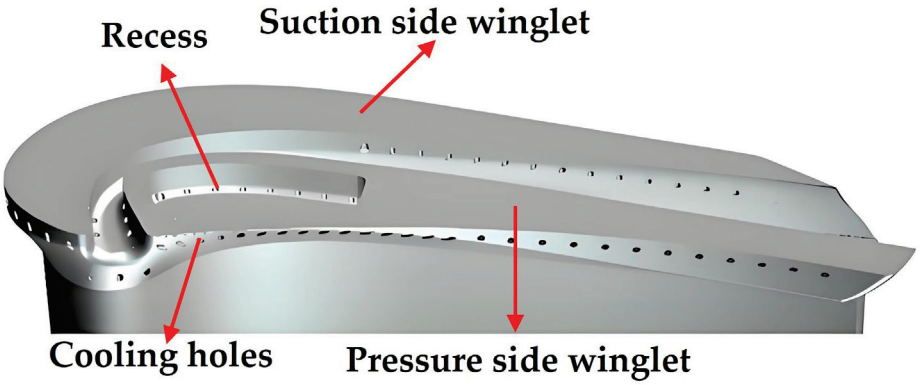



**Figure 15.** Geometry of the winglet tip studied by O'Dowd et al. [78].

Applying the design concept of winglet to the suction-side squealer tip, research on the winglet–squealer tip configuration was initiated by Papa et al. [83], as shown in Figure 16. They found that the cavity of the winglet–squealer tip yielded a lower mass transfer coefficient compared to the conventional squealer tip. Saha et al. [84] studied the winglet–squealer tip with the winglets extending from the pressure side not only at a suction-side squealer tip but also at a full squealer tip, as shown in Figure 17. Adding a winglet to the flat tip led to a weaker leakage flow and a 7% decrease in the average heat transfer coefficient. For the full squealer tip, however, the winglet had a minimal effect on both leakage and heat transfer. The most significant improvement was observed on the suction-side squealer tip, where the winglet proved most effective, reducing heat transfer by 5.5% and the pressure loss coefficient by 27%. Joo and Lee [85,86] studied winglets extending from the circumferential edge of the squealer tip. The mass/heat transfer rate on the cavity floor of the winglet–squealer tip was lower than that on the winglet surface, and the discrepancy between them decreased as tip clearance increased. The cavity floor provided a lower mass/heat transfer rate by using the winglet at two lower tested tip clearances, but the contrary phenomenon was observed at two higher clearances. Yan et al. [87] studied the suction-side squealer tip with a pressure side winglet of different leading-edge angles and different coverage percentages. The conventional squealer, suction-side squealer tip, and the winglet–squealer tip were compared through numerical methods. They concluded that the removal of the pressure-side rim could weaken the heat transfer on the leading-edge cavity floor. Furthermore, replacing the pressure-side rim with a winglet could further reduce heat transfer while also reducing total pressure loss. The winglet leading-edge angle had little influence on the total pressure loss as well as the heat transfer distribution, although it could optimize localized high heat transfer. There was an optimal coverage percentage of the winglet that could significantly reduce the total pressure loss (13.8% reduction by 80% winglet coverage) and the heat transfer coefficient (15.8% reduction by 60% winglet coverage) in contrast to a conventional squealer tip. Yan et al. [88] conducted a numerical investigation into film cooling characteristics on a winglet–squealer tip based on studies of Kwak et al. [39,47]. The distributions of the heat transfer coefficient and film cooling effectiveness of the squealer tip were consistent with the experimental results. The suction-side squealer tip and the pressure-side winglet tip showed better performance in reducing total pressure loss, heat transfer characteristics, and film cooling effect compared with the conventional squealer tip, especially the pressure-side winglet, yielding the lowest heat transfer. The pressure-side winglet showed a higher film cooling effectiveness than the suction squealer tip under small tip clearance conditions. The authors also proposed that the pressure-side winglet tip was more sensitive to the blowing ratio and coolant ejection angle, which should be further investigated in the geometry optimization study.

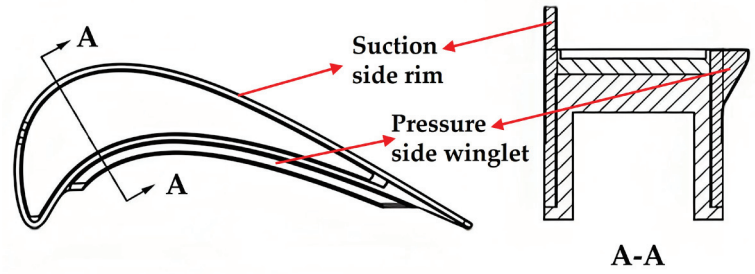



**Figure 16.** Schematics of winglet–squealer tip by Papa et al. [83].

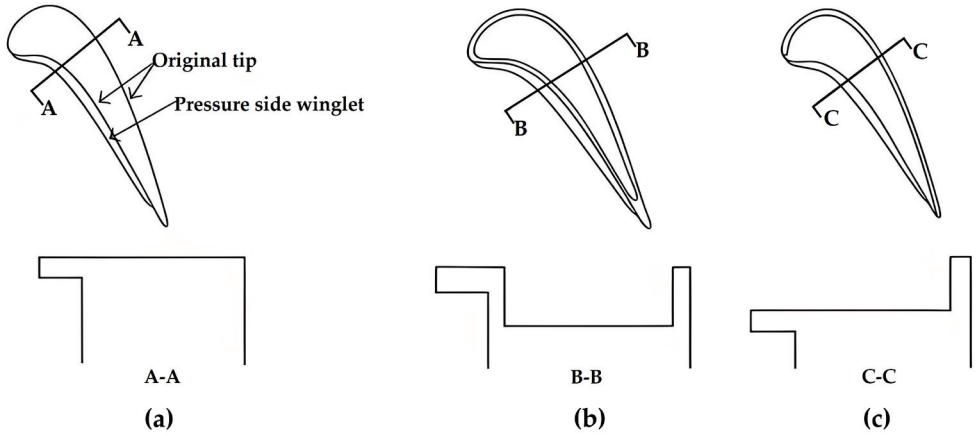



**Figure 17.** Schematics of (**a**) flat tip with winglet, (**b**) squealer tip with winglet, and (**c**) suction-side squealer with winglet [84].

Schabowski and Hodson [89] also studied a kind of winglet–squealer tip, as shown in Figure 18. These winglet–squealer tips were designed by adding squealer rims on the edges of the winglet platforms and were different from the winglet–squealer tips previously referred to, where the winglets extended from the squealer tip. The optimal design was the winglet with thin squealer rims because it had the combined effect of reducing driving pressure by the winglet and leakage flow blockage by the squealer rims. Schabowski et al. [90] then studied the optimization of a winglet–squealer tip. The optimized tip with the suction-side winglet and thin squealers significantly weakened the leakage loss related to the flat tip at all tested exit speed conditions. Jiang et al. [91] designed three squealer winglet structures that extended winglets from the cavity floors of the squealer tips and were equipped with rims at the edge of the winglets, presenting multi-cavity structures. Both reduced the average heat transfer coefficient and reduced leakage flow mass, and both sides of the squealer winglet tip showed the best performance, followed by the suction-side winglet tip. However, concerning the reduction in the total pressure loss coefficient, the suction-side winglet tip was superior to both sides of the squealer winglet tip, but the pressure-side winglet tip demonstrated adverse effects.

Coull et al. [92] used a novel parameterization method to design the geometry of the winglet tip. Figure 19 shows the change in efficiency and heat load for all designed winglets. It indicated that winglets extending from only the early suction side can significantly improve efficiency without increasing the overall heat transfer. Zhou et al. [93] introduced a novel philosophy to design suction-side winglet tips, driven by an analysis of the near-tip flow field, as shown in Figure 20. The driving pressure difference in the leakage flow was reduced by using the suction-side winglets. The leakage flow loss was also reduced by 18.1% for winglet-2 compared to the cavity tip. However, winglet designs suffered more severe heat load than the cavity tip. Zhong et al. [94,95] designed similar suction-side winglet tips based on the loss mechanism described in reference [93], as shown in Figure 21.

A two-sided winglet tip and a small suction-side winglet tip, whose winglet only extended from the leading edge, were considered. The small suction-side winglet tip showed the best aerothermal performance. The design of the winglet not extending to the trailing edge could prevent additional leakage driving forces and high heat load.



**Figure 18.** Squealer and winglet geometries in the study of Schabowski and Hodson [89].

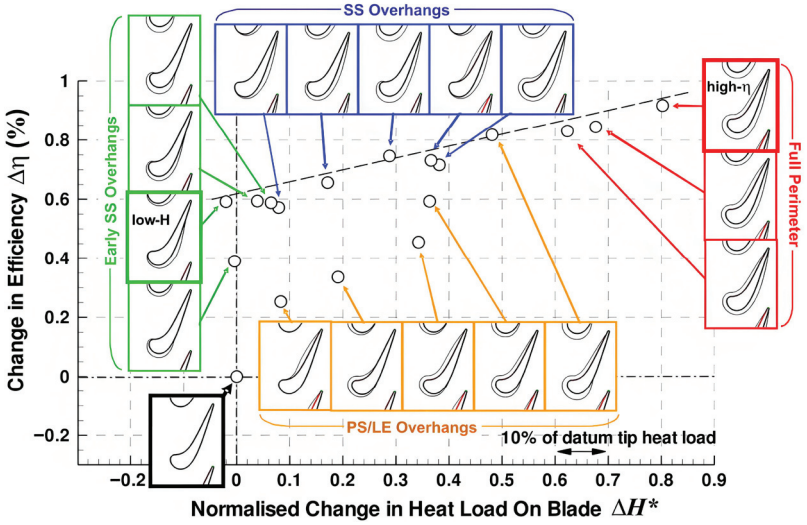



**Figure 19.** Changes in efficiency and heat load for winglet designs [92].

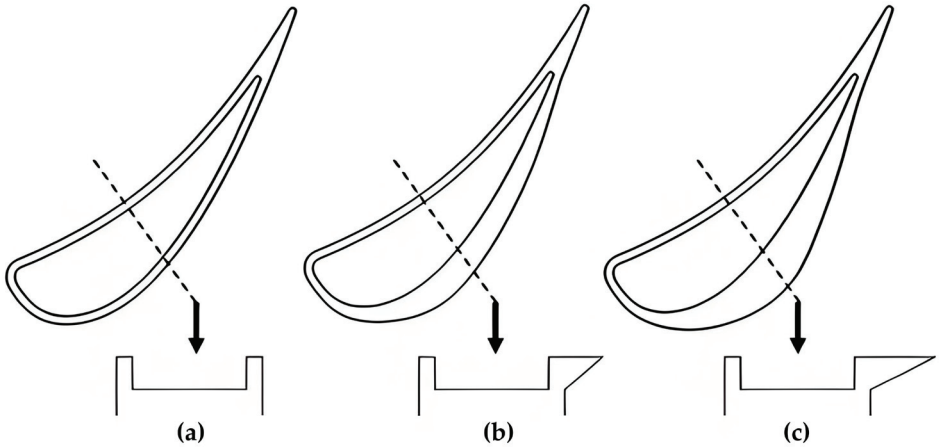



**Figure 20.** Tip geometries of cavity tip (**a**), winglet 1 (**b**), and winglet 2 (**c**) [93].

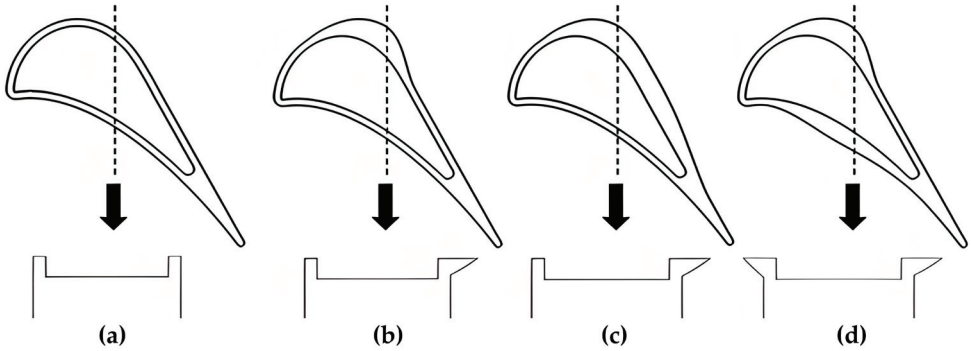



**Figure 21.** Tip geometries of cavity tip (**a**), winglet 1 (**b**), winglet 2 (**c**), and winglet 3 (**d**) [94].

A winglet on a turbine blade tip is an extending platform extending from the tip surface. Initially proposed with the same objective as the early research of turbine blades, the winglet tip aimed to reduce the leakage flow by decreasing the driven pressure difference across the tip, thereby enhancing the turbine efficiency. By reducing the driven pressure difference across the tip, winglets enhance turbine efficiency. However, their relatively complex geometry and larger surface area necessitate efficient cooling design. Extensive research has not only advanced the understanding of inherent winglet characteristics but also found the excellent performance of the combined design with squealer tips. Furthermore, multi-parameter shape optimization, guided by flow field and heat transfer characteristics, has significantly improved design specificity and effectiveness. Table 2 summarizes the features and advantages of the winglet tip and its modified designs.

**Table 2.** Features and advantages of the winglet tip and its modified designs.

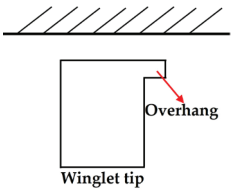
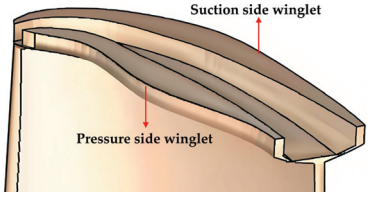
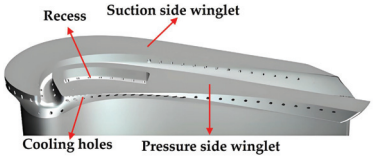
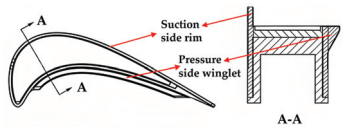
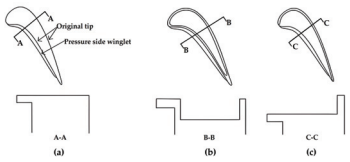
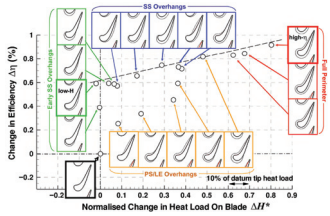
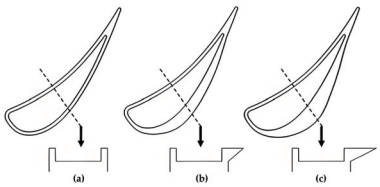
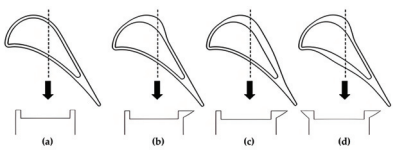
| Tip Configurations | Schematic Diagram | Results |
| --- | --- | --- |
| Winglet tip [6,72,73] |   | Result of 7% discharge coefficient reduction compared to flat tip. Result of 5% discrepancy with data from reference [6]. Suction-side winglet tip showed higher leakage reduction compared to suction-side winglet tip [72]. |
| Full-coverage winglet tip [74,75] | | High and lower mass/heat transfer at overhang region and original surface, respectively, compared to flat tip. Existing liner negative correlation trend between mass/heat transfer on the winglet bottom and the tip clearance. |
| Winglet tip with two aerofoils [76] |  | Result of 1.2–1.8% stage efficiency improvement and 30% tip loss exchange rate reduction compared to flat tip. |
| Winglet tip with two aerofoils [76,77] |   | Equivalent leakage flow loss with a two-fin shrouded tip. |

**Table 2.** *Cont.*

| Tip Configurations | Schematic Diagram | Results |
| --- | --- | --- |
| Winglet tip with two aerofoils and rectangle groove [78–81] |   | Showed 2.7 times higher averaged heat load than flat tip [78,79]. Showed 14% decreased Nusselt number with the endwall motion [80,81]. Showed 9% increased film cooling effectiveness with the endwall motion [80,81]. |
| Pressure-side winglet and suction-side squealer [83] |   | Lower mass transfer coefficient compared to conventional squealer tip. |
| Pressure-side winglet [84] |   | Result of 7% averaged heat transfer coefficient reduction compared to flat tip. |
| Pressure-side winglet and full squealer [84] | | Little reduction in leakage flow and virtually no reduction in heat compared to full squealer tip. |
| Pressure-side winglet and suction-side squealer [84] | | Resulted in 5.5% less heat transfer and 27% lower pressure loss compared to suction side squealer tip. |
| Full-coverage winglet and full squealer [85,86] | | Cavity floor showed lower mass/heat transfer than winglet surface. |
| Pressure-side winglet and suction-side squealer [87,88] | | The 60% winglet showed 13.8% total pressure loss reduction compared with conventional squealer tip [87]. The 80% winglet showed 15.8% heat transfer coefficient reduction compared with conventional squealer tip [88]. Result of 54.2% higher cooling effectiveness than conventional squealer tip at 1.5% tip clearance [88]. |
| Thin squealer on winglet [89,90] |  | Result of 19.4–26.6% lower leakage flow rate than flat tip. |
| Multi-cavity squealer tip [91] | | Suction-side arrangement performance best in reducing heat transfer, leakage flow, and pressure loss. |
| Winglet by a novel parameterization method [92] |   | Winglets extending from only the early suction side showed superior performance in improving efficiency. |
| Optimized suction side winglet–squealer tip [93] |   | Result of 18.1% leakage flow loss reduction compared to conventional squealer tip. |
| Optimized winglet–squealer tip [94,95] |   | Small suction-side winglet tip showed the best aerothermal performance. |

## 5. Unsteady Wake

The studies mentioned above were primarily conducted with steady uniform incoming conditions. This steady-state assumption remains rational and effective for blade design, as it presents performance averaged over extended operational periods. However, such an approach actually neglects some unsteady flow phenomena, particularly the interference caused by stator wakes. Consequently, advancing the understanding of unsteady characteristics is of great importance for gaining deeper insights into blade tip heat transfer mechanisms and further optimizing cooling structure design. In a gas turbine stage, the boundary layer shedding from the trailing edge of the upstream blades forms a wake that influences downstream flow. This wake critically affects turbine performance, influencing efficiency, loss generation, and noise emission. The heat transfer on the blade tip becomes particularly complex because of the interactions between wake and leakage flow boundary layer.

Hodson et al. [96] and Chaluvadi et al. [97] directly measured the unsteady flow field within rotors using pressure probes and a five-hole probe. Unlike measuring stationary a stationary blade, it is difficult to measure the flow field with rotating vanes and rotors. Laser technology measurements were taken by Binder [98], Zaccaria [99], and Göttlich [100] to obtain an unsteady flow field. Simplified experiments were conducted by Doorly [101], Ashworth [102], and Dullenkopf [103]. They used a rotating bar to simulate the motion of an upstream vane, generating an unsteady wake on the stationary blades. In the study of Guenette et al. [104], the effectiveness of this simulation approach was verified. Computational methods for unsteady prediction were developed by Rai et al. [105], Giles et al. [106], and Abhari et al. [107].

Sharma et al. [108] studied the three-dimensional unsteady wake downstream of the vane in a large-scale 1.5 stage turbine rig. They found that although the position of the rotor relative to the wake of the upstream guide vanes continuously changed, the tip leakage vortex itself behaved relatively stable. Zeschky et al. [109], Gallus et al. [110], and Volino et al. [111] also proposed that leakage flow was only slightly influenced by wake, while the leakage vortex had more interaction with the passage secondary vortex, as presented by Payne et al. [112] and Zhou et al. [113].

Ameri et al. [114] conducted a numerical study on the influence of unsteady wake on tip heat transfer. They proposed that the blade tip flow was dominated by the tip leakage flow, whose intensity was strong enough to diminish the effect of the unsteady wake. Therefore, the obtained results showed that the difference between the time-averaged Nusselt number from unsteady calculations and the steady values was small. In fact, the time-averaged results would hide the instantaneous high heat transfer regions, which suffered the most severe damage on the blade tips. This highlighted the necessity of capturing such instantaneous variations depending on unsteady research conditions. In transonic conditions, blade tip heat transfer was investigated by Thorpe et al. [115]. Although the influence of the wake interaction was limited, the interference effect of the vane trailing-edge shock is significant. When the blade's leading edge approaches the vane, a shock wave generated at the throat between the blade's leading edge and the vane suction side directly interacted with the tip surface, triggering an instantaneous increase in the heat transfer coefficient. Molter et al. [116], Rahman et al. [117], and Atkins et al. [118] studied the unsteady heat transfer at transonic turbine conditions. Significant pressure fluctuations induced by vane trailing-edge shocks were observed, along with localized severe heat transfer regions driven by unsteady shock–leakage flow interaction, particularly in squealer tips. These studies revealed that time-accurate results could be more representative of the actual gas turbine conditions.

Squealer tip geometries could weaken the influence of unsteady interactions, compared with the flat tip. Saxena et al. [26] found that the wake injecting into the tip gap brought higher turbulence strength, thus enhancing the overall heat transfer, especially at the sweet spot. The full squealer tip demonstrated the lowest heat transfer coefficients under the wake influence among different rim arrangements. An increase in cavity depth [119] or an increase in tip clearance [120] enhanced the influence of unsteadiness on heat transfer. This was because the vortex in the cavity provided a dampening effect on the wakes, preventing the immediate breakdown of the boundary layer that occurred on the flat tip. Furthermore, adding wake interaction with larger tip clearance resulted in higher time-averaged heat transfer. Polanka et al. [121] attributed the variations in flux fluctuations to the pressure fluctuations. In the study of Jiang et al. [122], as the blade tip approached or moved away from the vane wake, the pressure difference correspondingly increased or decreased, subsequently causing fluctuations in the heat transfer coefficient. The use of a multi-cavity tip resulted in elevated fluctuations only within the third and fourth cavities [68]. While the localized heat transfer increased, the overall heat transfer on the multi-cavity remained lower than that of a squealer tip. Zhou et al. [123] investigated vane–blade interaction and tip leakage flow with a winglet–squealer tip. Compared with a flat tip, the winglet–squealer tip significantly reduced the time-averaged leakage flow and increased the time-averaged efficiency. These could be attributed to the weakening of the unsteady interaction by the winglet guiding and stabilizing the leakage flow.

Mehendale et al. and Ou et al. [124,125] studied the influence of wake flow on blade heat transfer and film cooling. Under the interaction of the unsteady wake, the heat transfer coefficient significantly increased, while the film cooling effectiveness decreased with the disruption of film coverage. However, the relative increase in the heat flux without film cooling was higher than that which was cooled, contributing to a decrease in the heat flux ratio. This demonstrated the benefit of film cooling in the unsteady environment of actual turbines. Gao et al. [126,127] also found that the film cooling effectiveness decreased significantly because of the turbulent mixing of coolant and mainstream enhanced by the upstream wake. The compound angle-shaped holes shown in Figure 22 could maintain wider coolant coverage compared to axial-shaped holes under unsteady conditions, providing better cooling performance. Rallabandi et al. [128] found that coolant ejected from the pressure side reattached downstream on the surface, exhibiting higher cooling effectiveness than that from the suction side. They advised using compound angle-shaped holes arranged along the pressure side with high density ratio coolant ejection to reduce the influence of the wake interaction. Zhang et al. [129] investigated the axial arrangement of film cooling holes under unsteady conditions. They proposed that the film cooling holes were not recommended to be arranged at the leading edge. Because the cooling efficiency fluctuated the most at the leading edge due to wake effects, film holes may also disrupt the sweet spot. Jiang et al. [130] and You et al. [131,132] conducted unsteady investigations of film cooling on squealer tips, as shown in Figure 23. A finding reached from their studies was that when the wake interaction was strong, the coolant failed to provide adequate coverage, whereas when the wake interaction weakened, the cooling efficiency significantly improved. This revealed a severe challenge of the temporal mismatch between high cooling efficiency and high heat load. This showed that the key challenge of the temporal mismatch between high cooling effectiveness and high heat loads remained. To mitigate the localized transient overheating, further efforts should be devoted to cooling system improvement.

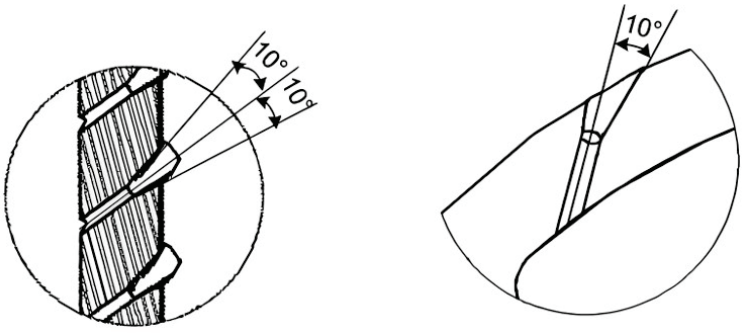



**Figure 22.** The compound angle-shaped holes [127].

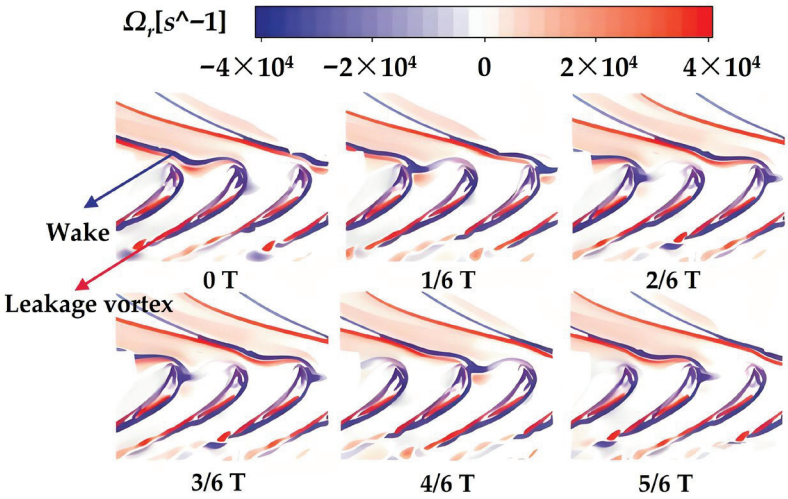



**Figure 23.** The vorticity contour on a middle plane of the tip clearance at different times [130].

## 6. Concluding Remarks

Thanks to decades of persistent efforts by researchers, significant progress has been made in fundamental theories, experimental techniques, and CFD technology. Acquiring accurate flow field data and detailed heat transfer distributions has become an advanced capability, and the research focus has shifted from understanding to optimization. To meet the demands of rapidly developing modern gas turbine engines, blade cooling design must keep pace accordingly.

Effective structure design can weaken the leakage flow and reduce the heat transfer coefficient on the tip surface. For the squealer tip, decreasing tip clearance and reducing leakage flow velocity through a sealing effect are the primary functions. While the design philosophy of the winglet tip is to weaken the leakage flow by reducing the driving pressure difference, adjusting these basal tip structures in detail can further weaken the high heat transfer region. Traditional optimization methods, whether through experiments or numerical simulations, demand substantial costs and long time cycles. Depending on machine learning to develop predictive models to assist in design has become an effective way to improve optimization efficiency. The establishment of a predictive model generally involves the following steps. The blade profile is parameterized to generate a certain amount of parameter data sets, which are then simulated. The obtained result files are used to build and train the network, followed by optimizing and validating the predictive model [133]. In this way, as long as the design parameters are input, the machine can provide prediction results. Once this technology matures, it will provide significant support for blade design.

Combining cooling injections with these inherent structure advantages can achieve excellent aerothermal performance. However, complex interactions exist between coolant

and leakage flow, and their manifestation varies across different tip geometries. Interactions on the targeted tip are suggested to be studied further. Although substantial research has enhanced our understanding of these effects on normal tips, studies on targeted tip configuration under unsteady interactions are rare. It is worth it to further optimize cooling design for advanced tip configurations under unsteady conditions. This optimization specifically addresses the temporal mismatch between high cooling efficiency and high heat load.

**Funding:** The authors gratefully acknowledge the support of the National Natural Science Foundation of China (Grant No. 12202192), the Fundamental Research Funds for the Central Universities: Key Laboratory of Aircraft Environment Control and Life Support, MIIT, Nanjing University of Aeronautics and Astronautics (Grant No. KLAECLS-E-202206), and Key Laboratory of Civil Aviation Emergency Science and Technology CAAC (Grant No. XCA2402202).

**Conflicts of Interest:** The authors declare no conflicts of interest.

## References

1. Denton, J.D. *Loss Mechanisms in Turbomachines*; American Society of Mechanical Engineers: New York, NY, USA, 1993. [CrossRef]
2. Schaub, U.W.; Vlasic, E.; Moustapha, S.H. Effect of tip clearance on the performance of a highly loaded turbine stage. In *AGARD, Technology Requirements for Small Gas Turbines*; TIB: Hannover, Germany, 1994; 11p, SEEN 94-34431 10-07.
3. Wadia, A.R. Numerical solution of two-and three-dimensional rotor tip leakage models. *AIAA J.* **1985**, *23*, 1061–1069. [CrossRef]
4. Chyu, M.K.; Moon, H.K.; Metzger, D.E. Heat transfer in the tip region of grooved turbine blades. *ASME J. Turbomach.* **1989**, *111*, 131–138. [CrossRef]
5. Ameri, A.A.; Steinthorsson, E. Prediction of Unshrouded Rotor Blade Tip Heat Transfer. In Proceedings of the ASME 1995 International Gas Turbine and Aeroengine Congress and Exposition, Houston, TX, USA, 5–8 June 1995; Heat Transfer, Electric Power, Industrial and Cogeneration. ASME: New York, NY, USA; Volume 4, p. V004T09A037. [CrossRef]
6. Booth, T.C.; Dodge, P.R.; Hepworth, H.K. Rotor-Tip Leakage: Part I—Basic Methodology. *ASME Eng. Power.* **1982**, *104*, 154–161. [CrossRef]
7. Moore, J.; Tilton, J.S. Tip Leakage Flow in a Linear Turbine Cascade. *ASME Turbomach.* **1988**, *110*, 18–26. [CrossRef]
8. Rains, D.A. Tip Clearance Flows in Axial Flow Compressors and Pumps. Ph.D. Thesis, California Institute of Technology, Pasadena, CA, USA, 1954.
9. Heyes, F.J.G.; Hodson, H.P.; Dailey, G.M. The Effect of Blade Tip Geometry on the Tip Leakage Flow in Axial Turbine Cascades. *ASME Turbomach.* **1992**, *114*, 643–651. [CrossRef]
10. Sjolander, S.A.; Amrud, K.K. Effects of Tip Clearance on Blade Loading in a Planar Cascade of Turbine Blades. *ASME Turbomach.* **1987**, *109*, 237–244. [CrossRef]
11. Yaras, M.; Zhu, Y.; Sjolander, S.A. Flow Field in the Tip Gap of a Planar Cascade of Turbine Blades. *ASME Turbomach.* **1989**, *111*, 276–283. [CrossRef]
12. Bindon, J.P. The Measurement and Formation of Tip Clearance Loss. *ASME Turbomach.* **1989**, *111*, 257–263. [CrossRef]
13. Dishart, P.T.; Moore, J. Tip Leakage Losses in a Linear Turbine Cascade. *ASME Turbomach.* **1990**, *112*, 599–608. [CrossRef]
14. Yaras, M.I.; Sjolander, S.A. Prediction of Tip-Leakage Losses in Axial Turbines. *ASME Turbomach.* **1992**, *114*, 204–210. [CrossRef]
15. Moore, J.; Moore, J.G.; Henry, G.S.; Chaudhry, U. Flow and Heat Transfer in Turbine Tip Gaps. *ASME Turbomach.* **1989**, *111*, 301–309. [CrossRef]
16. Bindon, J.P. Pressure Distributions in the Tip Clearance Region of an Unshrouded Axial Turbine as Affecting the Problem of Tip Burnout. In Proceedings of the ASME 1987 International Gas Turbine Conference and Exhibition, Turbomachinery, Anaheim, CA, USA, 31 May–4 June 1987; ASME: New York, NY, USA; p. V001T01A085. [CrossRef]
17. Harvey, N.W.; Newman, D.A.; Haselbach, F.; Willer, L. An Investigation Into a Novel Turbine Rotor Winglet: Part I—Design and Model Rig Test Results. In Proceedings of the ASME Turbo Expo 2006: Power for Land, Sea, and Air, Turbomachinery, Parts A and B, Barcelona, Spain, 8–11 May 2006; ASME: New York, NY, USA; Volume 6, pp. 585–596. [CrossRef]
18. Mayle, R.E.; Metzger, D.E. Heat transfer at the tip of an unshrouded turbine blade. In *International Heat Transfer Conference Digital Library*; Begel House Inc: Danbury, CT, USA, 1982. [CrossRef]
19. Metzger, D.E.; Dunn, M.G.; Hah, C. Turbine Tip and Shroud Heat Transfer. *ASME Turbomach.* **1991**, *113*, 502–507. [CrossRef]
20. Bunker, R.S.; Bailey, J.C.; Ameri, A.A. Heat Transfer and Flow on the First-Stage Blade Tip of a Power Generation Gas Turbine: Part 1—Experimental Results. *ASME Turbomach.* **2000**, *122*, 263–271. [CrossRef]
21. Ameri, A.A.; Bunker, R.S. Heat transfer and flow on the first-stage blade tip of a power generation gas turbine: Part 2—Simulation results. *J. Turbomach.* **2000**, *122*, 272–277. [CrossRef]

22. Azad, G.S.; Han, J.C.; Teng, S.; Boyle, R.J. Heat transfer and pressure distributions on a gas turbine blade tip. *J. Turbomach.* **2000**, *122*, 717–724. [CrossRef]
23. Yang, H.; Acharya, S.; Ekkad, S.V.; Prakash, C.; Bunker, R. Flow and heat transfer predictions for a flat-tip turbine blade. *Turbo Expo Power Land Sea Air* **2002**, *36088*, 271–283. [CrossRef]
24. Ameri, A.A.; Steinthorsson, E.; Rigby, D.L. Effects of Tip Clearance and Casing Recess on Heat Transfer and Stage Efficency in Axial Turbines. *ASME Turbomach.* **1999**, *121*, 683–693. [CrossRef]
25. Nasir, H.; Ekkad, S.V.; Kontrovitz, D.M.; Bunker, R.S.; Prakash, C. Effect of tip gap and squealer geometry on detailed heat transfer measurements over a high pressure turbine rotor blade tip. *J. Turbomach.* **2004**, *126*, 221–228. [CrossRef]
26. Saxena, V.; Nasir, H.; Ekkad, S.V. Effect of blade tip geometry on tip flow and heat transfer for a blade in a low-speed cascade. *Turbomachinery* **2004**, *126*, 130–138. [CrossRef]
27. Kwak, J.S.; Han, J.C. Heat transfer coefficients and film-cooling effectiveness on a gas turbine blade tip. *Heat Transf.* **2003**, *125*, 494–502. [CrossRef]
28. Zhang, Q.; He, L. Overtip choking and its implications on turbine blade-tip aerodynamic performance. *J. Propuls. Power* **2011**, *27*, 1008–1014. [CrossRef]
29. Shyam, V.; Ameri, A.; Chen, J. Analysis of Unsteady Tip and Endwall Heat Transfer in a Highly Loaded Transonic Turbine Stage. *ASME Turbomach.* **2012**, *134*, 041022. [CrossRef]
30. Wheeler, A.P.S.; Atkins, N.R.; He, L. Turbine Blade Tip Heat Transfer in Low Speed and High Speed Flows. *ASME Turbomach.* **2011**, *133*, 041025. [CrossRef]
31. Zhang, Q.; O'Dowd, D.O.; He, L.; Wheeler, A.P.S.; Ligrani, P.M.; Cheong, B.C.Y. Overtip Shock Wave Structure and Its Impact on Turbine Blade Tip Heat Transfer. *ASME Turbomach.* **2011**, *133*, 041001. [CrossRef]
32. Zhang, Q.; O'Dowd, D.O.; He, L.; Oldfield, M.L.G.; Ligrani, P.M. Transonic Turbine Blade Tip Aerothermal Performance With Different Tip Gaps—Part I: Tip Heat Transfer. *ASME Turbomach.* **2011**, *133*, 041027. [CrossRef]
33. Anto, K.; Xue, S.; Ng, W.F.; Zhang, L.J.; Moon, H.K. Effects of tip clearance gap and exit Mach number on turbine blade tip and near-tip heat transfer. *Turbo Expo Power Land Sea Air Am. Soc. Mech. Eng.* **2013**, *55164*, V03CT14A005. [CrossRef]
34. Sunden, B.; Xie, G. Gas turbine blade tip heat transfer and cooling: A literature survey. *Heat Transf. Eng.* **2010**, *31*, 527–554. [CrossRef]
35. Key, N.L.; Arts, T. Comparison of Turbine Tip Leakage Flow for Flat Tip and Squealer Tip Geometries at High-Speed Conditions. *ASME Turbomach.* **2006**, *128*, 213–220. [CrossRef]
36. Mischo, B.; Behr, T.; Abhari, R.S. Flow Physics and Profiling of Recessed Blade Tips: Impact on Performance and Heat Load. *ASME Turbomach.* **2008**, *130*, 021008. [CrossRef]
37. Metzger, D.E.; Bunker, R.S.; Chyu, M.K. Cavity Heat Transfer on a Transverse Grooved Wall in a Narrow Flow Channel. *ASME Heat Transf.* **1989**, *111*, 73–79. [CrossRef]
38. Azad, G.S.; Han, J.C.; Boyle, R.J. Heat transfer and flow on the squealer tip of a gas turbine blade. *J. Turbomach.* **2000**, *122*, 725–732. [CrossRef]
39. Kwak, J.S.; Han, J.C. Heat transfer coefficients on the squealer tip and near squealer tip regions of a gas turbine blade. *Heat Transf.* **2003**, *125*, 669–677. [CrossRef]
40. Yang, H.; Acharya, S.; Ekkad, S.V.; Prakash, C.; Bunker, R. Numerical simulation of flow and heat transfer past a turbine blade with a squealer-tip. *Turbo Expo Power Land Sea Air* **2002**, *36088*, 295–307. [CrossRef]
41. Ameri, A.A.; Steinthorsson, E.; Rigby, D.L. Effect of Squealer Tip on Rotor Heat Transfer and Efficiency. *ASME Turbomach.* **1998**, *120*, 753–759. [CrossRef]
42. Yang, D.; Feng, Z. Tip leakage flow and heat transfer predictions for turbine blades. *Turbo Expo Power Land Sea Air.* **2007**, *47934*, 589–596. [CrossRef]
43. Lee, S.W.; Chae, B.J. Effects of squealer rim height on aerodynamic losses downstream of a high-turning turbine rotor blade. *Exp. Therm. Fluid Sci.* **2008**, *32*, 1440–1447. [CrossRef]
44. Wang, J.; Sundén, B.; Zeng, M.; Wang, Q. Influence of Different Rim Widths and Blowing Ratios on Film Cooling Characteristics for a Blade Tip. *ASME Heat Transf.* **2012**, *134*, 061701. [CrossRef]
45. Li, J.; Du, K.; Song, L. Effects of tip cavity geometries on the aerothermal performance of the transonic turbine blade with cavity tip. *Inst. Mech. Eng. Part A J. Power Energy* **2016**, *230*, 319–331. [CrossRef]
46. Yang, D.; Yu, X.; Feng, Z. Investigation of Leakage Flow and Heat Transfer in a Gas Turbine Blade Tip With Emphasis on the Effect of Rotation. *ASME Turbomach.* **2010**, *132*, 041010. [CrossRef]
47. Kwak, J.S.; Han, J.C. Heat transfer coefficients and film cooling effectiveness on the squealer tip of a gas turbine blade. *J. Turbomach.* **2003**, *125*, 648–657. [CrossRef]
48. He, K. Investigations of film cooling and heat transfer on a turbine blade squealer tip. *Appl. Therm. Eng.* **2017**, *110*, 630–647. [CrossRef]

49. Li, C.; Xiang, J.; Song, L.; Li, J. An aerothermal analysis of the effects of tip gap height and cavity depth of a gas turbine blade. *Int. J. Therm. Sci.* **2020**, *158*, 106521. [CrossRef]
50. Ma, H.; Zhang, Q.; He, L.; Wang, L. Cooling injection effect on a transonic squealer tip—Part I: Experimental heat transfer results and CFD validation. *J. Eng. Gas Turbines Power* **2017**, *139*, 052506. [CrossRef]
51. Ma, H.; Zhang, Q.; He, L.; Wang, L. Cooling injection effect on a transonic squealer tip—Part II: Analysis of aerothermal interaction physics. *J. Eng. Gas Turbines Power* **2017**, *139*, 052507. [CrossRef]
52. Azad, G.S.; Han, J.C.; Bunker, R.S.; Lee, C.P. Effect of squealer geometry arrangement on a gas turbine blade tip heat transfer. *Heat Transf.* **2002**, *124*, 452–459. [CrossRef]
53. Kwak, J.S.; Ahn, J.; Han, J.C.; Lee, C.P.; Bunker, R.S.; Boyle, R.; Gaugler, R. Heat transfer coefficients on the squealer tip and near-tip regions of a gas turbine blade with single or double squealer. *J. Turbomach.* **2003**, *125*, 778–787. [CrossRef]
54. Kwak, J.S.; Ahn, J.; Han, J.C. Effects of rim location, rim height, and tip clearance on the tip and near tip region heat transfer of a gas turbine blade. *Int. J. Heat Mass Transf.* **2004**, *47*, 5651–5663. [CrossRef]
55. Bunker, R.S.; Bailey, J.C. Effect of squealer cavity depth and oxidation on turbine blade tip heat transfer. *Turbo Expo Power Land Sea Air Am. Soc. Mech. Eng.* **2001**, *78521*, V003T01A038. [CrossRef]
56. Camci, C.; Dey, D.; Kavurmacioglu, L. Tip leakage flows near partial squealer rims in an axial flow turbine stage. *Turbo Expo Power Land Sea Air* **2003**, *36894*, 79–90. [CrossRef]
57. Camci, C.; Dey, D.; Kavurmacioglu, L. Aerodynamics of tip leakage flows near partial squealer rims in an axial flow turbine stage. *Turbomachinery* **2005**, *127*, 14–24. [CrossRef]
58. Mhetras, S.; Narzary, D.; Gao, Z.; Han, J.C. Effect of a cutback squealer and cavity depth on film-cooling effectiveness on a gas turbine blade tip. *ASME Turbomach.* **2008**, *130*, 021002. [CrossRef]
59. Gao, Z.; Narzary, D.; Mhetras, S.; Han, J. Effect of Inlet Flow Angle on Gas Turbine Blade Tip Film Cooling. *ASME Turbomach.* **2009**, *131*, 031005. [CrossRef]
60. Naik, S.; Georgakis, C.; Hofer, T.; Lengani, D. Heat Transfer and Film Cooling of Blade Tips and Endwalls. *ASME Turbomach.* **2012**, *134*, 041004. [CrossRef]
61. Lu, S.; Ma, H.; Zhang, Q.; Teng, J. Cutback squealer tip trailing edge cooling performance. *Int. J. Heat Mass Transf.* **2020**, *154*, 119632. [CrossRef]
62. Jeong, J.Y.; Kim, W.; Kwak, J.S.; Park, J.S. Heat transfer coefficient and film cooling effectiveness on the partial cavity tip of a gas turbine blade. *J. Turbomach.* **2019**, *141*, 071007. [CrossRef]
63. Li, L.; Tu, C.; Wang, C.; Sun, Y.; Zou, J.; Zhang, J. Control of the leakage flow and heat transfer characteristics at the blade tip by cavity filling. *Results Eng.* **2023**, *20*, 101446. [CrossRef]
64. Du, K.; Wang, X.; Huang, X.; Liu, C.; Sunden, B. Turbine blade tip aerothermal characteristics considering the influences of cavity tip shaping. *Int. J. Therm. Sci.* **2024**, *204*, 109234. [CrossRef]
65. Cernat, B.C.; Pátý, M.; De Maesschalck, C.; Lavagnoli, S. Experimental and numerical investigation of optimized blade tip shapes—Part I: Turbine rainbow rotor testing and numerical methods. *J. Turbomach.* **2019**, *141*, 011006. [CrossRef]
66. Park, J.S.; Lee, S.H.; Kwak, J.S.; Lee, W.S.; Chung, J.T. Measurement of blade tip heat transfer and leakage flow in a turbine cascade with a multi-cavity squealer tip. ASME Turbine Blade Tip Symposium. *Am. Soc. Mech. Eng.* **2013**, *56079*, V001T02A006. [CrossRef]
67. Du, K.; Li, Z.; Li, J.; Sunden, B. Influences of a multi-cavity tip on the blade tip and the over tip casing aerothermal performance in a high pressure turbine cascade. *Appl. Therm. Eng.* **2019**, *147*, 347–360. [CrossRef]
68. Jiang, S.; Li, Z.; Li, J.; Song, L. Effects of the novel rib layouts on the tip leakage flow pattern and heat transfer performance of turbine blade. *Proc. Inst. Mech. Eng. Part G J. Aerosp. Eng.* **2020**, *234*, 1446–1459. [CrossRef]
69. Park, J.S.; Lee, S.H.; Lee, W.S.; Chung, J.T.; Kwak, J.S. Heat transfer and secondary flow with a multicavity gas turbine blade tip. *J. Thermophys. Heat Transf.* **2016**, *30*, 120–129. [CrossRef]
70. Huang, M.; Zhang, K.; Li, Z.; Li, J. Effect of multi-cavity on the aerothermal performance robustness of the squealer tip under geometric and operational uncertainties. *Energy* **2024**, *287*, 129691. [CrossRef]
71. Bi, S.; Mao, J.; Chen, P.; Han, F.; Wang, L. Effect of multiple cavities and tip injection on the aerothermal characteristics of the squealer tip in turbine stage. *Appl. Therm. Eng.* **2023**, *220*, 119631. [CrossRef]
72. Dey, D.; Camci, C. Aerodynamic tip desensitization of an axial turbine rotor using tip platform extensions. *Turbo Expo Power Land Sea Air. Am. Soc. Mech. Eng.* **2001**, *78507*, V001T03A069. [CrossRef]
73. Willinger, R.; Haselbacher, H. *On the Modeling of Tip Leakage Flow in Axial Turbine Blade Rows*; American Society of Mechanical Engineers: New York, NY, USA, 2000. [CrossRef]
74. Kang, D.B.; Lee, S.W. Heat/mass transfer over the plane tip equipped with a full coverage winglet in a turbine cascade: Part 1–winglet bottom surface data. *Int. J. Heat Mass Transf.* **2015**, *88*, 965–973. [CrossRef]
75. Seo, Y.C.; Lee, S.W. Heat/mass transfer over the plane tip equipped with a full coverage winglet in a turbine cascade: Part 2–tip surface data. *Int. J. Heat Mass Transf.* **2015**, *88*, 974–981. [CrossRef]

76. Harvey, N.W.; Ramsden, K. A computational study of a novel turbine rotor partial shroud. *J. Turbomach.* **2001**, *123*, 534–543. [CrossRef]
77. Willer, L.; Haselbach, F.; Newman, D.A.; Harvey, N.W. An Investigation Into a Novel Turbine Rotor Winglet: Part 2—Numerical Simulation and Experimental Results. *Turbo Expo Power Land Sea Air* **2006**, *4241*, 597–605. [CrossRef]
78. O'Dowd, D.O.; Zhang, Q.; He, L.; Oldfield, M.L.G.; Ligrani, P.M.; Cheong, B.C.Y.; Tibbott, I. Aerothermal performance of a winglet at engine representative Mach and Reynolds numbers. *J. Turbomach.* **2011**, *133*, 041026. [CrossRef]
79. Zhou, C.; Hodson, H.; Tibbott, I.; Stokes, M. Effects of winglet geometry on the aerodynamic performance of tip leakage flow in a turbine cascade. *J. Turbomach.* **2013**, *135*, 051009. [CrossRef]
80. Zhou, C.; Hodson, H.; Tibbott, I.; Stokes, M. Effects of Endwall Motion on the Aero-Thermal Performance of a Winglet Tip in a HP Turbine. *ASME Turbomach.* **2012**, *134*, 061036. [CrossRef]
81. O'Dowd, D.O.; Zhang, Q.; He, L.; Cheong, B.C.Y.; Tibbott, I. Aerothermal performance of a cooled winglet at engine representative Mach and Reynolds numbers. *J. Turbomach.* **2013**, *135*, 011041. [CrossRef]
82. Zhang, Q.; He, L. Impact of wall temperature on turbine blade tip aerothermal performance. *J. Eng. Gas Turbines Power* **2014**, *136*, 052602. [CrossRef]
83. Papa, M.; Goldstein, R.J.; Gori, F. Effects of tip geometry and tip clearance on the mass/heat transfer from a large-scale gas turbine blade. *J. Turbomach.* **2003**, *125*, 90–96. [CrossRef]
84. Saha, A.K.; Acharya, S.; Prakash, C.; Bunker, R. Blade tip leakage flow and heat transfer with pressure-side winglet. *Turbo Expo Power Land Sea Air* **2003**, *36886*, 497–507. [CrossRef]
85. Joo, J.S.; Lee, S.W. Heat/mass transfer over the cavity squealer tip equipped with a full coverage winglet in a turbine cascade: Part 1–data on the winglet top surface. *Int. J. Heat Mass Transf.* **2017**, *108*, 1255–1263. [CrossRef]
86. Lee, S.W.; Joo, J.S. Heat/mass transfer over the cavity squealer tip equipped with a full coverage winglet in a turbine cascade: Part 2–data on the cavity floor. *Int. J. Heat Mass Transf.* **2017**, *108*, 1264–1272. [CrossRef]
87. Yan, X.; Huang, Y.; He, K.; Li, J.; Feng, Z. Numerical investigations into the effect of squealer–winglet blade tip modifications on aerodynamic and heat transfer performance. *Int. J. Heat Mass Transf.* **2016**, *103*, 242–253. [CrossRef]
88. Yan, X.; Huang, Y.; He, K. Investigations into heat transfer and film cooling effect on a squealer-winglet blade tip. *Int. J. Heat Mass Transf.* **2017**, *115*, 955–978. [CrossRef]
89. Schabowski, Z.; Hodson, H. The reduction of over tip leakage loss in unshrouded axial turbines using winglets and squealers. *J. Turbomach.* **2014**, *136*, 041001. [CrossRef]
90. Schabowski, Z.; Hodson, H.; Giacche, D.; Power, B.; Stokes, M.R. Aeromechanical optimization of a winglet-squealer tip for an axial turbine. *J. Turbomach.* **2014**, *136*, 071004. [CrossRef]
91. Jiang, S.; Li, Z.; Li, J. Effects of the squealer winglet structures on the heat transfer characteristics and aerodynamic performance of turbine blade tip. *Int. J. Heat Mass Transf.* **2019**, *139*, 860–872. [CrossRef]
92. Coull, J.D.; Atkins, N.R.; Hodson, H.P. Winglets for improved aerothermal performance of high pressure turbines. *J. Turbomach.* **2014**, *136*, 091007. [CrossRef]
93. Zhou, C.; Zhong, F. A novel suction-side winglet design philosophy for high-pressure turbine rotor tips. *J. Turbomach.* **2017**, *139*, 111002. [CrossRef]
94. Zhong, F.; Zhou, C.; Ma, H.; Zhang, Q. Heat transfer of winglet tips in a transonic turbine cascade. *J. Eng. Gas Turbines Power* **2017**, *139*, 012605. [CrossRef]
95. Zhong, F.; Zhou, C. Effects of tip gap size on the aerodynamic performance of a cavity-winglet tip in a turbine cascade. *J. Turbomach.* **2017**, *139*, 101009. [CrossRef]
96. Hodson, H.P. Measurements of Wake-Generated Unsteadiness in the Rotor Passages of Axial Flow Turbines. *ASME Eng. Gas Turbines Power* **1985**, *107*, 467–475. [CrossRef]
97. Chaluvadi, V.S.P.; Kalfas, A.I.; Hodson, H.P. Vortex transport and blade interactions in high pressure turbines. *J. Turbomach.* **2004**, *126*, 395–405. [CrossRef]
98. Binder, A.; Forster, W.; Mach, K.; Rogge, H. Unsteady Flow Interaction Caused by Stator Secondary Vortices in a Turbine Rotor. *ASME Turbomach.* **1987**, *109*, 251–256. [CrossRef]
99. Zaccaria, M.A.; Lakshminarayana, B. Unsteady Flow Field Due to Nozzle Wake Interaction With the Rotor in an Axial Flow Turbine: Part I—Rotor Passage Flow Field. *ASME Turbomach.* **1997**, *119*, 201–213. [CrossRef]
100. Göttlich, E.; Woisetschläger, J.; Pieringer, P.; Hampel, B.; Heitmeir, F. Investigation of Vortex Shedding and Wake-Wake Interaction in a Transonic Turbine Stage Using Laser-Doppler-Velocimetry and Particle-Image-Velocimetry. *ASME Turbomach.* **2006**, *128*, 178–187. [CrossRef]
101. Doorly, D.J.; Oldfield, M.L.G. Simulation of the Effects of Shock Wave Passing on a Turbine Rotor Blade. *ASME Eng. Gas Turbines Power* **1985**, *107*, 998–1006. [CrossRef]
102. Ashworth, D.A.; LaGraff, J.E.; Schultz, D.L.; Grindrod, K.J. Unsteady Aerodynamic and Heat Transfer Processes in a Transonic Turbine Stage. *ASME Eng. Gas Turbines Power* **1985**, *107*, 1022–1030. [CrossRef]

103. Dullenkopf, K.; Schulz, A.; Wittig, S. The Effect of Incident Wake Conditions on the Mean Heat Transfer of an Airfoil. *ASME Turbomach.* **1991**, *113*, 412–418. [CrossRef]
104. Guenette, G.R.; Epstein, A.H.; Giles, M.B.; Haimes, R.; Norton, R.J.G. Fully Scaled Transonic Turbine Rotor Heat Transfer Measurements. *ASME Turbomach.* **1989**, *111*, 1–7. [CrossRef]
105. Rai, M.A.N. Unsteady three-dimensional Navier-Stokes simulations of turbine rotor-stator interaction. In Proceedings of the 23rd Joint Propulsion Conference, San Diego, CA, USA, 29 June–2 July 1987; p. 2058. [CrossRef]
106. Giles, M.B. Stator/rotor interaction in a transonic turbine. *J. Propuls. Power* **1990**, *6*, 621–627. [CrossRef]
107. Abhari, R.S.; Guenette, G.R.; Epstein, A.H.; Giles, M.B. Comparison of Time-Resolved Turbine Rotor Blade Heat Transfer Measurements and Numerical Calculations. *ASME Turbomach.* **1992**, *114*, 818–827. [CrossRef]
108. Sharma, O.P.; Butler, T.L.; Joslyn, H.D.; Dring, R.P. Three-dimensional unsteady flow in an axial flow turbine. *J. Propuls. Power* **1985**, *1*, 29–38. [CrossRef]
109. Gallus, H.E.; Zeschky, J.; Hah, C. Endwall and Unsteady Flow Phenomena in an Axial Turbine Stage. *ASME Turbomach.* **1995**, *117*, 562–570. [CrossRef]
110. Zeschky, J.; Gallus, H.E. Effects of Stator Wakes and Spanwise Nonuniform Inlet Conditions on the Rotor Flow of an Axial Turbine Stage. *ASME Turbomach.* **1993**, *115*, 128–136. [CrossRef]
111. Volino, R.J.; Galvin, C.D.; Brownell, C.J. Effects of Unsteady Wakes on Flow Through High Pressure Turbine Passages With and Without Tip Gaps. In Proceedings of the ASME Turbo Expo 2014: Turbine Technical Conference and Exposition, Turbomachinery, Düsseldorf, Germany, 16–20 June 2014; ASME: New York, NY, USA; Volume 2C, p. V02CT38A056. [CrossRef]
112. Payne, S.J.; Ainsworth, R.W.; Miller, R.J.; Moss, R.; Harvey, N. Unsteady loss in a high pressure turbine stage. *Int. J. Heat Fluid Flow* **2003**, *24*, 698–708. [CrossRef]
113. Zhou, K.; Zhou, C. Aerodynamic interaction between an incoming vortex and tip leakage flow in a turbine cascade. *J. Turbomach.* **2018**, *140*, 111004. [CrossRef]
114. Ameri, A.A.; Rigby, D.L.; Steinthorsson, E.; Heidmann, J.; Fabian, J.C. Unsteady Analysis of Blade and Tip Heat Transfer as Influenced by the Upstream Momentum and Thermal Wakes. In Proceedings of the ASME Turbo Expo 2008: Power for Land, Sea, and Air. Heat Transfer, Parts A and B, Berlin, Germany, 9–13 June 2008; ASME: New York, NY, USA; Volume 4, pp. 1095–1103. [CrossRef]
115. Thorpe, S.J.; Yoshino, S.; Thomas, G.A.; Ainsworth, R.W.; Harvey, N.W. Blade-tip heat transfer in a transonic turbine. *Proc. Inst. Mech. Eng. Part A J. Power Energy* **2005**, *219*, 421–430. [CrossRef]
116. Molter, S.M.; Dunn, M.G.; Haldeman, C.W.; Bergholz, R.F.; Vitt, P. Heat-flux measurements and predictions for the blade tip region of a high-pressure turbine. *Turbo Expo Power Land Sea Air* **2006**, *4238*, 49–60. [CrossRef]
117. Rahman, H.; Kim, S.I.; Hassan, I.; El Ayoubi, C. Unsteady tip leakage flow characteristics and heat transfer on turbine blade tip and casing. *Turbo Expo Power Land Sea Air* **2010**, *44021*, 2353–2362. [CrossRef]
118. Atkins, N.R.; Thorpe, S.J.; Ainsworth, R.W. Unsteady Effects on Transonic Turbine Blade-Tip Heat Transfer. *ASME Turbomach.* **2012**, *134*, 061002. [CrossRef]
119. Du, K.; Li, Z.; Li, J. Numerical investigation of the blade tip and overtip casing aerothermal performance in a high pressure turbine stage. *Turbo Expo Power Land Sea Air Am. Soc. Mech. Eng.* **2016**, *49781*, V05AT13A011. [CrossRef]
120. Teng, S.; Han, J.C.; Azad, G.M.S. Detailed heat transfer coefficient distributions on a large-scale gas turbine blade tip. *Heat Transf.* **2001**, *123*, 803–809. [CrossRef]
121. Polanka, M.D.; Clark, J.P.; White, A.L.; Meininger, M.; Praisner, T.J. Turbine Tip and Shroud Heat Transfer and Loading: Part B—Comparisons Between Prediction and Experiment Including Unsteady Effects. *Turbo Expo Power Land Sea Air* **2003**, *36886*, 691–702. [CrossRef]
122. Jiang, S.; Li, Z.; Li, J. Effects of rib design on the unsteady tip heat transfer amplitude for a turbine rotor blade. *J. Therm. Sci. Eng. Appl.* **2022**, *14*, 101011. [CrossRef]
123. Zhou, Z.; Chen, S.; Wang, S. Unsteady winglet-cavity tip on leakage flow in a high-pressure turbine stage of low-aspect ratio. *Proc. Inst. Mech. Engineers. Part C J. Mech. Eng. Sci.* **2018**, *232*, 3708–3721. [CrossRef]
124. Mehendale, A.B.; Han, J.; Ou, S.; Lee, C.P. Unsteady Wake Over a Linear Turbine Blade Cascade With Air and CO2 Film Injection: Part II—Effect on Film Effectiveness and Heat Transfer Distributions. *ASME Turbomach.* **1994**, *116*, 730–737. [CrossRef]
125. Ou, S.; Han, J.; Mehendale, A.B.; Lee, C.P. Unsteady Wake Over a Linear Turbine Blade Cascade With Air and CO2 Film Injection: Part I—Effect on Heat Transfer Coefficients. *ASME Turbomach.* **1994**, *116*, 721–729. [CrossRef]
126. Gao, Z.; Narzary, D.P.; Han, J.C. Film cooling on a gas turbine blade pressure side or suction side with axial shaped holes. *Int. J. Heat Mass Transf.* **2008**, *51*, 2139–2152. [CrossRef]
127. Gao, Z.; Narzary, D.P.; Han, J. Film-Cooling on a Gas Turbine Blade Pressure Side or Suction Side With Compound Angle Shaped Holes. *ASME Turbomach.* **2009**, *131*, 011019. [CrossRef]
128. Rallabandi, A.P.; Li, S.; Han, J. Unsteady Wake and Coolant Density Effects on Turbine Blade Film Cooling Using Pressure Sensitive Paint Technique. *ASME Heat Transf.* **2012**, *134*, 081701. [CrossRef]

129. Zhang, B.; Qiang, X.; Teng, J.; Lu, S. Unsteady passing wake effects on turbine blade tip aerodynamic and aerothermal performance with film cooling. *Turbo Expo Power Land Sea Air Am. Soc. Mech. Eng.* **2019**, *58653*, V05BT22A002. [CrossRef]
130. Jiang, S.; Li, Z.; Li, J.; Song, L. Numerical investigations on the unsteady leakage flow and heat transfer characteristics of the turbine blade squealer tip. *J. Glob. Power Propuls. Soc.* **2023**, *7*, 1–12. [CrossRef] [PubMed]
131. You, Y.; Ding, L. Numerical investigation of unsteady film cooling on turbine blade squealer tip with pressure side coolant. *Int. Commun. Heat Mass Transf.* **2023**, *143*, 106720. [CrossRef]
132. You, Y.; Ding, L. Unsteady numerical study of film cooling and heat transfer on turbine blade squealer tip with coolant jet. *Numer. Heat Transf. Part A Appl.* **2025**, *86*, 2734–2761. [CrossRef]
133. Du, Q.; Li, Y.; Yang, L.; Liu, T.; Zhang, D.; Xie, Y. Performance prediction and design optimization of turbine blade profile with deep learning method. *Energy* **2022**, *254*, 124351. [CrossRef]

**Disclaimer/Publisher's Note:** The statements, opinions and data contained in all publications are solely those of the individual author(s) and contributor(s) and not of MDPI and/or the editor(s). MDPI and/or the editor(s) disclaim responsibility for any injury to people or property resulting from any ideas, methods, instructions or products referred to in the content.

*energies*

MDPI

*Article*

# Numerical Analysis of Heat Transfer Process and Mechanisms for High-Temperature Air Flowing Across Staggered Lined Fine Tubes

**Qinyi Zhang [1], Yi Feng [1], Chunxiao Zhu [1], Jiaxin Zheng [1], Xin Xu [1], Min Du [1], Zhengyu Mo [1] and Licheng Sun [1,2,*]**

[1] State Key Laboratory of Intelligent Construction and Healthy Operation and Maintenance of Deep Underground Engineering, College of Water Resource & Hydropower, Sichuan University, Chengdu 610065, China; 15862159407@163.com (Q.Z.); fengyscu@163.com (Y.F.); zhu.chunxiao@foxmail.com (C.Z.); z646037869@163.com (J.Z.); xux@stu.scu.edu.cn (X.X.); dmscu2009@scu.edu.cn (M.D.); mozhengyu@scu.edu.cn (Z.M.)

[2] Guangdong Provincial Key Laboratory of Deep Earth Sciences and Geothermal Energy Exploitation and Utilization, Institute of Deep Earth Sciences and Green Energy, College of Civil and Transportation Engineering, Shenzhen University, Shenzhen 518060, China

* Correspondence: sunlicheng@scu.edu.cn

**Abstract**

This study investigates the flow and heat transfer mechanisms of high-temperature air flowing across staggered lined fine tubes in a SABRE-type precooler. Large-Eddy Simulation (LES) was employed to model three-dimensional unsteady flow under constant-property and variable-property air models at inlet temperatures of 400–800 K. The results show that increasing temperature substantially enhances vorticity, turbulent kinetic energy, heat flux, and Nusselt number, while flow separation and pressure drop are intensified. However, when temperature-dependent air properties are incorporated, the wake width increases and the separated shear layers become thicker, while the turbulence/unsteadiness intensity decreases. Consequently, the near-wall shear is reduced and the heat transfer coefficients are lower. Compared with variable-property predictions, constant-property models overestimate the average Nusselt number by 20–40% and the local pressure drop by 40–65%, and they underestimate the air-side temperature drop along the tube rows. These findings demonstrate that real-gas effects significantly alter both aerodynamic resistance and thermal performance. Overall, accurate representation of temperature-dependent air properties is essential for the reliable design, evaluation, and optimization of micro-tube precoolers.

**Keywords:** SABRE; precooler; staggered lined fine tubes; variable thermophysical properties; flow and heat transfer characteristics

## 1. Introduction

The SABRE (Synergetic Air-Breathing Rocket Engine) is the propulsion system designed for the single-stage orbiting SKYLON aircraft, developed by Reaction Engines Limited (REL) [1,2]. This engine adopts a closed-loop helium cycle and incorporates a precooler to transfer thermal energy from the high-temperature intake air to liquid hydrogen, effectively mitigating issues related to hydrogen embrittlement and thermal management [3,4]. A key component of this system is the precooler, which comprises approximately 300,000 microtubes with an outer diameter of 0.98 mm and a wall thickness of 40 μm [5,6]. The structure and operating principle of the precooler are illustrated in Figure 1. The header distributes helium, which subsequently moves from inside to outside

while high-temperature incoming air travels in the opposite direction, creating a counter-flow heat exchange mechanism. This arrangement enables the precooler to rapidly cool the inlet airflow of 400 kg/s from over 1000 °C to −150 °C within 20 ms at *Ma* = 5.0, achieving a power-to-weight ratio of up to 667 kW/kg and substantially enhancing the engine's overall thrust-to-weight ratio [7,8]. Consequently, the outstanding heat transfer capability of the precooler has been a subject of focus within the research community, leading to numerous studies on system performance evaluation [9–11], parameter optimization [12–14], numerical simulation [15,16], and experimental validation [17].

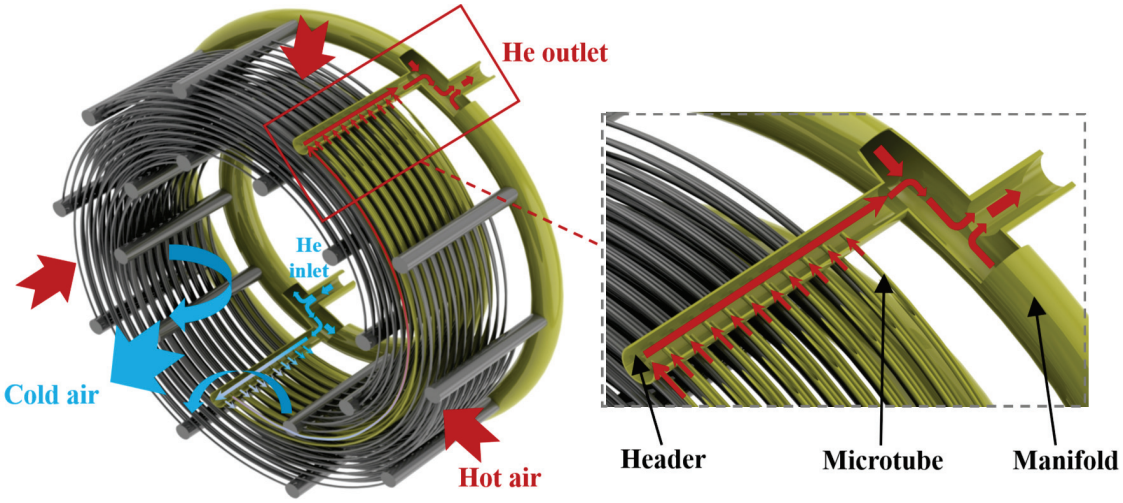



**Figure 1.** SABRE-type precooler.

Since high-temperature air passes through an array of fine tubes in a staggered arrangement, the precooler experiences a more intense convective heat exchange process. The following features of such fine tubes are important: (1) their extremely small size, (2) their very large temperature differences between the gas and wall of the tube, and (3) their complicated airflow behavior under highly compact tube packing. Over the past few years, systematic studies have been carried out by researchers about the external flow and heat transfer properties of tubes of varied characteristic sizes. These studies help explain the underlying differences between fine tubes and conventional tubes and thus enhance our understanding of heat transfer in fine-tube configurations.

Bacellar et al. [18] examined the air-side heat transfer of staggered tube bundles whose diameter varied between 0.5 and 2.0 mm and concluded that smaller diameter tubes deliver significantly better heat transfer performance at the same inlet velocity. This finding is in line with that of Zhang et al. [19], who demonstrated that smaller diameter tubes, i.e., bigger curvature ratios of tubes tend to induce a boundary-layer separation, which helps to enhance heat transfer. Collectively, these studies indicate that changes in tube diameter can change significantly the flow structures in the exterior and, therefore, have a robust impact on the heat transfer behavior. In an attempt to further explain the effect of tube diameter on flow characteristic, Li et al. [20] conducted a comparative numerical examination of wake flow behind 1 mm and 22 mm diameter single tubes. A large, symmetric vortex was detected at *Re* = 500 behind the 22 mm tube which causes significant fluid perturbation and facilitates the exchange of heat in the wake. By contrast, only a small-scale vortex developed behind the 1 mm tube, resulting in weaker flow disturbance and thus a more limited degree of heat transfer enhancement. However, Qin et al. [21] reported contrasting results, finding that under identical Reynolds number conditions and with *Ma* < 0.1, the wake structures and dimensionless velocity field distributions were highly similar across tubes of different diameters. Additionally, Guan et al. [22] conducted a study on the heat transfer

https://doi.org/10.3390/en19030796

behavior of water flowing over micro-pillar structures inside a confined rectangular channel. Their results demonstrated that under a heat flux of 3 W/cm$^2$, pronounced differences in vortex behavior were observed among micro-pillars with diameters of 300, 600, and 3000 μm. Larger-diameter cylinders, due to the increased flow path length and associated frictional resistance losses, promoted earlier flow separation and formed substantially longer recirculation zones, ultimately yielding stronger heat transfer capability.

On one hand, as discussed above, the external flow characteristics of micro-scale heat exchange tubes differ substantially from those of conventional tubes. Previous work by our research group has similarly shown that when air flows over a single micro-scale tube, high-frequency vortex shedding occurs, with the shedding frequency for a 1 mm tube being approximately an order of magnitude higher than that for a 3 mm tube [23]. On the other hand, much of the earlier research on tube-bundle heat exchangers has centered on conventional tube dimensions and relatively modest temperature differences, and thus has largely neglected the effects that temperature-dependent fluid properties may exert on the flow and heat transfer behavior [24,25]. In this paper, the present work uses numerical simulations to examine how high-temperature air flows and transfers heat across staggered fine tubes, accounting for both constant-property and temperature-dependent air models under various inlet temperatures. Based on these analyses, the variations in flow behavior and heat transfer performance among four tubes arranged along the flow direction are examined. The findings are expected to offer theoretical guidance for the design and optimization of precooler systems.

## 2. Numerical Methods

### *2.1. Geometric Model*

The computational model in this study is constructed with reference to the precooler design parameters reported by REL and domestic research institutions [26–29], as illustrated in Figure 2. The simulation domain consists of four full circular tubes and six half-circular tubes arranged across seven rows. The heat-exchange tubes have an outer diameter ($D$) and an inner diameter ($d$) of 1$D$ and 0.9$D$, respectively. The tubes are configured in a staggered arrangement, with a transverse pitch ($S_T$) of 2$D$ and a longitudinal pitch ($S_L$) of 1.5$D$. To minimize the effects of inlet flow development and potential backflow at the outlet, extension sections of length 8$D$ are added upstream and downstream of the computational domain. In the spanwise ($z$) direction, the tube length is set to $\pi D$ to adequately capture three-dimensional vortex structures and ensure complete development of the flow field [30,31].

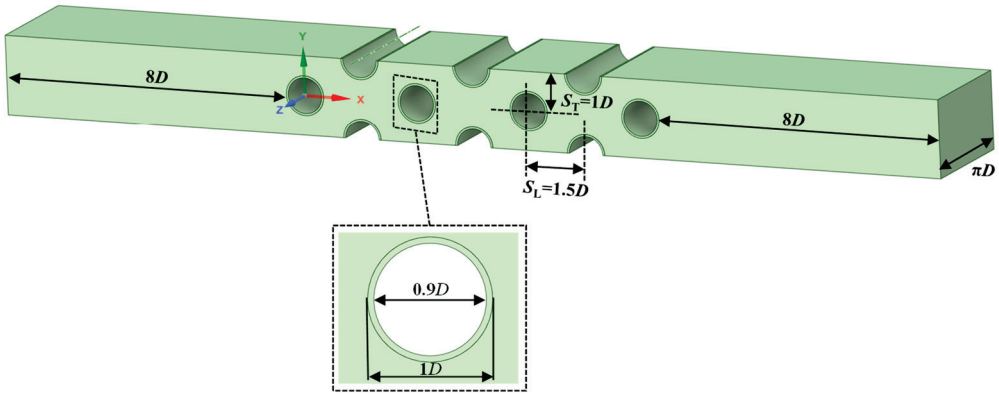



**Figure 2.** Computational domain and geometric configuration of the staggered fine tubes.

### 2.2. Numerical Setup

All numerical simulations were performed using ANSYS Fluent 2023 R2. The fluid motion and heat transfer were governed by the conservation equations of mass, momentum, and energy, and the three-dimensional unsteady Navier–Stokes equations were solved with a pressure-based algorithm. Large Eddy Simulation (LES) was adopted because it is more capable than Reynolds-Averaged Navier–Stokes (RANS) models of resolving transient, highly unsteady vortex structures [32,33]. The Smagorinsky-Lilly model was employed to represent the subgrid-scale contribution of unresolved small-scale vortices to the resolved flow field. This selection was primarily based on its good robustness and computational stability in high-Reynolds-number turbulent flows. To account for strong temperature gradients and property variations caused by high inflow temperatures, the model implementation incorporates fluid properties (density, dynamic viscosity, thermal conductivity, etc.) that vary with local temperature, enabling the subgrid eddy viscosity coefficient to indirectly reflect the influence of the temperature field on subgrid stresses. Furthermore, the computational grid was sufficiently refined near the wall and in regions with significant temperature gradients (ensuring a dimensionless wall distance $y^+ < 1$ for the first grid layer) to directly resolve more scales of the flow and heat transfer processes. This approach reduces reliance on the SGS model in critical areas, thereby ensuring computational accuracy. Pressure-velocity coupling was handled using the SIMPLE scheme. For spatial discretization, the bounded central differencing scheme was applied to the momentum equations, and a second-order upwind scheme was used for the energy equation, while the pressure field was discretized using a second-order formulation. Time advancement relied on a second-order implicit scheme.

The main boundary conditions are shown in Figure 3. The flow inside the precooler is predominantly turbulent. For complex flow passages, turbulence may occur at relatively low Reynolds numbers ($Re < 1000$) [28]. Referring to the Reynolds number ranges adopted in previous studies ($0 < Re \leq 6000$) [20,28,33], $Re = 1000$ is selected as the turbulent operating condition in the present study. A velocity inlet was prescribed at the upstream boundary, and the inlet velocity was adjusted in each case so that the Reynolds number remained fixed at 1000. The inlet air temperatures were set to 400, 600, and 800 K. To incorporate compressibility effects and temperature-dependent variations in thermophysical properties, air was treated as an ideal gas [34], with viscosity, thermal conductivity, and specific heat capacity evaluated from polynomial correlations fitted to REFPROP data from the National Institute of Standards and Technology (NIST). Figure 4 illustrates the temperature dependence of these properties at an air pressure of 0.165 MPa, corresponding to the precooler intake condition. A pressure outlet with a gauge pressure of 0 Pa was applied downstream. Symmetry conditions were imposed on the upper and lower boundaries in the $y$-direction, while periodic boundaries were used in the $z$-direction. The inner surface of each tube was kept at a constant temperature of 300 K, and the external tube wall was treated as a no-slip, coupled boundary. It should be noted that a constant wall temperature of 300 K is prescribed for the heat transfer tubes in this study. This treatment represents an idealized equivalent assumption, whose physical implication is that the coolant (helium) inside the tubes possesses sufficient, or effectively infinite, heat transfer capacity to maintain the wall temperature at a constant low level. The primary purpose of this simplification is to concentrate the computational resources and analytical focus on the complex flow and heat transfer mechanisms on the high-temperature air side, particularly the unique effects arising from the strong temperature dependence of air properties. By fixing the wall temperature, the air-side physical processes can be effectively isolated and highlighted, avoiding the interference introduced by the complex coupled heat transfer between the internal and external flows, and thereby enabling a clearer interpretation of the core

https://doi.org/10.3390/en19030796

mechanisms addressed in this study. Convergence criteria for the continuity, momentum, and energy equations were all set to $10^{-6}$. A fixed time step of $\Delta t = 2.5 \times 10^{-6}$ s was used in the unsteady numerical simulations. Under the most demanding condition considered in this study (800 K with variable properties), the dominant vortex shedding frequency was approximately $4.7 \times 10^4$ Hz, corresponding to a characteristic shedding period of about $2.13 \times 10^{-5}$ s. Thus, each shedding cycle was resolved by approximately 8–9 time steps, satisfying the Nyquist sampling criterion for resolving the dominant unsteady mode. The tube walls were assumed to be Inconel 718, and their thermal conductivity was calculated using Equation (1) [35]. The four complete tubes aligned in the streamwise direction are referred to as Tube 1 through Tube 4, and the subsequent analysis focuses exclusively on these tubes.

$$\lambda = 1.11 \times 10^{-5} T_t^2 - 0.001986 T_t + 14.37 \quad (1)$$

where $T_t$ is the thermodynamic temperature of the tube.

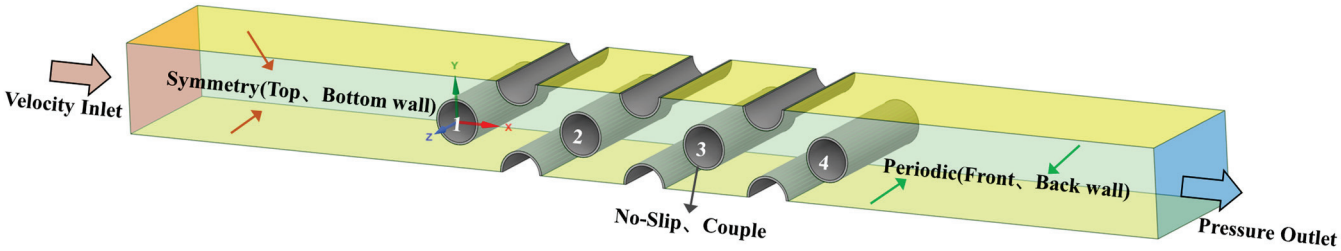



**Figure 3.** Boundary conditions applied in the staggered fine tubes simulations.

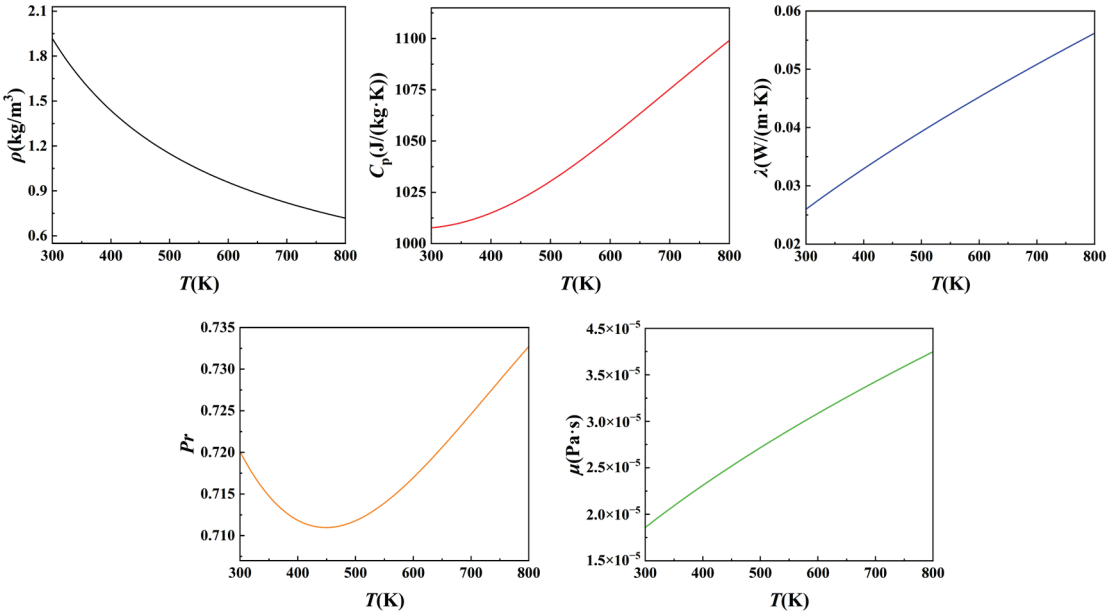
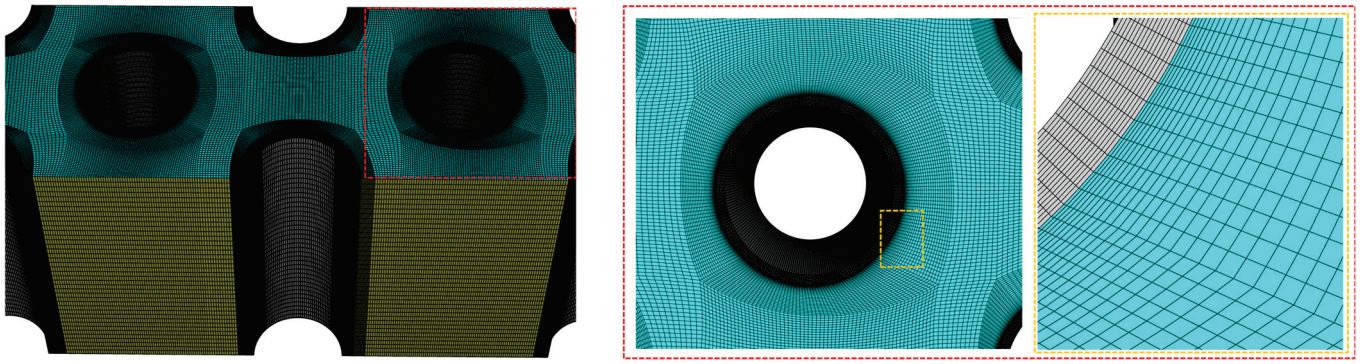



**Figure 4.** Dependences of air physical properties on air temperature at 0.165 MPa air pressure.

### *2.3. Mesh Independence*

The entire computational domain was discretized using structured grids generated with ICEM CFD 2023 R2. An O-grid layout was generated around each tube, and the mesh was locally refined near the wall to resolve the boundary layer and capture flow separation. The first-layer cell height next to the tube surface was set to 2 μm, with a growth rate of 1.12. A total of 25 grid layers were distributed in the wall-normal direction, ensuring that the wall resolution satisfied the requirement of $y^+ < 1$ along all tube surfaces. The computational mesh is shown in Figure 5.



(**a**) (**b**)

**Figure 5.** Mesh generation: (**a**) meshing of the partial computational domain; (**b**) locally refined mesh.

To evaluate mesh independence, six mesh configurations of different densities were created by varying the numbers of grid nodes in the circumferential, radial, and spanwise directions around each tube and its surrounding region. Figure 6a presents the outlet air temperature as a function of the total cell count for an inlet temperature of 400 K. When the overall number of cells exceeded 6.39 million, further refinement produced less than a 1% change in the outlet temperature, indicating that the solution had become effectively insensitive to the mesh resolution. Consequently, the mesh with 6.39 million cells was adopted for all simulations in our study. To further reduce numerical uncertainty, we additionally carried out simulations using multiple time-step sizes, and the outlet air temperature was also employed as the evaluation metric, as shown in Figure 6b. The results demonstrate that once the time step reaches $2.5 \times 10^{-6}$ s, further reduction in the time step leads to only minor differences in the predicted outlet temperature (less than 0.5%). Therefore, a time step of $2.5 \times 10^{-6}$ s was adopted in the present simulations as a good compromise between accuracy and computational cost.

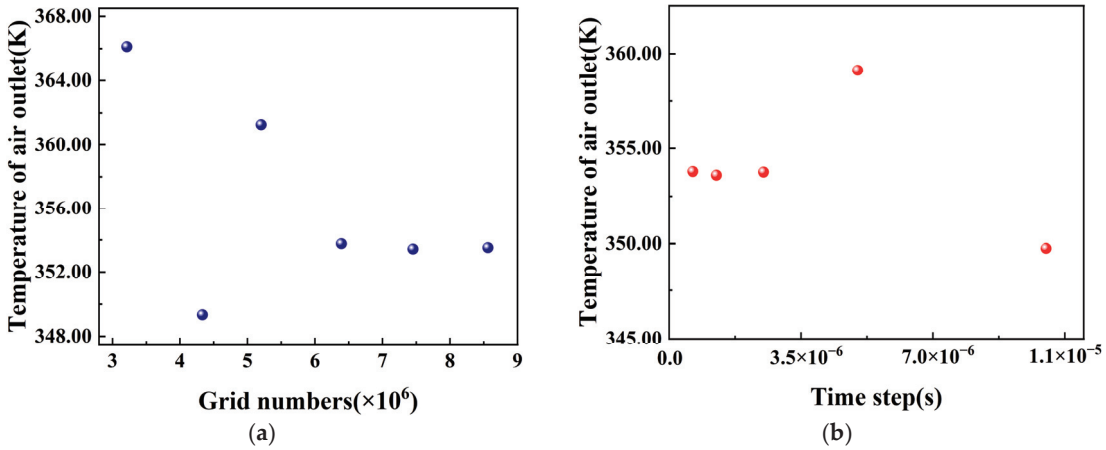



**Figure 6.** Independence verification of outlet air temperature: (**a**) grid number; (**b**) time step.

### *2.4. Data Reduction*

The Reynolds number (*Re*) is defined as:

$$Re = \frac{\rho u_{\max} D}{\mu} \tag{2}$$

where $\rho$ and $\mu$ denote the air density and dynamic viscosity, respectively; $u_{\max}$ is the average air velocity at the minimum cross section, given as:

$$u_{\max} = \frac{S_T/D}{S_T/D - 1} u_{in} \tag{3}$$

where $u_{in}$ is the inlet air velocity.

It should be noted that under high-temperature conditions, significant variations in air density and dynamic viscosity lead to corresponding changes in the local Reynolds number, even though the inlet Reynolds number is fixed at 1000. An evaluation based on the local temperature field indicates that the local Reynolds number varies within a range of approximately 8–15% relative to the inlet Reynolds number, solely due to property variations. This variation is an inherent physical consequence of high-temperature air flow and is insufficient to alter the overall flow scale or dominant flow structures. Therefore, comparisons between constant-property and variable-property cases remain physically consistent, with the observed differences primarily attributable to the effects of temperature-dependent air properties on local flow and heat transfer characteristics.

This study focuses on the local Nusselt number corresponding to each individual tube. The local Nusselt number ($Nu_l$) is given by:

$$Nu_l = \frac{hD}{\lambda} = \frac{q}{T_f - T_w} \times \frac{D}{\lambda} \tag{4}$$

where $h$ denotes the external convective heat transfer coefficient; $\lambda$ is the thermal conductivity of air; $q$ is the heat flux at the outer surface of tube; $T_w$ represents the temperature of tube outer surface; $T_f$ is the average air temperature, given as:

$$T_f = \frac{T_{front} + T_{back}}{2} \tag{5}$$

where $T_{front}$ and $T_{back}$ represent the average temperatures at the frontal and rear cross-sections of tube, respectively. The positions of these two cross-sections are illustrated in Figure 7.

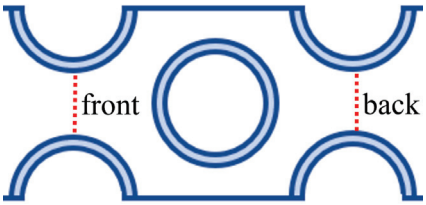



**Figure 7.** The locations of the frontal and rear cross-sections of tube.

The local pressure drop ($\Delta P_l$) is given by:

$$\Delta P_l = P_{front} - P_{back} \tag{6}$$

where $P_{front}$ and $P_{back}$ represent the average pressures at the frontal and rear cross-sections of tube, respectively.

All time-averaged quantities presented in this paper, including the Nusselt number, local pressure drop, and surface friction coefficient, were obtained by performing time averaging on unsteady numerical simulation results after the flow reached a statistically steady state. The unsteady simulations employed a fixed time step of $\Delta t = 2.5 \times 10^{-6}$ s.

For each operating condition, the initial transient phase was first discarded, and a time interval during which the flow characteristics remained stable was selected for statistical averaging. As mentioned earlier, all operating conditions studied in this paper satisfy the Nyquist sampling theorem, thereby ensuring sufficient representativeness of the statistical results.

Statistical convergence was evaluated by progressively extending the averaging duration and monitoring the variations in the time-averaged Nusselt number, pressure drop,

https://doi.org/10.3390/en19030796

and friction coefficient. Convergence was considered achieved when the changes in these averaged quantities remained below 1% with further increases in the averaging duration. The same time-averaging strategy was applied to all operating conditions to ensure the reliability and comparability of results under different temperature and property conditions.

### *2.5. Validation of Numerical Model*

The numerical methodology was validated by comparing the present simulation results with the experimental measurements provided in Ref. [36]. Figures 8a and 8b show the comparative results for the Nusselt number (*Nu*) and friction factor (*f*), respectively, where *f* is defined by Equation (7). The results derived from the simulated profile of *Nu* and *f* are consistent with the experiment data of the studied conditions. Both parameters have the mean relative error lower than 6% which is a high consistency between the two datasets. This rapport shows that the numerical model can be used to reliably model the necessary flow and heat transfer features in the scope of this study.

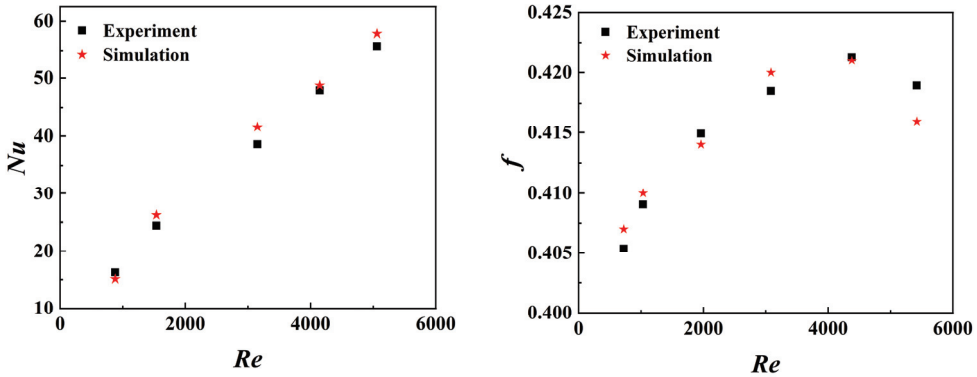



**Figure 8.** Comparisons of the numerical and experimental results [36]: (**a**) Nusselt number; (**b**) friction factor.

It should be noted that, for the condition of high-temperature air flow across microtubes, there is currently a lack of experimental or database results that can independently quantify the effects of temperature-dependent properties. The temperature-dependent thermophysical properties adopted in this study are all sourced from standard databases and have been validated in numerous studies on high-temperature gas flow and heat transfer. Based on this, the calculated Nusselt numbers, friction coefficients, and their development trends under variable-property conditions exhibit physical consistency, without unphysical oscillations or anomalies, indicating that the treatment of temperature-dependent properties in this work is physically reasonable. Furthermore, although the validation of the numerical model corresponds to a relatively moderate temperature range, the governing equations, turbulence modeling strategy, and wall treatment employed are not inherently dependent on a specific temperature level. Instead, they are grounded in the continuum assumption and the mechanisms of high-Reynolds-number shear-layer-dominated flow. When extrapolating the model to an inlet temperature as high as 800 K, this study enhances physical consistency by incorporating temperature-dependent air thermophysical properties (density, viscosity, specific heat, and thermal conductivity) to explicitly account for high-temperature effects.

$$f = \frac{2\Delta P}{N_L \times \rho u_{max}^2} \tag{7}$$

where $N_L$ denotes the number of tube rows in the longitudinal direction.

https://doi.org/10.3390/en19030796

## 3. Results

### *3.1. Flow Characteristics*

In order to have a better knowledge about the mechanisms of flow governing the crossflow of air between staggered fine tubes, the discussion commences with the unsteady wake movements in various temperature conditions and thermophysical-property model. As shown in Figure 9, the time traces of the lift coefficients reveal that both temperature and property variations have a clear impact on wake dynamics. At 400 K, Tube 1 in the constant-property case exhibits pronounced, periodic lift oscillations with relatively large amplitudes. In contrast, when variable properties are applied, the oscillations weaken notably and the lift signal becomes much smoother. These differences correspond directly to the vorticity structures illustrated in Figure 10, where the changes in shear-layer development and vortex shedding align with the observed lift-coefficient behavior. Under constant properties, the shear layer behind the tube undergoes strong roll-up and generates regular vortex shedding. In contrast, when variable properties are considered, the vorticity intensity weakens and the recirculation zone becomes more stable (highlighted by the black solid-line box in Figure 10), consistent with the nearly non-oscillatory lift response of Tube 1. As the inlet temperature increases to 600 K and 800 K, the oscillation frequency under constant properties rises, while the flow under variable properties gradually becomes more unstable. Nonetheless, the discrepancy between the two conditions diminishes with increasing temperature.

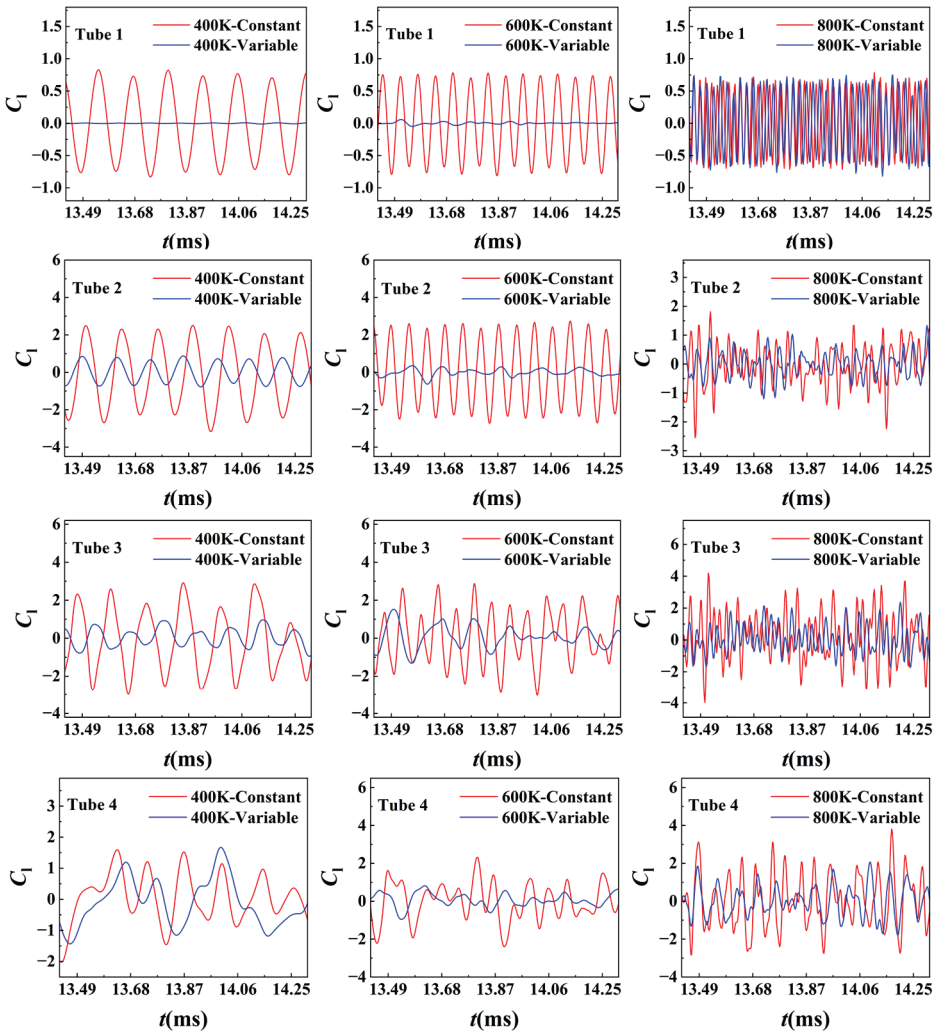



**Figure 9.** Time histories of lift coefficient for Tubes 1–4 under constant- and variable-property conditions at inlet temperatures of 400, 600, and 800 K.

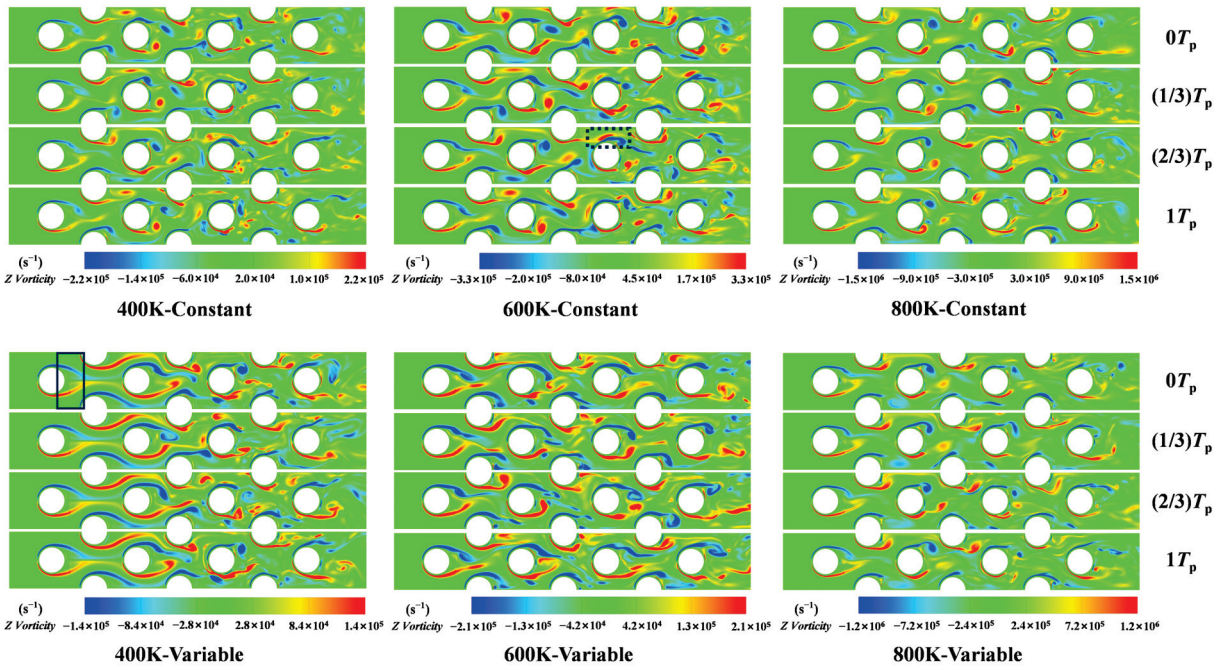



**Figure 10.** Instantaneous spanwise vorticity contours of the staggered fine tubes under constant- and variable-property conditions at inlet temperatures of 400, 600, and 800 K.

The turbulent kinetic energy (TKE) distribution shown in Figure 11 further demonstrates that under high-temperature conditions, the TKE around Tubes 2–4 increases markedly, which is fully consistent with the intensified lift oscillations observed in the lift-coefficient curves. In contrast, under variable-property conditions at 400 K, the TKE near Tube 1 is almost negligible (highlighted by the white dashed-line box in Figure 11), indicating that the incoming flow remains nearly laminar or only weakly turbulent. As a consequence, a stable Kármán vortex street does not form, and the lift acting on Tube 1 remains nearly constant in time. At this temperature, the overall TKE under variable-property conditions is noticeably lower than that predicted with constant properties, indicating weaker wake instability and correspondingly smaller lift fluctuations.

Additional insight into the governing flow mechanisms can be gained from the velocity and temperature fields shown in Figures 12 and 13. Under high-temperature conditions, the increase in flow velocity may raise concerns about compressibility effects. Taking the 800 K variable-property case as an example, the inlet velocity is 52.2 m/s, and numerical results show that the local maximum velocity is approximately 190 m/s. Based on the estimated speed of sound for air at 800 K (approximately 560–570 m/s), the corresponding maximum local Mach number is about 0.33. This maximum Mach number occurs only in the locally accelerated region of the shear layer around the tube, while the vast majority of the computational domain exhibits Mach numbers below 0.3. According to classical compressible flow theory, compressibility effects in this Mach number range are generally weak, with their influence primarily manifested through temperature-dependent thermophysical property changes, rather than through pressure wave-dominated compression waves or shock structures. Therefore, within the parameter range covered in this study, it is reasonable to neglect the effects of high-Mach-number compressibility on the overall flow and heat transfer characteristics.

For the constant-property model, increasing the temperature accelerates the shear-layer roll-up process and strengthens wake unsteadiness, thereby increasing vorticity production and TKE and resulting in more pronounced lift oscillations. In contrast, when temperature-dependent properties are considered, the flow velocity at the same nominal

https://doi.org/10.3390/en19030796

temperature is reduced and the downstream wake becomes visibly broader (as marked by the black box in Figure 13). This broader wake weakens shear-layer roll-up and suppresses periodic vortex shedding, thereby decreasing lift variability. Overall, rising temperature promotes stronger wake unsteadiness, while neglecting the associated property variations leads to an overprediction of both vortex shedding intensity and lift-oscillation amplitude.

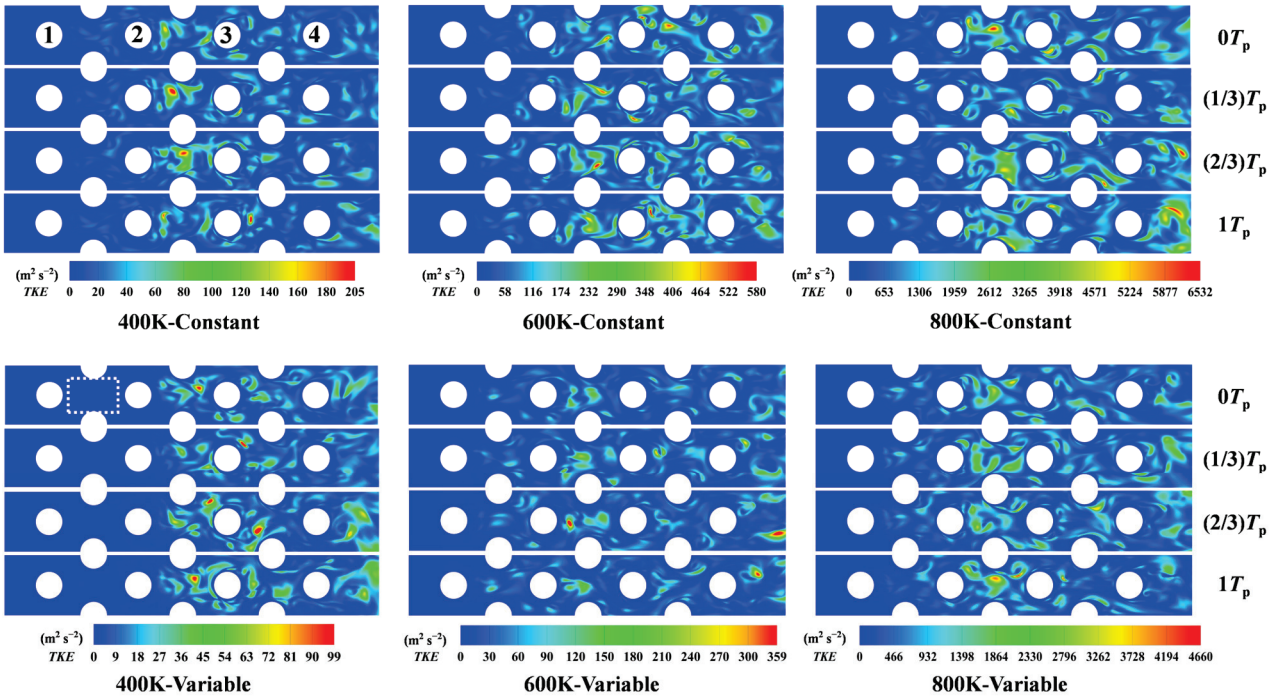



**Figure 11.** Instantaneous TKE contours of the staggered fine tubes under constant- and variable-property conditions at inlet temperatures of 400, 600, and 800 K.

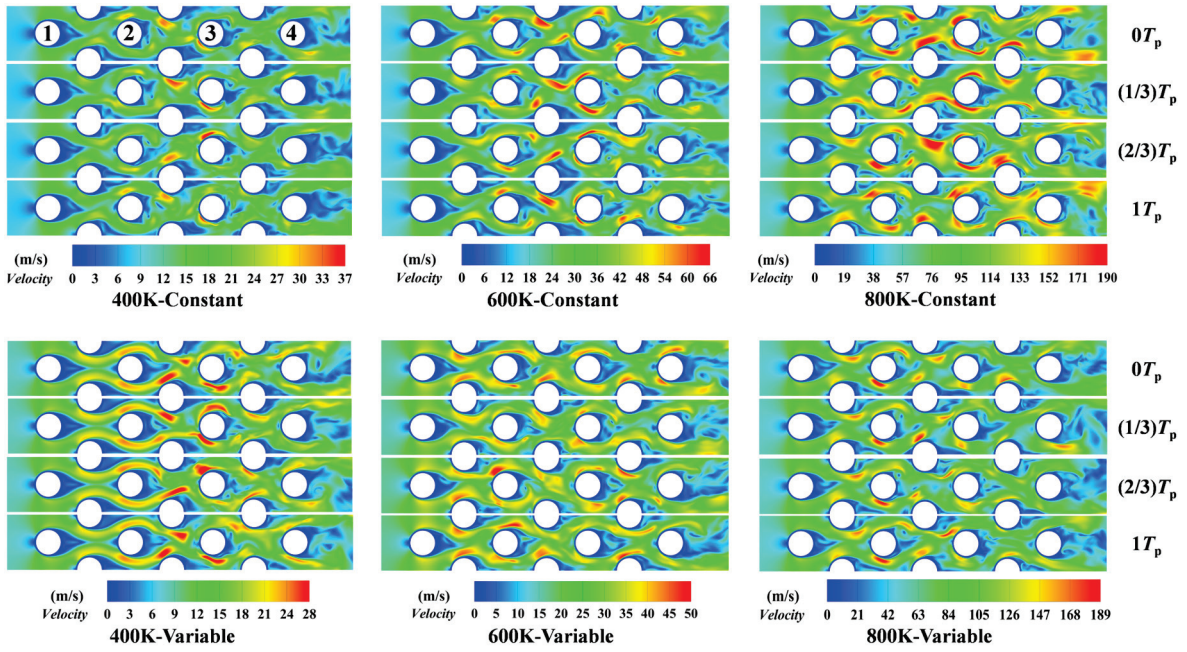



**Figure 12.** Instantaneous velocity contours of the staggered fine tubes under constant- and variable-property conditions at inlet temperatures of 400, 600, and 800 K.

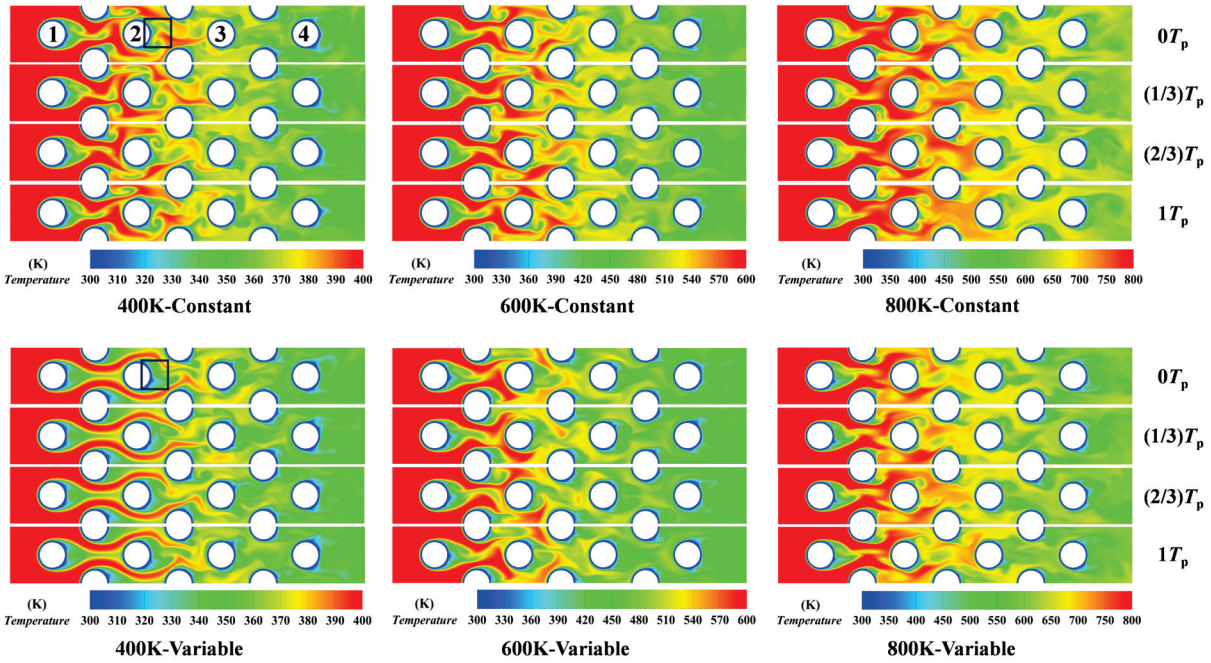



**Figure 13.** Instantaneous temperature contours of the staggered fine tubes under constant- and variable-property conditions at inlet temperatures of 400, 600, and 800 K.

To analyze the wake turbulence behind the staggered fines tubes, the streamwise distribution of Reynolds stress was examined. The sampling line was located along the wake centerline downstream of the second tube row, starting 0.1 mm downstream of the second tube center and ending 0.1 mm upstream of the windward surface of the third tube, aligned with the main flow direction.

Figure 14 shows the streamwise Reynolds stress distributions at inlet temperatures of 400 K, 600 K, and 800 K. Non-monotonic variations are observed for all temperatures; however, the detailed behaviors differ significantly. At 400 K and 600 K, pronounced fluctuations persist throughout the sampling region, and clear differences are observed between the constant-property and variable-property cases. In contrast, at 800 K, the Reynolds stress profiles obtained using different property treatments are generally similar, exhibiting comparable streamwise variation patterns.

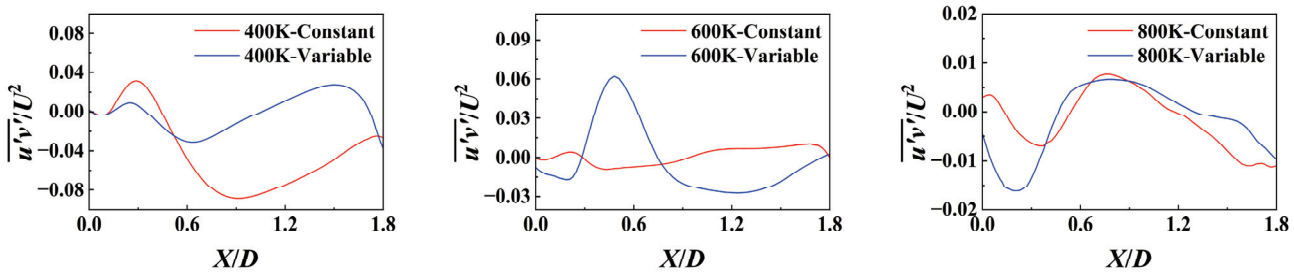



**Figure 14.** Streamwise distributions of normalized Reynolds shear stress along the wake centerline downstream of Tube 2 under constant- and variable-property conditions at 400–800 K.

This difference is mainly associated with the magnitude of temperature variations in the wake region. At 400 K and 600 K, appreciable temperature gradients remain downstream of the second tube row, and the use of variable properties alters the local viscosity and momentum diffusion, leading to differences in the Reynolds stress distribution. At 800 K, the flow field is globally at a high temperature level, and the relative temperature

https://doi.org/10.3390/en19030796

variation in the wake is smaller, resulting in a weaker influence of property treatment on the Reynolds stress profiles.

To quantitatively characterize wake unsteadiness in the fine tubes, a monitoring point was placed on the wake centerline 0.5 mm downstream of Tube 2, and the time history of the streamwise velocity was sampled to compute the corresponding power spectral density (PSD). This location lies in the near-wake region and can effectively capture vortex-shedding-induced velocity fluctuations while representing typical wake structures inside the bundle. In addition, to validate the wake dynamics from the perspective of global aerodynamic response, frequency-domain analyses were also conducted for the lift-coefficient time histories of all four tube rows. For both the monitoring-point velocity signal and the lift signals, the spectra were obtained using Fast Fourier Transform (FFT). A total sampling duration of approximately $3.0 \times 10^{-3}$ s was used, covering about 140 complete shedding cycles, which ensures statistical convergence of the spectra and provides sufficient frequency resolution. Moreover, the Strouhal number estimated from the inlet velocity of 52.2 m/s and the tube outer diameter of 1 mm is approximately 0.9, consistent with the typical range $St \approx$ O(1) for shear-layer-dominated vortex shedding from circular cylinders at high Reynolds numbers. This agreement further confirms that the dominant spectral peaks are physically meaningful rather than numerical artifacts.

As shown in Figure 15, both inlet temperature and thermophysical property treatment significantly alter the dominant unsteady scales and the spectral energy distribution in the tube-bundle wake. Under the constant-property conditions, the PSD at the monitoring point exhibits sharp and highly concentrated dominant peaks at all three temperatures, indicating the presence of a strong single dominant periodic mode in the wake, i.e., the typical vortex-shedding frequency. The dominant frequency shifts noticeably to higher values as the inlet temperature increases: it is approximately 15,663 Hz at 400 K and rises to 31,237 Hz at 600 K, suggesting that elevated temperature intensifies shear-layer roll-up, accelerates the vortex-shedding process, and enhances wake unsteadiness. At 800 K under constant properties, the spectral energy distribution transitions from a "single-peak-dominated" pattern to a broader-band spectrum, with a dominant peak around 19,118 Hz. This reflects a more strongly nonlinear wake state at high temperature, where multi-scale disturbances are amplified and the energy is no longer concentrated at a single frequency.

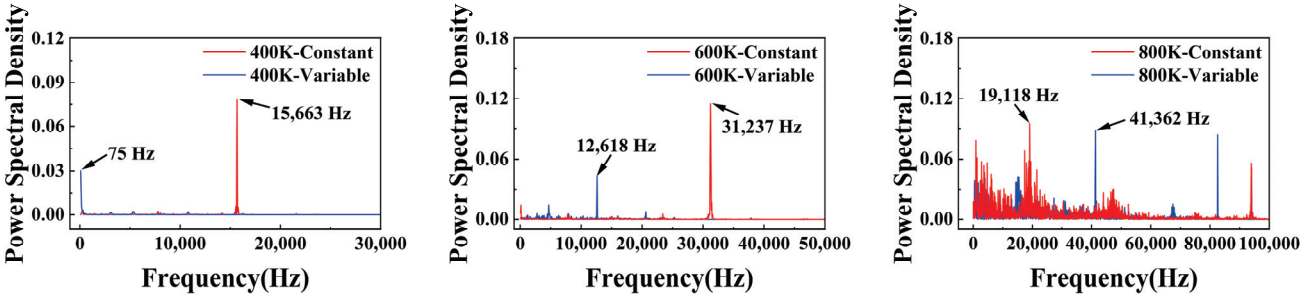



**Figure 15.** PSD of the streamwise velocity at the monitoring point located 0.5 mm downstream of Tube 2 on the wake centerline under constant- and variable-property conditions at 400–800 K.

In contrast, the variable-property cases generally show weaker dominant peaks and a more dispersed spectral distribution. This indicates that once temperature-dependent variations in viscosity, density, and other properties are taken into account, the periodic fluctuations in the wake become less concentrated and the dominant shedding mode is less pronounced than that predicted under constant properties. For example, at 400 K under variable properties, the dominant peak nearly vanishes and only a weak low-frequency peak around 75 Hz is observed, suggesting that periodic shedding is strongly weakened and the

https://doi.org/10.3390/en19030796

wake unsteadiness is substantially reduced. At 600 K under variable properties, a dominant peak appears at approximately 12,618 Hz, yet its magnitude remains much weaker than that of the constant-property case, indicating that unsteadiness begins to develop but the shedding process is still weak. When the temperature rises to 800 K under variable properties, a distinct high-frequency dominant peak emerges at about 41,362 Hz, indicating that high-temperature forcing enhances wake unsteadiness; however, the energy remains relatively broadband, implying a more complex shear-layer instability with pronounced multi-scale features. Overall, the monitoring-point PSD results demonstrate that increasing temperature elevates the characteristic wake frequency and strengthens unsteadiness, whereas neglecting property variations markedly amplifies the peak intensity and reinforces a "single-frequency-dominated" behavior, thereby tending to overestimate the periodicity and instability of vortex shedding in the wake.

Figure 16 presents the spectra of the lift coefficients for all four tubes, and the overall trends are consistent with those obtained from the monitoring-point PSD. Under constant-property conditions, higher dominant frequencies and more concentrated energy peaks are observed at all temperatures, whereas the variable-property cases exhibit lower dominant frequencies, weaker peaks, and more pronounced broadband distributions. Along the tube rows, downstream tubes are influenced by upstream vortex impingement and vortex merging, which may introduce secondary peaks in the constant-property spectra. In contrast, the spectra obtained under variable-property conditions tend to contain more scattered frequency components, indicating a less coherent wake governed by more intricate unsteady dynamics. These frequency-domain features are consistent with the flow-field contours: increasing temperature generally enhances vorticity and turbulent kinetic energy (TKE), promoting shear-layer instability and increasing the shedding frequency; when temperature-dependent properties are incorporated, the wake is weakened and both vorticity and TKE are reduced, suppressing shear-layer roll-up and the shedding process, which leads to reduced peak intensity and a more dispersed energy distribution. A particularly notable case occurs at 400 K under variable-property conditions, where some tube rows (e.g., Tube 1) exhibit almost no periodic shedding, and the resulting wake structures carry much lower frequencies and substantially weaker energy content than those predicted under constant properties. Overall, treating the fluid as having constant properties tends to overpredict both the shedding frequency and its associated spectral energy, whereas incorporating realistic temperature-dependent properties yields a wake that evolves toward a more complex multi-scale behavior with substantially reduced unsteady energy levels.

These unsteady wake characteristics also affect the near-wall flow around each tube, making it necessary to examine the circumferential distribution of the friction coefficient. As shown in Figure 17, all tubes exhibit a distinct peak on the windward side, and the magnitude follows the order Tube 3 > Tube 2 > Tube 4 > Tube 1. The hierarchy is also consistent with the flow field: the tubes in the middle-row face a more powerful near-wall shear since it is affected by both acceleration due to the mainstream and the vortex structures expelled by the upstream tubes. Tube 1 on the other hand is highly free of upstream disturbances and thus has the lowest shear. At 800 K, all tubes drop their values of friction and their points of separation shift upstream. This migration represents improved vorticity and TKE with elevated temperature, which enhance the loss of momentum in the boundary layer and enhance the separation of flows sooner.

https://doi.org/10.3390/en19030796

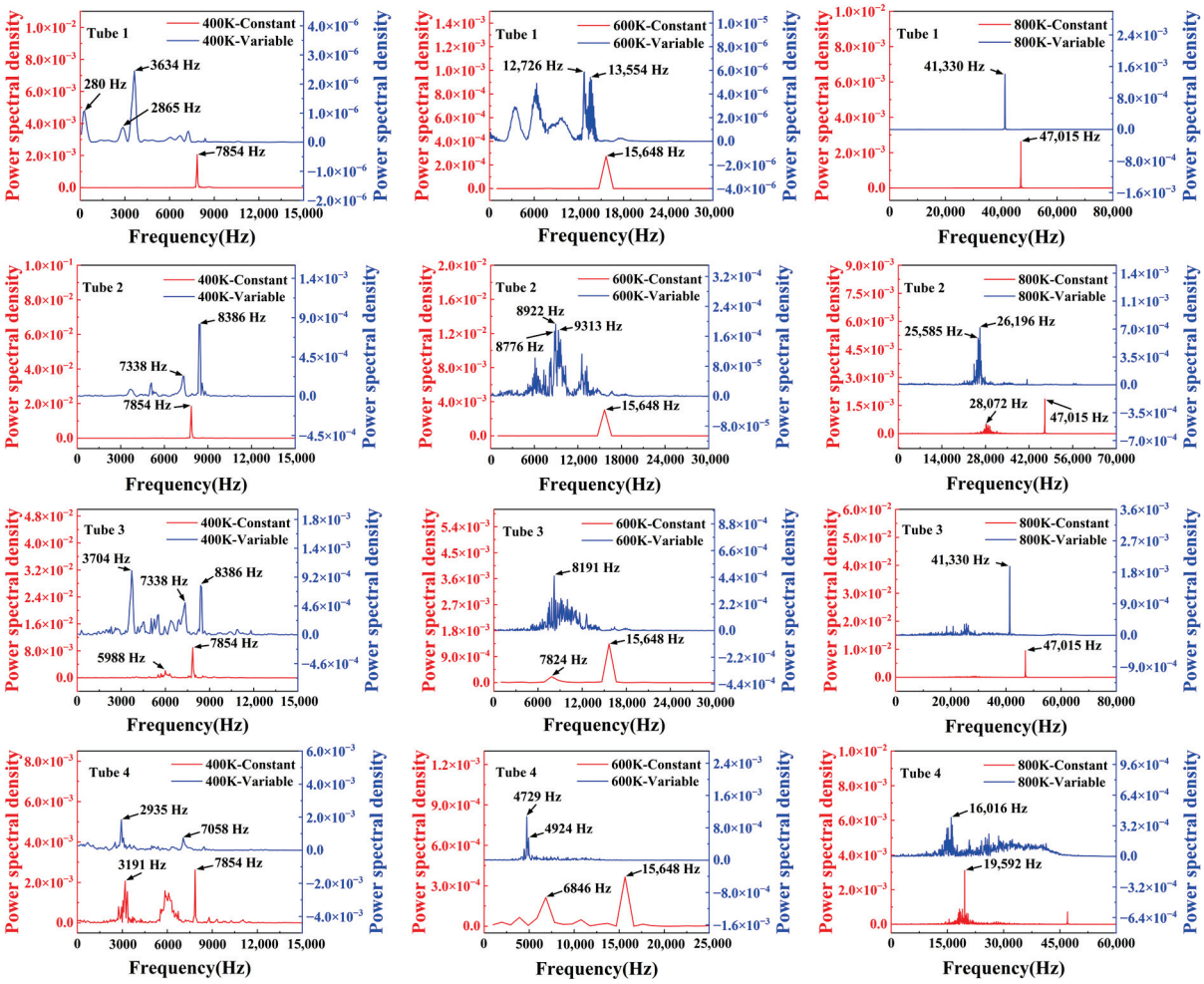



**Figure 16.** PSD of the lift coefficient for Tubes 1–4 under constant- and variable-property conditions at inlet temperatures of 400, 600, and 800 K.

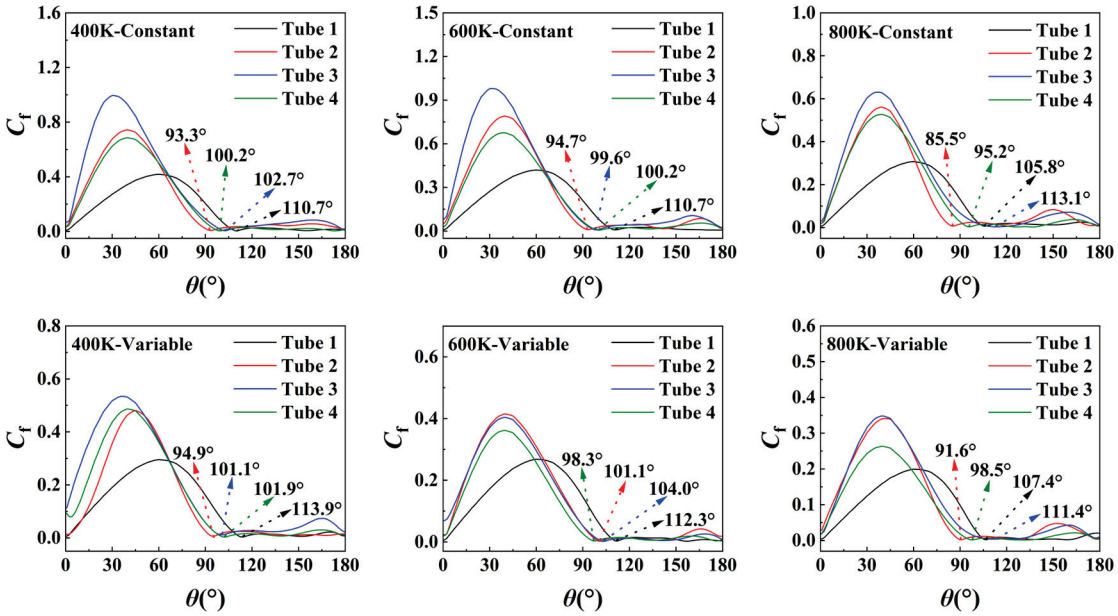



**Figure 17.** Circumferential distributions of surface friction coefficient for Tubes 1–4 under constant- and variable-property conditions at inlet temperatures of 400, 600, and 800 K.

https://doi.org/10.3390/en19030796

Under variable-property conditions, the friction coefficients decrease further with increasing temperature, and the separation angles advance correspondingly. Combined with the contour results—showing a larger low-velocity wake region (a wider velocity-deficit zone) and reduced vorticity and TKE—it becomes evident that temperature-dependent properties decrease the local Reynolds number and thicken the boundary layer, thereby weakening near-wall shear and reducing the tendency for shear-layer reattachment. Moreover, at the same temperature, the constant-property cases consistently overestimate the friction coefficient, indicating that neglecting temperature-dependent property variations leads to an overprediction of near-wall shear.

These near-wall shear characteristics further influence the overall flow resistance acting on the tubes, particularly the pressure distribution along the flow direction. Figure 18 illustrates the variations in pressure drop across the four tubes under different temperatures and fluid-property conditions. Under all operating conditions, the local pressure drop decreases markedly along the flow direction. For example, at 400 K under constant-property conditions, the pressure drop decreases from 254 Pa at Tube 1 to 86 Pa at Tube 4; under variable-property conditions, it decreases from 147 Pa to 39 Pa. This trend suggests that the momentum dissipation and wake weakening caused by the upstream tubes markedly reduce the aerodynamic loading on the downstream ones.

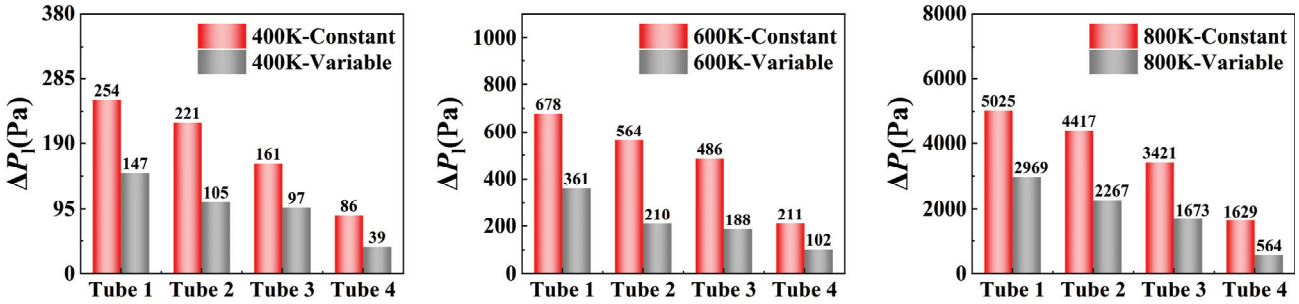



**Figure 18.** Local pressure drop across Tubes 1–4 under constant- and variable-property conditions at inlet temperatures of 400, 600, and 800 K.

As temperature increases, the pressure drop across each tube rises steeply. For Tube 1, for instance, elevating the temperature from 400 K to 800 K causes the pressure drop to increase from 254 Pa to 5025 Pa under constant-property assumptions, and from 147 Pa to 2969 Pa under variable properties—both representing nearly a twentyfold growth. This substantial increase is consistent with the progressively stronger shear-layer roll-up and vortex shedding revealed in the vorticity fields, and also aligns with the velocity-field trend: higher temperature leads to a reduction in air density, which in turn produces a significant increase in flow velocity.

At the same temperature, the pressure drop under variable-property conditions is consistently much lower than that under constant-property conditions. For example, at 600 K, the pressure drops for the four tubes under constant properties are 678, 564, 486, and 211 Pa, respectively, whereas under variable properties they decrease to only 361, 210, 188, and 102 Pa. The contour plots show that under variable-property conditions, the low-velocity wake region expands and both vorticity magnitude and TKE are reduced. This effect is particularly pronounced for Tubes 1–2 at 400 K, where the TKE is close to zero. These observations indicate that real fluid property variations enhance viscous diffusion, weaken near-wall shear, and consequently reduce local flow resistance. Overall, treating the flow with constant properties leads to a systematic overprediction of the local pressure drop on each tube. When temperature-dependent variations in fluid properties are included, the flow resistance decreases notably, primarily because

https://doi.org/10.3390/en19030796

vortex shedding is weakened and the associated turbulent structures are substantially reduced. From a system design perspective, the overestimation of pressure drop under constant property assumptions implies an amplified prediction of the required pump or compressor power. Since the driving power is typically approximately proportional to the pressure loss, this deviation may lead to overly conservative component sizing, which is particularly pronounced in high-temperature air-breathing systems. Therefore, considering temperature-dependent property variations is crucial for obtaining more realistic and reliable engineering conclusions when evaluating aerodynamic losses and overall system efficiency.

### *3.2. Heat Transfer Characteristics*

Since wake dynamics and near-wall shear play a central role in determining thermal transport, it is necessary to further examine the heat transfer behavior of the fine tubes. Figure 19 shows the average surface heat flux for each tube under different operating conditions, and the overall trends align well with the flow-field contours. Tubes 2 and 3 exhibit the highest heat-flux levels, which is consistent with the vorticity and TKE distributions indicating that the middle-row tubes experience the strongest shear layers and the most concentrated TKE. The vortices shed from upstream tubes repeatedly impinge on the downstream tubes, enhancing near-wall mixing and thereby steepening the local temperature gradient. For Tube 4, the temperature contours indicate a noticeably thicker near-wall thermal boundary layer on its lee side, which reduces the wall-normal temperature gradient and leads to the lowest heat flux. In addition, the incoming flow reaching Tube 4 has already been substantially cooled by the upstream rows, further weakening the local thermal driving force. Tube 1, unaffected by upstream vortex disturbances, relies mainly on the direct impingement of the incoming flow and therefore shows only a moderate level of heat transfer.

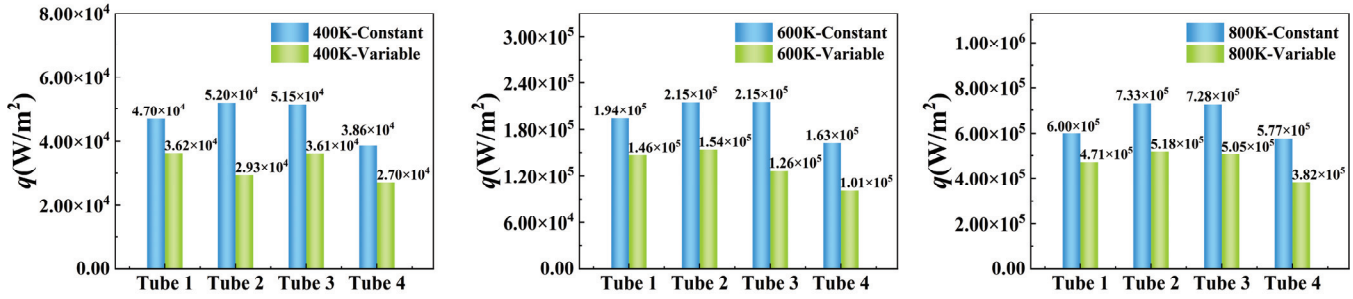



**Figure 19.** Comparison of average surface heat flux for Tubes 1–4 under constant- and variable-property conditions at inlet temperatures of 400, 600, and 800 K.

As the temperature increases from 400 K to 800 K, the heat flux of all tubes increases by several orders of magnitude. This rise is consistent with the stronger vorticity and higher TKE observed in the contour fields, as well as the thinner near-wall thermal boundary layers at elevated temperatures. The combined effects of intensified shear-layer instability and the larger temperature difference between the solid surface and the air substantially reinforce the heat-transfer process.

At the same temperature, the heat flux under variable-property conditions is noticeably lower than that under constant-property conditions (approximately 20–30% lower at 800 K). The contour analysis indicates that under variable-property conditions, the bulk flow velocity decreases, the recirculation region expands, and both the vorticity magnitude and TKE are reduced. These changes significantly reduce the near-wall velocity and temperature gradients. Consequently, assuming constant properties leads to an overestimation of the surface heat transfer capability.

https://doi.org/10.3390/en19030796

To further elucidate how heat transfer varies along the tube surface, the circumferential and average Nusselt numbers were analyzed. As shown in Figures 20 and 21, the circumferential *Nu* distributions follow similar patterns under all operating conditions: *Nu* peaks on the windward side due to strong heat transfer in the stagnation region and a thin near-wall thermal boundary layer, then decreases rapidly after separation, forming a pronounced trough within the separated zone. A partial recovery occurs near the reattachment region, where shear-layer reattachment and enhanced mixing promote thermal-boundary-layer thinning.

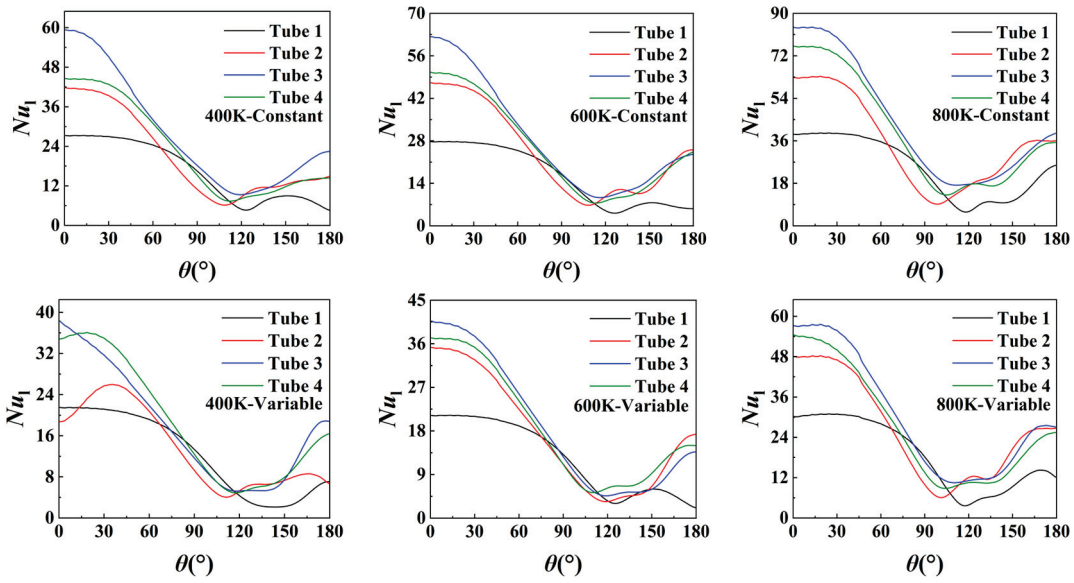



**Figure 20.** Circumferential distributions of *Nu* for Tubes 1–4 under constant- and variable-property conditions at inlet temperatures of 400, 600, and 800 K.

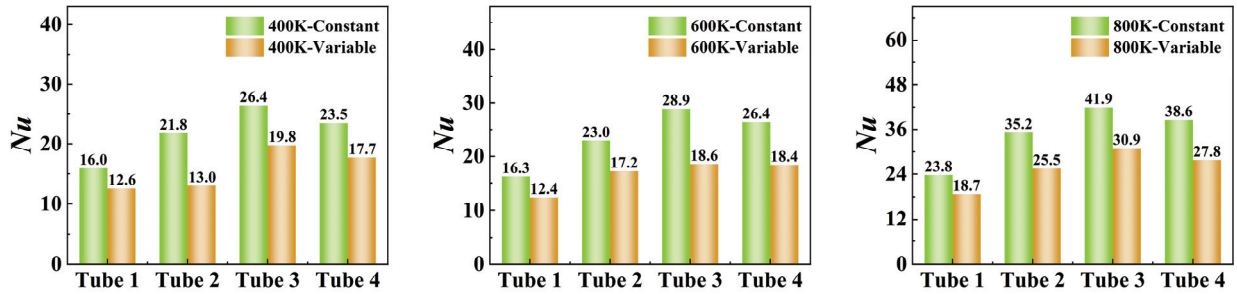



**Figure 21.** Average Nusselt number of Tubes 1–4 under constant- and variable-property conditions at inlet temperatures of 400, 600, and 800 K.

More importantly, the row-wise variation in the average *Nu* can be explained by the evolution of wake–tube interactions. Tube 1 exhibits the lowest heat-transfer level because it encounters an undisturbed incoming flow with relatively weaker near-wall turbulence, leading to a more stable boundary layer and reduced wall-normal transport. In contrast, the middle-row tubes experience strong disturbances originating from upstream wakes. In particular, Tube 3 achieves the highest average *Nu* because it is subjected to (i) wake-induced flow acceleration and larger local velocity gradients on the windward side, which effectively increase the local Reynolds number and convective transport, and (ii) intense vortex impingement and elevated turbulence intensity in the near-wake, which disrupt the boundary layer and strengthen the near-wall velocity/temperature gradients. These effects also enhance the heat-transfer recovery in the reattachment region, thereby increasing the surface-averaged *Nu*. For the last-row tube (Tube 4), although upstream fluctuations still

https://doi.org/10.3390/en19030796

exist, part of the kinetic energy has already been dissipated and the approaching fluid has been pre-cooled by the upstream tubes, resulting in a reduced available temperature difference and a slightly lower average *Nu* than Tube 3, while remaining higher than the upstream tubes overall.

As the inlet temperature increases from 400 K to 800 K, the near-reattachment *Nu* is substantially enhanced, resulting in a significant increase in the average *Nu*. This enhancement is attributed to the increased thermal driving force together with stronger shear-layer instability and higher turbulence intensity at elevated temperatures, which promote wall-normal mixing and thermal-boundary-layer thinning.

Regarding variable-property effects, incorporating realistic temperature-dependent properties leads to lower circumferential *Nu* values over the entire surface compared with constant-property predictions, with the most pronounced reduction near the stagnation region and a weakened recovery in the reattachment zone. This reduction is mainly caused by temperature-dependent variations in viscosity and density, which decrease the effective local Reynolds number and thicken the boundary layer, leading to weaker near-wall velocity and temperature gradients. In addition, the reduced wake turbulence intensity under variable-property conditions diminishes the reattachment-related heat-transfer enhancement. Overall, constant-property assumptions tend to overpredict both the magnitude and the coherence of convective heat transfer in the fines tubes.

Beyond the surface heat transfer behavior, it is also necessary to examine how the air temperature evolves as it passes through the tube rows. Figure 22 shows the distribution of the local temperature drop across the four rows under different operating conditions. The temperature fields indicate that the air is gradually cooled as it moves around the tubes, and the magnitude of this temperature drop diminishes steadily in the downstream direction. This behavior can be attributed to the fact that Tube 1 encounters the largest initial temperature difference relative to the 300 K tube wall, providing the strongest thermal driving force for heat transfer. After successive heat exchange with the upstream tubes, the air temperature decreases, leading to a substantially reduced temperature difference when it reaches the downstream tubes. As a result, the temperature drops across Tubes 2 and 3 are smaller than that across Tube 1, while Tube 4 exhibits the smallest temperature drop.

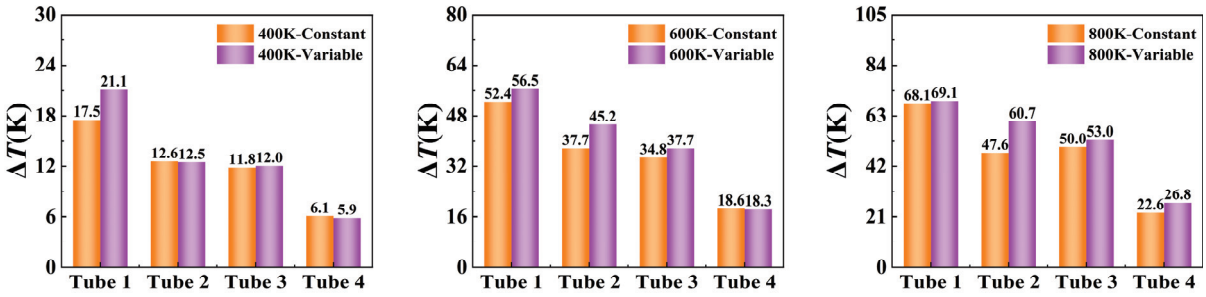



**Figure 22.** Air temperature drop across Tubes 1–4 under constant- and variable-property conditions at inlet temperatures of 400, 600, and 800 K.

As the inlet temperature increases from 400 K to 800 K, the temperature drop across all tube rows increases substantially. For example, the temperature drop of Tube 1 rises from approximately 17.5 K to nearly 68 K. This indicates that a higher incoming-flow temperature provides a stronger solid–air temperature difference as the driving force for heat transfer. Coupled with the enhanced TKE and intensified shear-layer disturbances at elevated temperatures, the sensible heat transfer from the air to the tube wall is significantly strengthened, thereby improving the overall cooling performance of the system.

At the same temperature, the temperature drop under variable-property conditions is generally greater than that under constant-property conditions, a trend particularly evident

https://doi.org/10.3390/en19030796

in the first three rows (e.g., at 600 K, the temperature drop of Tube 2 increases from 37.7 K to 45.18 K). The underlying mechanism is as follows: although variable properties reduce the local surface heat flux, the accompanying decrease in air density at higher temperatures lowers the mass flow rate. The velocity fields indicate that under variable-property conditions, the low-velocity wake (velocity-deficit) region expands and the bulk flow velocity decreases, leading to a reduced mass flow rate through the fine tubes. Because the reduction in mass flow rate outweighs the decrease in heat flux, the air undergoes a larger temperature drop per unit mass, thereby producing a larger overall temperature difference. (For the 600 K case, the outlet mass flow rate decreases from $9.6227 \times 10^{-5}$ kg/s (constant properties) to $6.5960 \times 10^{-5}$ kg/s (variable properties), i.e., a reduction of about 31.5%. Meanwhile, the mass-weighted outlet temperature decreases from 462.44 K to 447.20 K, corresponding to a larger temperature drop under variable properties (152.80 K vs. 137.56 K). Using $Q_{air} = |m|(h_{in} - h_{out})$, we obtained $Q_{air}$ = 13.92 W for the constant-property case and 10.44 W for the variable-property case. Although the overall heat removal rate is lower under variable properties, the enthalpy drop per unit mass is larger ($\Delta h$ = 158.25 kJ/kg vs. 144.66 kJ/kg) and the mass flow rate is significantly reduced, which together lead to a larger temperature decrease in the air). In summary, the cooling performance of air flowing over fine tubes is jointly governed by the local temperature driving force, the heat transfer capability of the upstream tube rows, and the flow parameters (including velocity, vorticity, and TKE). Additionally, constant-property assumptions tend to underestimate the air temperature drop, demonstrating that temperature-dependent property variations play a critical role in accurately predicting the cooling performance of fine tubes.

To assess how temperature-dependent property variations affect the flow and heat transfer behavior of air flowing across fine tubes, the average *Nu* and local pressure drop for both constant-property and variable-property models were compiled and compared for each tube, as summarized in Table 1. The findings indicate that the use of constant-property assumptions is always followed by an overestimation of both flow and heat transfer performance. The predicted *Nu* is, on average, approximately 20–40% greater than the variable-property calculation, and local pressure drop is also overestimated to even higher proportions, usually 40–65%. These inconsistencies underscore the fact that temperature-dependent variations in fluid properties should not be neglected since they may cause significant errors and especially when determining pressure drop. Generally, consideration of real-property effects is critical to the proper predictive character of the flow and heat transfer of high temperature air flowing over fine tubes. It is particularly important to this consideration when estimating the pressure drops, since the failure to consider property variations would greatly overestimate the flow resistance and may negatively affect the design and optimization of the engineering process of precoolers.

**Table 1.** Error in average *Nu* and local pressure drop under constant- and variable-property conditions.

| Inlet Air Temperature | Tube Number | Average *Nu* | Local Pressure Drop |
|---|---|---|---|
| 400 K | 1 | 21.3% | 42.1% |
| | 2 | 40.5% | 52.5% |
| | 3 | 25.3% | 39.8% |
| | 4 | 24.6% | 54.7% |
| 600 K | 1 | 23.9% | 46.8% |
| | 2 | 25.0% | 62.8% |
| | 3 | 35.8% | 61.3% |
| | 4 | 30.4% | 51.7% |
| 800 K | 1 | 21.3% | 40.9% |
| | 2 | 27.5% | 48.7% |
| | 3 | 26.3% | 51.1% |
| | 4 | 28.0% | 65.4% |

https://doi.org/10.3390/en19030796

## 4. Discussion

Proper modeling of the thermophysical characteristics of air as a function of temperature is important to the technological prediction of the thermal-hydraulic characteristics of micro-scale precooler tubes. Neglecting real-gas effects leads to notable overestimations of both heat transfer capability and pressure losses, which may further resulting in oversized components, underestimated cooling demands, or insufficient performance margins in SABRE-type precooler designs. Thus, incorporating variable air properties is fundamental to the reliable design, assessment, and optimization of precooler systems. Current research still faces multiple limitations. Future work should address these existing shortcomings by conducting more systematic and in-depth studies to refine theoretical frameworks and guide engineering practices. Specifically, subsequent efforts could proceed from the following aspects:

(1) The present study still has some limitations, such as the consideration of a single Reynolds number. Future work will systematically investigate a broader Reynolds number range, from low to high (e.g., $Re$ = 300–3000 or wider), to establish generalized correlations applicable to full operating conditions and to provide more comprehensive data support for the optimal design of precoolers.

(2) The present model has limitations regarding the extrapolation of the number of tube rows in the streamwise direction. Future work will systematically increase the number of tube rows to identify the critical condition required to achieve fully developed flow, thereby establishing more general design guidelines.

(3) To facilitate an in-depth investigation of the air-side flow and heat transfer mechanisms in fine tubes, an idealized constant wall temperature boundary condition is adopted in the present study. Under this assumption, the conclusions are most directly applicable to operating conditions with strong cooling capacity on the cold side or well-controlled coolant temperatures. However, the actual operation of a SABRE precooler involves strongly coupled, transient heat transfer between the hot (air) and cold (helium) fluids, resulting in complex spatiotemporal variations in the wall temperature. Therefore, extending the air-side fundamental mechanisms revealed in this study to practical engineering scenarios with fully coupled hot–cold side interactions represents a critical step toward real-world applications. Future work will focus on developing fully coupled, transient numerical models that simultaneously account for the internal and external flows under prescribed inlet conditions (mass flow rate, pressure, and temperature), in order to systematically investigate the heat transfer characteristics and dynamic wall temperature evolution under dual-sided convective effects. This will help establish a comprehensive theoretical bridge from fundamental mechanisms to engineering design, providing a more solid basis for the refined design and dynamic control of precoolers.

(4) This study primarily reveals the evolution of flow and heat transfer mechanisms under a limited number of tube rows. The current model has limitations regarding extrapolation to a greater number of tube rows along the flow direction. In future research, the number of tube rows will be systematically increased to determine the critical conditions for achieving fully developed flow, thereby establishing more universal design criteria.

(5) It should be noted that the strong property variations at significantly elevated temperatures may enhance shear layer instability and affect local heat transfer and resistance distributions, aspects not directly covered by the existing validation data. Therefore, the results under high-temperature conditions in this study are more suitable for revealing trends and relative variations in flow and heat transfer rather than serving as absolute quantitative predictions. Further validation of the model's applicability

https://doi.org/10.3390/en19030796

under extreme conditions through high-temperature experiments or higher-fidelity simulations remains necessary in future work.

(6) The present results also show that high-frequency vortex shedding develops when air flows across staggered fine tubes. A promising direction for future research is to examine how these fine tubes respond to the disturbances generated by such high-frequency shedding. Insights from this investigation would help establish a more comprehensive theoretical basis for improving precooler design and guiding performance optimization.

## 5. Conclusions

This work numerically examined the flow and heat transfer behavior of high-temperature air passing over staggered fine tubes, considering both constant-property and temperature-dependent property models. The key findings can be summarized as follows:

(1) The unsteady flow characteristics of fine tubes are highly sensitive to temperature. Rising inlet temperature significantly strengthens shear-layer instability, vortex shedding, and TKE, thereby enhancing heat transfer and increasing pressure drop. However, when temperature-dependent air properties are incorporated, the wake width increases and the separated shear layers become thicker, while the turbulence/unsteadiness intensity is reduced. As a result, vortex shedding becomes less periodic and less regular, the wake vortices are more scattered, and the near-wall shear is substantially weakened.

(2) These flow modifications directly influence thermal performance. Middle-row tubes achieve the highest heat transfer due to strong vortex impingement. Higher inlet temperatures greatly increase *Nu* and heat flux.

(3) Temperature drop through the tube rows decreases along the flow direction, yet increases markedly with inlet temperature. Under variable-property conditions, reduced density and mass flow rate yield a larger temperature drop per unit mass, despite lower surface heat flux. Constant-property models underestimate this cooling effect.

(4) Overall, constant-property assumptions overpredict both heat transfer and flow resistance performance, with local pressure drop errors reaching 40–65% and Average *Nu* errors 20–40%.

**Author Contributions:** Conceptualization, L.S.; methodology, Q.Z.; software, Q.Z. and Y.F.; validation, C.Z. and J.Z.; formal analysis, X.X.; investigation, Q.Z. and Y.F.; resources, Y.F.; data curation, L.S.; M.D. and Z.M.; writing—original draft preparation, Q.Z.; writing—review and editing, L.S.; M.D. and Z.M.; visualization, Q.Z.; supervision, L.S.; project administration, L.S. All authors have read and agreed to the published version of the manuscript.

**Funding:** This research was funded by The National Science and Technology Major Project, 2025ZD1009905 and by The National Natural Science Foundation of China, 12075160, and by The National Key R&D Program of China, 2021YFB1507403, and by The Natural Science Foundation of Sichuan Province, 2025ZNSFSC0445, 2026NSFSC1345.

**Data Availability Statement:** The original contributions presented in this study are included in the article. Further inquiries can be directed to the corresponding author.

**Acknowledgments:** During the preparation of this manuscript/study, the authors used DeepSeek for the purposes of generating text. The authors have reviewed and edited the output and take full responsibility for the content of this publication.

**Conflicts of Interest:** The authors declare no conflicts of interest. The funders had no role in the design of the study.

## Abbreviations

The following abbreviations are used in this manuscript:

| | |
|---|---|
| LES | Large-Eddy Simulation |
| SABRE | Synergetic Air-Breathing Rocket Engine |
| REL | Reaction Engines Limited |
| RANS | Reynolds-Averaged Navier–Stokes |
| NIST | National Institute of Standards and Technology |
| TKE | Turbulent Kinetic Energy |
| FFT | Fast Fourier Transform |

## References


1. Deng, F.; Tan, H.; Dong, H.; Fu, Q.; Chen, J. Progress on Key Technologies of Hypersonic Aerospace Plane with Pre-Cooled Combined Propulsion. *J. Propuls. Technol.* **2018**, *39*, 1. (In Chinese) [CrossRef]
2. Wei, X.; Wang, Z.; Yu, X.; Zhao, M.; Feng, Y.; Xu, S.; Qin, J. Numerical Investigation on the Flow and Heat transfer Characteristics of Tube-Bundle Precooler Based on the Multi-Layer Grid Superposition Method. *Therm. Sci. Eng. Prog.* **2025**, *67*, 104090. [CrossRef]
3. Ding, W.; Eri, Q.; Kong, B.; Wang, C. The Effect of Inlet Pressure Distortion on the Performance of an Axisymmetric Compact Tube Heat Exchanger with Radial Counter Flow Type for Hypersonic Pre-Cooled Aero-Engine. *J. Mech. Sci. Technol.* **2022**, *36*, 3181–3191. [CrossRef]
4. Wang, C.; Eri, Q.; Wang, Y.; Ding, W. Flow and Heat Transfer Characteristics of Intake-Precooler System for Hypersonic PreCooled Aero-engine. *Appl. Therm. Eng.* **2023**, *229*, 120596. [CrossRef]
5. Zhang, J. Research on the Flow and Heat Transfer Mechanism of Cryogenic Fluid in the Micro/Mini-Channel of Combined Cycle Engine Precooler. Ph.D. Thesis, National University of Defense Technology, Changsha, China, 2018. (In Chinese) [CrossRef]
6. Wu, Y.; Xu, R.; Wang, C.; Jiang, P. Novel Three-Equation Porous Media Model for Prediction of Compact Heat Exchanger and Its Case Study for Microtube Bundle Precooler. *Int. J. Heat Mass Tran.* **2025**, *248*, 127177. [CrossRef]
7. Li, W.; Zhang, L.; Shen, L.; Wang, C.; Qin, J. Overview of Precooled Turbine-Based Combined Cycle Engine and Its Key Technologies. *Aeroengine* **2024**, *50*, 16–29. (In Chinese) [CrossRef]
8. Wei, X.; Jin, F.; Yao, Z.; Ji, H. Numerical Investigation on the Heat Transfer of Air/Helium Precooler for Air-Breathing Pre-Cooled Engine. *Therm. Sci.* **2024**, *28*, 913–927. [CrossRef]
9. Lu, Y.; Jiang, S.; Che, Y.; Zhang, Z.; Wang, X. Coupling Characteristics of the Bowed Micro-Tubes for Precooled Heat Exchangers Under Different Inflow Speeds. *Phys. Fluids* **2025**, *37*, 075155. [CrossRef]
10. Xie, P.; Liu, Y.; Yuan, W. An Investigation on Aerodynamic and Thermodynamic Characteristics of a Precooled Intake for the Supersonic Precooled Turbine Engine. *Appl. Therm. Eng.* **2025**, *278*, 127458. [CrossRef]
11. Wang, Z.; Ma, T.; Wang, B.; Gu, M. Heat Exchange Micro-Tube Vibration Analysis and Reliability Evaluation Methods for Diaphragm Micro-channel Pre-coolers. *China Mech. Eng.* **2024**, *35*, 869–876. (In Chinese) [CrossRef]
12. Wei, X.; Jin, F.; Ji, H.; Jin, Y. Thermodynamic Analysis of Key Parameters on the Performance of Air Breathing Pre-Cooled Engine. *Appl. Therm. Eng.* **2022**, *201*, 117733. [CrossRef]
13. Li, N.; Yan, X.; Chen, X.; Zhou, X.; Su, W.; Duan, Z. Efficient Prediction of Heat Transfer Characteristics of Compact Heat Exchangers. *J. Aerosp. Power.* **2025**, *40*, 20230811. (In Chinese) [CrossRef]
14. Ma, H.; Zhang, W.; Su, W.; An, H. Modal Decomposition and Rapid Prediction of Flow and Heat Transfer in Microtubes of Precooler. *Acta Aerodyn. Sin.* **2025**, *43*, 110–120. (In Chinese) [CrossRef]
15. Ding, W.; Eri, Q.; Kong, B.; Zhang, Z. Numerical Investigation of a Compact Tube Heat Exchanger for Hypersonic Pre-Cooled Aero-Engine. *Appl. Therm. Eng.* **2020**, *170*, 114977. [CrossRef]
16. Li, S.; Ma, T.L.; Liu, H.T.; Zhang, Z.G.; Xiang, Z.H.; Mo, Z.Y.; Sun, L.C. Numerical Analysis of Effects of Pre-Cooler Structure Parameter on Its Performance in SABRE. *J. Propuls. Technol.* **2022**, *43*, 257–264. (In Chinese) [CrossRef]
17. Mi, Y.; Liu, M.; Wu, H.; Zhao, R.; Zhu, K. Experimental Study on Frost Formation on the Surface of Ultra-Low Temperature Circular Tubes Under Forced Convection Conditions. *Int. J. Heat Mass Tran.* **2025**, *249*, 127280. [CrossRef]
18. Bacellar, D.; Aute, V.; Huang, Z.; Radermacher, R. Airside Friction and Heat Transfer Characteristics for Staggered Tube Bundle in Crossflow Configuration with Diameters from 0.5 mm to 2.0 mm. *Int. J. Heat Mass Tran.* **2016**, *98*, 448–454. [CrossRef]
19. Zhang, J.; Li, G.; Nan, X.; Ma, Y.; Tang, G. Design and Flow Heat Transfer of Mini-Channel Helium Heat Exchanger in Combined Engine. *J. Rocket. Propul.* **2021**, *47*, 9–18. (In Chinese)
20. Li, S.; Li, J.; Liu, Z. Simulation Study on Flow and Heat Transfer of Cross-Arrangement Tube Bundle. *J. Therm. Sci.* **2023**, *32*, 1435–1444. [CrossRef]

21. Qin, Y.; Zhuang, L.; Liu, Q.; Liu, Z.; Wen, J. Numerical Investigation on Heat Transfer Characteristics of Staggered Tube Bundles in Cross Flow. *J. Aerosp. Power.* **2023**, *38*, 2718–2728. (In Chinese) [CrossRef]
22. Guan, N.; Luan, T.; Liu, Z.G.; Zhang, C.W.; Jiang, G. Vortex Distribution and Mixed Convection of Liquid Flow Across Micro-Cylinders in a Rectangular Channel. *Heat Mass Transfer.* **2016**, *52*, 657–670. [CrossRef]
23. Wei, M. Study on the Heat Transfer of High-Temperature Air Traversing Microtubule Bundles Flow Under Quenching Cold Conditions. Master's Thesis, Sichuan University, Chengdu, China, 2024. (In Chinese)
24. Su, L. Precooling Turbine Cooling Air for Aviation Engines. Master's Thesis, Shenyang Aerospace University, Shenyang, China, 2018. (In Chinese)
25. Gu, L.; Min, J.; Wu, X.; Yang, L. Airside Heat Transfer and Pressure Loss Characteristics of Bare and Finned Tube Heat Exchangers Used for Aero Engine Cooling Considering Variable Air Properties. *Int. J. Heat Mass Tran.* **2017**, *108*, 1839–1849. [CrossRef]
26. Wei, X.; Jin, F.; Liu, T.; Ji, H. Numerical Study on Flow and Heat Transfer of Air Precooler in SABRE. *J. Rocket. Propul.* **2019**, *45*, 8–16. (In Chinese)
27. Li, C.P.; Wang, Y.S.; Wang, H.J.; Wei, Y.Q. Numerical Analysis of Heat Transfer in Precooler for Hybrid Airbreathing Rocket Engines. *J. Eng. Thermophys.* **2017**, *38*, 811–816. (In Chinese)
28. Li, G.; Ma, T.L.; Liu, H.T.; Zhang, Z.G.; Tang, J.G.; Sun, L.C. Evaluation and Analysis of Applicability of Zukauskas Correlation to Microtubular Pre-Cooler. *J. Propuls. Technol.* **2021**, *42*, 2754–2761. (In Chinese) [CrossRef]
29. Linton, D.; Thornber, B. Direct Numerical Simulation of Transitional Flow in a Staggered Tube Bundle. *Phys. Fluids* **2016**, *28*, 024111. [CrossRef]
30. Lei, C.; Cheng, L.; Kavanagh, K. Spanwise Length Effects on Three-Dimensional Modelling of Flow over a Circular Cylinder. *Comput. Methods Appl. Mech. Eng.* **2001**, *190*, 2909–2923. [CrossRef]
31. Labbé, D.F.L.; Wilson, P.A. A Numerical Investigation of the Effects of the Spanwise Length on the 3-D Wake of a Circular Cylinder. *J. Fluid. Struct.* **2007**, *23*, 1168–1188. [CrossRef]
32. Yao, L.; Fu, C.; Zhang, J.; Li, Z.; Zou, Z. Heat Transfer Performance of Pre-Cooler Under Unsteady Inflow Pressure Condition Using Dynamic Mode Decomposition Method. *J. Aerosp. Power.* **2020**, *35*, 2064–2077. (In Chinese) [CrossRef]
33. Chen, Y.; Li, Z.; Zhang, J.; Zou, Z. Large Eddy Simulation on the Staggered Tube Bundle of the Compact Precooler. *J. Aerosp. Power.* **2021**, *36*, 701–712. (In Chinese) [CrossRef]
34. Xie, J.; Li, S.; Yan, H.; Xie, G. Numerical Analysis on Thermal–Hydraulic Performances of Staggered Tube Bundles for an Aero-Engine Compact Precooler. *J. Therm. Anal. Calorim.* **2020**, *141*, 387–399. [CrossRef]
35. Li, Y.; Jiang, S.; Chen, X.; Sun, F.; Wang, S.; Lu, Y. Study on the Effects of Structural Parameters of the Pre-Cooler on the Performance of Combined Power Generation Engines. *Symmetry* **2024**, *16*, 1471. [CrossRef]
36. Wen, J.; Qin, Y.; Xu, G.; Liu, Z.; Dong, B.; Wu, S.; Zhuang, L. Experimental and Numerical Analysis of Airside Thermal-Hydraulic Characteristics of Small-Diameter Tube Bundle Under Compressible Flow Conditions. *Int. Commun. Heat Mass* **2025**, *168*, 109429. [CrossRef]


**Disclaimer/Publisher's Note:** The statements, opinions and data contained in all publications are solely those of the individual author(s) and contributor(s) and not of MDPI and/or the editor(s). MDPI and/or the editor(s) disclaim responsibility for any injury to people or property resulting from any ideas, methods, instructions or products referred to in the content.

energies

MDPI

*Article*

# Dynamic Thermal Resistance-Capacity Modeling and Thermal Short-Circuit Analysis: A Study on Natural Convection in a Direct-Expansion $CO_2$ Downhole Heat Exchanger

**Yang Yu [1,2], Jing Wang [1], Xinyue Li [1], Jinyu Zhao [1], Shuman Wang [1], Fei Ma [1,*], Jun Zhao [1] and Yang Li [1,*]**

[1] Laboratory of Efficient Utilization of Low and Medium Grade Energy, School of Mechanical Engineering, Tianjin University, Tianjin 300350, China; yuyangbit@tju.edu.cn (Y.Y.); ximugu@tju.edu.cn (J.W.); xyl_2001@tju.edu.cn (X.L.); zhaojinyu@tju.edu.cn (J.Z.); wangshuman138@163.com (S.W.); zhaojun@tju.edu.cn (J.Z.)

[2] China Automotive Technology and Research Center Co., Ltd., Tianjin 300300, China

* Correspondence: mafei@tju.edu.cn (F.M.); liyangtju@tju.edu.cn (Y.L.); Tel.: +86-13702157073 (Y.L.)

**Abstract**

This study addresses the challenge of thermal accumulation and low efficiency in conventional ground heat exchangers for building heating and cooling applications. A novel direct-expansion $CO_2$ borehole heat exchanger (BHE) backfilled with well water is proposed to enhance heat transfer and mitigate soil thermal imbalance. A dynamic thermal resistance-capacity model (TRCM) coupling $CO_2$ phase change with natural convection in well water is developed and validated against full-scale field experiments (135 m depth), with prediction errors below 5% under cooling conditions (MAPE 2.29%, RMSE 2.49%). Quantitative analysis reveals that natural convection in well water enhances overall heat transfer by 14.9% compared to soil-backfilled systems, despite intensifying thermal short-circuiting. Two practical enhancement strategies for building energy efficiency are proposed: (1) adding insulation to the rising pipe, which increases the heat transfer rate by up to 35.1%; and (2) implementing artificial well-water circulation, which achieves up to 50.5% enhancement, with an equivalent coefficient of performance (COP) reaching 52.5 under intermittent operation. The proposed system and the parametric analysis of these strategies offer effective solutions for improving the energy performance of ground-source heat pumps in buildings, contributing to reduced operational energy consumption and enhanced system reliability.

**Keywords:** direct-expansion BHE; TRCM; $CO_2$; natural convection; GCHP; enhanced heat transfer

## 1. Introduction

In response to the global energy crisis and climate change, developing efficient and environmentally friendly technologies for building heating and cooling is of paramount importance [1]. Ground source heat pump (GSHP) systems have garnered significant attention due to their ability to utilize the relatively constant temperature of the shallow subsurface for efficient heat exchange [2]. Among these, direct-expansion ground source heat pump (DX-GSHP) systems omit the intermediate heat transfer fluid, allowing the refrigerant to evaporate or condense directly within the underground heat exchanger. This configuration theoretically offers higher heat transfer efficiency and a simpler system

structure [3]. However, their widespread application still faces challenges. In particular, conventional soil-buried heat exchangers are constrained by the soil's relatively low thermal conductivity and specific heat capacity [4], which can lead to performance degradation and thermal (or cold) accumulation in the borehole region [5].

To overcome these limitations, employing a borehole heat exchanger (BHE)—i.e., placing the heat exchanger inside a water-filled borehole—has emerged as a promising alternative [6]. By leveraging water's high specific heat capacity and the potential for natural convection, this configuration is expected to significantly reduce thermal resistance and mitigate heat accumulation [7]. Several studies have explored innovative BHE designs. Yang et al. [8] constructed a coaxial BHE with spiral fins attached to the inner wall of the outer pipe, effectively balancing heat transfer enhancement and hydraulic resistance. Ren et al. [9] proposed a novel BHE and investigated its influencing factors. Their results demonstrated that the heat transfer efficiency could be enhanced by up to 48.8%. These studies confirm the potential of water-filled boreholes, yet they primarily focus on structural modifications of the heat exchanger itself, with limited attention to the coupled thermal-hydraulic behavior within the borehole.

Meanwhile, the use of $CO_2$ as a natural working fluid has attracted considerable interest due to its favorable flow and heat transfer properties, as well as its large temperature glide in transcritical cycles [10]. These characteristics are particularly advantageous when combined with the large temperature difference potential of BHEs, giving rise to the so-called direct-expansion $CO_2$ BHE. Li et al. [11] proposed a novel direct-expansion BHE using supercritical $CO_2$ and reported a 168.8% increase in effective unit heat flux compared to previous designs. Austin et al. [12] optimized gas cooler length using a finite volume model, achieving an 18% improvement in system COP. Eslami-Nejad et al. [13] conducted theoretical calculations for a 30 m deep direct-expansion $CO_2$ BHE, reporting a specific heat exchange rate of 71 W/m. Hakkaki-Fard et al. [14] compared this system with an air-source counterpart and found it to have the lowest energy consumption under most operating scenarios. Eslami-Nejad et al. [15] performed a one-year heating simulation and reported an average heat pump COP of 2.8. Ghazizade-Ahsaee et al. [16] investigated the effects of compressor speed, water temperature, and gas cooler length, observing that both COP and exergy efficiency first increase and then decrease with the temperature difference between the soil and the evaporator outlet. Gao and Gao [17] developed a full system model and identified an optimal ground loop pressure of 14.6 MPa for maximizing COP. Nguyen et al. [18] demonstrated that incorporating an internal heat exchanger could improve COP by 22%. Despite these valuable contributions, most existing studies have focused either on overall system performance or on the refrigerant-side behavior, often simplifying the heat transfer processes within the borehole. Specifically, the complex interplay between natural convection in the well water and the thermal short-circuit effect between the U-tube legs—two phenomena that exert opposing influences on overall heat transfer—remains insufficiently understood [19,20].

From a modeling perspective, research on convective heat transfer in BHEs has largely relied on experimental and numerical simulation approaches. Alobaid et al. [21] integrated convective heat transport into a three-dimensional numerical model to evaluate groundwater flow effects in deep sedimentary aquifers. Liu and Han [22] numerically analyzed convective heat transfer in rock fractures under varying experimental parameters. Yao et al. [23] systematically evaluated the thermal and hydrodynamic performance of a microchannel heat exchanger using combined experimental and numerical methods. Kumar and Sahu [24] numerically investigated convective heat transfer from a rotating elliptical cylinder in non-Newtonian fluids. Ghaderi Sane et al. [25] performed transient simulations to study the effects of superhydrophobic surfaces on flow-induced vibrations

https://doi.org/10.3390/en19092015

and heat transfer. While these studies provide valuable insights, they incur significant computational costs and are not well-suited for coupling with dynamic models that account for $CO_2$ flow and phase change inside tubes.

Conversely, thermal resistance models commonly used in direct-expansion $CO_2$ BHE studies often oversimplify the well water region—either by assuming pure conduction or by employing empirical correlations [26–28]. Alternatively, they may not fully account for the dynamic characteristics of $CO_2$ flow and phase change within the tubes, nor their coupling with natural convection in the well water [29,30]. As a result, a model that simultaneously integrates $CO_2$ flow and phase change, natural convection in well water, soil heat transfer, and the thermal short-circuit effect is still lacking. Such a model is essential for revealing the fundamental mechanisms of this technology, evaluating its performance limits, and guiding enhancement designs.

To address the aforementioned research gaps, this study aims to develop a thermal resistance-capacity model (TRCM) capable of accurately simulating the transient heat transfer process in a direct-expansion $CO_2$ BHE. The model is designed to integrate $CO_2$ flow and phase change, natural convection in well water, soil heat transfer, and the thermal short-circuit effect within a unified framework. The study will quantitatively analyze the dual role of natural convection-both enhancing overall heat transfer and intensifying thermal short-circuiting-and will propose two systematic performance enhancement strategies: the rising pipe insulation method and the artificial well-water circulation method. The influence of key design parameters on these strategies will be comprehensively explored.

The scientific novelty of this work lies in three key aspects. First, a novel TRCM is developed that innovatively incorporates equivalent thermal resistance terms to account for the effect of $CO_2$ flow on heat transfer while providing a detailed characterization of natural convection in the well water and thermal short-circuiting between the U-tube legs. Unlike existing models that often simplify the well water region as pure conduction or rely on empirical correlations, the proposed model captures the coupled dynamics between the refrigerant and the water-filled borehole environment. Second, a dimensionless thermal short-circuit coefficient is introduced as a quantitative metric to evaluate the severity of the short-circuit effect, enabling a more nuanced analysis of the trade-off between heat transfer enhancement and parasitic thermal losses. Third, two practical enhancement strategies-one passive and one active-are proposed and systematically evaluated, offering a comparative understanding of their effectiveness and optimization potential.

The contributions of this study to the field are twofold. From a methodological perspective, the validated TRCM provides a computationally efficient yet accurate tool for the design, simulation, and performance assessment of direct-expansion $CO_2$ BHE systems. From an engineering perspective, the quantitative analysis of natural convection's dual role, together with the proposed insulation and artificial circulation methods, offers actionable insights and design guidelines for improving the energy efficiency and operational reliability of ground-source heat pump systems in building applications.

## 2. Model Development and Experimental Validation

### *2.1. Model Development*

#### 2.1.1. Physical Model

Building upon the large-temperature-difference heat transfer characteristics of direct-expansion $CO_2$ BHEs, a novel direct-expansion $CO_2$ BHE is proposed, as illustrated in Figure 1.

https://doi.org/10.3390/en19092015

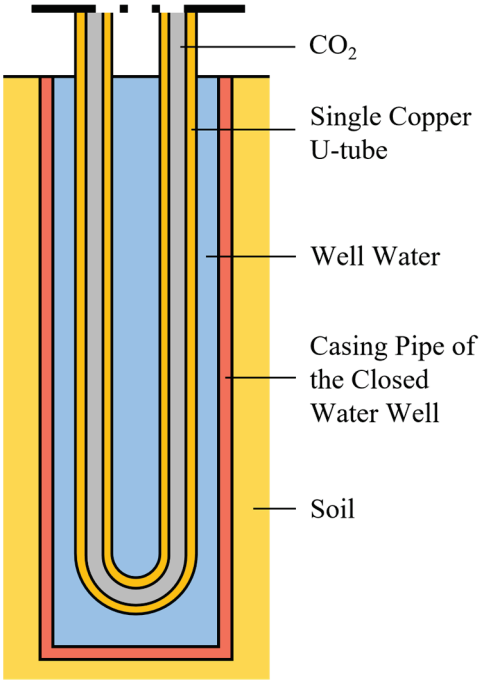



**Figure 1.** Configuration of direct expansion $CO_2$ BHE.

#### 2.1.2. TRCM

The following assumptions are made: (1) The thermophysical properties of the heat exchange pipe, well casing, and soil are assumed to be isotropic and constant. The properties of $CO_2$ and well water are dynamically retrieved based on their current temperature and pressure, corresponding to pure $CO_2$ and pure water, respectively. (2) As the experimental system includes two series-connected three-stage oil separators, the influence of lubricating oil on heat transfer and pressure drop is neglected in the model [31]. (3) The influence of the semicircular elbow at the $CO_2$ inlet on the local pressure variation is neglected, but its effect is accounted for through an equivalent flow thermal resistance term. (4) All boundaries of the model, except for the $CO_2$ inlet and outlet, are assumed to be adiabatic.

Figure 2 illustrates the nodal network of the TRCM for direct expansion $CO_2$ BHE. The model incorporates two types of thermal resistance. The first type is the conventional heat transfer resistance, encompassing conductive and convective resistances. The second type comprises equivalent thermal resistance terms designed to account for the influence of $CO_2$ flow on heat transfer. The model also includes two categories of temperature nodes. The first category consists of nodes with thermal mass, which are governed by ordinary differential equations. The second category comprises nodes without thermal mass, introduced to facilitate the representation of the heat transfer process; these include the inner and outer wall surfaces of the heat exchange pipe and the well casing. As these wall surfaces are assumed to have no thickness, they possess no thermal mass. Their temperatures, when required, are calculated from the temperatures of adjacent nodes with thermal mass using steady-state heat transfer formulas. Furthermore, when the vertical nodal spacing is non-uniform, or when dealing with nodes involving variable properties such as $CO_2$ and well water, the thermal resistances or capacities of control volumes at different layers are not equal. In practical calculations, each layer is treated separately and indexed by the layer number $i$.

https://doi.org/10.3390/en19092015

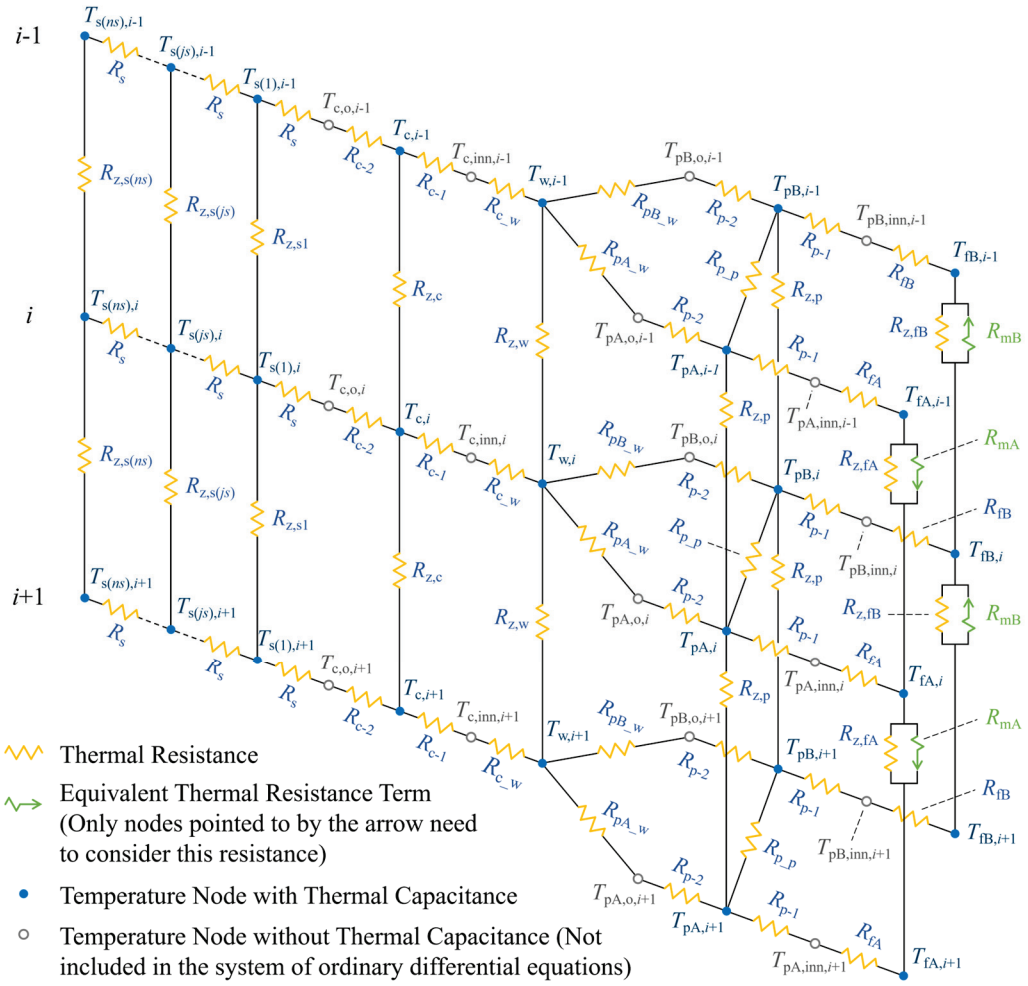



**Figure 2.** Thermal resistance and capacity network of direct expansion $CO_2$ BHE.

The transient heat transfer for a given computational node can be described by the following equation [32]:

$$C_x \frac{\mathrm{d}T_x}{\mathrm{d}\tau} = \sum_{k=1}^{n_{k,x}} \frac{T_k - T_x}{R_k} \quad \forall x = 1 \ldots n_x \tag{1}$$

The thermal resistance $R_f$ of $CO_2$ convection heat transfer is calculated according to the following formula:

$$R_f = \frac{1}{\mathrm{Nu}_f \lambda_f \pi} \tag{2}$$

According to the experimental research conducted by Gupta et al. [33], the calculation correlation of Nu number is as follows:

$$\mathrm{Nu}_f = 0.01 \mathrm{Re}_f^{0.89} \mathrm{Pr}_f^{-0.14} \left( \frac{\rho_{f,\mathrm{Wall}}}{\rho_f} \right)^{0.93} \left( \frac{\lambda_{f,\mathrm{Wall}}}{\lambda_f} \right)^{0.22} \left( \frac{\mu_{f,\mathrm{Wall}}}{\mu_f} \right)^{-1.13} \tag{3}$$

The inner part $R_{p\text{-}1}$ and the outer part $R_{p\text{-}2}$ of the heat resistance of the heat exchange tube are calculated according to the following formula:

$$R_{p\text{-}1} = \frac{\ln\left(d_{p,\mathrm{mid}} / d_{p,\mathrm{inn}}\right)}{2\pi\lambda_p} \tag{4}$$

https://doi.org/10.3390/en19092015

$$R_{\text{p-2}} = \frac{\ln\left(d_{\text{p,o}}/d_{\text{p,mid}}\right)}{2\pi\lambda_{\text{p}}} \tag{5}$$

where $d_{\text{p,mid}}$ is equivalent diameters corresponding to the central point of heat capacity of the heat exchange tube, and is calculated by the following formula:

$$d_{\text{p,mid}} = \sqrt{\frac{d_{\text{p,inn}}^2 + d_{\text{p,o}}^2}{2}} \tag{6}$$

If the insulation layer is added at the top of the riser, ignoring the influence of the heat capacity of the insulation layer on heat transfer is equivalent to adding a thermal resistance $R_{\text{ins}}$ outside the riser:

$$R_{\text{ins}} = \frac{\ln\left(\left(d_{\text{p,o}} + 2\delta_{\text{ins}}\right)/d_{\text{p,o}}\right)}{2\pi\lambda_{\text{ins}}} \tag{7}$$

For the natural convection thermal resistance in well water, Spitler et al. [34] gave the thermal resistance calculation formula for a single U tube:

$$R_{\text{p_w}} = \frac{1}{2\pi d_{\text{p,o}} h_{\text{p_w}}} \tag{8}$$

$$R_{\text{c_w}} = \frac{1}{\pi d_{\text{c,inn}} h_{\text{c_w}}} \tag{9}$$

$$h_{\text{p/c_w}} = \frac{\text{Nu}_{\text{p/c_w}}\lambda_{\text{w}}}{D_{\text{w}}} \tag{10}$$

The Nu number of natural convection adopts the subsection Nu number formula proposed by Yang [35]:

$$\text{Nu}_{\text{p/c_w}} = \begin{cases} 0.59\text{Ra}_{\text{p/c_w}}^{1/4} & \text{Gr}_{\text{p/c_w}} \le 3 \times 10^9 \\ 0.0292\text{Ra}_{\text{p/c_w}}^{0.39} & 3 \times 10^9 < \text{Gr}_{\text{p/c_w}} \le 2 \times 10^{10} \\ 0.11\text{Ra}_{\text{p/c_w}}^{1/3} & \text{Gr}_{\text{p/c_w}} > 2 \times 10^{10} \end{cases} \tag{11}$$

Among them,

$$\text{Ra}_{\text{p/c_w}} = \text{Gr}_{\text{p/c_w}}\text{Pr}_{\text{w}} \tag{12}$$

$$\text{Gr}_{\text{p/c_w}} = \frac{g\beta_{\text{w}}\Delta T_{\text{p/c_w}} D_{\text{w}}^3}{v_{\text{w}}^2} \tag{13}$$

It should be noted that when calculating the natural convection thermal resistance $R_{\text{pB-w}}$ between the riser and the well water under the condition of adding insulation layer, the heat exchange tube temperature $T_{\text{pB}}$ in Gr number needs to be replaced by insulation layer temperature $T_{\text{ins}}$, and $T_{\text{ins}}$ is calculated by the steady-state heat transfer formula:

$$T_{\text{ins}} = \frac{\left(R_{\text{ins}} + 2R_{\text{p_2}}\right)T_{\text{w}} - \left(R_{\text{ins}} + 2R_{\text{pB-w}}\right)T_{\text{pB}}}{2R_{\text{p_2}} - 2R_{\text{pB-w}}} \tag{14}$$

In order to quantitatively analyze the influence mechanism of heat transfer enhancement or weakening in different scenarios, the thermal resistance $R_{\text{p_c}}$ from the outer wall of the heat exchange tube (from the outer wall of the insulation layer in the case of adding insulation layer) to the inner wall of the well tube can be defined by the following formula:

$$R_{\text{p_c}} = \frac{R_{\text{pA_w}} + R_{\text{pB_w}}}{2} + R_{\text{c_w}} \tag{15}$$

https://doi.org/10.3390/en19092015

The thermal resistance $R_{p_p}$ between heat exchange tubes is calculated by the formula proposed by Hellström [36]:

$$R_{p_p} = \frac{1}{\pi\lambda_w}\left[\ln\left(\frac{2\theta_1\left(\theta_2^2+1\right)^{\theta_4}}{\theta_2\left(\theta_2^2-1\right)^{\theta_4}}\right) - \frac{\theta_3^2\left(1+\left(4\theta_4\theta_2^2/\left(\theta_2^4-1\right)\right)\right)^2}{1-\theta_3^2+8\theta_4\theta_2^2\theta_3^2\left(\theta_2^4+1\right)/\left(\theta_2^4-1\right)^2}\right] \tag{16}$$

$$\theta_1 = \frac{d_{c,inn}}{d_{p,o}}, \quad \theta_2 = \frac{d_{c,inn}}{S}, \quad \theta_3 = \frac{\theta_2}{2\theta_1}, \quad \theta_4 = \frac{\lambda_w-\lambda_s}{\lambda_w+\lambda_s} \tag{17}$$

The inner part $R_{c\text{-}1}$ and the outer part $R_{c\text{-}2}$ of well pipe thermal resistance are calculated according to the following formula:

$$R_{c\text{-}1} = \frac{\ln(d_{c,mid}/d_{c,inn})}{2\pi\lambda_c} \tag{18}$$

$$R_{c\text{-}2} = \frac{\ln(d_{c,o}/d_{c,mid})}{2\pi\lambda_c} \tag{19}$$

$$d_{c,mid} = \sqrt{\frac{d_{c,inn}^2+d_{c,o}^2}{2}} \tag{20}$$

In order to ensure the formal unity of the equations of the thermal resistance and heat capacity model, the influence of the flow in the $CO_2$ tube on the heat transfer is also expressed in the form of thermal resistance:

$$R_m = \frac{\Delta z}{m\overline{c_f}} \tag{21}$$

The flow equivalent thermal resistance between the lowermost $CO_2$ temperature node of the downcomer and the riser is calculated by the following formula:

$$R_{mA_B} = \frac{\delta_{(ni)}+\pi S/2}{m\left(c_{f,A(ni)}+c_{f,B(ni)}\right)/2} \tag{22}$$

In order to characterize the influence of artificial well water circulation on heat transfer, the equivalent flow thermal resistance $R_{m,w}$ in the vertical direction is added to the heat transfer model of well water nodes, which is calculated by the following formula:

$$R_{m,w} = \frac{\Delta z}{V_{INJ}\rho_w\overline{c_w}} \tag{23}$$

Other vertical thermal conductivities are calculated by the following formula:

$$R_z = \frac{(\Delta z)^2}{\overline{\lambda}A} \tag{24}$$

The pressure change in each $CO_2$ node can be calculated by the following formula [37]:

$$\Delta P_f = \begin{cases} \Delta P_{f,g}+\Delta P_{f,a}+\Delta P_{f,F} & \text{downcomer} \\ -\Delta P_{f,g}+\Delta P_{f,a}+\Delta P_{f,F} & \text{riser} \end{cases} \tag{25}$$

$$\Delta P_{f,g} = g\overline{\rho_f}\Delta z \tag{26}$$

$$\Delta P_{f,a} = \left(\frac{m}{A_f}\right)^2\left(\frac{1}{\rho_{f,in}}-\frac{1}{\rho_{f,out}}\right) \tag{27}$$

https://doi.org/10.3390/en19092015

$$\Delta P_{f,F} = -f\frac{m^2\Delta z}{2d_f\rho_f A_f^2} \tag{28}$$

$$\begin{cases} f = \frac{64}{\mathrm{Re_f}} & \mathrm{Re_f} < 2300 \\ f = 0.06539\exp\left(-\left(\frac{\mathrm{Re_f}-3516}{1248}\right)^2\right) & 2300 \le \mathrm{Re_f} \le 3400 \\ \frac{1}{\sqrt{f}} = -2.34\lg\left(\frac{\varepsilon}{1.72d_{p,inn}} - \frac{9.26}{\mathrm{Re_f}}\lg\left(\left(\frac{\varepsilon}{29.36d_{p,inn}}\right)^{0.95} + \left(\frac{18.35}{\mathrm{Re_f}}\right)^{1.108}\right)\right) & 3400 < \mathrm{Re_f} < 2\times10^6 \end{cases} \tag{29}$$

Moreover, in order to characterize the significance of thermal short circuit, the dimensionless coefficient $\eta_{SC}$ is defined:

$$\eta_{SC} = \frac{H_{out} - H_{f,min}}{H_{in} - H_{f,min}} \tag{30}$$

2.1.3. Simulation Parameter Setting

The cooling condition is simulated numerically. The inlet pressure of $CO_2$ is 10 MPa, the inlet temperature is 100 °C, and the mass flow rate is 50 g/s. The initial ambient temperature is set to 14.5 °C, the simulation duration is 120 h, and the time step is automatically adjusted according to the convergence. Moreover, to further analyze the dynamic influence of related parameters of insulation layer method on strengthening effect, the parameter influence calculation of insulation layer thickness, thermal conductivity and length is carried out. The SG and control groups for these parameters are listed in Table 1:

**Table 1.** SG and control group of the parameters of insulation method.

| Parameter | Unit | SG | Control Group |
|---|---|---|---|
| Insulation layer length | m | 30 | 10, 20, 40, 50 |
| Insulation layer thickness | mm | 2 | 0.5, 1, 4 |
| Thermal conductivity of insulation layer | W/(m·K) | 0.025 | 0.13, 0.42 |

All other parameters remain identical to those of the SG mentioned previously, and the simulation runtime is likewise 120 h.

*2.2. Field Experiment*

2.2.1. Experimental System

The schematic of the experimental system is shown in Figure 3. A 193 m deep water well was drilled. To avoid any impact on the subsurface environment, the well is fully enclosed, meaning that there is no exchange between the well water and the surrounding groundwater. The heat exchanger is a single U-tube with a total depth of 135 m, and fixing brackets are installed at approximately 3 m intervals along its length.

The geometric parameters of the BHE are listed in Table 2.

**Table 2.** Geometrical parameters of BHE.

| Name | Value | Name | Value | Name | Value |
|---|---|---|---|---|---|
| $d_{p,inn}$ | 8 mm | $d_{p,o}$ | 12 mm | $d_{c,inn}$ | 263 mm |
| $d_{c,o}$ | 273 mm | $L_{cen}$ | 160 mm | $L$ | 135 m |

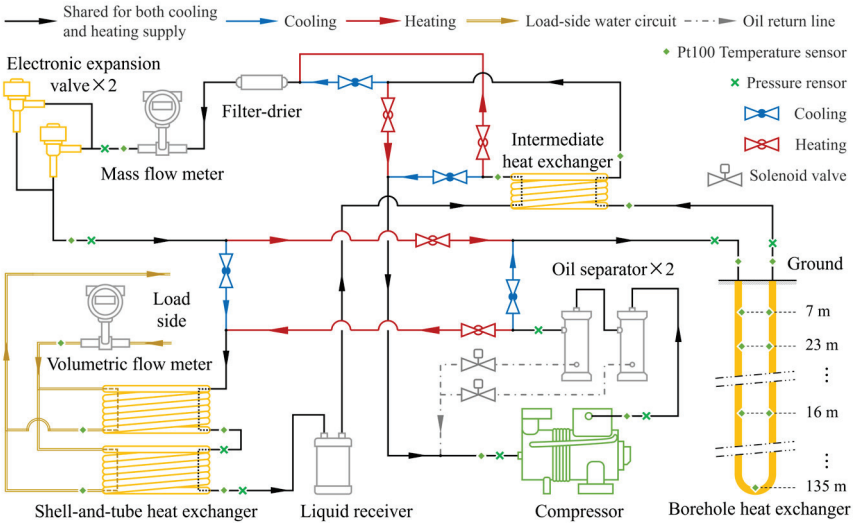



**Figure 3.** Schematic diagram of direct expansion $CO_2$ heat pump system.

The physical property parameters relevant to the experiment are presented in Table 3.

**Table 3.** Physical parameters of experiment [38,39].

| Zone | $\rho$ kg/m$^3$ | $c$ J/(kg·K) | $\lambda$ W/(m·K) |
|---|---|---|---|
| U-tube | 8930 | 385 | 398.0 |
| Well pipe | 7872 | 481 | 64.9 |
| Soil | 1220 | 2070 | 1.5 |

The measurement error of the platinum resistance temperature sensors for the above-ground $CO_2$ pipeline wall temperature is $\pm 0.1$ °C, and the acquisition error of the paperless recorder is $\pm 0.2\%$. The average experimental temperature difference between the inlet and outlet is approximately 60.7 °C. Based on this, the measurement error $Err_{T,HP}$ for the above-ground $CO_2$ pipeline wall temperature is calculated as

$$Err_{T,HP} = \pm\sqrt{\left(\frac{\pm 0.1}{60.7}\right)^2 + (\pm 0.002)^2} \approx \pm 0.26\% \quad (31)$$

The measurement error of the pressure transmitter is $\pm 0.5\%$, and the measurement error of the flow meter is $\pm 1\%$. Therefore, the total measurement error $Err_Q$ for the heat transfer rate of the BHE is calculated as

$$Err_Q = \pm\sqrt{(\pm 0.0026)^2 + (\pm 0.005)^2 + (\pm 0.01)^2} = \pm 1.15\% \quad (32)$$

2.2.2. Heat Transfer Model Validation

The geometric and thermophysical parameters used in the model are identical to those of the experimental setup. For model validation, the initial temperature distribution of well water and soil was set to the measured steady-state values prior to the start of each experiment. This ensures that the simulation starts from the same initial conditions as the experiment. Therefore, at $\tau = 0$, the simulated and experimental values coincide by definition, which is reflected in Figure 4.

https://doi.org/10.3390/en19092015

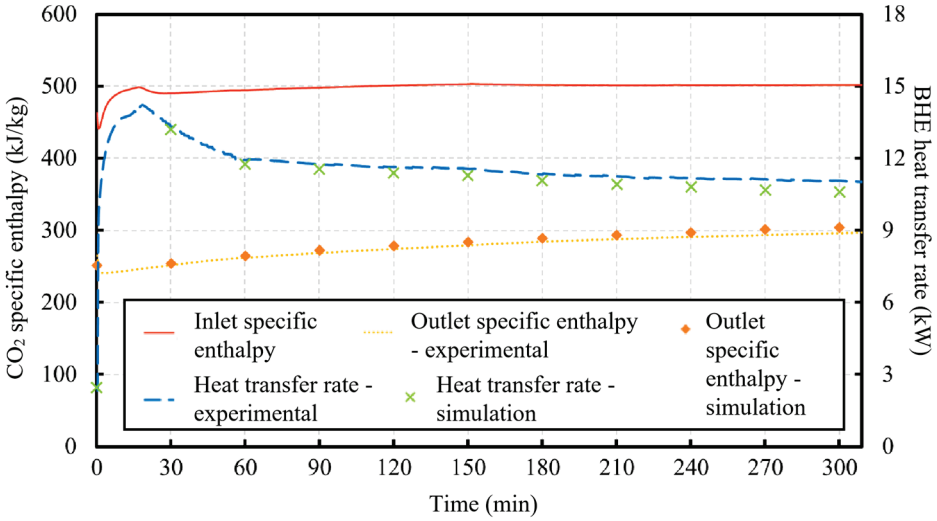



**Figure 4.** Model validation result of cooling condition: heat transfer rate.

Figure 4 shows a comparison between the simulated and experimental results for the $CO_2$ outlet specific enthalpy and the heat transfer rate of the BHE under cooling conditions. The results indicate a high degree of agreement between the simulations and experiments for both specific enthalpy and heat transfer rate. The calculated mean absolute percentage error (MAPE) and root mean square error (RMSE) for the heat exchanger's heat transfer rate are 2.29% and 2.49%, respectively.

## 3. Analysis of Natural Convection Impact on Heat Transfer

The backfilling of the borehole with well water enhances convective heat transfer. Natural convection, on one hand, reduces the overall thermal resistance between the $CO_2$ and the surrounding soil. On the other hand, it can also intensify the thermal short-circuiting between the legs of the heat exchange U-tube. To further quantify these two opposing effects, three scenarios were designed for comparison with the standard group (SG) condition. The SG condition corresponds to the experimental case described earlier, where the well is backfilled with water.

Case 1: Natural convection within the well water is neglected; only conductive heat transfer is considered in the water.

Case 2: The well water is replaced with the same soil as in the SG condition. This configuration, while retaining the same borehole geometry and U-tube arrangement, represents a soil-backfilled scenario within the same model framework, serving as a reference for comparison rather than a direct representation of all conventional DX-GSHP designs.

Case 3: An insulation layer is added to the upward-flowing leg (rising pipe) of the U-tube. Based on prior calculation results indicating that the thermal short-circuit effect is more pronounced in the upper section of the exchanger, this insulation layer starts from the top of the rising pipe. It has a length of 10 m and a thickness of 2 mm, as illustrated in Figure 5.

A 120 h simulation was conducted for the three scenarios, as shown in Figure 6. The results indicate that Case 1 exhibits the poorest heat transfer performance, followed by Case 2. In contrast, Case 3 shows a significant improvement in heat transfer rate compared to the SG. Figure 7 provides a more intuitive visualization, demonstrating that the thermal short-circuit effect at the top of the rising pipe is effectively mitigated in the insulation scenario.

https://doi.org/10.3390/en19092015

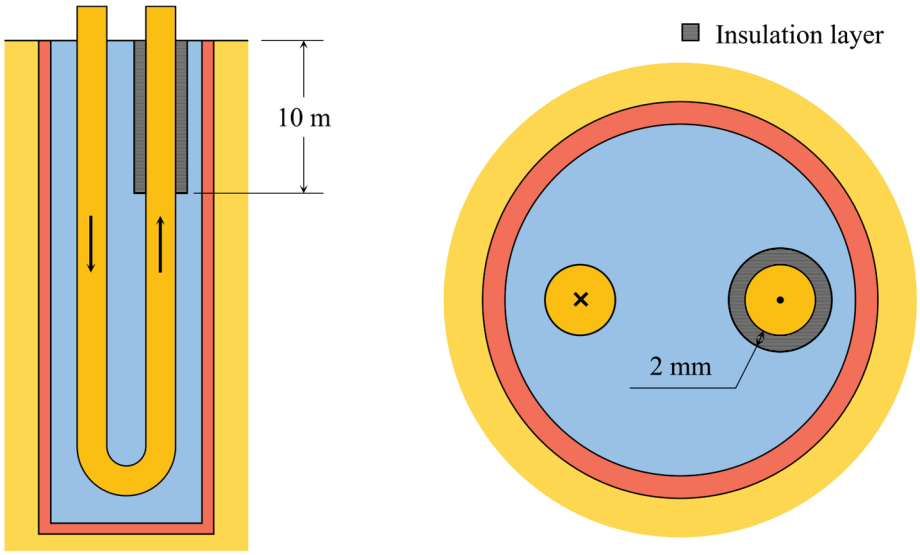



**Figure 5.** Layout of adding an insulation to the upper upward pipe.

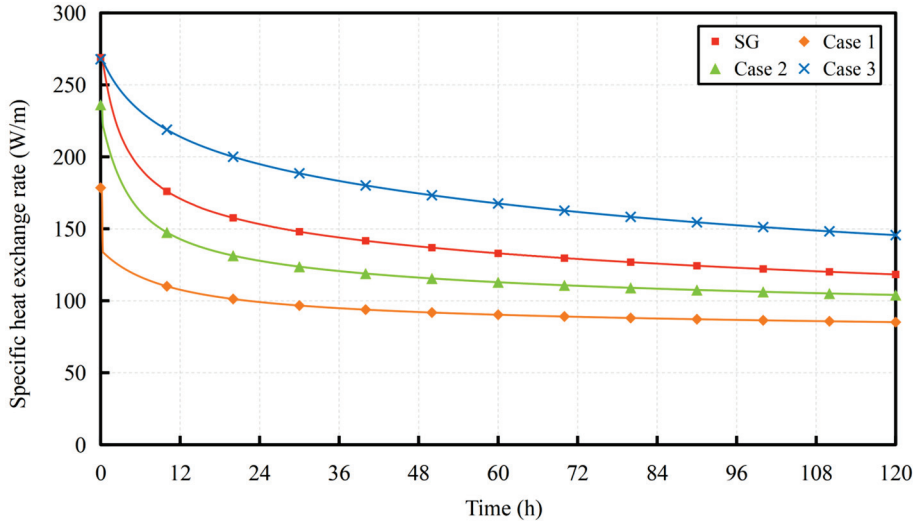



**Figure 6.** Change curves of unit heat flux under different scenarios.

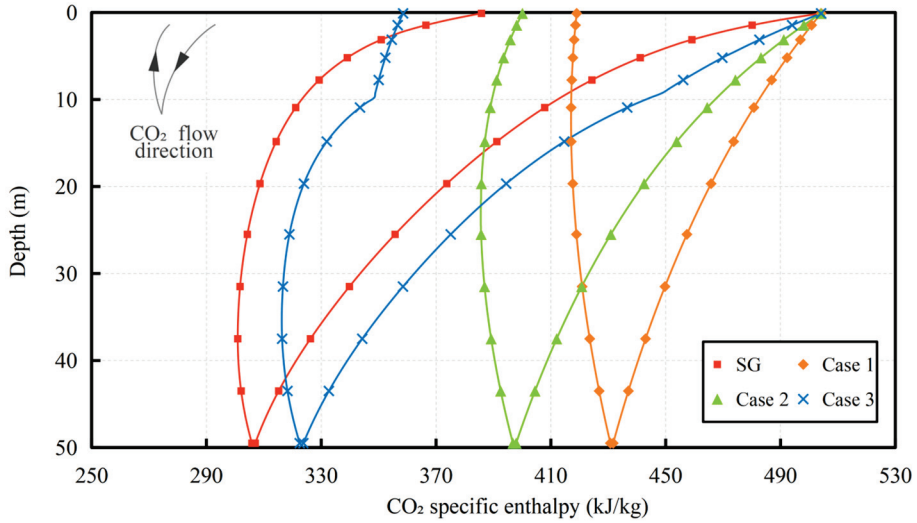



**Figure 7.** $CO_2$ enthalpy under different scenarios at the end of operation.

https://doi.org/10.3390/en19092015

Figure 8 compares the average unit-length heat flux and the thermal resistance $R_{p_c}$ at the end of the operating period for the different scenarios. Calculations show that compared to the SG, $R_{p_c}$ increased by a factor of 13.2 for Case 1 and 5.6 for Case 2, respectively. Conversely, $R_{p_c}$ decreased by 16.2% for the scenario with the insulation layer. Correspondingly, the average unit-length heat flux decreased by 33.3% for Case 1 and 14.9% for Case 2, respectively, compared to the SG. In contrast, the average SHER increased by 24.3% for Case 3.

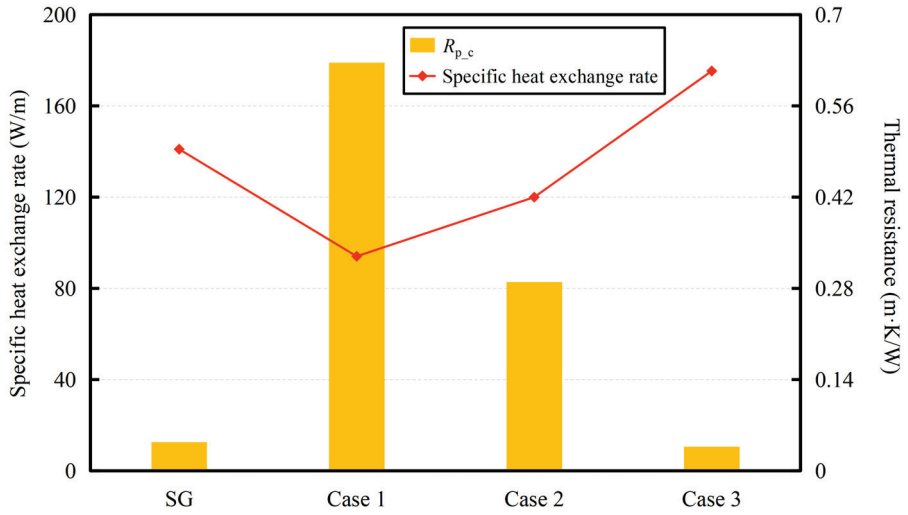



**Figure 8.** Average unit heat flux and thermal resistance from U-pipe to well casing $R_{p_c}$ at the end of operation under each scenario.

While $R_{p_c}$ reflects the overall heat transfer capability of the exchanger, further analysis can be performed using the defined dimensionless thermal short-circuit coefficient $\eta_{SC}$, as shown in Figure 9. The results show that $\eta_{SC}$ is significantly lower for both Case 1 and Case 2 compared to the SG. This indicates that natural convection indeed intensifies the thermal short-circuit effect. In contrast, Case 3 manages to alleviate the thermal short-circuit effect while maintaining a low $R_{p_c}$. This achieves a better balance between reducing the overall thermal resistance and mitigating the short-circuit effect, leading to a more significant improvement in the heat transfer rate.

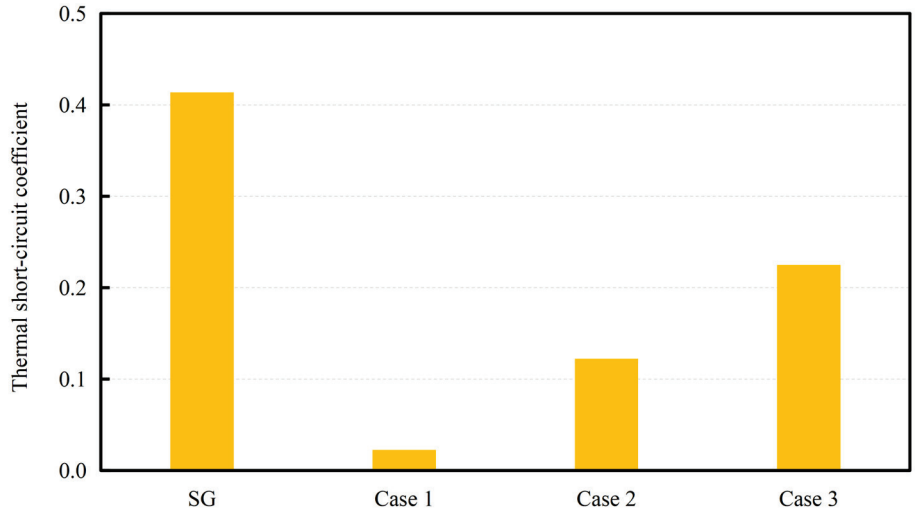



**Figure 9.** Thermal short-circuit coefficient $\eta_{SC}$ at the end of operation under each scenario.

https://doi.org/10.3390/en19092015

In summary, under cooling conditions, natural convection within the well water enhances the overall heat transfer capacity of the direct-expansion $CO_2$ BHE, while simultaneously intensifying the thermal short-circuit effect between the legs of the U-tube. However, its positive role in enhancing heat transfer is more dominant. Furthermore, adding an insulation layer to the outer wall of the upper section of the rising pipe can effectively weaken the thermal short-circuit effect while maintaining a relatively low total thermal resistance, leading to a further increase in the heat transfer rate.

## 4. Enhanced Heat Transfer Design

### *4.1. Heat Transfer Enhancement Using the Insulation Layer Method*

#### 4.1.1. Influence of Insulation Length

As shown in Figure 10, adding insulation layers of various lengths can all significantly increase the heat transfer rate. Notably, when the insulation length is 30 m or greater, the heat transfer rate essentially ceases to increase with further length. The calculated average heat transfer rate improvements over the entire operating period for the 10–50 m insulation groups, compared to the group without insulation, are 24.3%, 31.9%, 34.3%, 34.1%, and 32.2%, respectively (no change needed, but ensure consistent decimal format). Figure 11 illustrates the variation in $CO_2$ specific enthalpy along the flow path for each group. For the 10 m and 20 m groups, it is evident that the enthalpy rise caused by thermal short-circuiting is effectively suppressed once the $CO_2$ enters the insulated section of the pipe. The $\eta_{SC}$ values for the 10–50 m groups are 0.22, 0.14, 0.11, 0.12, and 0.13, respectively, showing a significant reduction compared to the value of 0.41 for the group without insulation.

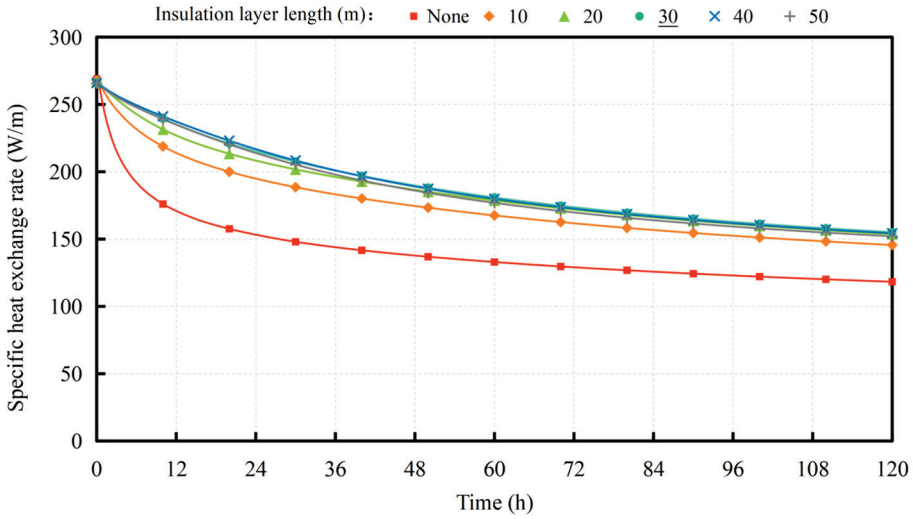



**Figure 10.** Change curves of unit heat flux under different insulation lengths. The standard group is underlined for comparison with other groups.

It is noteworthy that the average heat transfer rates for the 40 m and 50 m groups are actually lower than that of the 30 m group. This indicates that extending the insulation beyond approximately 40 m has a detrimental effect on heat transfer. This phenomenon can be explained by the temperature distribution within the well for the case without insulation, as shown in Figure 12.

https://doi.org/10.3390/en19092015

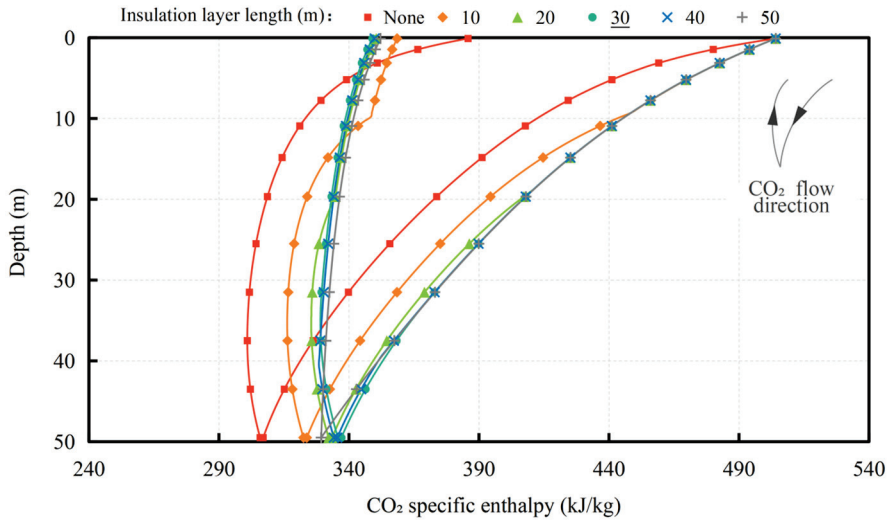



**Figure 11.** $CO_2$ enthalpy under different insulation lengths at the end of operation. The standard group is underlined for comparison with other groups.

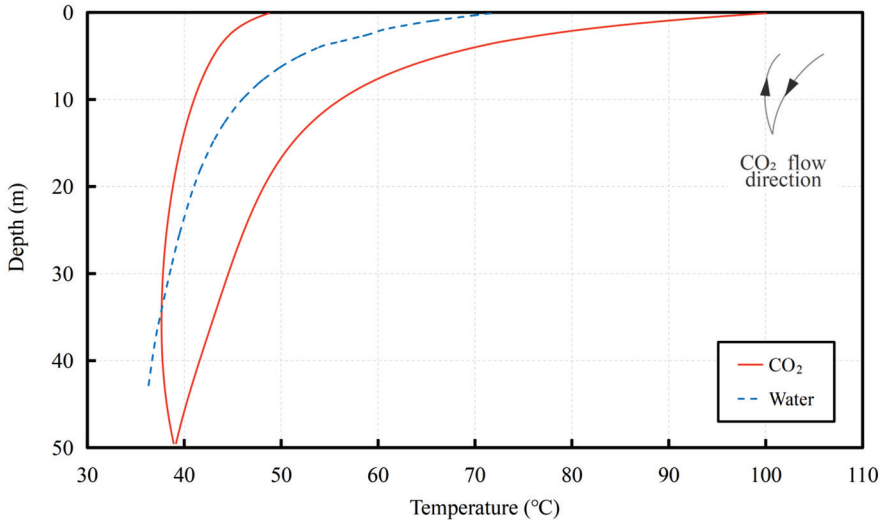



**Figure 12.** Distribution of $CO_2$ and well water temperature without insulation at the end of operation.

It can be observed that, at depths greater than approximately 35 m, the temperature of the $CO_2$ within the rising pipe is lower than that of the surrounding well water. This means that the $CO_2$ in the rising pipe between 35 m and 50 m depth is still capable of releasing heat. Therefore, adding insulation to this section would, conversely, reduce the overall heat transfer. For the specific design conditions considered here, balancing heat transfer performance and cost, a recommended insulation length is suggested to be in the range of 20–30 m.

#### 4.1.2. Influence of Insulation Thickness

As shown in Figure 13, even adding a very thin insulation layer of 0.2 mm provides a significant effect in mitigating thermal short-circuiting. This is because its thermal resistance is approximately 0.2 m·K/W, which is about 1287 times greater than that of the heat exchange pipe itself. The calculated average heat transfer rate improvements over the entire operating period for insulation thicknesses of 0.2–4 mm, compared to the case without insulation, are 23.3%, 29.8%, 32.6%, 34.3%, and 35.1%, respectively. It is evident that once the insulation thickness exceeds 1 mm, the rate of improvement in heat transfer with increasing thickness becomes very small. Figure 14 presents the variation in $CO_2$-specific

https://doi.org/10.3390/en19092015

enthalpy along the flow path at the end of the operating period for each group. The $\eta_{SC}$ values for the 0.2–4 mm groups are 0.22, 0.16, 0.13, 0.11, and 0.10, respectively.

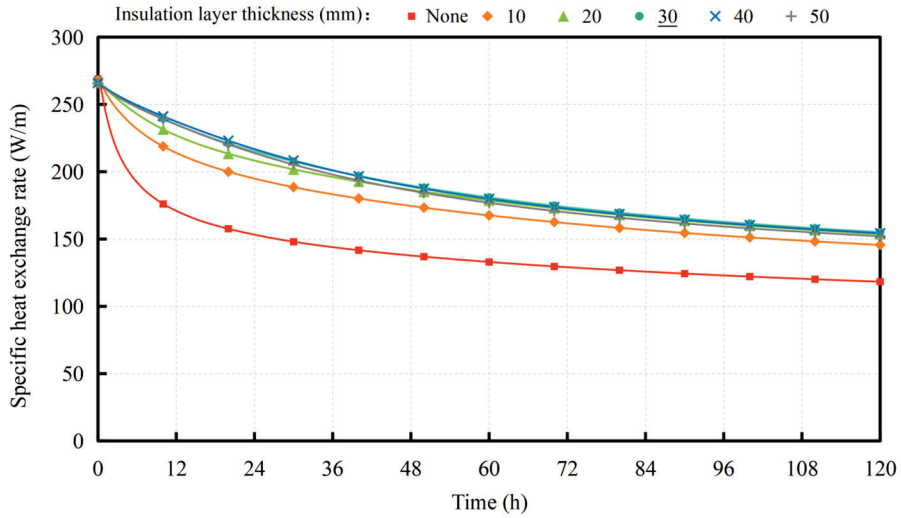



**Figure 13.** Change curves of unit heat flux under different insulation thicknesses. The standard group is underlined for comparison with other groups.

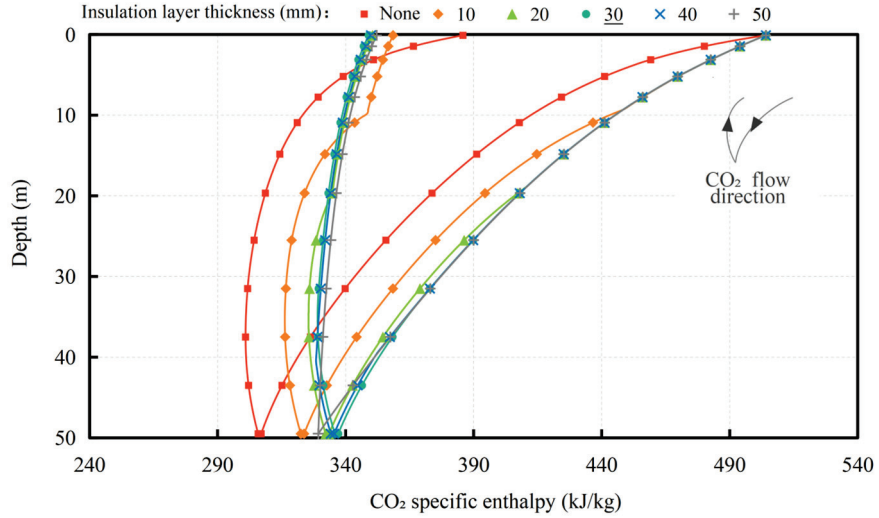



**Figure 14.** $CO_2$ enthalpy under different insulation thicknesses at the end of operation. The standard group is underlined for comparison with other groups.

#### 4.1.3. Influence of Insulation Thermal Conductivity

In the parameter sets for insulation thermal conductivity, values of 0.025 W/(m·K), 0.13 W/(m·K), and 0.42 W/(m·K) correspond to typical values for polyurethane, polyvinyl chloride (PVC), and high-density polyethylene, respectively. As shown in Figure 15, it can be observed that even without using conventional high-performance insulation materials, simply adding a layer of common plastic pipe around the heat exchange tube can significantly enhance the heat exchanger's performance. Calculations show that, compared to the case without insulation, the groups with thermal conductivities of 0.025 W/(m·K), 0.13 W/(m·K), and 0.42 W/(m·K) achieve average heat transfer rate improvements of 34.3%, 27.5%, and 17.1%, respectively.

https://doi.org/10.3390/en19092015

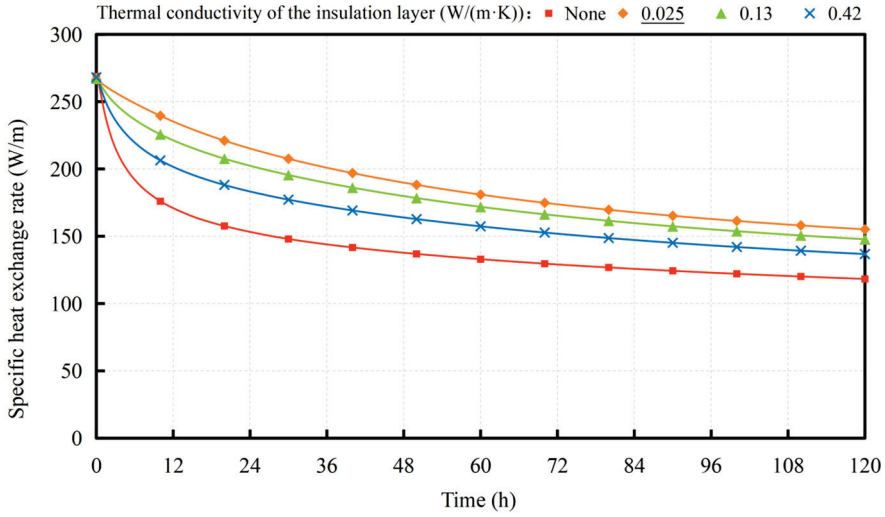



**Figure 15.** Change curves of unit heat flux under different insulation thermal conductivities. The standard group is underlined for comparison with other groups.

Figure 16 shows the variation in $CO_2$ specific enthalpy along the flow path for each group at the end of the operating period. The corresponding $\eta_{SC}$ values for the groups with thermal conductivities of 0.025 W/(m·K), 0.13 W/(m·*p*K), and 0.42 W/(m·K) are 0.11, 0.18, and 0.28, respectively.

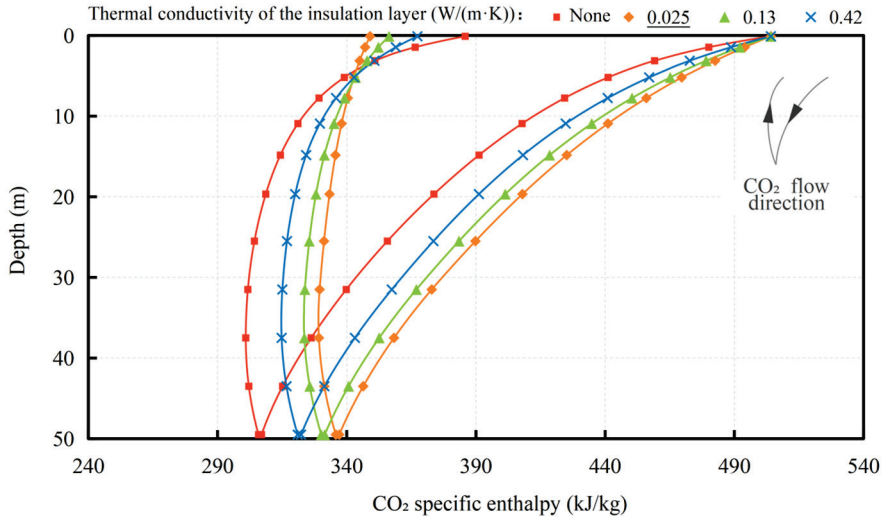



**Figure 16.** $CO_2$ enthalpy under different insulation thermal conductivities at the end of operation. The standard group is underlined for comparison with other groups.

### *4.2. Heat Transfer Enhancement Using the Artificial Well-Water Circulation Method*

Although the insulation layer method can provide significant enhancements for cooling operation, it may have a detrimental effect on heating performance. This is because thermal short-circuiting is not a concern during heating, and the insulation layer would add unnecessary thermal resistance. One solution is to branch off an uninsulated pipe of the same size from the rising pipe at the bottom of the insulated section, dedicated to heating operation. Another approach is the artificial well-water circulation method. As illustrated in Figure 17, a small circulation pump is used to inject high-temperature water from the top layer of the well into the bottom layer through an insulated pipe. This promotes a more uniform vertical temperature distribution in the well water, which also helps to mitigate thermal short-circuiting and increase the heat exchange rate.

https://doi.org/10.3390/en19092015

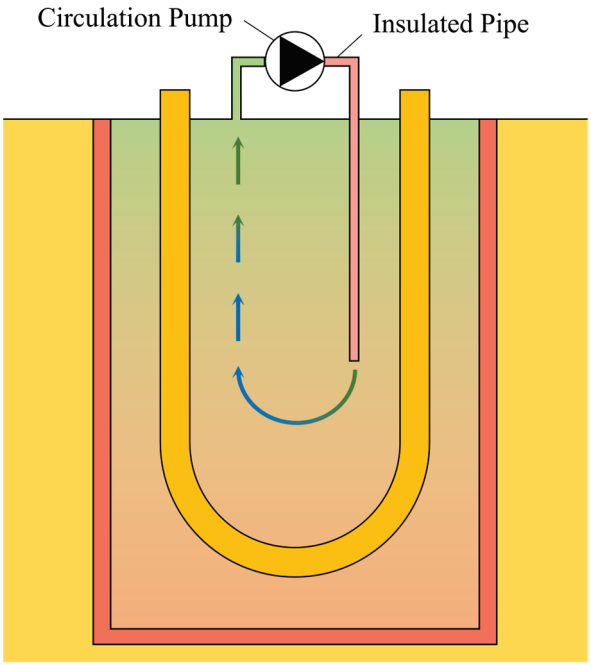



**Figure 17.** Layout of artificial well-water circulation method.

Compared to the passive optimization of the insulation method, this approach belongs to active optimization, thus offering greater flexibility for control and optimization. To investigate the dynamic influence of different design and operational parameters on the enhancement effect of the artificial circulation method, a parametric study was conducted focusing on injection depth, injection flow rate, and injection interval. The standard values and control groups for these parameters are listed in Table 4. For the injection interval, the control groups include intervals of 5, 10, 20, 40, and 80 min, which are used for the parametric analysis of heat transfer performance. In addition, to evaluate the equivalent COP over a wider range, longer intervals (160, 320, and 640 min) are also considered in Section 4.2.4.

**Table 4.** SC and control group of the parameters of artificial well-water circulation method.

| Parameter | Unit | SG | Control Group |
|---|---|---|---|
| Injection depth | m | 20 | 5, 10, 35, 50 |
| Injection flow rate | $m^3/h$ | 0.5 | 0.05, 0.1, 0.2, 1 |
| Injection interval (parametric study) | min | 0 | 5, 10, 20, 40, 80 |

Here, an injection interval of 0 min represents continuous injection throughout the entire operation period. All other parameters are identical to those of the SG in the previous section, and the simulation runtime is likewise 120 h.

It is noteworthy that, beyond balancing water temperature, the injection flow itself may influence heat transfer by inducing forced convection, potentially resulting in mixed convection. According to a general criterion [40], the effect of natural convection cannot be neglected when $Gr/Re^2 \geq 0.1$, and heat transfer can be considered as purely natural convection when $Gr/Re^2 \geq 10$. For this case study, using the maximum injection flow rate group for calculation, the minimum Gr across all layers is approximately $1.57 \times 10^8$, yielding $Gr/Re^2 \approx 86.6$. This global criterion suggests that natural convection remains dominant over the majority of the well water domain.

However, it is important to acknowledge that the injection process generates a localized momentum disturbance, particularly near the discharge point, where the flow

https://doi.org/10.3390/en19092015

regime may deviate from the global average. In the immediate vicinity of the injection outlet, forced convection effects are more pronounced, and a mixed convection regime may exist locally. Nevertheless, the spatial extent of this region is limited relative to the overall height of the well (135 m), and the thermal resistance associated with this localized region is small compared to the total thermal resistance of the well water column. Therefore, treating the entire well water domain as pure natural convection remains a reasonable approximation for the purpose of this study. This approach avoids the high computational cost of CFD simulations while providing sufficiently accurate results for engineering design and parametric analysis, as validated by the good agreement between model predictions and experimental measurements (Section 2.2.2).

#### 4.2.1. Influence of Injection Depth

As shown in Figure 18, it can be seen that the artificial well-water circulation method also provides significant enhancement to heat transfer, and the heat transfer rate increases with greater injection depth. Calculations show that for the average heat transfer rate over the entire operating period, the 5–50 m injection depth groups achieved improvements of 12.0%, 21.7%, 34.4%, 48.0%, and 50.5%, respectively, compared to the group without artificial circulation. When the injection depth exceeds 35 m, the rate of improvement in heat transfer essentially stops increasing with further depth. Therefore, for this design scenario and considering only the heat transfer enhancement effect, 35 m is recommended as the preferred injection depth based on parametric analysis.

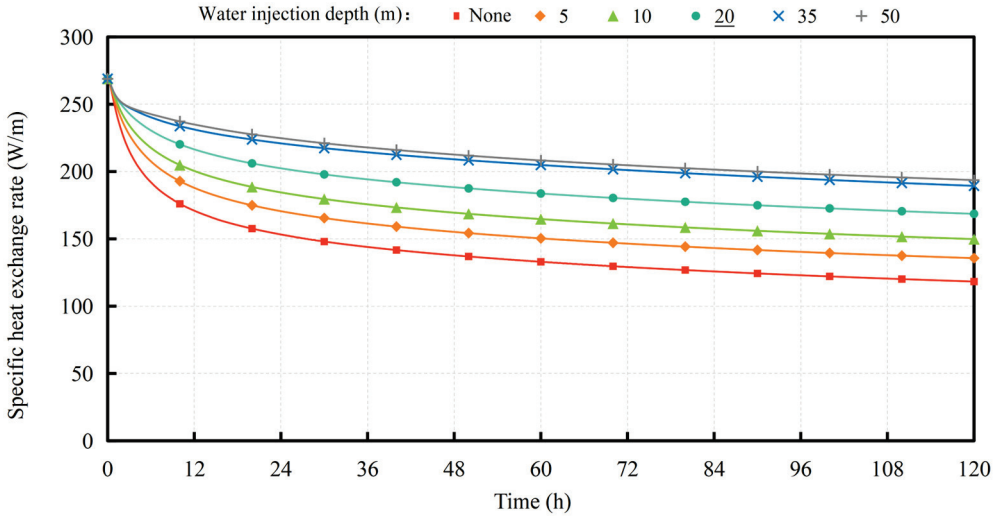



**Figure 18.** Change curves of unit heat flux under different water injection depths. The standard group is underlined for comparison with other groups.

As shown in Figure 19, the influence of artificial water injection on well water temperature can be clearly observed. At the injection outlet, due to the influx of warmer water from the upper layers, the local temperature increases significantly. Under the effect of artificial circulation, the overall temperature of the well water decreases with increasing injection depth. Even with an injection depth of only 5 m, the temperature at the very top layer of water can be significantly reduced from 71.6 °C (without circulation) to 57.6 °C.

Figure 20 shows the variation in $CO_2$ specific enthalpy along the flow path for each group at the end of the operating period. The $\eta_{SC}$ values for the 5–50 m injection depth groups are 0.34, 0.27, 0.19, 0.13, and 0.08, respectively. These results indicate that the severity of the thermal short-circuit effect decreases significantly with increasing injection depth. When water is injected from the very bottom of the heat exchanger, the thermal short-circuit effect is almost eliminated.

https://doi.org/10.3390/en19092015

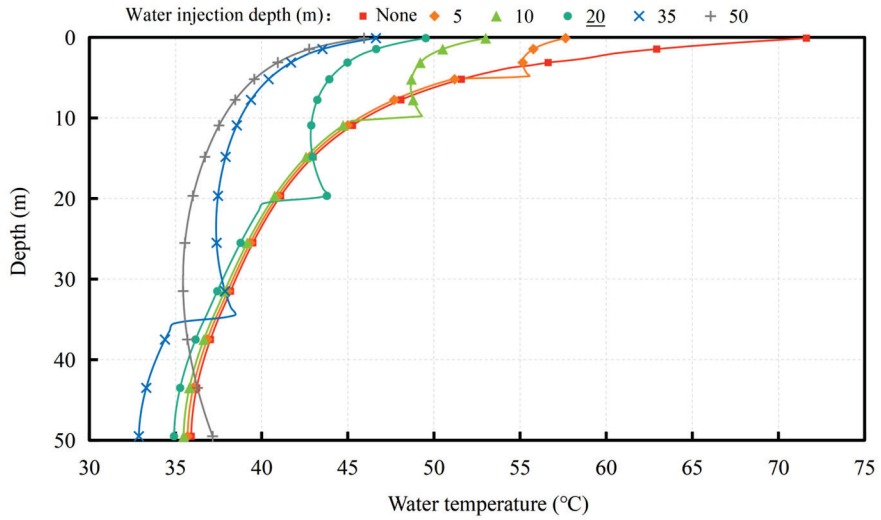



**Figure 19.** Vertical temperature of well water under different water injection depths at the end of operation. The standard group is underlined for comparison with other groups.

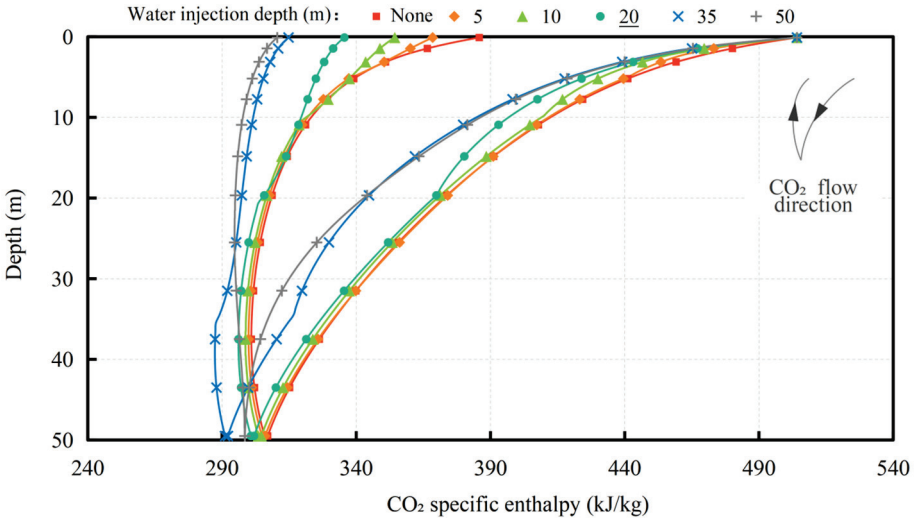



**Figure 20.** $CO_2$ enthalpy under different water injection depths at the end of operation. The standard group is underlined for comparison with other groups.

#### 4.2.2. Influence of Injection Flow Rate

As shown in Figure 21, even with a low injection flow rate of 0.05 $m^3$/h, a relatively significant enhancement in heat transfer is observed. When the flow rate reaches 1 $m^3$/h, the resulting heat transfer rate shows almost no difference compared to the 0.5 $m^3$/h group. Therefore, for this specific design scenario and considering only the heat transfer enhancement effect, 0.5 $m^3$/h is recommended as the preferred injection flow rate based on parametric analysis. The calculated average heat transfer rate improvements over the entire operating period for flow rates of 0.05 $m^3$/h to 1 $m^3$/h, compared to the group without artificial circulation, are 13.3%, 21.6%, 29.4%, 34.4%, and 35.3%, respectively.

As shown in Figure 22, the influence of artificial water injection on well water temperature can be clearly observed. At the injection outlet, due to the influx of warmer water from the upper layers, the local temperature increases significantly. Under the effect of artificial circulation, the overall temperature of the well water decreases with increasing injection flow rate. Even with a flow rate of only 0.05 $m^3$/h, the temperature at the very top layer of water can be significantly reduced from 71.6 °C (without circulation) to 57.6 °C.

https://doi.org/10.3390/en19092015

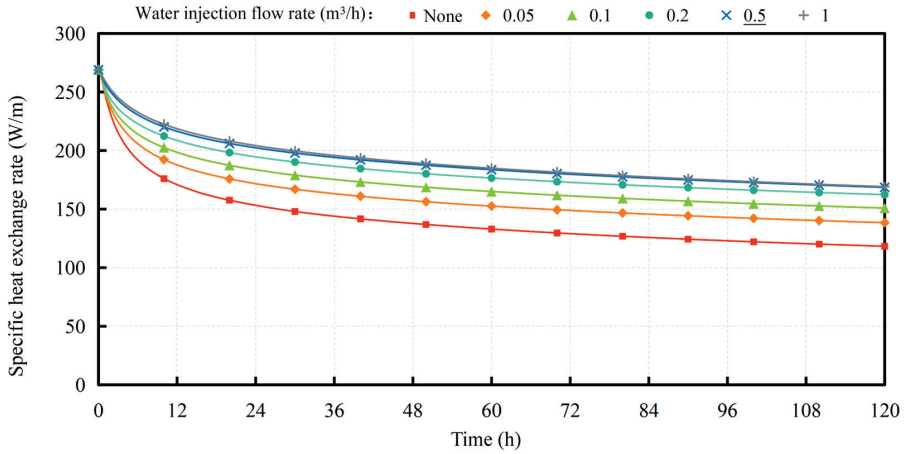



**Figure 21.** Change curves of unit heat flux under different injection flow rates. The standard group is underlined for comparison with other groups.

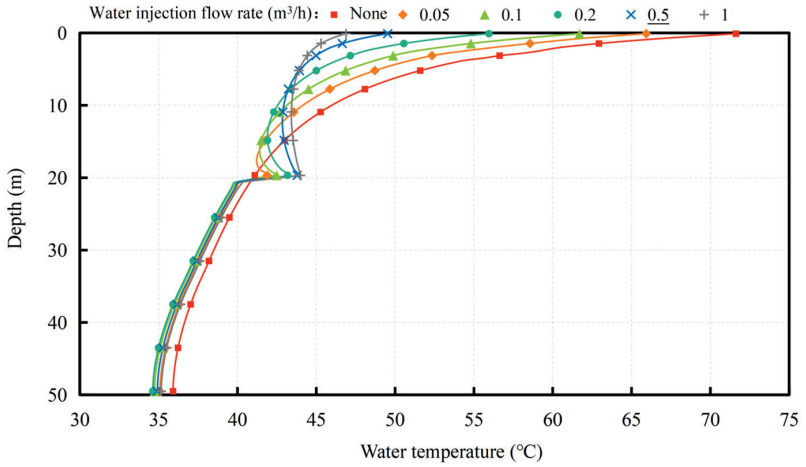



**Figure 22.** Vertical temperature of well water under different injection flow rates at the end of operation. The standard group is underlined for comparison with other groups.

Figure 23 shows the variation in $CO_2$ specific enthalpy along the flow path for each group at the end of the operating period. These results demonstrate that the severity of the thermal short-circuit effect decreases with increasing injection flow rate, as a higher flow rate promotes more effective mixing and temperature equalization within the well water.

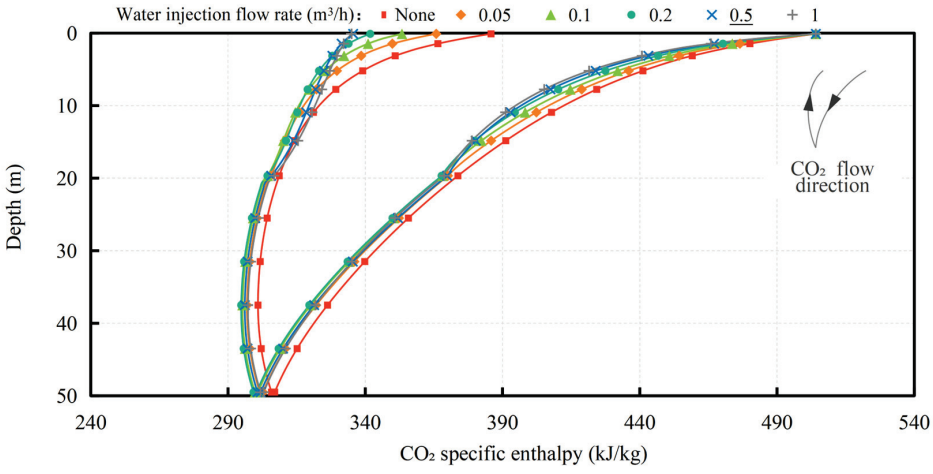



**Figure 23.** $CO_2$ enthalpy under different injection flow rates at the end of operation. The standard group is underlined for comparison with other groups.

https://doi.org/10.3390/en19092015

4.2.3. Influence of Injection Interval

Due to the high thermal capacity of the well water, a certain amount of time is required for its temperature to rise. Therefore, an intermittent operation strategy can be employed: water is injected for a period, followed by an idle period, and this cycle is repeated to reduce pump energy consumption. For all simulated groups, except for the case of continuous injection, each injection event lasted for 5 min.

As shown in Figure 24, for the groups with injection intervals of 40 min and 80 min, a clear fluctuation in the heat transfer rate is observable. The heat transfer rate increases rapidly when artificial circulation is activated and gradually decreases when it is stopped. Calculations of the average heat transfer rate over the entire operating period show that the groups with injection intervals ranging from 0 min (continuous) to 80 min achieved improvements of 34.4%, 31.1%, 27.6%, 21.4%, 14.1%, and 8.2%, respectively, compared to the group without artificial circulation.

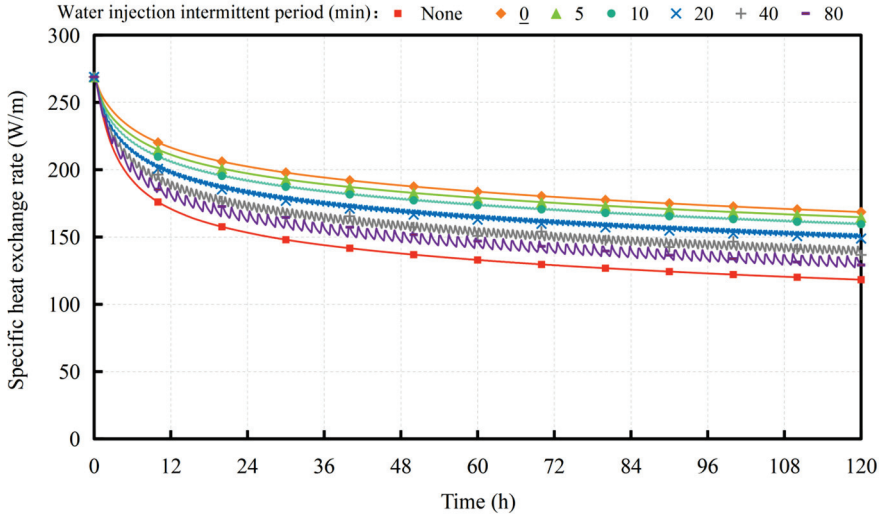



**Figure 24.** Change curves of unit heat flux under different injection intervals. The standard group is underlined for comparison with other groups.

In Figure 25, it can be observed that a shorter injection interval leads to a more balanced temperature distribution in the well water above the injection depth, resulting in a better heat transfer enhancement effect.

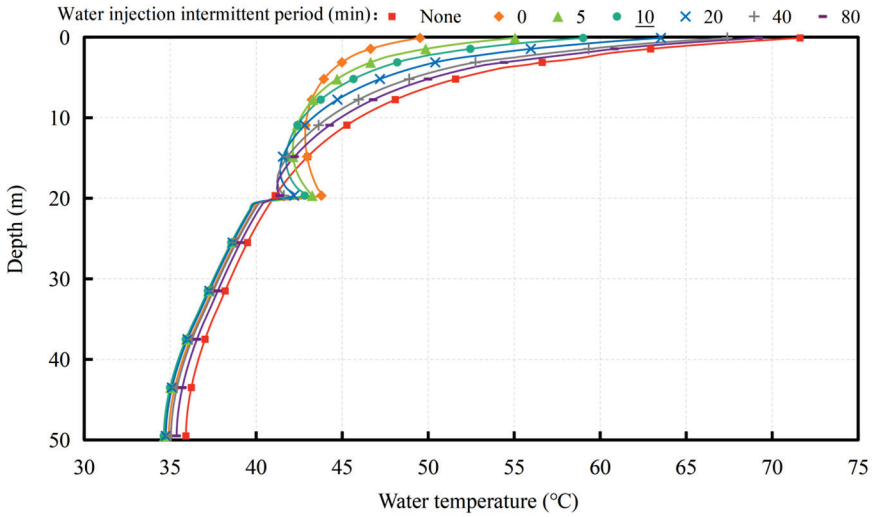



**Figure 25.** Vertical temperature of well water under different injection intervals at the end of operation. The standard group is underlined for comparison with other groups.

https://doi.org/10.3390/en19092015

Overall, in terms of its potential for enhancing heat transfer, the artificial well-water circulation method demonstrates greater potential than the insulation layer method. Furthermore, it allows for targeted optimization of control strategies during operation, based on actual loads and heat transfer characteristics.

4.2.4. Equivalent COP Analysis

To evaluate the economic viability of the artificial circulation method over a broader range of operating strategies, the equivalent COP was analyzed not only for the injection intervals listed in Table 4 (0 to 80 min), but also for longer intervals (160, 320, and 640 min). This extended set allows for a clearer observation of the trend in equivalent COP as the injection interval increases.

Since this method introduces new power-consuming equipment (the pump), its economic viability is further assessed by calculating an equivalent COP. The equivalent COP is obtained by dividing the increase in heat transfer rate (compared to the case without artificial circulation) by the pump's electrical power consumption. If this equivalent COP is higher than the unit COP of a conventional direct expansion $CO_2$ heat pump, it indicates that the artificial circulation method not only improves heat transfer but also offers favorable economic performance. It is important to clarify that the equivalent COP defined here is not the overall system COP of the heat pump. Rather, it is a marginal efficiency metric that quantifies the additional heat transfer gained per unit of electrical energy consumed by the circulation pump. It is calculated as

$$\mathrm{COP} = \frac{Q_{\text{with circulation}} - Q_{\text{without circulation}}}{P_{\text{pimp}}} \tag{33}$$

Taking an injection depth of 5 m as an example, a head of 6 m (1.2 times the depth) was specified, and a Grundfos UPS 25-62K circulation pump (Grundfos Holding A/S, Bjerringbro, Denmark) was selected. According to the pump's performance curve, this pump delivers a flow rate of 0.5 $m^3/h$ at the required 6 m head under the selected operating condition, with a corresponding power consumption of 115 W. Since the injection interval significantly affects both energy consumption and heat transfer, comparative simulations of equivalent COP and heat transfer rate were conducted for different injection intervals. The operating conditions were identical to those of the SG in the previous section.

As shown in Figure 26, the calculation results indicate that even with the circulation pump operating continuously, the average equivalent COP can reach 7.4. This is already significantly higher than the typical unit COP of a conventional direct expansion $CO_2$ heat pump. When intermittent injection is employed with intervals less than 160 min, the equivalent COP increases with the interval duration, reaching a maximum of 52.5. This is because the percentage reduction in heat transfer rate is lower than the percentage reduction in pump operating time. However, when the interval reaches 640 min, the enhancement effect of artificial circulation on the heat transfer rate becomes very weak, causing the equivalent COP to begin decreasing.

In summary, the equivalent COP of the artificial well-water circulation method is significantly higher than the unit COP of a conventional direct expansion $CO_2$ heat pump. During operation, the injection-intermittent control strategy can be optimized based on actual conditions to achieve the best balance between heat transfer performance and pump energy consumption.

https://doi.org/10.3390/en19092015

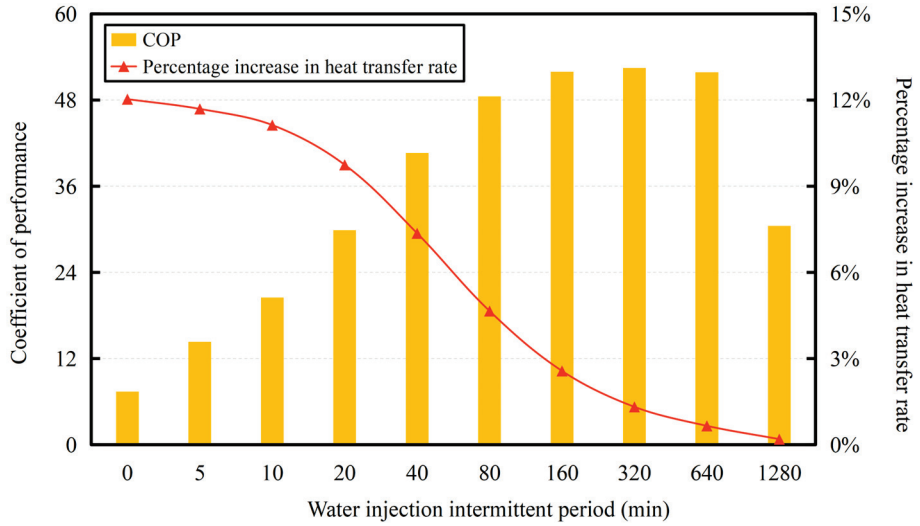



**Figure 26.** Equivalent COP and increase ratio of heat exchange rate under different injection intervals.

## 5. Conclusions

This paper first established a TRCM suitable for direct expansion $CO_2$ BHE and validated its accuracy through experiments. Subsequently, by establishing different scenarios, it quantitatively analyzed the dual role (positive and negative) of natural convection in well water on the heat transfer performance of the system. Following this, targeting the characteristics of the thermal short-circuit effect, two methods—the insulation layer method and the artificial well-water circulation method—were proposed to further enhance the heat exchanger's performance. The main conclusions are as follows:

(1) Natural convection within the well water enhances the overall heat transfer capacity of the exchanger while simultaneously intensifying the thermal short-circuit effect between the legs of the heat exchange U-tube. However, its positive effect on heat transfer enhancement is more dominant. Compared to the soil-backfilled scenario (Case 2) defined within the same model framework-which serves as a representative reference for a conventional direct expansion $CO_2$ ground-coupled heat exchanger under the conditions considered-employing the water-backfilled BHE configuration (SG) increases the heat transfer rate by 14.9%.

(2) Adding an insulation layer to the upper section of the rising pipe can effectively mitigate the thermal short-circuit effect and increase the heat transfer rate. Compared to the case without insulation, the average heat transfer rate improvement can reach up to 35.1%. Furthermore, the insulation length is not "the longer, the better". Excessively long insulation can adversely affect the normal heat exchange at the bottom of the rising pipe, thereby reducing the total heat transfer rate. For the design conditions considered in this study, balancing heat transfer performance and cost, a recommended insulation length is suggested to be in the range of 20–30 m.

(3) Artificially circulating the well water promotes a more uniform vertical temperature distribution within the well. This also helps to alleviate thermal short-circuiting and enhances heat transfer. Compared to the case without artificial circulation, employing the artificial well-water circulation method can increase the average heat transfer rate by up to 50.5%. Moreover, its equivalent COP can reach 7.4 under continuous injection operation and up to 52.5 under intermittent injection operation. These results demonstrate that this enhancement method achieves a favorable balance between heat transfer enhancement and pump energy consumption.

Future work could employ computational fluid dynamics (CFD) or localized temperature and velocity measurements to further characterize the flow field near the injection

https://doi.org/10.3390/en19092015

point, which would provide a more detailed understanding of the mixed convection regime and could inform further refinements of the model.

**Author Contributions:** Conceptualization, Y.Y. and Y.L.; methodology, X.L. and Y.L.; software, J.W.; validation, Y.Y. and J.Z. (Jinyu Zhao); formal analysis, J.Z. (Jun Zhao); investigation, S.W. and X.L.; resources, J.W. and S.W.; data curation, J.W.; writing—original draft preparation, Y.Y. and J.Z. (Jinyu Zhao); writing—review and editing, F.M.; visualization, F.M. and J.Z. (Jun Zhao); supervision, F.M.; project administration, Y.L.; funding acquisition, J.Z. (Jun Zhao). All authors have read and agreed to the published version of the manuscript.

**Funding:** This work was supported by National Natural Science Foundation of China (No.52306266).

**Data Availability Statement:** The original contributions presented in this study are included in the article. Further inquiries can be directed to the corresponding authors.

**Conflicts of Interest:** Author Yang Yu was employed by the company China Automotive Technology and Research Center Co., Ltd. The remaining authors declare that the research was conducted in the absence of any commercial or financial relationships that could be construed as a potential conflict of interest.

## Nomenclature

| Symbols | |
|---|---|
| $A$ | horizontal cross-sectional area of the control body where the node is located ($m^2$) |
| $c$ | specific heat capacity ($J \cdot kg^{-1} \cdot K^{-1}$) |
| $D_w$ | well hydraulic diameter (m) |
| Gr | Grashof number |
| $H$ | specific enthalpy ($J \cdot kg^{-1}$) |
| $l$ | length (m) |
| $L$ | depth (m) |
| $L_{cen}$ | U-tube Shank Spacing (m) |
| $m$ | mass flow rate ($kg \cdot s^{-1}$) |
| Nu | Nusselt number of convective heat transfer |
| Pr | Prandtl number |
| $R$ | thermal resistance ($K \cdot W^{-1}$) |
| Ra | Rayleigh number |
| Re | Reynolds number |
| $S$ | center distance between two branches of U-shaped pipe (m) |
| $T$ | temperature (K) |
| $\tau$ | time (s) |
| $\lambda$ | thermal conductivity ($W \cdot m^{-1} \cdot k^{-1}$) |
| $\rho$ | density ($kg \cdot m^{-3}$) |
| $\delta$ | thickness (mm) |
| $\mu$ | dynamic viscosity (Pa·s) |
| $\beta$ | coefficient of cubic expansion ($k^{-1}$) |
| $v$ | kinematic viscosity ($m^2 \cdot s^{-1}$) |
| $\Delta P_{f,g}$ | gravity pressure variation term (Pa) |
| $\Delta P_{f,a}$ | accelerated pressure change term (Pa) |
| $\Delta P_{f,F}$ | friction pressure change term (Pa) |
| Abbreviate | |
| BHE | borehole heat exchanger |
| COP | coefficient of performance |
| DX | Direct expansion |
| GSHP | Ground source heat pump |
| MAPE | Mean absolute percentage error |
| PVC | polyvinyl chloride |

| | |
|---|---|
| RMSE | Root mean square error |
| SHER | specific heat exchange rate |
| SG | standard group |
| TRCM | thermal resistance and capacity model |
| Subscripts | |
| A, B | downcomer, riser |
| c | well pipe |
| f | $CO_2$ |
| *i* | index along the vertical direction in the TRCM |
| INJ | injection |
| inn, o | inner wall surface of the pipe, outer wall surface of the pipe |
| ins | insulating layer |
| ini | initial temperature (°C) |
| in, out | entrance, exit |
| -1, -2 | inner part of the thermal resistance, outer part of the thermal resistance |
| m | equivalent thermal resistance of $CO_2$ flow |
| mid | equivalent diameter corresponding to the central point of heat capacity action |
| min | minimum value |
| *ns* | number of soil radial segments in the TRCM |
| *js* | soil radial segment index in the TRCM |
| p | U-tube |
| s | soil |
| w | water |
| z | vertical direction |

## References


1. Hannula, E.; Häkkinen, A.; Uribe, F.; Solonen, A.; de Wiljes, J.; Roininen, L. Partially stochastic deep learning with uncertainty quantification for building thermal modeling. *Build. Environ.* **2026**, *289*, 114118. [CrossRef]
2. Bez, F.; Jahangir, E.; Rouabhi, A.; Tran, C.T. Assessment of common hypotheses adopted in borehole sizing for Ground-Source Heat Pump (GSHP) systems. *Appl. Therm. Eng.* **2026**, *287*, 129433. [CrossRef]
3. Li, Y. Dynamic Heat Transfer Characteristics And Heat Transfer Enhancement of Direct-Expansion Carbon Dioxide Downhole Heat Exchanger and Its Array. Ph.D. Thesis, Tianjin University, Tianjin, China, 2021.
4. Han, N.; Zhao, Q.; Huang, T.; Huang, F.; Wu, Y.; Wang, K.; Zhou, S.; Zhang, W. Analysis of the factors influencing the performance of medium-shallow borehole heat exchangers coupled with a ground source heat pump system. *Environ. Prog. Sustain. Energy* **2025**, *44*, 14614. [CrossRef]
5. Liao, Z.; Huang, G.; Zhuang, C.; Zhang, H.; Cheng, L.; Gan, F. Research on the thermal balance of a novel independent heat extraction-release double helix energy pile in long-term operation. *Renew. Energy* **2024**, *236*, 121396. [CrossRef]
6. Liu, D.; Gu, D.; Zhang, W.; Hu, M.; Dai, C.; Tian, L.; Shangguan, S. Experimental study of a novel downhole heat exchanger utilizing working fluids for enhanced heat exchange. *Case Stud. Therm. Eng.* **2025**, *76*, 107429. [CrossRef]
7. Song, X.; Shi, Y.; Li, G.; Yang, R.; Xu, Z.; Zheng, R.; Wang, G.; Lyu, Z. Heat extraction performance simulation for various configurations of a downhole heat exchanger geothermal system. *Energy* **2017**, *141*, 1489–1503. [CrossRef]
8. Yang, X.; Liu, Q.; Lu, G. Heat Transfer Enhancement in Coaxial Downhole Heat Exchangers: Influence of Spiral Fins at the Bottom Section. *Energies* **2025**, *18*, 2361. [CrossRef]
9. Ren, S.; Lin, R.; Zheng, H.; Wang, X.; Yang, Z. Regulating geofluid-circulation surrounding a dual-branch well to improve geothermal production of downhole heat exchanger. *Appl. Therm. Eng.* **2025**, *273*, 126475. [CrossRef]
10. Askari, I.B.; Ghazizade-Ahsaee, H.; Shahsavar, A.; Keshtegar, B. Machine learning-based multi-objective optimization of a carbon dioxide direct-expansion geothermal heat pump comprising an internal heat exchanger and expander. *Appl. Therm. Eng.* **2025**, *274*, 126699. [CrossRef]
11. Li, Y.; Xu, W.; Ma, L.; Zhao, J.; Li, W.; Wang, S.; Liu, J. Dynamic heat transfer analysis of a direct-expansion $CO_2$ downhole heat exchanger. *Appl. Therm. Eng.* **2021**, *189*, 116733. [CrossRef]
12. Austin, B.T.; Sumathy, K. Parametric study on the performance of a direct-expansion geothermal heat pump using carbon dioxide. *Appl. Therm. Eng.* **2011**, *31*, 3774–3782. [CrossRef]
13. Eslami-Nejad, P.; Ouzzane, M.; Aidoun, Z. Modeling of a two-phase $CO_2$-filled vertical borehole for geothermal heat pump applications. *Appl. Energy* **2014**, *114*, 611–620. [CrossRef]

14. Hakkaki-Fard, A.; Eslami-Nejad, P.; Aidoun, Z.; Ouzzane, M. A techno-economic comparison of a direct expansion ground-source and an air-source heat pump system in Canadian cold climates. *Energy* **2015**, *87*, 49–59. [CrossRef]
15. Eslami-Nejad, P.; Ouzzane, M.; Aidoun, Z. A quasi-transient model of a transcritical carbon dioxide direct-expansion ground source heat pump for space and water heating. *Appl. Therm. Eng.* **2015**, *91*, 259–269. [CrossRef]
16. Ghazizade-Ahsaee, H.; Ameri, M. Energy and exergy investigation of a carbon dioxide direct-expansion geothermal heat pump. *Appl. Therm. Eng.* **2018**, *129*, 165–178. [CrossRef]
17. Gao, Y.; Gao, T. Simulation study on the performance of direct expansion geothermal refrigeration system using carbon dioxide transcritical cycle. *Energy Procedia* **2019**, *158*, 5479–5487. [CrossRef]
18. Nguyen, A.; Eslami-Nejad, P.; Badache, M.; Bastani, A. Influence of an internal heat exchanger on the operation of a $CO_2$ direct expansion ground source heat pump. *Energy Build.* **2019**, *202*, 109343. [CrossRef]
19. Nguyen, A.; Eslami-Nejad, P. A transient coupled model of a variable speed transcritical $CO_2$ direct expansion ground source heat pump for space heating and cooling. *Renew. Energy* **2019**, *140*, 1012–1021. [CrossRef]
20. Gao, Y.; Cheng, Y.; Nan, S. Heat transfer performance of the underground $CO_2$ pipe in the direct expansion ground source heat pump. *Energy Procedia* **2017**, *105*, 4955–4962. [CrossRef]
21. Alobaid, O.; Ezekiel, C.J.; Daniilidis, A.; Finkbeiner, T.; Mai, P.M. Groundwater-induced advective heat transfer in U-shaped closed-loop geothermal system: Application for a Red Sea rift sedimentary basin. *Geotherm. Energy* **2025**, *13*, 40. [CrossRef]
22. Liu, W.; Han, A. Research on the Convective Heat Transfer of Water in Granite Fractures Based on Numerical Experiments. *J. Res. Sci. Eng.* **2022**, *4*, 21. [CrossRef] [PubMed]
23. Yao, Z.; Wen, P.; Yang, J.; Jiang, Y.; Jiao, R. Enhanced heat transfer and flow characteristics of a bionic fish scale microchannel heat exchanger made by powder bed fusion (PBF) additive manufacturing. *Int. Commun. Heat Mass Transf.* **2026**, *172*, 110268. [CrossRef]
24. Kumar, D.; Sahu, A.K. Convective heat transfer from a rotating elliptic cylinder to non-Newtonian fluid in laminar flow condition. *Int. J. Heat Fluid Flow* **2026**, *117*, 110097. [CrossRef]
25. Sane, A.G.; Esmaeili, M.; Rabiee, A.H. Dual benefits of superhydrophobic surfaces: Suppression of flow-induced vibrations and enhancement of heat transfer in cylindrical structures. *Ocean Eng.* **2026**, *344*, 123643. [CrossRef]
26. Beauchamp, B.; Lamarche, L.; Kajl, S. A numerical model of a U-tube vertical ground heat exchanger used as an evaporator. *J. Energy Power Eng.* **2013**, *7*, 237–249.
27. Kim, M.; Lee, G.; Baik, Y.-J.; Ra, H.-S. Performance evaluation of geothermal heat pump with direct expansion type vertical ground heat exchanger. *Heat Transf. Eng.* **2015**, *36*, 1046–1052. [CrossRef]
28. Rousseau, C.; Fannou, J.-L.C.; Lamarche, L.; Ouzzane, M.; Kajl, S. Modeling and experimental validation of a transient direct expansion geothermal heat exchanger. *Geothermics* **2015**, *57*, 95–103. [CrossRef]
29. Rousseau, C.; Fannou, J.-L.C.; Lamarche, L.; Kajl, S. Modeling and experimental validation of a transient direct expansion heat pump. *Int. J. Renew. Energy Dev.* **2017**, *6*, 145–155. [CrossRef]
30. Gao, Y.; Gao, T.; Zhao, L. Study on the heat transfer performance of boiling in vertical buried tube of direct expansion ground source heat pump. *Energy Procedia* **2019**, *158*, 5494–5503. [CrossRef]
31. Zhao, H. Heat Transfer Research on Two-Phase Flow in Subterranean Heat Exchangers of Direct Expansion Ground-Coupled Heat Pump System. Master's Thesis, Shenyang Architecture University, Shenyang, China, 2012.
32. Wang, J.; Ding, Y.; Liang, G.; Li, X.; Luo, Y.; Hou, P.; Li, Y.; Zhao, J. A review on direct expansion ground heat exchanger: Experimental advancement, system instability, and heat transfer model. *Renew. Sustain. Energy Rev.* **2026**, *226*, 116227. [CrossRef]
33. Gupta, S.; Saltanov, E.; Mokry, S.J.; Pioro, I.; Trevani, L.; McGillivray, D. Developing empirical heat-transfer correlations for supercritical $CO_2$ flowing in vertical bare tubes. *Nucl. Eng. Des.* **2013**, *261*, 116–131. [CrossRef]
34. Spitler, J.D.; Javed, S.; Ramstad, R.K. Natural convection in groundwater-filled boreholes used as ground heat exchangers. *Appl. Energy* **2016**, *164*, 352–365. [CrossRef]
35. Yang, S. Improvement of the basic correlating equations and transition criteria of natural convection heat transfer. *Heat Transf. Res.* **2001**, *30*, 293–300. [CrossRef]
36. Hellström, G. Ground Heat Storage: Thermal Analyses of Duct Storage Systems. I. Theory. Ph.D. Thesis, University of Lund, Lund, Sweden, 1992.
37. Wang, Z.; Sun, B.; Wang, J.; Hou, L. Experimental study on the friction coefficient of supercritical carbon dioxide in pipes. *Int. J. Greenh. Gas Control* **2014**, *25*, 151–161. [CrossRef]
38. Li, S. Research on Heat Transfer Performance and Parameter Influence in Closed LoopMedium-Deep Downhole Heat Exchange. Master's Thesis, Tianjin University, Tianjin, China, 2018.

39. Ruan, C.; Feng, S.; Mou, S.; Cheng, W.; Zhao, S. An analysis of the characteristics of thermal physical properties and their influencing factors in the Tianjin area. *Hydrogeol. Eng. Ceology* **2017**, *44*, 158–163.
40. Yang, S.; Tao, W. *Heat Transmission Science*; Higher Education Press: Beijing, China, 2006.

**Disclaimer/Publisher's Note:** The statements, opinions and data contained in all publications are solely those of the individual author(s) and contributor(s) and not of MDPI and/or the editor(s). MDPI and/or the editor(s) disclaim responsibility for any injury to people or property resulting from any ideas, methods, instructions or products referred to in the content.

https://doi.org/10.3390/en19092015

energies

MDPI

*Article*

# A Study on the Thermal Management Performance of Server-Oriented Memory Liquid Cooling Solutions

**Yanling Chen [1], Zhongyun Tian [1,2,*], Mingzhi Kong [1], Lei Sun [1], Lizhi Zhou [1], Wujun Wang [1] and Mengyao Liu [1]**

[1] IEIT Systems Co., Ltd., Jinan 250101, China
[2] School of Architecture and Design, Harbin Institute of Technology, Harbin 150001, China
* Correspondence: zhongyun_tian@163.com

**Abstract**

The rapid increase in memory power density has made memory thermal management a critical challenge in high-density servers, where extremely limited DIMM spacing significantly reduces the effectiveness of air cooling. Compared with CPUs and GPUs, memory-level liquid cooling has received less systematic study, particularly regarding the influence of cold plate structural design on thermal and hydraulic performance under realistic server conditions. In this paper, three engineering-feasible memory liquid cooling solutions (water-flowing cold plate, clamp-type cold plate and heat-pipe-based cold plate) are experimentally compared on a high-density server system. Experiments are conducted at coolant inlet temperatures of 37–50 °C with a fixed flow rate of 0.8–1.5 L/min. Memory, CPU, and voltage regulator temperatures, as well as system pressure drop, are measured. Results show that memory temperature increases with coolant inlet temperature for all configurations, while their relative performance remains unchanged. Memory temperatures range from 62.04 to 71.13 °C, 57.65 to 66.98 °C, and 66.22 to 76.07 °C, with corresponding pressure drops of 24.19–26.69 kPa, 32.73–35.98 kPa, and 27.00–29.96 kPa. These results provide insight into the role of coolant distribution and flow-path topology in memory thermal performance.

**Keywords:** liquid-cooled server; data center; high-density server; memory liquid cooling

## 1. Introduction

With the rapid growth of large-scale artificial intelligence model training, scientific computing, cloud workloads, and database applications [1], computing systems have continued to evolve toward higher bandwidth, higher capacity, and higher density [2].

Significant improvements in bandwidth and access latency have made DDR5 memory a key enabler of server performance scaling [3]. However, under high-frequency operation, the operating current and power consumption of DDR5 memory modules are substantially increased, resulting in a heat flux density that is approximately 30 to 60 percent higher than that of the DDR4 generation [4]. When multiple DDR5 modules are deployed in parallel, the power consumption of a single module can reach 12 to 18 W, while high-performance registered DIMMs can exceed 20 W [5]. In typical dual-socket or quad-socket servers, the combined thermal load generated by 16 to 32 memory modules operating simultaneously becomes non-negligible [6]. As a result, the memory subsystem has gradually emerged as a critical component in the thermal management of high-density servers [7].

Unlike CPUs or GPUs, memory modules exhibit inherent geometric disadvantages for heat dissipation. DDR5 memory chips are arranged in dense arrays on a single DIMM, and

the spacing between adjacent DIMMs is typically less than 7.6 mm, which is much smaller than the characteristic dimensions of CPU cooling regions [8]. Such confined spacing significantly restricts convective pathways [9] and increases local flow resistance, making effective heat transfer difficult to achieve with air cooling under high-load conditions [10]. Previous studies have shown that when memory temperatures exceed 85 °C, error rates increase exponentially, particularly under high-frequency refresh modes, where device behavior becomes more sensitive [11]. In addition, temperature fluctuations accelerate thermomechanical fatigue, which shortens the service life of memory modules [12]. As server power density continues to increase, the limitations of conventional air cooling in managing memory thermal loads have become increasingly evident and are a key factor constraining system reliability and performance stability [13].

In parallel with the rapid increase in server power density, data centers have undergone a structural transition from traditional air-cooled architectures toward hybrid and fully liquid-cooled systems [14]. Direct-to-chip and cold plate-based liquid cooling have been increasingly adopted at the processor level to accommodate the rising thermal design power of CPUs and GPUs, while simultaneously reducing fan power consumption and improving overall energy efficiency [15]. At the system scale, liquid cooling enables higher rack-level power density, relaxed airflow constraints, and more flexible thermal zoning compared with conventional air-cooled designs [13]. As a result, liquid cooling is no longer limited to extremely high-performance computing platforms but is progressively being deployed in mainstream enterprise and cloud servers.

Despite this transition, the memory subsystem has largely remained air-cooled, even as its power density and thermal sensitivity continue to increase [16]. This mismatch between processor-level liquid cooling and memory-level air cooling leads to localized thermal bottlenecks and limits the effectiveness of system-level thermal optimization [17]. Consequently, extending liquid cooling to the memory subsystem is becoming a necessary step for achieving balanced thermal management in next-generation high-density servers.

Liquid cooling is regarded as one of the most promising thermal management technologies for high-heat-flux electronic systems due to its high heat transfer coefficient, large thermal capacity, and ability to remove substantial heat with minimal temperature differences [18]. In CPU, GPU, and system-level liquid cooling architectures, the effectiveness and energy-efficiency advantages have been well demonstrated, thereby reducing data center power usage effectiveness [19]. However, compared with processors, liquid-cooled memory remains in an early stage of research and industrial application. This is primarily attributed to several factors. First, the spacing between memory modules is minimal, which makes the layout of conventional cold plates difficult [20]. Second, memory modules are frequently replaced, which requires good assembly compatibility and modular design [21]. Third, liquid cooling pathways must be designed to avoid adverse impacts on the thermal management of voltage regulators, power-delivery components, and surrounding devices [22]. Fourth, cold plate structures must balance thermal performance, flow resistance, cost, and manufacturing complexity [23].

In recent years, only a limited number of studies have investigated the use of cold plates combined with flexible tubing for DIMM cooling [24]. However, most of these approaches rely on serial coolant flow configurations [25], which causes the coolant temperature to increase progressively along the flow path. As a result, the temperatures of downstream DIMMs remain consistently higher than those of upstream modules [14]. Some studies have proposed parallel flow strategies to improve temperature uniformity [26]. Nevertheless, challenges remain regarding flow distribution, structural arrangement, and manufacturing complexity [27]. In addition, other studies have explored the incorporation of phase change materials, heat pipes, and vapor chambers to enhance temperature uni-

https://doi.org/10.3390/en19092150

formity [28]. However, the actual flow resistance, pressure requirements, and long-term reliability of these approaches in high-density server environments have not yet been systematically validated [29].

Given the challenges discussed above, this study uses a realistic high-density server system. It focuses on the thermal management of DDR5 memory and proposes three liquid cooling structures suitable for engineering deployment. Compared with conventional studies that primarily focus on microchannel parameters, flow path configurations, or the thermal performance of a single cold plate, this work makes several distinct contributions.

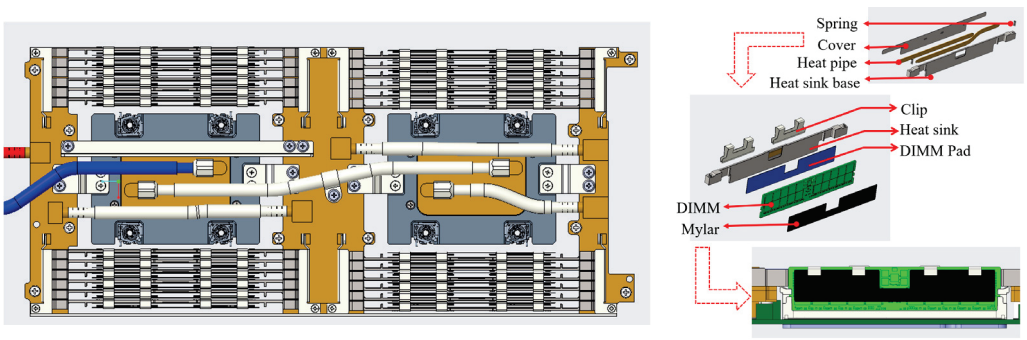
An experimental platform with controllable coolant temperature, flow rate, pressure drop, and airflow conditions is established, enabling the coupled thermal behavior of DDR5 memory, CPUs, and voltage regulator modules to be systematically measured. The three cooling structures are comprehensively compared with respect to thermal performance, temperature uniformity, hydraulic characteristics, cost and weight considerations, and system-level thermal coupling, thereby revealing the mechanisms by which structural design influences practical cooling performance. Finally, the scalability and deployment potential of liquid-cooled memory structures for future high-power DDR5 and DDR6 memory systems are discussed to guide modular liquid cooling design in data centers. The results of this study give systematic experimental evidence and clear structure–performance relationships for optimizing memory liquid cooling in high-density servers, thereby supporting the large-scale adoption of memory liquid cooling in practical data center applications.

## 2. Experimental System Design

### *2.1. Memory Liquid Cooling Structures*

To compare the cooling effectiveness of different liquid cooling structures for DDR5 memory in high-density servers, three cold plate designs with practical engineering feasibility were designed and fabricated in this study. These include a water-cooled cold plate, a clamp-type cold plate, and a heat-pipe-based memory liquid cooling structure. The three designs differ substantially in flow channel configuration, heat transfer pathways, manufacturing processes, and assembly methods. The geometric configurations of the three memory liquid cooling structures are illustrated in Figure 1.

Figure 1 presents schematic diagrams of three memory liquid cooling configurations: the clamp-type memory liquid cooling structure (mode 1), the water-flowing memory liquid cooling structure (mode 2), and the heat-pipe-based memory liquid cooling structure (mode 3). These three designs differ significantly in structural layout, heat-transfer pathways, and coolant routing, corresponding to distinct thermal performance characteristics and engineering application scenarios.




(**a**)

**Figure 1.** *Cont.*

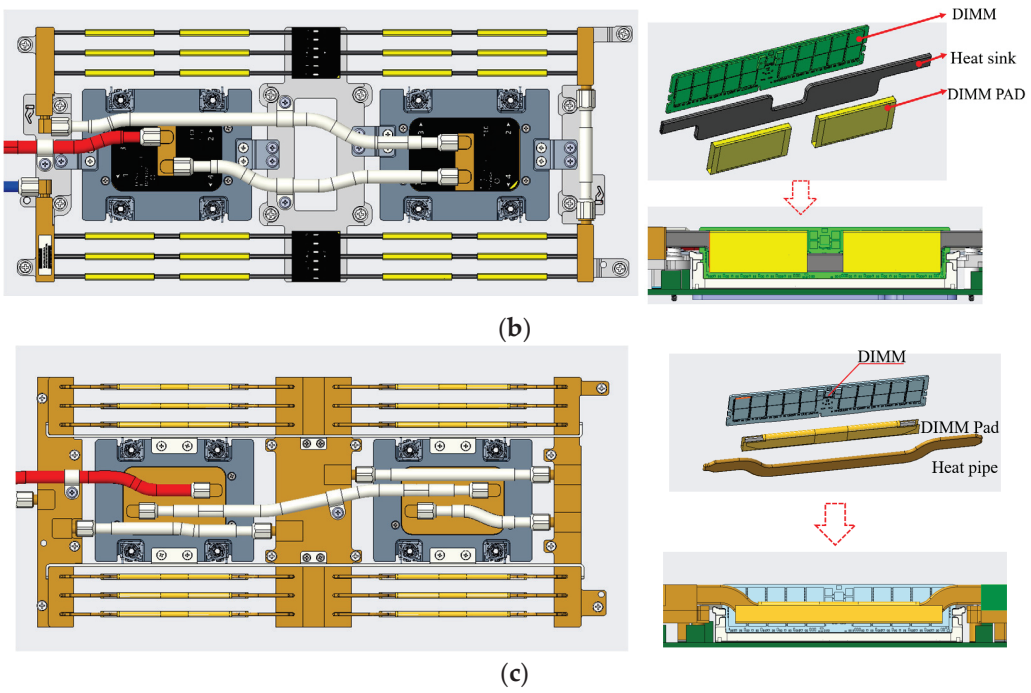



**Figure 1.** Schematic diagrams of the three memory liquid cooling configurations. (**a**) Clamp-type cold plate for memory liquid cooling (mode 1). (**b**) Water-flowing cold plate for memory liquid cooling (mode 2). (**c**) Heat-pipe-based cold plate for memory liquid cooling (mode 3).

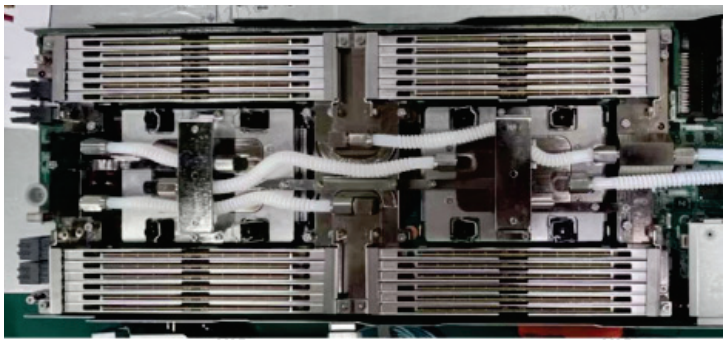
The clamp-type memory liquid cooling structure (mode 1) comprises two symmetrically arranged high-thermal-conductivity metal clamping plates. Ultra-thin flattened heat pipes are embedded on the inner surfaces of the clamping plates, and the assembly is secured on both sides of the DIMM using an elastic clamping mechanism. This structure is compatible with memory modules from different manufacturers and specifications, providing good assembly adaptability. Thermal interface pads are applied between the memory chips and the clamping plates to reduce interfacial thermal resistance. The heat transfer path follows a multi-stage process involving a vapor chamber, heat pipes, and water-flowing cold plates. Heat generated by the memory chips is first spread laterally within the vapor chamber and then rapidly transferred through U-shaped heat pipes to water-cooling channels on both sides, where it is dissipated. Owing to the high effective thermal conductivity of the heat pipes, low flow resistance and good temperature uniformity are achieved on the coolant side. However, under high heat-flux conditions, the cooling capacity may be constrained by heat-transfer limits or by dry-out in the heat pipes.

The water-flowing, memory liquid cooling structure (mode 2) employs a composite design comprising stainless-steel coolant channels and an internal flow distributor. The cold plate body is typically manufactured from an aluminum alloy, and multiple coolant-flow channels are formed by precision computer numerical control machining. The coolant flows directly through regions corresponding to the memory chips. Thermal interface pads are placed between the heat sink and the DIMM to enhance thermal contact between the chips and the cold plate. A key feature of this structure is the direct or near-direct contact between the coolant channels and the memory chips, which significantly shortens the heat transfer path and reduces thermal resistance. Due to the relatively short flow paths, the coolant temperature rise along the channels is limited, thereby reducing temperature differences among chip locations and leading to a more uniform temperature distribution across the memory module. As a result, high cooling efficiency is achieved under high power-density and rapid thermal-response conditions.

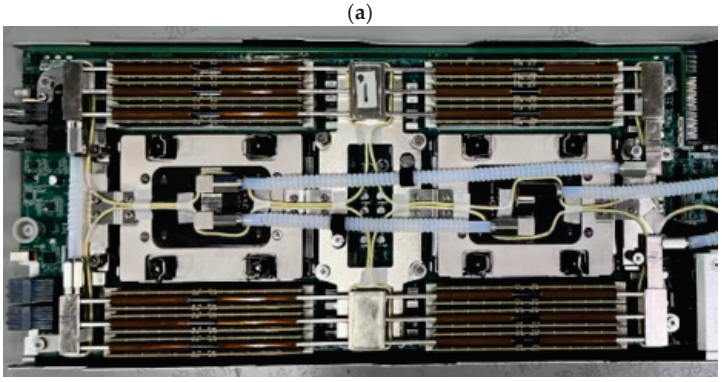
https://doi.org/10.3390/en19092150

The heat-pipe-based memory liquid cooling structure (mode 3) collects and transfers heat generated by the memory chips to a centralized water-flowing cooling region via flat heat pipes mounted on one or both sides of the DIMM. Effective thermal coupling between the memory chips and the evaporator sections of the heat pipes is achieved using thermal interface pads or metal contact structures. Heat is rapidly conducted through the heat pipes to the condenser sections and is ultimately dissipated via heat exchange with the coolant. In this configuration, the combination of heat pipes and coolant channels forms a compact installation structure that facilitates assembly and maintenance. Compared with direct water cooling, coolant routing is simplified, and flow resistance is reduced. However, the thermal performance of this structure is also limited by the heat-transfer capacity of the heat pipes, and performance bottlenecks may occur under extremely high heat-flux conditions.

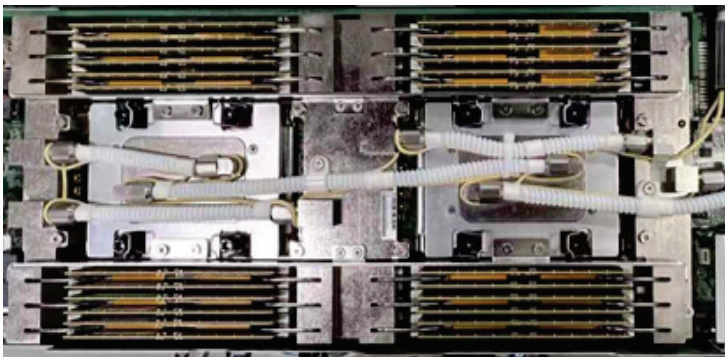
To further illustrate the operation of the internal flow channels, Figure 2 shows the experimental setup for the three memory liquid cooling configurations installed on the server platform.



(**a**)



(**b**)



(**c**)

**Figure 2.** Experimental setup of the three memory liquid cooling configurations. (**a**) Clamp-type cold plate for memory liquid cooling (mode 1). (**b**) Water-flowing cold plate for memory liquid cooling (mode 2). (**c**) Heat-pipe-based cold plate for memory liquid cooling (mode 3).

https://doi.org/10.3390/en19092150

### *2.2. Thermal Coupling Layout of the Memory and CPU Regions*

The DDR5 DIMM chip arrangement is highly compact. The spacing between adjacent memory chips is approximately 7.5 mm. In comparison, the typical gap between two DIMMs is only about 4 mm. This constrained space not only severely limits air convection but also imposes strict constraints on cold plate design. The cold plate must cover the chip surfaces without interfering with DIMM insertion and removal, and it must avoid interference with voltage regulator modules, airflow paths, and CPU cold plates. To reproduce thermal coupling among multiple heat sources in a realistic server environment, a test platform is built on a server node. For all three memory liquid cooling configurations, a serial coolant-routing strategy is adopted, in which the coolant first flows through the memory region and then enters the CPU cold plate. This arrangement is selected because DDR5 modules are more temperature-sensitive under high-bandwidth operating conditions, and prioritizing memory cooling improves overall system stability. In addition, a dedicated cooling channel is designed for the voltage regulator region, where liquid cooling is applied to ensure stable operation of the VR modules.

### *2.3. Liquid Cooling Loop and Experimental Platform*

A closed-loop liquid cooling system is used in the experiments. The system consists of a circulation pump, a plate heat exchanger, a temperature-controlled cooling source, a flow meter, differential pressure sensors, a temperature acquisition module, and insulated piping. The experimental system can supply coolant at temperatures accurately controlled between 25 °C and 55 °C. The maximum cooling capacity of a single node is 8000 W, and a vapor compression refrigeration cycle is used to ensure stable cooling for the server. The test system is connected to the server cold plates using quick-disconnect couplings. The schematic diagram and the experimental setup of the system are shown in Figures 3 and 4, respectively.

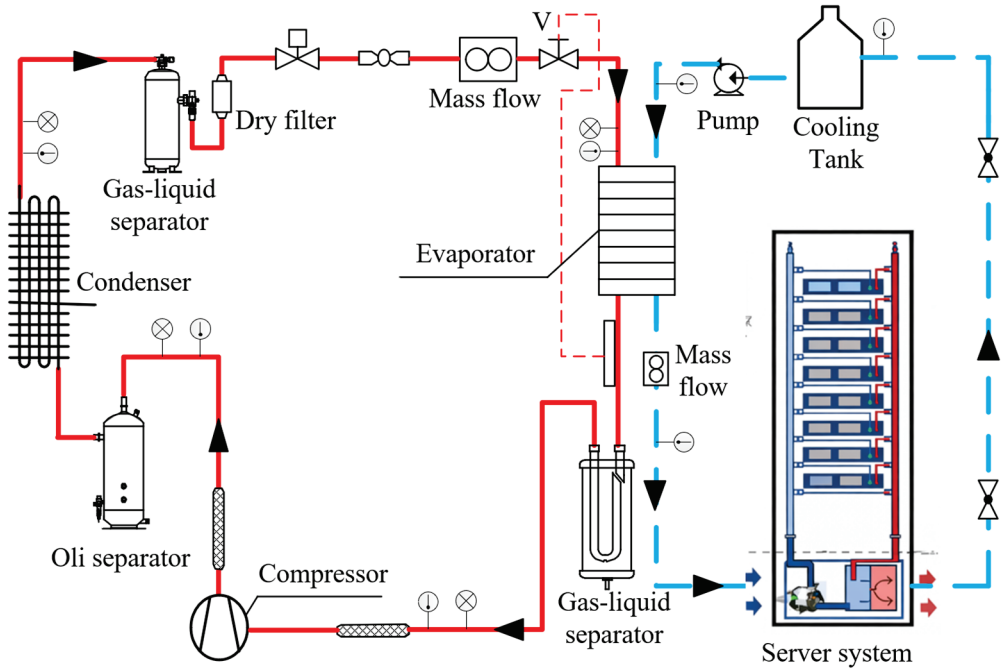



**Figure 3.** Schematic diagram of the server liquid cooling loop.

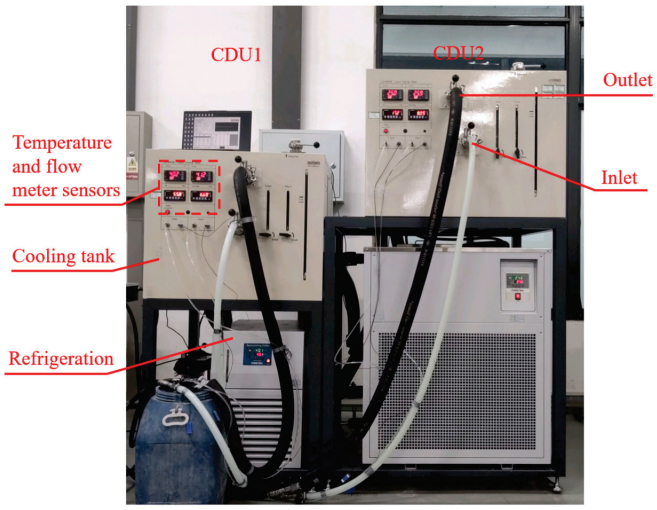



**Figure 4.** Experimental setup of the server liquid cooling test platform.

A 25% glycol–water solution provides adequate corrosion protection and good material compatibility for server liquid cooling loops. It also maintains stable viscosity and acceptable hydraulic performance under the tested temperature range. Accordingly, a 25% glycol–water solution is used as the coolant. The coolant inlet temperature is set to 37 °C, 40 °C, 45 °C, and 50 °C, while the flow rate is fixed at 1.0 L/min. All experiments are conducted in a temperature-controlled chamber maintained at 25 °C to minimize external disturbances.

### *2.4. Temperature and Flow Measurement System*

To accurately determine the temperature distribution in DDR5 memory chips, this study employs two measurement methods. These include surface-mounted thermocouples and the internal temperature registers integrated within the DIMMs. All thermocouples are calibrated in a constant-temperature bath, yielding a nominal accuracy of ±0.2 °C. The thermocouples are attached to the top surfaces of the memory chips using high-temperature adhesive to minimize variations in contact thermal resistance. Coolant flow rate and pressure drop are measured using high-precision sensors. The measurement locations and sensor specifications are summarized in Table 1. The arrangement of temperature measurement points on the DDR5 chips is illustrated in Figure 5.

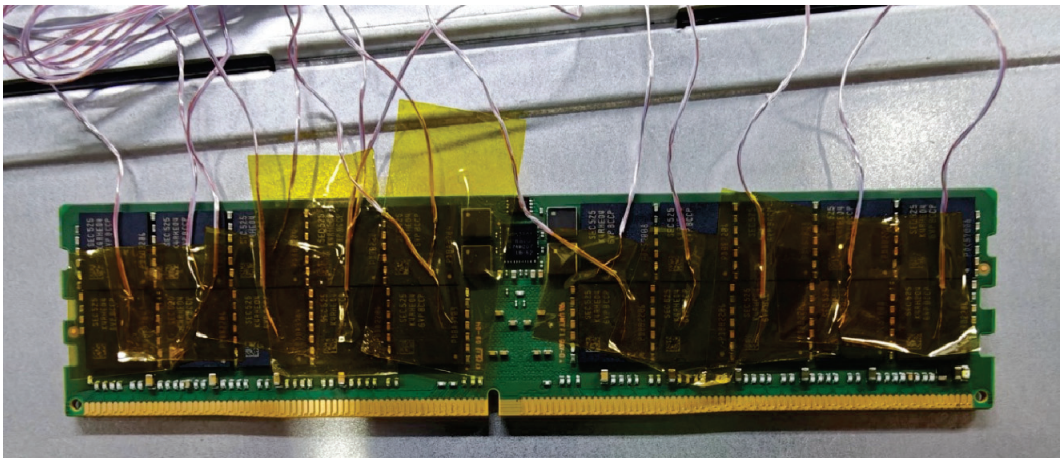


**Figure 5.** Layout of temperature measurement points on the DDR5 chips.

**Table 1.** Sensor locations and accuracy specifications for temperature, flow rate, and pressure drop measurements.

| Measurement Location | Sensor Type | Accuracy | Range |
|---|---|---|---|
| DDR5 front die | T-type surface-mounted thermocouple | ±0.2 °C | 0.0~100.0 °C |
| DDR5 middle dies | T-type surface-mounted thermocouple | ±0.2 °C | 0.0~100.0 °C |
| DDR5 rear die | T-type surface-mounted thermocouple | ±0.2 °C | 0.0~100.0 °C |
| DIMM temperature register | Integrated module temperature sensor | ±0.2 °C | 0.0~100.0 °C |
| CPU hotspot | Motherboard digital temperature sensor | ±0.2 °C | 0.0~100.0 °C |
| Voltage regulator module | Motherboard digital temperature sensor | ±0.2 °C | 0.0~100.0 °C |
| Coolant inlet temperature | Pt100 resistance temperature probe | ±0.1 °C | 0.0~150.0 °C |
| Coolant outlet temperature | Pt100 resistance temperature probe | ±0.1 °C | 0.0~150.0 °C |
| Flow rate | Coriolis mass flow meter | ±0.05 L/min | 0.6~10.0 L/min |
| Pressure drop | Differential pressure sensor | FS ±0.1% | 2.00~200.00 kPa |

### *2.5. Experimental Conditions*

A total of 12 operating conditions is designed, comprising three cold plate configurations and four coolant inlet temperatures. Each condition is tested three times. Steady-state operation is defined as a temperature variation of less than 0.2 °C within 30 min. After the steady state is reached, data is recorded for 20 min and averaged. The experimental condition matrix is summarized in Table 2. During all experiments, each DDR5 DIMM operated at a steady electrical power of 13.85 W, resulting in a total memory heat load of 332.4 W per node. The same memory workload and power level were maintained across all cooling configurations to ensure consistent thermal boundary conditions.

**Table 2.** Uncertainty assessment of measured parameters.

| Measured Quantity | Main Sources of Uncertainty | Individual Uncertainty | Combined Uncertainty (95% Confidence Level) |
|---|---|---|---|
| DDR5 chip temperature | Thermocouple calibration error; sensor placement deviation; interface heat transfer variation | ±0.2 °C; ±0.3 °C | ±0.36 °C |
| SPD module temperature | Accuracy of the internal register sensor | ±1 °C | ±1 °C |
| CPU temperature | Motherboard digital sensor | ±1 °C | ±1 °C |
| VR temperature | Motherboard sensor error; local airflow fluctuation | ±1 °C | ±1.1 °C |
| Flow rate | Mass flow meter accuracy; pump speed fluctuation | ±1% full scale; ±0.01 L/min | ±0.02 L/min |
| Pressure drop | Differential pressure sensor error; zero drift | ±0.5 kPa | ±0.5 kPa |
| Coolant heat absorption | Temperature difference uncertainty; flow rate uncertainty | Temperature difference ±0.25 °C | ±3% |

### *2.6. Uncertainty Assessment*

To verify the reliability of the measured data, the uncertainties associated with temperature, flow rate, pressure drop, and coolant heat absorption are evaluated using the error-propagation method. A heat balance between the electrical input power and the heat absorbed by the coolant is used for cross-validation. The typical deviation is within ±3 percent, which indicates that the overall experimental system is reliable. The combined uncertainty results are summarized in Table 2.

https://doi.org/10.3390/en19092150

## 3. Results

This section presents a comprehensive analysis of the thermal performance of the three cold plate configurations under different operating conditions, including temperature control capability, temperature uniformity, hotspot distribution, coupled temperatures of the VR and CPU regions, pressure drop characteristics, and system-level heat balance consistency. Unless otherwise specified, all experiments are conducted at a flow rate of 1.0 L/min and an ambient temperature of 25 °C.

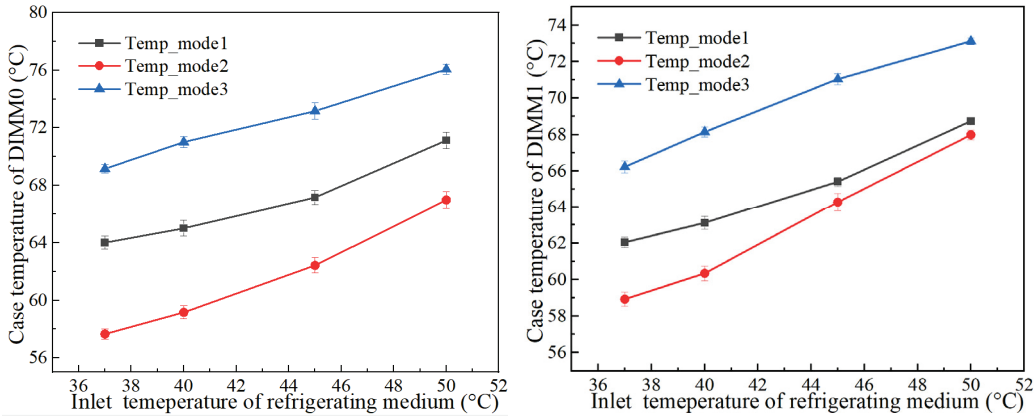
To facilitate heat-load-normalized comparison, an effective memory-to-coolant thermal resistance was introduced. The thermal resistance between memory and coolant ($R_{\text{mem-cool}}$) is defined as

$$R_{\text{mem}-\text{cool}} = \frac{T_{\text{mem,avg}} - T_{\text{cool,in}}}{Q_{\text{mem}}} \quad (1)$$

where $T_{\text{mem,avg}}$ denotes the average temperature of the monitored memory devices, $T_{\text{cool,in}}$ is the coolant inlet temperature, and $Q_{\text{mem}}$ represents the applied memory heat load. This metric characterizes the overall heat transfer effectiveness from the memory devices to the coolant under the tested conditions.

### *3.1. Effect of Coolant Inlet Temperature on Memory Thermal Performance*

Figure 6 shows the effect of the coolant inlet temperature on the memory temperatures of DIMM0 and DIMM1 across the three cooling modes. Across the investigated inlet temperature range, clear temperature separation among the three modes is maintained for both DIMMs, with mode 2 consistently exhibiting the lowest memory temperature, mode 3 the highest, and mode 1 falling in between.




(**a**) DIMM0 (**b**) DIMM1

**Figure 6.** Effect of inlet coolant temperature on DIMM temperature.

Quantitatively, the total temperature increase of DIMM0 over the tested inlet temperature range is 7.12 °C, 9.33 °C, and 6.92 °C for modes 1, 2, and 3, respectively, while the corresponding increases for DIMM1 are 6.70 °C, 9.05 °C, and 6.89 °C. As indicated by the separation between the error bars, the observed temperature differences between the cooling modes exceed the combined measurement uncertainty for both DIMMs.

These results indicate that increasing the coolant inlet temperature primarily shifts the absolute memory temperature level. The differences among the cooling modes arise from their distinct memory-to-coolant thermal resistances, which lead to different temperature offsets as the inlet temperature varies.

As shown in Figure 7, the thermal resistance of both DIMM0 and DIMM1 decreases monotonically with increasing inlet coolant temperature for all three cooling configurations. This trend can be partially attributed to reduced coolant viscosity at elevated temperatures.

https://doi.org/10.3390/en19092150

As the inlet temperature rises, the coolant's dynamic viscosity decreases, increasing the Reynolds number at the same volumetric flow rate. The enhanced turbulence intensity strengthens fluid mixing near the heat transfer surface, thereby improving the convective heat transfer coefficient and reducing the convective thermal resistance on the coolant side. In addition, the thermal resistance is also influenced by the changing temperature difference between the memory devices and the coolant. Although the absolute memory temperatures increase with higher inlet temperatures, the relative ranking among the three cooling modes remains unchanged, indicating that the dominant structural thermal resistance and contact conditions are not significantly affected by inlet temperature variation. Among the three configurations, the direct liquid-cooled design (mode 2) consistently exhibits the lowest thermal resistance, followed by the clamp-type cold plate (mode 1), while the heat-pipe-assisted solution (mode 3) shows the highest thermal resistance across the tested temperature range. This suggests that, under steady-state operating conditions, the overall cooling effectiveness is primarily governed by the module's structural thermal resistance, while the inlet coolant temperature mainly affects the convective component of the thermal resistance network.

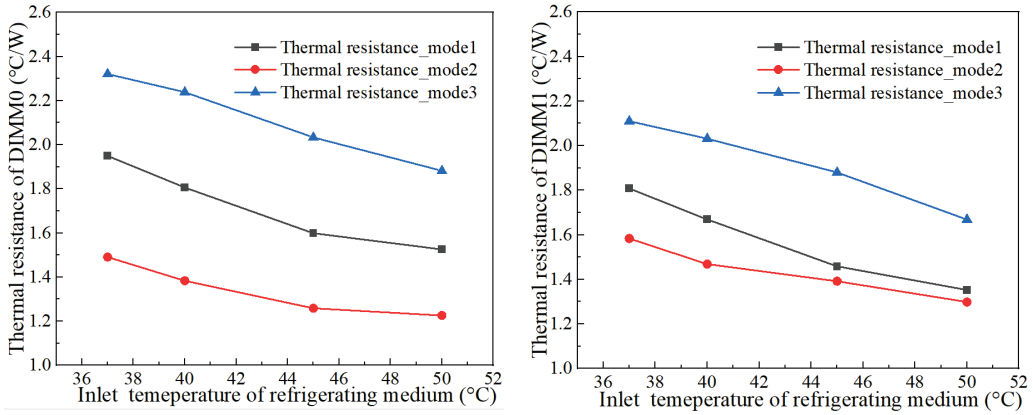



**Figure 7.** Effect of inlet coolant temperature on the thermal resistance of a DIMM.

### *3.2. Effect of Cold Plate Geometry on VR Temperature*

Figure 8 compares the VR module temperatures under different coolant inlet temperatures for the three cooling modes. For both VR0 and VR1, the three modes exhibit distinct temperature levels across the entire inlet temperature range, with mode 2 operating at the lowest temperature and mode 1 at the highest.

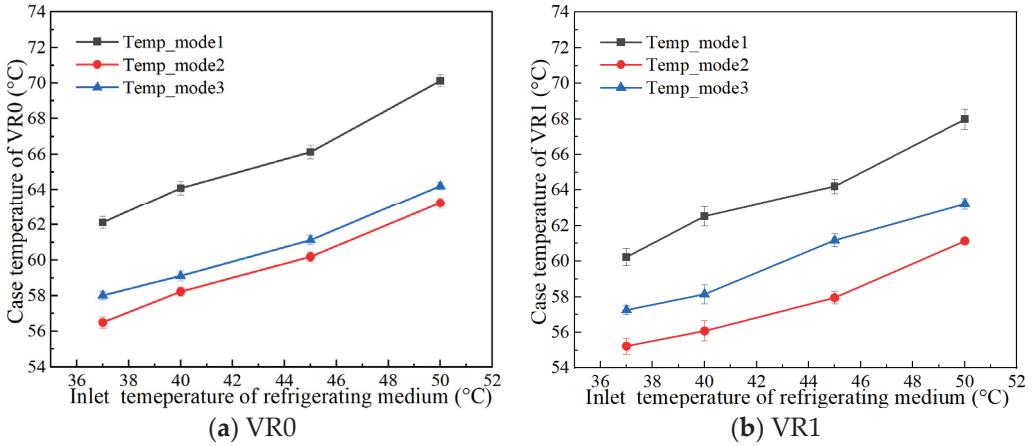



**Figure 8.** Effect of inlet coolant temperature on VR temperature.

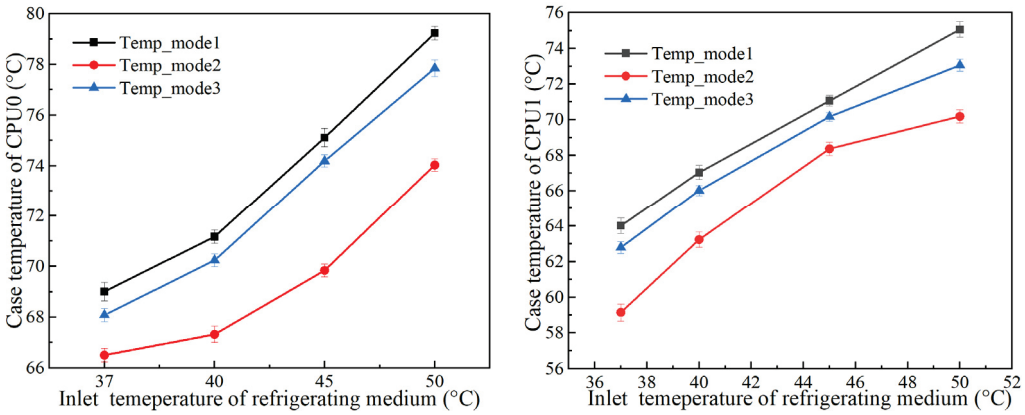
https://doi.org/10.3390/en19092150

The magnitude of temperature variation with inlet temperature differs among the cooling modes. For VR0, the total temperature increases from 37 °C to 50 °C and is 8.00 °C for mode 1, compared with 6.73 °C and 6.19 °C for modes 2 and 3, respectively. A similar trend is observed for VR1, where mode 1 shows a larger temperature increase (7.75 °C) than modes 2 (5.91 °C) and 3 (5.97 °C).

These differences can be attributed to variations in the local thermal environment around the VR modules induced by the different cold plate geometries, which affect heat spreading and convective heat removal in the vicinity of the VR components.

### *3.3. Coupled Effect of Cold Plates on CPU Temperature*

Figure 9 shows the effect of coolant inlet temperature on the temperatures of CPU0 and CPU1 for the three cooling modes. For all modes, CPU temperature increases as the inlet temperature rises from 37 °C to 50 °C, while the relative temperature ranking among the three modes remains unchanged.




(**a**) CPU0 (**b**) CPU1

**Figure 9.** Effect of inlet coolant temperature on CPU temperature.

For both CPUs, mode 2 consistently exhibits the lowest temperature, whereas modes 1 and 3 show higher temperatures with only minor differences between them. Over the investigated inlet temperature range, the temperature rise of CPU0 is 10.24 °C, 7.53 °C, and 9.77 °C for modes 1, 2, and 3, respectively, while the corresponding values for CPU1 are 11.05 °C, 11.04 °C, and 10.26 °C. These results indicate that increasing coolant inlet temperature raises the absolute CPU temperature but does not alter the relative thermal performance of the three cooling modes.

### *3.4. Pressure Drop and Hydraulic Performance of the Cold Plates*

Figure 10 presents the system frictional pressure drop ($\Delta P$) of cooling system for the three cooling modes at different inlet coolant temperatures, with a fixed flow rate. Over the investigated temperature range, $\Delta P$ shows a moderate decreasing trend for all cooling modes, while the relative differences among the modes remain clearly distinguishable.

Across all inlet temperature conditions, mode 2 consistently exhibits the highest pressure drop, whereas mode 1 maintains the lowest, with mode 3 falling between the two. The variation in pressure drop with inlet temperature is comparatively slight in mode 1, indicating a relatively weak sensitivity of its hydraulic behavior to changes in coolant temperature.

These results suggest that differences in pressure drop among the cooling modes are primarily determined by their flow-path geometries rather than by the inlet coolant temperature. Consequently, at the fixed flow rate considered in this study, the hydraulic

https://doi.org/10.3390/en19092150

penalty associated with each cooling mode is mainly determined by the cooling structure's inherent design, while variations in inlet temperature play a secondary role.

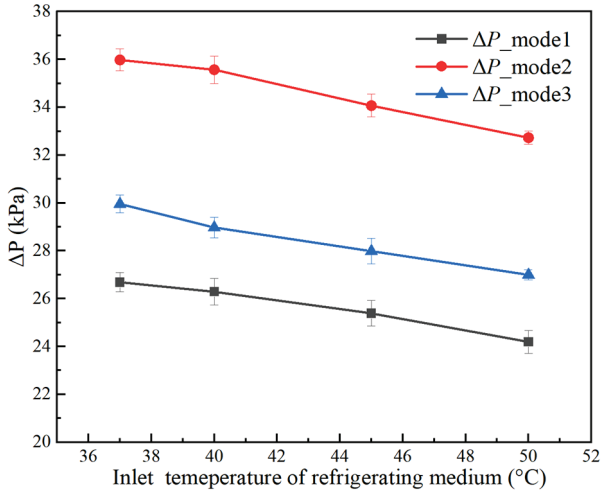



**Figure 10.** Effect of cooling configuration on frictional pressure drop (Δ*P*) in the flow channels.

### *3.5. Coupled Effect of Refrigerating Medium Flow Rate on Flow and Heat Transfer Characters of the Cold Plates*

As illustrated in Figure 11, increasing the coolant flow rate results in a pronounced, nearly monotonic reduction in the thermal resistance of both DIMM0 and DIMM1 across all three cooling configurations. Among the three configurations, mode 2 consistently achieves the lowest thermal resistance, while mode 3 exhibits the highest values. The relative ranking among the three modes remains unchanged with increasing flow rate, suggesting that the intrinsic structural and contact thermal resistances of each cooling design govern their comparative performance.

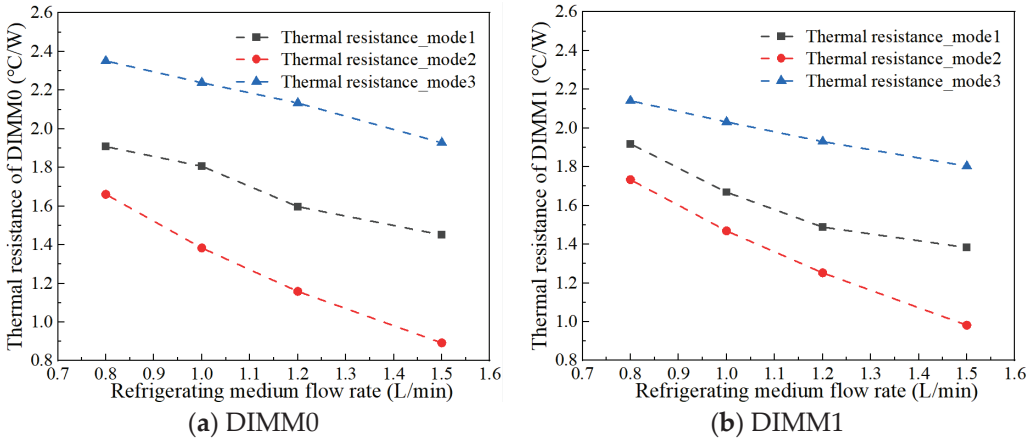



**Figure 11.** Effect of coolant flow rate on DIMM resistance.

However, as shown in Figure 12, the improvement in thermal performance is accompanied by a continuous increase in frictional pressure drop (ΔP) with increasing flow rate. Mode 1 exhibits the lowest pressure drop, while mode 2 shows the highest hydraulic resistance across the tested range, with mode 3 lying between the two. This indicates that although mode 2 provides superior heat transfer performance, it imposes the largest pumping power requirement. The rate of thermal resistance reduction diminishes at higher flow rates, implying diminishing returns once the coolant-side resistance becomes less dominant within the overall thermal resistance network. Therefore, further increasing the flow rate yields limited thermal benefits while substantially increasing hydraulic penalties.

https://doi.org/10.3390/en19092150

From a system-level perspective, an optimal design should balance thermal performance and pumping power consumption rather than pursuing maximum heat transfer alone.

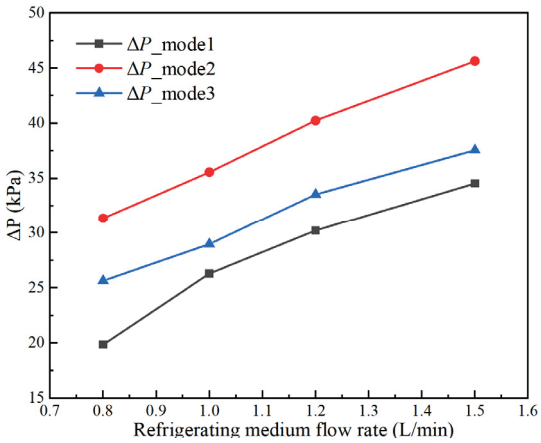



**Figure 12.** Effect of coolant flow rate on frictional pressure drop (Δ*P*).

## 4. Discussion

The performance differences among the three DIMM liquid cooling configurations are primarily due to variations in flow-channel topology and coolant distribution. Material selection and overall cold plate dimensions play a secondary role. Under identical operating conditions, DIMM thermal behavior is primarily governed by the ability to limit coolant temperature rise along the flow path in a constrained DIMM layout.

The water-flowing cold plate achieves the optimal DIMM thermal performance, which is enabled by its parallel short-channel design. This configuration effectively suppresses coolant temperature accumulation along the main flow direction and ensures sufficient low-temperature coolant is supplied to the memory region. Since DDR5 DIMM modules are linearly arranged with minimal spacing, even small coolant temperature gradients can lead to noticeable discrepancies in memory temperature. The results demonstrate that controlling along-path coolant temperature rise is more effective than introducing additional heat-spreading structures.

At the system level, VR temperature is influenced by cold plate geometry through airflow interaction in the DIMM region. Larger cold plate volume and height can partially obstruct airflow, thereby reducing local convective heat transfer around the VR modules. More compact structures introduce less airflow disturbance and consequently lead to lower VR temperatures. In the serial cooling configuration investigated in this study, the impact of memory liquid cooling on CPU temperature remains limited within the tested operating range. However, this coupling effect may become more pronounced as memory power density increases. Apparent differences are also observed in hydraulic performance. System pressure drop is mainly determined by flow path length and the degree of flow parallelization. Designs with higher flow parallelization achieve lower pressure drop. This characteristic is beneficial for system integration and for reducing pump power.

From a manufacturing and reliability perspective, the three liquid cooling configurations also exhibit distinct characteristics. The water-cooled plate uses a relatively simple channel topology and conventional metallic materials, which are compatible with mature machine or extrusion processes. Its structure contains no moving or phase-change components, resulting in predictable thermal behavior and favorable long-term reliability under continuous operation. The clamp-type cold plate improves serviceability by enabling repeated DIMM installation and replacement; however, its thermal performance and reliability are more sensitive to assembly tolerances, variations in contact pressure, and aging of

the thermal interface material. These factors may introduce performance dispersion across large-scale deployments.

The heat-pipe-based cold plate offers excellent temperature uniformity but requires more complex manufacturing processes, including vacuum sealing and charging the working fluid. Its long-term reliability is inherently linked to the integrity of the heat pipe and vapor chamber, as well as resistance to degradation under repeated thermal cycling. In high-density server environments with elevated and fluctuating heat flux, these reliability considerations become increasingly critical. Overall, the results indicate that manufacturing complexity, assembly robustness, and long-term operational stability must be considered alongside thermal and hydraulic performance when selecting liquid cooling solutions for practical DIMM deployment.

## 5. Conclusions

In this study, three memory liquid cooling configurations were compared under identical operating conditions: a water-flowing cold plate, a clamp-type cold plate, and a heat-pipe-based cold plate. The results show that coolant inlet temperature consistently affects memory, VR, and CPU temperatures across all configurations. As the coolant inlet temperature increases from 37 °C to 50 °C, memory temperature increases for all three cooling modes. Over the investigated range, memory temperature is maintained at approximately 57.65–66.98 °C for the water-flowing cold plate, 62.04–71.13 °C for the clamp-type cold plate, and 66.22–76.07 °C for the heat-pipe-based cold plate. The water-flowing cold plate exhibiting the lowest memory temperature and the heat-pipe-based cold plate exhibiting the highest.

A similar trend is observed for VR temperature. As the coolant inlet temperature increases, VR temperature rises to approximately 62.12–70.12 °C for the clamp-type cold plate, 57.26–64.21 °C for the heat-pipe-based cold plate, and 55.23–63.23 °C for the water-flowing cold plate. Despite differences in cold plate geometry, the relative temperature ranking remains stable across the investigated conditions. CPU temperature also increases with coolant inlet temperature for all three cooling modes. Across the investigated range, CPU temperature is maintained at approximately 59.15–70.19 °C for the water-flowing cold plate, 64.01–75.06 °C for the clamp-type cold plate, and 62.79–77.85 °C for the heat-pipe-based cold plate. The influence of upstream memory cooling on CPU temperature remains limited within the tested operating range.

Apparent differences in hydraulic performance are observed. As the coolant inlet temperature increases from 37 °C to 50 °C, the system pressure drop decreases for all three cooling modes. The pressure drop ranges from 32.73 to 35.98 kPa for the water-flowing cold plate, from 27.00 to 29.96 kPa for the heat-pipe-based cold plate, and from 24.19 to 26.69 kPa for the clamp-type cold plate.

Future work can be extended in three directions. First, multi-scale CFD methods can be applied to establish quantitative relationships between cold plate geometric parameters and coolant distribution, thereby supporting refined optimization of the flow channel topology. Second, the variation in interface thermal resistance under high heat-flux conditions should be investigated to develop low-resistance interface structures better suited to memory chip array layouts. Third, memory liquid cooling structures can be further studied in multi-heat-source coupled systems to develop liquid-loop design strategies for coordinated cooling of memory, CPUs, and accelerator devices, to meet the thermal requirements of DDR6 and future higher-power-density components.

**Author Contributions:** Conceptualization, Y.C. and Z.T.; methodology, M.K.; software, L.S. and M.K.; validation, Y.C. and W.W.; resources, Y.C.; data curation, Y.C.; writing—original draft preparation, Y.C. and L.Z.; writing—review and editing, Z.T. and M.L.; visualization, L.S.; supervision, M.K.; project

administration, Y.C.; funding acquisition, Y.C. All authors have read and agreed to the published version of the manuscript.

**Funding:** This research received no external funding.

**Data Availability Statement:** The original contributions presented in this study are included in the article. Further inquiries can be directed to the corresponding author.

**Conflicts of Interest:** All author were employed by the IEIT Systems Co., Ltd. The authors declare that the research was conducted in the absence of any commercial or financial relationships that could be construed as a potential conflict of interest.

## Nomenclature

| | |
|---|---|
| $T_{\text{cool,in}}$ | coolant inlet temperature (°C) |
| $T_{\text{mem,avg}}$ | average temperature of the monitored memory devices (°C) |
| $Q_{\text{mem}}$ | applied memory heat load (W) |
| $R_{\text{mem-cool}}$ | thermal resistance between memory and coolant (°C/w) |
| Abbreviations | |
| DDR4 | Double Data Rate 4 |
| DDR5 | Double Data Rate 5 |
| DIMM | Dual In-line Memory Module |
| CPU | Central Processing Unit |
| GPU | Graphics Processing Unit |
| VR | Voltage Regulator |

## References

1. Yu, Z.; Wu, J.; Sun, Z. Development of a dynamic bottom-up model for city-scale residential building stock to estimate greenhouse gas emissions. *Environ. Dev. Sustain.* **2025**. [CrossRef]
2. Mutlu, O.; Olgun, A.; Yüksel, İ.E. Memory-Centric Computing: Solving Computing's Memory Problem. In Proceedings of the 2025 IEEE International Memory Workshop (IMW), Monterey, CA, USA, 18–21 May 2025; pp. 1–4. [CrossRef]
3. Guo, Z.; Yin, J.; Bai, Y.; Zhu, D.; Shi, K.; Wang, G.; Cao, K.; Zhao, W. Spintronics for Energy- Efficient Computing: An Overview and Outlook. *Proc. IEEE* **2021**, *109*, 1398–1417. [CrossRef]
4. Hassan, H.; Olgun, A.; Yağlıkçı, A.G.; Luo, H.; Mutlu, O.; Zurich, E. Self-Managing DRAM: A Low-Cost Frame-work for Enabling Autonomous and Efficient DRAM Maintenance Operations. In Proceedings of the 2024 57th IEEE/ACM International Symposium on Microarchitecture (MICRO), Austin, TX, USA, 2–6 November 2024; pp. 949–965. [CrossRef]
5. Kim, K.; Park, M. Present and Future, Challenges of High Bandwith Memory (HBM). In Proceedings of the 2024 IEEE International Memory Workshop (IMW), Seoul, Republic of Korea, 12–15 May 2024; pp. 1–4. [CrossRef]
6. Kumar, A.A. Semantic memory: A review of methods. models, and current challenges. *Psychon. Bull. Rev.* **2021**, *28*, 40–80. [CrossRef] [PubMed]
7. Olgun, A.; Osseiran, M.; Yağlıkçı, A.G.; Tuğrul, Y.C.; Luo, H.; Rhyner, S.; Salami, B.; Luna, J.G.; Mutlu, O. Read Dis-turbance in High Bandwidth Memory: A Detailed Experimental Study on HBM2 DRAM Chips. In Proceedings of the 2024 54th Annual IEEE/IFIP International Conference on Dependable Systems and Networks (DSN), Brisbane, Australia, 24–27 June 2024; pp. 75–89. [CrossRef]
8. Modi, H.; Shahi, P.; Simon, V.S.; Chintaparthy, L.S.R.; Gupta, G.; Sivakumar, A.; Saini, S.; Bansode, P.; Ago-nafer, D. Experimental Study of Improved Chassis and Duct Redesign for Air-Cooled Server. In Proceedings of the 2023 22nd IEEE Intersociety Conference on Thermal and Thermomechanical Phenomena in Electronic Systems (ITherm), Orlando, FL, USA, 30 May–2 June 2023; pp. 1–8. [CrossRef]
9. Choe, J. Memory Technology 2021: Trends & Challenges. In Proceedings of the 2021 International Conference on Simulation of Semiconductor Processes and Devices (SISPAD), Dallas, TX, USA, 27–29 September 2021; pp. 111–115. [CrossRef]
10. Kandasamy, R.; Ho, J.Y.; Liu, P.; Wong, T.N.; Toh, K.C.; Chua, S.J. Two-phase spray cooling for high ambient tem-perature data centers: Evaluation of system performance. *Appl. Energy* **2022**, *305*, 117816. [CrossRef]
11. Kim, J.; Choi, H.; Lee, S.; Lee, H. Computational study of single-phase immersion cooling for high-energy density server rack for data centers. *Appl. Therm. Eng.* **2025**, *264*, 125476. [CrossRef]
12. Isazadeh, A.; Ziviani, D.; Claridge, D.E. Thermal management in legacy air-cooled data centers: An overview and perspectives. *Renew. Sustain. Energy Rev.* **2023**, *187*, 113707. [CrossRef]

13. Hnayno, M.; Chehade, A.; Klaba, H.; Bauduin, H.; Polidori, G.; Maalouf, C. Performance analysis of new liquid cooling topology and its impact on data centres. *Appl. Therm. Eng.* **2022**, *213*, 118733. [CrossRef]
14. Azarifar, M.; Arik, M.; Chang, J.-Y. Liquid cooling of data centers: A necessity facing challenges. *Appl. Therm. Eng.* **2024**, *247*, 123112. [CrossRef]
15. Ahmadi, V.E.; Barestrand, H.A.; Summers, J.; Yilmaz, C. Performance evaluation of two-phase direct-to-chip liq-uid cooling combined with air cooling for data centers. *Case Stud. Therm. Eng.* **2026**, *78*, 107650. [CrossRef]
16. Al Kez, D.; Foley, A.M.; Hasan Wong, F.W.B.M.; Dolfi, A.; Srinivasan, G. AI-driven cooling technologies for high-performance data centres: State-of-the-art review and future directions. *Sustain. Energy Technol. Assess.* **2025**, *82*, 104511. [CrossRef]
17. Orville, T.; Tajwar, M.; Bihani, R.; Saha, P.; Hannan, M.A. Enhancing Thermal Efficiency in Power Electronics: A Review of Advanced Materials and Cooling Methods. *Thermo* **2025**, *5*, 30. [CrossRef]
18. Chen, H.; Li, D. Current Status and Challenges for Liquid-Cooled Data Centers. *Front. Energy Res.* **2022**, *10*, 952680. [CrossRef]
19. Yuan, X.; Zhou, X.; Pan, Y.; Kosonen, R.; Cai, H.; Gao, Y.; Wang, Y. Phase change cooling in data centers: A review. *Energy Build.* **2021**, *236*, 110764. [CrossRef]
20. Liu, C.; Yu, H. Experimental Investigations on Heat Transfer Characteristics of Direct Contact Liquid Cooling for CPU. *Buildings* **2022**, *12*, 913. [CrossRef]
21. Ishimaru, K. Challenges of Flash Memory for Next Decade. In Proceedings of the 2021 IEEE International Reliability Physics Symposium (IRPS), Monterey, CA, USA, 21–25 March 2021; pp. 1–5. [CrossRef]
22. Dubey, P.; Pulugundla, G.; Srouji, A.K. Direct Comparison of Immersion and Cold-Plate Based Cooling for Au-tomotive Li-Ion Battery Modules. *Energies* **2021**, *14*, 1259. [CrossRef]
23. Gui, C.; Wang, Y.; Shen, C.; Wang, S.; Wang, R.; Lv, Z.; Lin, B.; Tian, W.; Li, Z.; Zhang, X.; et al. Advanced Cold Plate Liquid Cooling Solution for Hyper-scale Data Center Application. In Proceedings of the 2023 22nd IEEE Intersociety Conference on Thermal and Thermomechanical Phenomena in Electronic Systems (ITherm), Orlando, FL, USA, 30 May–2 June 2023; pp. 1–6. [CrossRef]
24. Sun, Q.; Zhi, G.; Zhou, S.; Dong, X.; Shen, Q.; Tao, R.; Qi, J. Advanced Design and Manufacturing Approaches for Structures with Enhanced Thermal Management Performance: A Review. *Adv. Mater. Technol.* **2024**, *9*, 2400263. [CrossRef]
25. Xue, Z.H.; Ai, B.C.; Qu, W. Data center energy conservation study utilizing loop heat pipes as a chip-level cooling technique and its industrial application. *Appl. Therm. Eng.* **2023**, *220*, 119715. [CrossRef]
26. Asgari, S.; MirhoseiniNejad, S.; Moazamigoodarzi, H.; Gupta, R.; Zheng, R.; Puri, I.K. A gray-box model for re-al-time transient temperature predictions in data centers. *Appl. Therm. Eng.* **2021**, *185*, 116319. [CrossRef]
27. Regany, D.; Majós, F.; Barrau, J.; Rosell, J.; Ibáñez, M.; Fréchette, L.G.; Vilarrubí, M. Design and test of shape memory alloy fins for self-adaptive liquid cooling device. *Appl. Therm. Eng.* **2022**, *206*, 118010. [CrossRef]
28. Guo, R.; Li, L. Heat dissipation analysis and optimization of lithium-ion batteries with a novel parallel-spiral serpentine channel liquid cooling plate. *Int. J. Heat Mass Transf.* **2022**, *189*, 122706. [CrossRef]
29. Huang, X.; Yan, J.; Zhou, X.; Wu, Y.; Hu, S. Cooling Technologies for Internet Data Center in China: Principle, Energy Efficiency, and Applications. *Energies* **2023**, *16*, 7158. [CrossRef]


**Disclaimer/Publisher's Note:** The statements, opinions and data contained in all publications are solely those of the individual author(s) and contributor(s) and not of MDPI and/or the editor(s). MDPI and/or the editor(s) disclaim responsibility for any injury to people or property resulting from any ideas, methods, instructions or products referred to in the content.

*energies*

MDPI

*Article*

# A Dual-Factor Defrosting Model for Air-Source Heat Pumps Considering Ambient Temperature and Compressor Frequency

**Xuyan Xu [1], Tao Zhang [2,*], Dongming Li [2], Wanchun Sun [2], Zhijiang Wu [2] and Yansheng Xu [2,*]**

[1] Department of Industrial Engineering, Tsinghua University, Beijing 100084, China; xuxy19@mails.tsinghua.edu.cn
[2] School of Energy and Automotive Engineering, Shunde Polytechnic University, Foshan 528000, China
* Correspondence: zhangtao5524@163.com (T.Z.); 10222@sdpt.edu.cn (Y.X.)

**Abstract**

This study presents a novel investigation into the coupled effects of ambient temperature and compressor frequency on frosting behavior and thermal performance of inverter-driven air-source heat pumps (ASHPs) under low-temperature, high-humidity conditions. Unlike previous studies that focused on single environmental parameters, this work systematically explores temperature–frequency coupling. Experiments were conducted on a 3-HP DC inverter low-ambient-temperature ASHP unit using a multi-climate simulated enthalpy difference test bench. Single-factor analysis shows that frosting is most severe at 0 °C, where the frost growth rate peaks. Regarding compressor frequency, the coefficient of performance (COP) initially increases and then decreases with frequency. The maximum COP occurs near 45 Hz, representing the optimal energy efficiency balance in this experimental system. Sensitivity analysis demonstrates that relative humidity contributes less than 5% to performance degradation at the critical 10% COP reduction point. Thus, ambient temperature and compressor frequency are the core determinants of defrosting timing. A dual-factor prediction model for the critical defrosting air-to-coil temperature difference ($\Delta T$) is developed using temperature ($t$) and frequency ($f$) as independent variables. Validation confirms that the model maintains prediction error within 10% under both single-factor and multi-factor coupling conditions. Collectively, this research quantifies the coupled effects of ambient temperature and compressor frequency on frosting performance and provides a novel theoretical framework for precise defrosting control in inverter ASHPs based on performance attenuation.

**Keywords:** air-source heat pump; frosting characteristics; compressor frequency; coupled effects; dual-factor model; precise defrosting

## 1. Introduction

As a high-efficiency and environmentally friendly heating technology, air source heat pumps (ASHP) have been widely used in building heating, industrial and agricultural drying, and other fields due to their advantages such as convenient installation, high energy efficiency ratio and strong applicability. Against the backdrop of the "dual carbon" target, promoting the large-scale application of air source heat pumps in cold and frigid regions has become one of the important paths for energy conservation and emission reduction in the building sector [1]. According to statistics, the sales of air source heat pumps in China reached RMB 22.7 billion in 2021, an increase of nearly 25% year-on-year [2], showing a continuous growth trend. However, during practical operation, frost can readily

accumulate on the evaporator surface under conditions of low ambient temperature and high relative humidity. This frost accumulation leads to increased heat transfer resistance and reduced airflow, consequently degrading the unit's heating capacity and escalating energy consumption. In severe cases, it can precipitate frequent defrosting cycles and even interrupt heating provision, thereby compromising operational reliability [3]. This technical bottleneck restricts the efficient and stable operation of air source heat pumps in low-temperature and high-humidity environments and has become a research hotspot of common concern in academia and industry.

Accurate judgment of the defrost node is the core issue affecting the operating efficiency and economy of air source heat pumps. Ma et al. [2] clearly pointed out in their latest review that the key challenge of defrost control is how to accurately identify the degree of frost and optimize the defrost start-stop logic. Suboptimal defrosting decisions, whether premature or delayed, significantly increased system energy consumption and compromised component reliability. The study by Klingebiel et al. [4] further quantified this impact, demonstrating that a deviation of 20 min from the optimal defrost start time could lead to a system efficiency reduction of up to 9.1%. If defrost is too early, the unit will fall into an ineffective operating state of "defrosting without frost", resulting in energy waste and unnecessary heating interruption. Conversely, if defrosting was initiated too late, excessive frost accumulation severely deteriorated the evaporator's heat exchange performance, leading to a significant attenuation of heating capacity and potentially causing safety issues such as compressor liquid hammer. Therefore, accurately identifying the critical defrosting point and achieving on-demand defrosting had become a cutting-edge topic in ASHP technology research.

Domestic and international scholars have conducted in-depth research on defrosting control strategies. Traditional defrosting control methods mainly relied on timers and temperature-time difference logic. Their simple structure and low cost led to widespread application in early products. However, because these methods could not adapt to complex and variable climatic conditions, their control accuracy was limited, resulting in significant efficiency losses. The study by Klingebiel et al. [4] showed that compared to an optimal defrost strategy, the efficiency loss of a timer-based control strategy (60 min interval) could reach 16.0%. While demand-based control reduced the loss to 7.0%, parameter trade-offs still existed under different frosting intensity conditions, limiting the overall system efficiency improvement.

To overcome the limitations of traditional methods, researchers have devoted efforts to developing refined control strategies based on thermodynamic parameters. Liu et al. proposed a novel frosting suppression control strategy for variable-speed air source heat pumps based on condensing-frosting performance maps, which optimises operating parameters to effectively suppress frosting while maintaining a high COP [5]. Compared with conventional control, this strategy increases the cyclic heating duration by 157.68% and reduces the daily defrosting frequency, defrosting duration, and defrosting energy consumption by 59.09%, 36.30%, and 32.96%, respectively [5]. Li et al. [6] developed a prediction model for the optimal defrosting initiation time for air source heat pumps with different configurations and operating modes. By establishing a cubic function relationship between a comprehensive index of configuration and operation (CICO) and the optimal initiation time, the model can predict the defrosting start time for different units. When the CICO value increases from 3.14 to 22.44, the optimal defrosting initiation time increases from 22 min to 148 min. Tang et al. experimentally studied the influence of frosting on heat pump performance through the operating characteristics of the outdoor fan and proposed a novel time-current-temperature difference (T-I-T) defrosting control method. The results show that the defrosting current threshold decreases with decreasing frosting severity; after

https://doi.org/10.3390/en19122787

applying this method, the defrosting frequency is reduced by 39.80%, and the average COP is increased by 10.60% [7]. Chung et al. [8] used a differential pressure sensor to monitor the pressure difference inside and outside the evaporator and found that the average pressure difference at the bottom of the evaporator could most accurately reflect the frost growth. By dimensionlessly processing the critical pressure difference, this method can be effectively applied to different fan speeds and heat exchanger specifications. In nine sets of verification experiments under different outdoor conditions, its root mean square error of prediction was as low as 5.5%.

In recent years, the rapid development of artificial intelligence technology has provided new ideas for breaking through the dependence on traditional models. Klingebiel et al. [9] proposed a self-optimizing defrosting start controller based on deep reinforcement learning, which can generate control rules autonomously by interacting with the environment using only the measurement values of standard temperature sensors. Hardware-in-the-loop tests were conducted under dynamic environmental conditions. The results show that the seasonal energy coefficient of the proposed controller is 7.1% higher than that of the time-type controller and 9.1% higher than that of the demand-type controller. Additionally, the heating capacity is increased by 4.9%. Under the fault condition of simulated airflow blockage, the efficiency is improved by 16.6% through an online learning adaptive adjustment strategy. Guo et al. [10] proposed a data-driven evaluation method for defrosting effect based on the heating capacity decay model. The frost state is identified by monitoring the heating capacity decay, and an on-demand defrosting control strategy is developed based on a fully connected neural network. The degree of frost is divided into six categories to achieve real-time identification. After application, the defrosting frequency is reduced by 66.3%, and the power consumption is reduced by 6.0%.

The development of image processing technology provides a more intuitive means of quantifying the degree of frost. Wang et al. [11] proposed a defrosting start control method based on image grayscale recognition. They developed corresponding image recognition equipment and control strategies. Experimental results showed that the defrosting accuracy of the method reached 93.33% in complex and variable environments. Compared with traditional temperature-time control, the defrosting accuracy was improved by 42.86%, and the average COP of the unit was improved by 36.60%. Zheng et al. [12] applied multi-threshold segmentation technology to divide the grayscale image into frost-free area, moderate frost area and heavy frost area, introduced the frost coefficient P (0~1) to evaluate the degree of frost, set P = 0.3 to start defrosting and P = 0.05 to end defrosting. Experiments verified that the method is applicable to a variety of outdoor environments.

While the aforementioned studies have advanced defrosting control technology from different perspectives, a key gap remains in current research. Most existing studies treat ambient temperature and relative humidity as the primary inputs. The unit's own operating parameters—especially compressor frequency—are largely ignored or considered as constants. Compressor frequency directly affects refrigerant mass flow rate, evaporation temperature, and heat exchange performance. Therefore, it profoundly influences frost growth rate and the timing of performance deterioration. A few recent studies have begun to acknowledge the role of frequency. For example, Wei et al. [13] studied the frosting performance of variable-frequency ASHPs under different climatic regions. They found that frequency significantly alters the frosting map boundaries. However, they did not develop a quantitative model linking frequency to the critical defrosting point. Consequently, a systematic exploration of the coupling relationship between compressor frequency, frost dynamics, and the defrosting critical point is still lacking. This current research status restricts the accuracy of defrosting control. It also limits the full release of the performance potential of inverter-driven ASHPs.

https://doi.org/10.3390/en19122787

In view of this, an enthalpy difference laboratory capable of accurately simulating various climatic conditions was built in this study. Using a 3 HP DC inverter low-ambient-temperature air-source heat pump (chilled water) unit as the research object, frosting experiments were systematically conducted under different ambient temperatures, compressor frequencies, and relative humidity conditions. By analyzing the frost layer growth pattern and the variation characteristics of performance parameters such as heating capacity, power consumption, and COP of the unit, the frosting characteristics under the coupling effect of temperature and frequency and their impact mechanism on system performance were revealed. The main contributions of this work are threefold. First, the coupled effect of ambient temperature and compressor frequency on the critical defrosting air-to-coil temperature difference ($\Delta T$) is quantified for the first time. Single-factor analysis shows that frosting is most severe at 0 °C and that the COP peaks at around 45 Hz, beyond which energy efficiency declines. Second, a novel dual-factor prediction model $\Delta T = f(t, f)$ that explicitly includes a cross-term to capture the temperature–frequency interaction is proposed. The model achieves high accuracy ($R^2 = 0.908$, RMSE = 0.82 °C) with a prediction error below 10%. Third, the model is validated under both single-factor and multi-factor coupled conditions (varying humidity and frequency), and it is demonstrated that relative humidity has a negligible effect (<5%) on the critical $\Delta T$, confirming that temperature and frequency are the core determinants of defrosting timing. This research fills the gap in existing defrosting control strategies that neglect the influence of compressor frequency, providing a theoretical framework and a practical engineering tool for achieving truly intelligent, precise, and performance-attenuation-based defrosting control in inverter air-source heat pumps.

## 2. Experimentation

### *2.1. Experimental Platform*

To conduct in-depth research on the operating characteristics and performance of air-source heat pump units under different environments, this study constructed a comprehensive experimental platform based on the enthalpy difference (water system) laboratory. This experimental platform aims to simulate diverse climatic conditions and load scenarios, enabling high-precision measurement and analysis of key performance parameters of the unit. The overall platform integrates functions such as environmental simulation, load simulation, data acquisition, and unit monitoring and control, providing a reliable foundation for subsequent systematic experiments. The overall appearance of the experimental platform is shown in Figure 1.




**Figure 1.** External view of the experimental prototype.

https://doi.org/10.3390/en19122787

### 2.2. Air Source Heat Pump Unit

The experiment used a 3HP DC inverter low-ambient-temperature air-source heat pump (chilled water) (TMEGA, Foshan, China) unit as the test object. This unit features full DC inverter control, allowing independent adjustment of compressor and fan speeds as well as the electronic expansion valve opening. This facilitates the flexible setting of different operating parameters during the experiment to investigate their impact on unit performance. The system uses R410A as the refrigerant. The main performance parameters of the unit are shown in Table 1. It has a compact structure, high control precision, and is suitable for stable operation over a wide temperature range.

**Table 1.** Parameter of air source heat pump unit.

| Parameter | Numerical Values |
|---|---|
| Unit power supply specifications | 220 V/50 Hz |
| Rated heating capacity (outdoor −12°C, outlet water 55°C) | 6.1 kW |
| Rated heating input power (outdoor −12°C, outlet water 55°C) | 2.52 kW |
| Rated heating current (outdoor −12°C, outlet water 55°C) | 11.45 A |
| Rated outlet water temperature | 41 °C |
| Maximum water temperature | 60 °C |
| Scope of work | −35~45 °C |
| Protection level | IP × 4 |
| Unit noise | ≤62 dB |
| Differential pressure between inlet and outlet water of the unit | 30 kPa |
| Rated circulating water volume | 1.09 $m^3$/h |
| External dimensions | 900 × 365 × 865 mm |
| Main unit control size | DN25 |
| Equipment weight | 110 kg |

### 2.3. Environmental Simulation System

To accurately simulate the operating environment of an air-source heat pump, the experimental setup includes two independent environmental simulation chambers: an indoor chamber and an outdoor chamber. The indoor temperature can be adjusted within the range of 5–50 °C, while the outdoor temperature range is −25–55 °C, and the relative humidity can be controlled between 20% and 95%. The system employs a PLC and intelligent power regulator for coordinated control, combined with electric heating and humidification devices, to ensure rapid and stable operation, providing realistic and controllable atmospheric conditions for unit performance testing.

### 2.4. Water System Simulation

To simulate actual water-side load, an independent water circulation testing system was installed on the outdoor side of the test bench. This system allows for continuous flow rate adjustment within the range of 0–7 $m^3$/h and uses turbine flow meters and resistance thermometers to monitor the supply and return water temperatures and flow rates in real time, thereby accurately calculating the unit's heating capacity and energy efficiency. The introduction of the water system enables the test bench to be suitable not only for air-side performance studies but also for comprehensively evaluating the unit's thermal performance on the water side.

### 2.5. Data Acquisition and Measurement System

To ensure the comprehensiveness and accuracy of experimental data, the experimental platform is equipped with a multi-parameter synchronous acquisition system. This system includes temperature and humidity sensors, pressure transmitters, thermocouples, an energy analyzer, and a high-precision flow meter, covering various key parameters from

https://doi.org/10.3390/en19122787

the air, water, and electrical sides (Table 2). All sensors are rationally arranged according to measurement specifications and are monitored and recorded in real time via a data acquisition instrument and host computer software, providing a reliable basis for subsequent data analysis.

**Table 2.** Parameters of main data acquisition equipment.

| Equipment | Model/Type | Measurement Parameters | Accuracy/Range | Sampling Interval |
|---|---|---|---|---|
| Platinum resistance thermometer | Pt-100 | air temperature and humidity | ±0.1 °C | real time |
| Differential pressure transmitter | — | wind static pressure | 0–300 Pa | real time |
| Turbine flow meter | — | Water flow | 0–3 $m^3$/h, ±0.5% FS | 6 s |
| thermocouple | K type | Coil temperature | −200~260 °C | 6 s |
| Electrical parameter instrument | — | Voltage, current, power | ±0.5% | real time |
| Data acquisition system | Industrial PC + Data Acquisition Card | Multi-channel synchronous acquisition | 16-bit resolution | |

### 2.6. Experimental Conditions

The variables in this experiment included ambient temperature, humidity, and compressor frequency. The experimental conditions were set using a single variable method. The temperature was set to 6 °C, 3 °C, 0 °C, −3 °C, −6 °C, −9 °C, and −12 °C, for a total of 7 conditions. The compressor frequency was set to 30 Hz, 45 Hz, 60 Hz, 76 Hz, and 90 Hz, for a total of 5 conditions. The humidity was set to 70%, 75%, 80%, and 85%. The specific experimental conditions for the temperature, compressor frequency, and humidity groups are shown in Tables 3, 4, and 5, respectively. In addition, in order to fully observe the changes in the unit's COP, the unit's original variable frequency control and defrosting settings were turned off, and it was operated in fixed frequency mode with manual defrosting.

**Table 3.** Temperature condition.

| Experiment Number | Temperature (°C) | Other Variable Value |
|---|---|---|
| 1-1 | 6 | Frequency: All frequency operating conditions<br>Relative humidity: 85% |
| 1-2 | 3 | |
| 1-3 | 0 | |
| 1-4 | −3 | |
| 1-5 | −6 | |
| 1-6 | −9 | |
| 1-7 | −12 | |

**Table 4.** Frequency operating condition.

| Experiment Number | Frequency Setting (Hz) | Other Variable Value |
|---|---|---|
| 2-1 | 30 | Temperature: All temperature conditions<br>Relative humidity: 85% |
| 2-2 | 45 | |
| 2-3 | 60 | |
| 2-4 | 76 | |
| 2-5 | 90 | |

https://doi.org/10.3390/en19122787

**Table 5.** Relative humidity operating condition.

| Experiment Number | Relative Humidity (%) | Other Variable Value |
|---|---|---|
| 3-1 | 70 | |
| 3-2 | 75 | Temperature: 3 °C, 0 °C, −6 °C |
| 3-3 | 80 | Frequency: 76 Hz |
| 3-4 | 85 | |

### *2.7. Data Processing*

When studying unit performance, frosting characteristics and performance indicators cannot usually be directly derived from measured data. Therefore, it is necessary to perform formula conversion and processing on the measured data in order to accurately assess the unit's heating capacity and energy efficiency. Heating capacity and coefficient of performance (COP), as key parameters for measuring unit performance, rely on a comprehensive analysis of variables such as environmental conditions and unit operating status for calculation.

The unit's heating capacity is determined by the water flow rate and supply and return water temperatures of the water system, and its calculation formula is shown in Equation (1):

$$Q = c_w \rho_w V_w \left(t_{wg} - t_{wh}\right) \tag{1}$$

where $Q$— heat output of the unit (kW);

$c_w$—specific heat capacity of water ((kJ/(kg·°C));
$\rho_w$—water density (kg/m$^3$);
$V_w$—water system volumetric flow rate (m$^3$/s);
$t_{wg}$—water supply temperature (°C);
$t_{wh}$—return water temperature (°C).

The COP (coefficient of performance) of a heat pump is an indicator of its energy efficiency. It represents the ratio of the heat provided by the heat pump per unit time to the power consumed. Its calculation formula is shown in Equation (2):

$$COP = Q/W \tag{2}$$

where $Q$—heat output of the unit (kW);

$W$—power consumed by the unit (kW).

During the frosting process of a heat pump, the air-to-coil temperature difference ($\Delta T$) is a key physical quantity that directly reflects the actual heat exchange state. However, the coil surface temperature measurement is easily affected by the location of the measuring point, resulting in variations. In contrast, the pressure fluctuation range at the evaporator outlet is smaller, providing a more stable and accurate reflection of the refrigerant saturation temperature within the coil. Therefore, this paper selects the evaporator outlet pressure as the observation basis and uses the pressure-temperature correspondence to calculate a more representative coil temperature, thereby calculating the air-to-coil temperature difference $\Delta T$. The calculation formula is shown in Equation (3):

$$\Delta T = t\ (^\circ\mathrm{C}) - \left(\frac{-2107.935}{ln((P+1)\times 100{,}000) - 21.8205} - 256.2377\right) \tag{3}$$

where $t$ —ambient temperature (°C).

$P$—gauge pressure (bar) at the evaporator outlet.

https://doi.org/10.3390/en19122787

*2.8. Uncertainty Analysis*

To evaluate the reliability of the experimental results, an uncertainty analysis was performed for the key derived parameters: heating capacity ($Q$), coefficient of performance (COP), and air-to-coil temperature difference ($\Delta T$). The measurement uncertainties of the primary instruments (Table 2) were propagated using the root-sum-square (RSS) method, assuming all input quantities are independent. The combined standard uncertainty $u_c(y)$ for a derived quantity $y = f(x1, x2, \ldots, xn)$ is calculated as

$$u_c(y) = \sqrt{\sum_{i=1}^{n} \left( \frac{\partial f}{\partial x_i} \cdot u(x_i) \right)^2} \tag{4}$$

where $u(x_i)$ is the standard uncertainty of the input $x_i$, and $\frac{\partial f}{\partial x_i}$ is the sensitivity coefficient.

The expanded uncertainty $U$ is then obtained by multiplying $u_c(y)$ by a coverage factor $k$ = 2, corresponding to a confidence level of approximately 95%:

$$U = k \cdot u_c(y) \tag{5}$$

Heating capacity $Q$ is given by $\mathrm{Q} = \mathrm{c_w \rho_w V_w (t_{wg} - t_{wh})}$. The relative combined uncertainty is

$$\frac{u_c(Q)}{Q} = \sqrt{\left( \frac{u(V_w)}{V_w} \right)^2 + \left( \frac{u(\Delta t_w)}{\Delta t_w} \right)^2} \tag{6}$$

where $\Delta t_w = t_{wg} - t_{wh}$. The turbine flow meter has an accuracy of ±0.5% of full scale (0–3 $\mathrm{m^3/h}$), yielding a standard uncertainty

$$u(V_w) = \frac{0.005 \times 3}{\sqrt{3}} \approx 0.00866\,\mathrm{m^3/h}$$

for a rectangular distribution. The Pt-100 sensors have an accuracy of ±0.1 °C each, so

$$u(\Delta t_w) = \frac{\sqrt{0.1^2 + 0.1^2}}{\sqrt{3}} \approx 0.0816\ ^\circ\mathrm{C}$$

The resulting relative expanded uncertainty for $Q$ is approximately ±5.1% ($k$ = 2).

Coefficient of performance $COP = Q/W$. The relative combined uncertainty is

$$\frac{u_c(\mathrm{COP})}{\mathrm{COP}} = \sqrt{\left( \frac{u_c(Q)}{Q} \right)^2 + \left( \frac{u(W)}{W} \right)^2} \tag{7}$$

The electrical parameter instrument has an accuracy of ±0.5% of the reading (assumed rectangular distribution). The relative standard uncertainty of $W$ is $0.005/\sqrt{3} \approx 0.00289$. Combining with the uncertainty of $Q$ gives a relative expanded uncertainty for COP of approximately ±6.2% ($k$ = 2).

Air-to-coil temperature difference $\Delta T = t - T_{\mathrm{coil}}(P)$, where $t$ is ambient temperature and $T_{\mathrm{coil}}(P)$ is the saturation temperature corresponding to the evaporator outlet pressure $P$. The combined uncertainty is

$$u_c(\Delta T) = \sqrt{u(t)^2 + u(T_{coil})^2} \tag{8}$$

The ambient temperature uncertainty $u(t) = 0.1/\sqrt{3} \approx 0.0577$ °C. The pressure transducer accuracy is ±0.5% FS (0–300 Pa), giving a standard uncertainty $u(P) = (0.005 \times 300)/\sqrt{3} \approx 0.866$ Pa. Using the saturation pressure-temperature relation for R410A, this translates to an uncertainty in $T_{\mathrm{coil}}$ of about ±0.3 °C (after calibration). Thus

https://doi.org/10.3390/en19122787

$u_c(\Delta T) \approx \sqrt{0.0577^2 + 0.173^2} \approx 0.182$ °C (assuming a typical value of $0.3/\sqrt{3} \approx 0.173$ °C for $u(T_{coil})$. The expanded uncertainty for $\Delta T$ is approximately ±0.36 °C ($k$ = 2).

All performance changes reported in this paper are significantly larger than the corresponding measurement uncertainties, confirming the statistical significance of the observed trends. This uncertainty analysis demonstrates that the experimental data are reliable for validating the proposed dual-factor defrosting model.

## 3. Results and Discussion

### *3.1. The Influence of Air Temperature*

Figure 2 shows the growth characteristics of frost layer thickness over time under various temperature conditions. Seven ambient temperature conditions were set: 6 °C, 3 °C, 0 °C, −3 °C, −6 °C, −9 °C, and −12 °C. The compressor frequency was 76 Hz, and the relative humidity was 85%. As can be seen from the figure, under different temperature conditions, the frost layer thickness exhibits a rapid initial growth followed by a slower growth over time, until the frost layer completely fills the gaps between the fins. This growth characteristic is determined by the physical mechanism of the frosting process: in the initial stage of frosting, the frost layer grows rapidly mainly in the vertical direction. This is because the fin surface temperature is low, and water vapor in the air quickly condenses into frost, leading to a rapid increase in frost layer thickness. As the frost layer thickens, the gaps between the fins are gradually filled, increasing thermal resistance, restricting airflow, and reducing the efficiency of water vapor transport. Therefore, the growth rate of the frost layer gradually slows down until the frost layer completely seals the gaps between the fins, at which point the frost layer growth tends to saturate. At lower ambient temperatures (−12 °C, −9 °C), the frost layer grows faster, especially at temperatures close to freezing (0 °C), where the water vapor content in the air is higher, the condensation rate is faster, and the frost layer can more easily cover the fin gaps in a shorter time. At higher temperatures (6 °C), the frost layer grows more slowly, and frost only begins to form on the surface after 40 min of operation. This is because the coil surface temperature is higher at this temperature, requiring a longer time to reach the conditions for frosting.

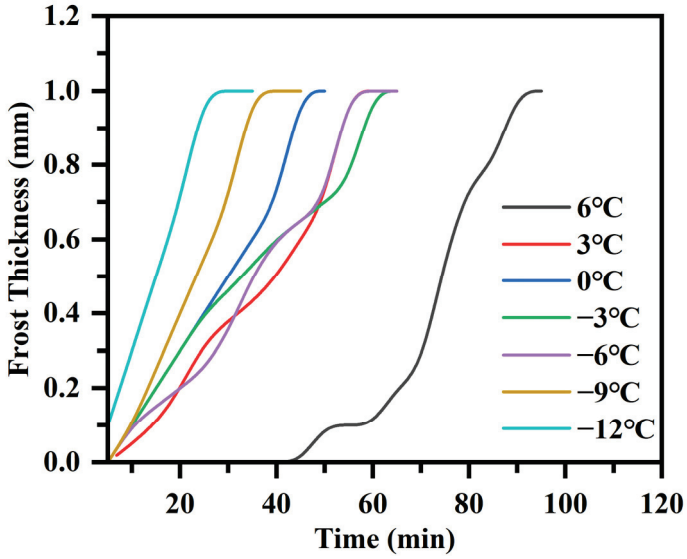



**Figure 2.** Changes in frost thickness with operating time under different ambient temperatures. The compressor frequency was 76 Hz, and the relative humidity was 85%.

Figure 3 shows the changes in unit heating capacity, power consumption, COP, and air-coil surface temperature difference over operating time under various temperature conditions. Seven temperature conditions were set: 6 °C, 3 °C, 0 °C, −3 °C, −6 °C, −9 °C, and −12 °C. The compressor frequency was 76 Hz, and the relative humidity was 85%. Figure 3a illustrates the change in unit heating capacity under different ambient temperatures. The initial heating capacity is mainly determined by the ambient temperature, showing a clear negative correlation. The lower the temperature (e.g., −12 °C), the worse the initial heating capacity, and the more gradual the decrease in heating capacity. At 6 °C, the frosting process is slow, and the heating capacity remains stable in the early stages due to the absence of frosting, only showing a significant decrease after a considerable period of operation. As operating time progresses, for a short period after frosting begins, the heating capacity briefly increases slightly due to the increased heat exchange capacity of the fins caused by the frost layer. Afterward, as the frost layer thickens, the heating capacity begins to decline rapidly. As can be seen from the figure, frosting is most severe at 0 °C, and the heating capacity declines the fastest. Ultimately, the heating capacity of all frosting conditions continued to decrease over time until the frost layer stabilized, at which point the rate of decrease gradually slowed down.

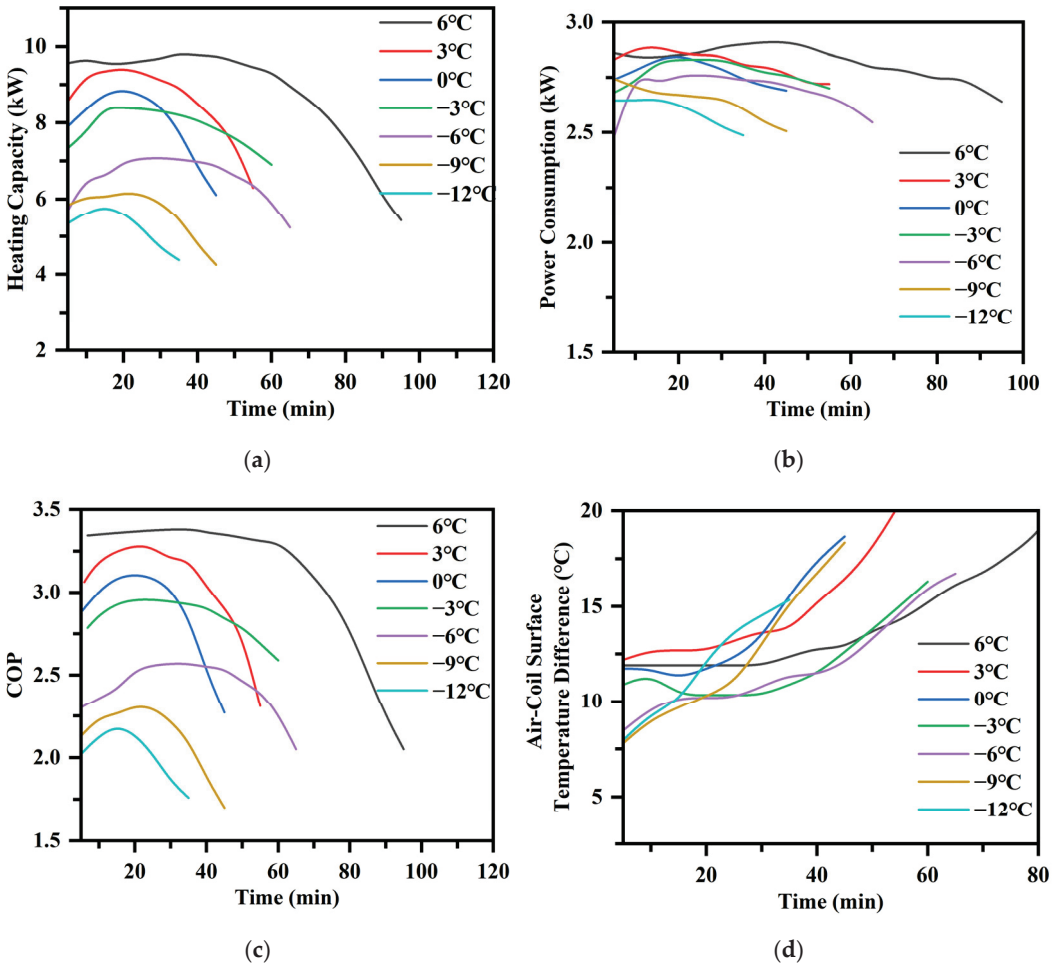



**Figure 3.** Changes in (**a**) unit heating capacity, (**b**) unit power consumption, (**c**) COP, and (**d**) temperature difference between air and coil surface over operating time at different ambient temperatures (6 °C, 3 °C, 0 °C, −3 °C, −6 °C, −9 °C, and −12 °C). The compressor frequency was 76 Hz, and the relative humidity was 85%.

Figure 3b depicts the power consumption characteristics of the heat pump during the frosting process at different ambient temperatures. Overall, the unit's power consumption

shows a slow decreasing trend as the frosting process progresses. The underlying mechanism is that the accumulation of frost increases the thermal resistance, leading to a decrease in evaporation temperature and thus reducing the refrigerant mass flow rate; consequently, the compressor's power consumption decreases.

Figure 3c plots COP against time (min) for each ambient temperature. In general, COP first increases slightly and then decreases gradually over time due to frost accumulation. Since the power consumption fluctuates gently throughout the entire frosting cycle, its changes have a weak impact on the system's COP (Figure 3b), making the COP trend mainly dependent on the decay of heating capacity. For temperatures above 0 °C (6 °C and 3 °C), the maximum occurs at the earliest time (10 min), because mild frosting quickly increases thermal resistance without any beneficial surface roughening effect. At temperatures below 0 °C, the maximum often appears at 20 min, indicating a short initial period of performance improvement before frosting dominates. This delay is caused by the fact that early-stage frost formation at subzero temperatures can enhance heat transfer by increasing surface roughness and turbulence, temporarily offsetting the insulation effect. The most severe relative COP drop (55.0%) occurs at −9 °C, followed by −12 °C (50.0%). The particularly large drop at −9 °C is attributed to a combination of a very low evaporating temperature and sustained frost growth, which leads to dense, highly insulating frost that accumulates rapidly after the initial enhancement period. At 0 °C, the drop is 34.6%, which is less than at −3 °C and below. This is because near 0 °C, frost grows quickly but remains relatively porous, causing less severe performance degradation than the dense frost formed at lower temperatures.

Figure 3d illustrates the variation in the temperature difference between the air and the coil surface during the defrosting process of the heat pump under different ambient temperatures. It can be seen that as time increases, the temperature difference between the coil and the air gradually increases, and the rate of increase accelerates. This is because as the frost layer continues to accumulate, the increased resistance in the air duct leads to a significant decrease in airflow, resulting in a reduction in the unit's heating capacity and a decrease in the evaporation temperature. The rising temperature difference between the coil and the air, and its accelerating rate, reflects the sharp deterioration of thermal performance in the later stages of defrosting. Furthermore, the rate of increase in temperature difference varies significantly under different ambient temperatures. For example, the rate of increase is higher at 0 °C than under other conditions, which is consistent with the pattern of frost layer thickness growth mentioned earlier at that temperature.

Figure 4 illustrates the relationship between the coefficient of performance (COP) of an air-source heat pump unit and the air-to-coil temperature difference ($\Delta T$) at a fixed compressor frequency. The figure contains five subplots corresponding to different compressor frequency conditions: (a) 30 Hz, (b) 45 Hz, (c) 60 Hz, (d) 76 Hz, and (e) 90 Hz. Taking the 76 Hz condition in Figure 4c as an example, the COP initially increases and then decreases with increasing air-to-coil temperature difference. When the temperature difference is small, the COP gradually increases and reaches a peak at a certain critical point. This upward phase can be attributed to the increased surface roughness of the fins due to the frost layer distribution during the initial frosting stage, which enhances airflow turbulence and heat exchange area, thereby improving heat exchange performance. However, when the temperature difference exceeds this critical value, the COP begins to decrease. This phenomenon can be attributed to the significant deterioration of evaporator heat exchange conditions caused by excessively large temperature differences, leading to a decrease in heating efficiency. Meanwhile, a decrease in ambient temperature also leads to a decrease in COP, especially at −12 °C, where the COP drop is more significant. This is mainly because the evaporator is more prone to frosting in low-temperature environments, resulting in

a further decrease in heat transfer efficiency. Furthermore, as shown in Figure 4a,b, when the ambient temperature is 6 °C, the COP does not show a clear variation with temperature difference, fluctuating within an air-to-coil temperature difference range of 8–10 °C. This is because when the compressor operates at low frequencies of 30 Hz and 45 Hz, the evaporator basically does not frost at 6 °C; thus, the unit performance tends to be stable with small fluctuations. However, at the same ambient temperature of 6 °C but with other frequencies (e.g., 60 Hz, 76 Hz, 90 Hz), frosting occurs, leading to a decrease in COP after an initial period. To cover a wide temperature range and achieve broader applicability, the rated condition of 76 Hz was selected for subsequent fixed-frequency studies to investigate the effects of other factors. This frequency provides more representative data for evaluating the coupled effects of ambient temperature and compressor frequency across different operating conditions.

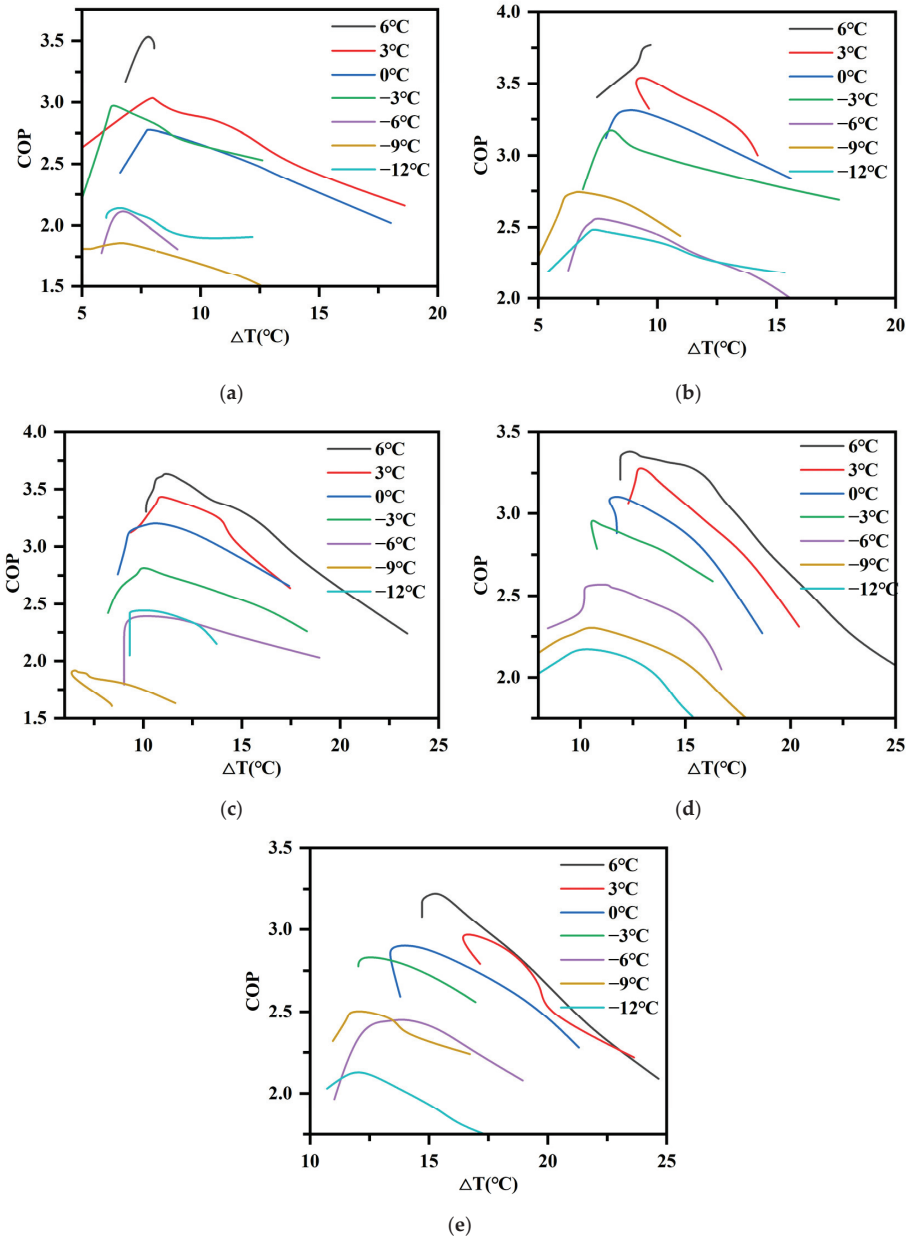



**Figure 4.** Changes in COP of the unit with air-to-coil temperature difference ($\Delta T$, temperature difference between the ambient temperature ($T_a$) and the coil surface temperature ($T_F$) converted from the evaporator outlet pressure) at different ambient temperatures (6 °C, 3 °C, 0 °C, −3 °C, −6 °C, −9 °C, and −12 °C) at a fixed frequency: (**a**) 30 Hz, (**b**) 45 Hz, (**c**) 60 Hz, (**d**) 76 Hz, (**e**) 90 Hz.

https://doi.org/10.3390/en19122787

### *3.2. The Influence of Compressor Frequency*

Figure 5a shows the characteristics of frost thickness variation over time under different compressor frequencies. Five frequency groups were set: 30 Hz, 45 Hz, 60 Hz, 76 Hz, and 90 Hz, with an ambient temperature of 0 °C and a relative humidity of 85%. As can be seen from Figure 5a, under different frequency conditions, the frost thickness generally shows a trend of rapid initial growth followed by a gradual slowdown until the frost completely fills the fin gaps. This phenomenon is closely related to the physical mechanism of the frosting process: in the initial stage of frosting, higher compressor frequencies typically correspond to larger refrigerant flow rates and lower evaporation temperatures, resulting in faster cooling of the fin surface and a higher water vapor condensation rate, thus causing the frost to grow faster in the vertical direction. As the frost thickens, airflow resistance increases, heat transfer resistance rises, and water vapor diffusion capacity decreases, leading to a gradual slowdown in the frost growth rate, which eventually stabilizes.

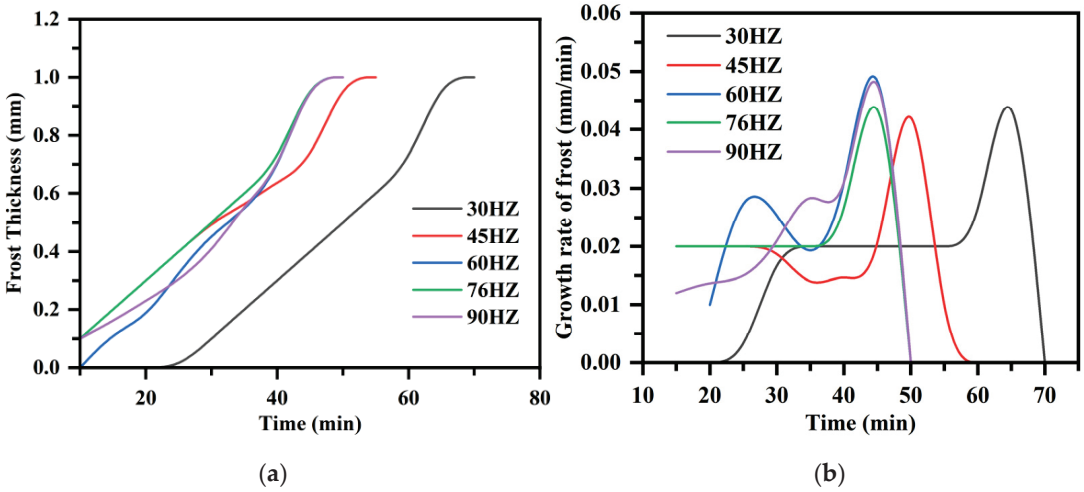



**Figure 5.** (**a**) Changes in frost thickness with running time at different compressor frequencies with an ambient temperature of 0 °C and a relative humidity of 85%. (**b**) The frost growth rate (mm/min) over time at an ambient temperature of 0 °C under five compressor frequencies (30, 45, 60, 76, and 90 Hz).

The frost growth rate exhibits a non-monotonic variation at different frequencies in Figure 5b. At 45 Hz, the growth rate remains low (≤0.02 mm/min) during the first 40 min, followed by a moderate peak of 0.06 mm/min at 50 min, after which it drops to zero. At higher frequencies (60, 76, and 90 Hz), the growth rate increases significantly after 35 min, reaching peak values of 0.066 mm/min (60 and 90 Hz) and 0.06 mm/min (76 Hz) around 45 min. The subsequent decline in growth rate is primarily because the frost layer has filled the fin gaps; further frost accumulation results in density increase rather than thickness growth. The higher frost growth rate at elevated frequencies can be explained by the increased refrigerant flow rate and lower evaporating temperature, which accelerate frost formation. At 30 Hz, the growth rate remains consistently low (≤0.06 mm/min) with a delayed peak at 65 min, indicating that lower frequencies slow down frosting but do not prevent it. Overall, Figure 5b clearly demonstrates that increasing compressor frequency accelerates frosting, with the most pronounced effects observed in the 60–90 Hz range.

Figure 6 shows the changes in unit heating capacity, unit power consumption, COP, and air-coil surface temperature difference with operating time at different compressor frequencies. Five frequency settings were set: 30 Hz, 45 Hz, 60 Hz, 76 Hz, and 90 Hz, with an ambient temperature of 0 °C and a relative humidity of 85%. Figure 6a reflects the dynamic process of unit heating capacity changing with frequency. The initial heating capacity is

https://doi.org/10.3390/en19122787

positively correlated with the compressor frequency. The higher the frequency (e.g., 90 Hz), the stronger the initial heating capacity, but the decrease in heating capacity is also more significant. At lower frequencies (e.g., 30 Hz), the initial heating capacity is smaller, but its decrease is more gradual. In the early stage of frosting, the growth of the frost layer under high-frequency conditions enhances the heat transfer capacity of the fin surface to some extent, resulting in a temporary increase in heating capacity. As the frost layer continues to accumulate, the airflow resistance increases and the thermal resistance rises, causing the heating capacity to show a downward trend under all operating conditions. Among them, the heating capacity declines most rapidly at 76 Hz due to the highest frosting rate. Ultimately, as frost growth stabilizes, the rate of decrease in heating capacity at each frequency gradually slows down and remains at a certain equilibrium level.

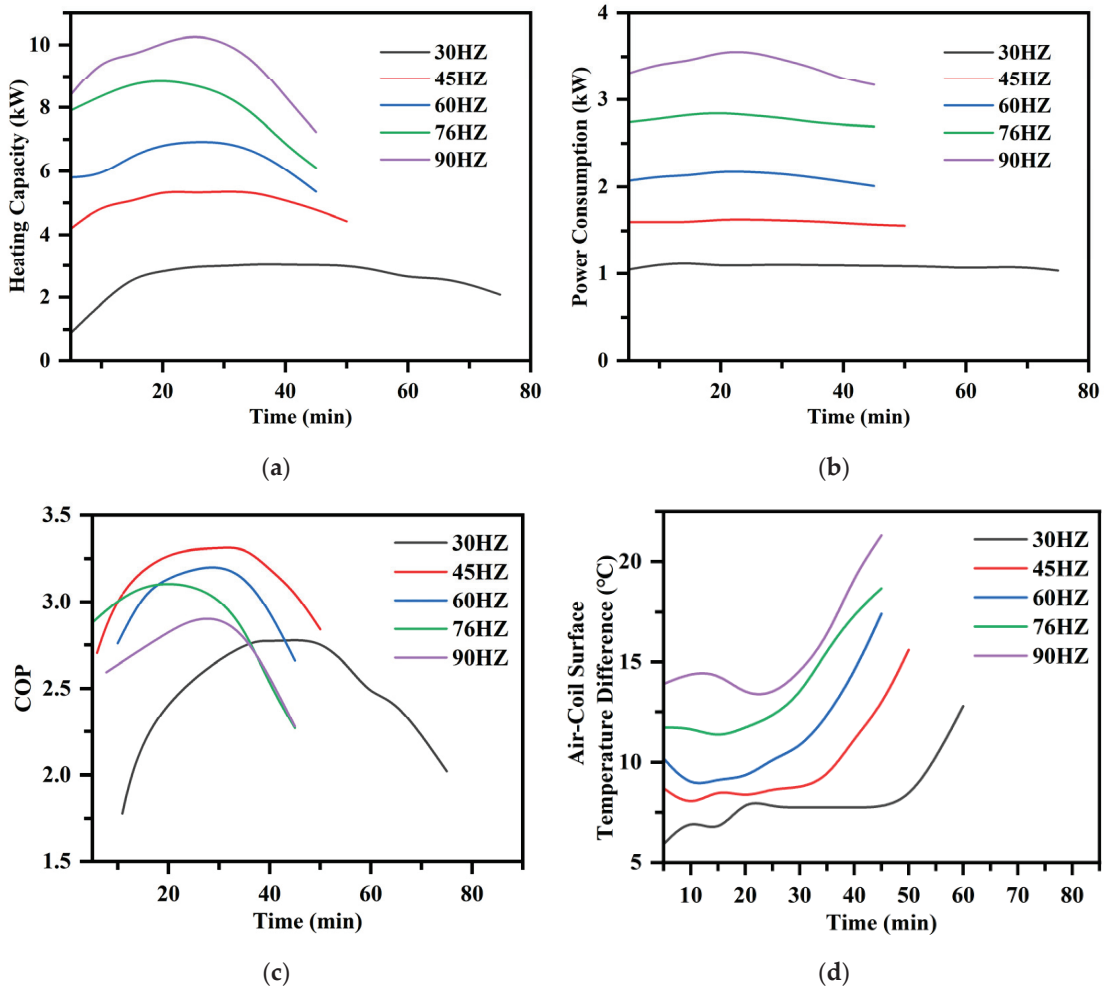



**Figure 6.** Changes in (**a**) unit heating capacity, (**b**) unit power consumption, (**c**) COP, and (**d**) air-coil surface temperature difference over operating time at different compressor frequencies with an ambient temperature of 0 °C and a relative humidity of 85%.

Figure 6b depicts the power consumption characteristics of the heat pump unit during the frosting process at different compressor frequencies. Overall, the unit's power consumption increases with increasing frequency, and at all frequencies, it shows a slow decreasing trend as the frosting process progresses. The underlying mechanism is that increasing the compressor frequency directly increases the refrigerant's mass flow rate and compression ratio, leading to a significant increase in power consumption. However, as the frost layer accumulates, the thermal resistance on the evaporator side increases, causing a decrease in evaporation temperature and pressure, further expanding the system pressure

https://doi.org/10.3390/en19122787

ratio. Simultaneously, the refrigerant flow rate also decreases. These two factors work together to gradually reduce the compressor's power consumption. At high-frequency operating conditions (e.g., 90 Hz), the power consumption decrease is more pronounced; while at low-frequency operating conditions (e.g., 30 Hz), due to the slow frost growth, the power consumption remains at a low level and changes relatively gradually.

As shown in the figure, the COP changes over time at different frequencies, indicating that the system performance coefficient exhibits a non-monotonic change characteristic of first increasing and then decreasing throughout the frosting cycle, consistent with the decay pattern of heating capacity (Figure 6c). This is because the heating benefit brought about by enhanced heat exchange in the early stage of frosting exceeds the slow increase in power consumption, leading to an increase in COP; while in the later stage of frost accumulation, the decrease in airflow and the deterioration of heat transfer intensify, resulting in a significant decrease in heating capacity and a subsequent decrease in COP. On the other hand, frequency has a significant impact on COP: when the frequency is too low, the refrigerant mass flow rate is insufficient, limiting the heating capacity; when the frequency is too high, the compressor power consumption increases sharply, and the energy efficiency ratio decreases. Therefore, the COP shows a trend of first increasing and then decreasing with frequency, reaching its maximum value at 45 Hz, indicating that this frequency achieves the optimal balance between heating capacity and power consumption in the current system.

Figure 6d illustrates the variation in the temperature difference between the air and the coil surface during the frosting process of a heat pump at different compressor frequencies over time. Overall, the air-to-coil temperature difference exhibits a typical non-monotonic variation characteristic with operating time: in the initial stage of frosting, the increased fin surface roughness due to frost growth enhances heat exchange to some extent, leading to a brief, slight decrease in temperature difference; however, as frost accumulates, airflow is significantly reduced due to duct blockage, resulting in a sharp deterioration in heat exchange performance. Simultaneously, the evaporation temperature gradually decreases, causing the temperature difference between the coil surface and the air to continuously increase, with the rate of increase gradually accelerating. Higher frequencies result in a larger refrigerant circulation per unit time and a greater heat exchange between the system and the air. However, under conditions of severe frosting leading to deteriorated heat exchange, the higher heat flux density exacerbates the heat transfer imbalance, resulting in a lower coil surface temperature and a significantly larger temperature difference between the coil and the air. Therefore, the temperature difference increases most dramatically at high frequencies (e.g., 90 Hz), while the temperature difference changes relatively gradually at low frequencies (e.g., 30 Hz).

Figure 7 illustrates the relationship between the coefficient of performance (COP) of an air-source heat pump unit and the air-to-coil temperature difference ($\Delta T$) at different compressor frequencies under a fixed ambient temperature. The figure contains six subplots corresponding to different temperature conditions: (a) 6 °C, (b) 3 °C, (c) 0 °C, (d) −3 °C, (e) −6 °C, (f) −9 °C, and (g) −12 °C. Overall, for any fixed frequency, COP exhibits a single-peak trend of first increasing and then decreasing with increasing $\Delta T$. However, the critical temperature difference corresponding to the peak value and the peak COP value differ significantly depending on the frequency. A key phenomenon is that the critical air-to-coil temperature difference corresponding to the optimal COP value also tends to increase with increasing compressor frequency. The main reason for this phenomenon is that increasing the frequency directly increases the refrigerant circulation flow rate and the system's heating capacity. At higher frequencies (such as 76 Hz or 90 Hz), the system requires a stronger heat exchange driving force (i.e., a larger temperature difference $\Delta T$)

https://doi.org/10.3390/en19122787

to fully realize its enhanced heating potential and overcome the significantly increased compressor power consumption due to high-frequency operation, thereby reaching the optimal COP. Therefore, the optimal COP for high-frequency operation occurs at a larger $\Delta T$. Conversely, at low frequencies (such as 30 Hz), the refrigerant flow is smaller, and the system requires less heat exchange driving force, so its optimal COP can be achieved at a smaller $\Delta T$. Taking 0 °C as an example, the peak COP at 45 Hz is higher than at other frequencies, indicating that the system achieves the best balance between heating capacity and power consumption under this mid-frequency condition. However, when the frequency increases to 76 Hz and 90 Hz, although the heating capacity is enhanced, the compressor power consumption increases sharply, resulting in a more significant decrease in COP in the high $\Delta T$ region and a rapid deterioration in system energy efficiency. In contrast, the COP curve changes relatively smoothly when operating at a low frequency of 30 Hz, with a low peak value and a wide distribution range. This is because the heat transfer intensity is limited at low refrigerant flow rates, and the system performance is less sensitive to air-to-coil temperature difference changes.

In summary, the compressor frequency not only determines the peak value of COP but also significantly affects the critical temperature difference required to achieve this optimal performance by changing the system's thermal balance and frosting characteristics.

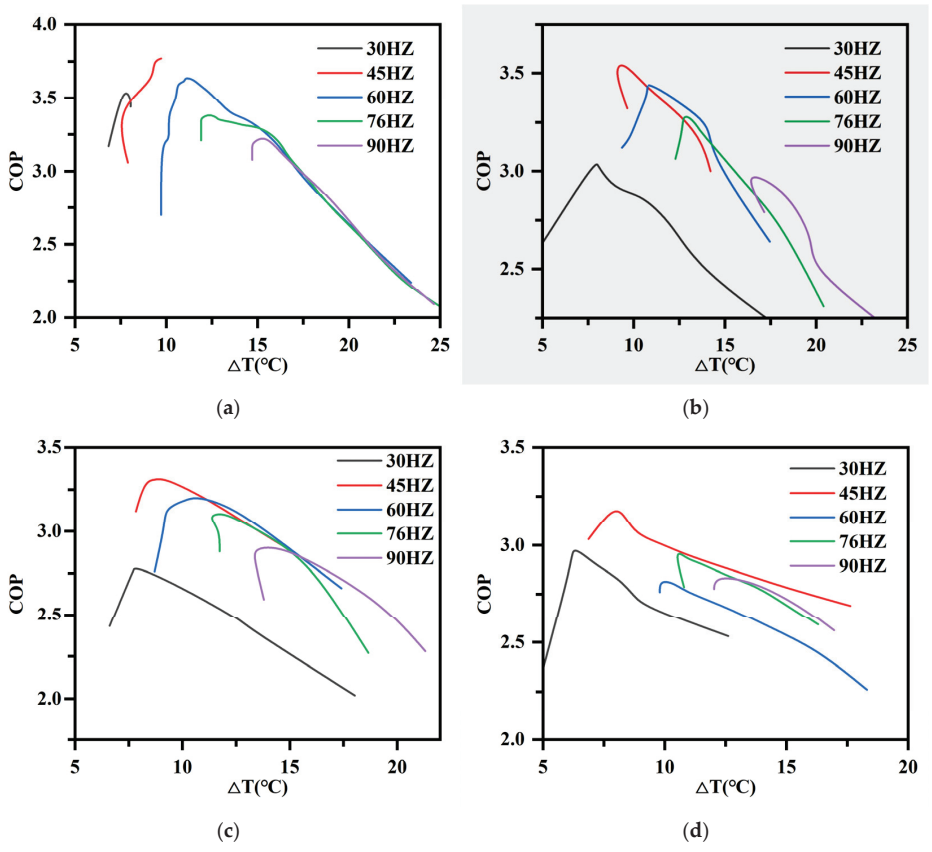



**Figure 7.** *Cont.*

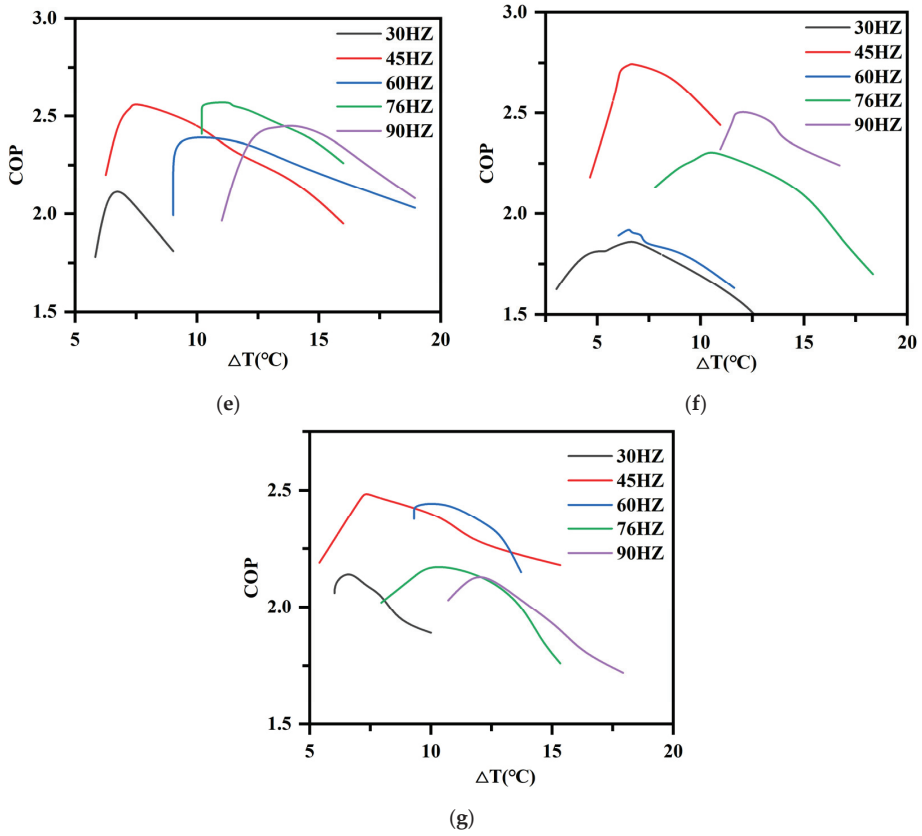



**Figure 7.** Changes in COP of the unit with air-to-coil temperature difference at different frequencies at a fixed temperature: (**a**) 6 °C, (**b**) 3 °C, (**c**) 0 °C, (**d**) −3 °C, (**e**) −6 °C, (**f**) −9 °C and (**g**) −12 °C.

### *3.3. The Influence of Ambient Humidity*

This study selected a 10% COP reduction as the criterion for unit defrosting to investigate the impact of ambient humidity on the defrosting trigger point under fixed-frequency (76 Hz) operation. As shown in Figure 8, at different ambient temperatures (3 °C, 0 °C, −6 °C), the key parameter characterizing evaporator heat transfer deterioration—the air-to-coil temperature difference—showed only a slight change with increasing ambient humidity, with an overall change rate of within 5%. This result indicates that although the frosting rate and frost accumulation are significantly affected by humidity, humidity is not a major influencing factor for determining the critical performance point of severe COP decline. This critical air-to-coil temperature difference is mainly determined by ambient temperature and compressor frequency; changes in humidity have a negligible impact and can be considered a secondary factor when formulating defrosting control strategies.

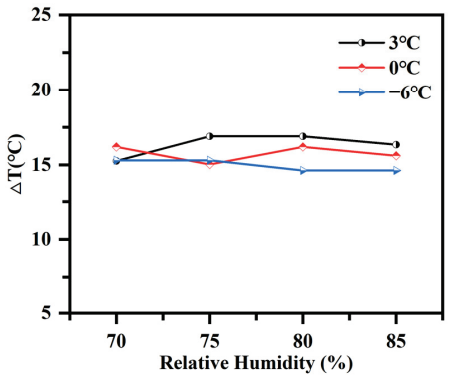



**Figure 8.** Air-to-coil temperature difference with relative humidity at a fixed frequency (76 Hz) and different ambient temperatures (3 °C, 0 °C, −6 °C) when the unit's COP is 10% lower than the initial COP.

*3.4. Establishment of Temperature–Frequency Two-Factor Fitting Model*

Based on the summary and analysis of previous experimental data, this study determined that outdoor ambient temperature ($t$) and compressor frequency ($f$) are the two most significant factors affecting the critical air-to-coil temperature difference ($\Delta T$) and established defrosting judgment conditions based on these. As shown in Table 6, this table summarizes the operating time and critical temperature difference ($\Delta T$) corresponding to a 10% COP reduction under different frosting ambient temperatures and compressor frequency conditions. The 10% COP reduction threshold was selected based on both engineering practice and the physical characteristics of the frosting process observed in the present experiments. In the field of ASHP defrosting control, a 10–15% reduction in heating capacity or COP is widely recognized as a reasonable criterion for initiating defrosting, because it represents a clear performance degradation while still avoiding excessive frost accumulation that could lead to system instability or safety issues (e.g., compressor liquid hammer). This value has been used in previous studies, such as by Klingebiel et al. [4], who adopted a 10% efficiency loss as the reference for evaluating defrosting controllers, and by Li et al. [14], who used a similar threshold to determine the optimal defrosting start time.

By fitting the data in the table, a dual-partition judgment function with outdoor ambient temperature and compressor frequency as independent variables was finally obtained, namely the critical air-to-coil temperature difference fitting formula:

$$\begin{aligned}\Delta \mathrm{T} = f(t,\, f) = \quad & (-43.8829921) + 0.109479735 \times f + 0.1874247533 \times (t \\ & +273) + (f - 61.575757576) \times ((t + 273 \\ & -269.45454545) \times 0.0009807284).\end{aligned}$$

A multivariate linear regression using the ordinary least-squares method was applied, with a model structure that includes linear terms for ambient temperature ($t$) and compressor frequency ($f$) as well as an interaction term $(f - f_0)(t - t_0)$ to capture their coupling effect. The regression was performed using standard statistical software on a data set of 33 valid points, covering five compressor frequencies (30, 45, 60, 76, 90 Hz) and seven ambient temperatures (6, 3, 0, −3, −6, −9, −12 °C) at 85% relative humidity; two points (45 Hz/6 °C and 30 Hz/6 °C) were excluded because no significant COP drop occurred. The coupling term adjusts the baseline linear prediction to match the experimental observation that raising the frequency at low temperatures causes a larger-than-additive increase in ΔT. For example, at −12 °C, increasing the frequency from 30 Hz to 90 Hz raises ΔT from 8.62 °C to 13.72 °C—a difference that the linear terms alone would underestimate. The positive 0.0009807284 thus captures the synergistic amplification of frequency effects at low temperatures, i.e., the more severe frosting caused by a high frequency in a cold environment.

To quantitatively evaluate the predictive accuracy of the proposed dual-factor model, the coefficient of determination ($R^2$) and the root-mean-square error (RMSE) were calculated based on the experimental data. The definitions are as follows:

$$R^2 = 1 - \frac{\sum_{i=1}^{n}\left(\Delta T_{\mathrm{meas},i} - \Delta T_{\mathrm{pred},i}\right)^2}{\sum_{i=1}^{n}\left(\Delta T_{\mathrm{meas},i} - \overline{\Delta T_{\mathrm{meas}}}\right)^2}$$

$$\mathrm{RMSE} = \sqrt{\frac{1}{n}\sum_{i=1}^{n}\left(\Delta T_{\mathrm{meas},i} - \Delta T_{\mathrm{pred},i}\right)^2}$$

https://doi.org/10.3390/en19122787

where $\Delta T_{\text{meas},i}$ is the measured critical air-to-coil temperature difference, $\Delta T_{\text{pred},i}$ is the value predicted by the model, $\overline{\Delta T_{\text{meas}}}$ is the mean of the measured values, and $n$ is the number of data points. Using the data listed in Table 6, the calculated $R^2$ is 0.908, and the RMSE is 0.82 °C. These results demonstrate that the dual-factor model exhibits excellent agreement with experimental measurements, with a prediction error well within the engineering acceptable range.

In addition, based on engineering practice, control thresholds under extreme conditions are defined to avoid defrosting too early or too late. The thresholds are set as follows: (1) running time greater than 20 min; (2) the fan operating current is more than 1.2 times the current when the fan is fully frosted at the corresponding fan frequency and lasts for 5 min. This forms an adaptive intelligent defrosting control technology.

The 20 min minimum run time threshold is derived directly from the experimental data in Table 6. Under the most severe frosting conditions tested, the earliest detected 10% COP reduction occurred at 20 min (at −12 °C, 90 Hz, with $\Delta T$ = 13.72 °C). Setting a minimum run time of 20 min ensures that only sustained frosting events—not transient measurement fluctuations—trigger defrosting, thereby avoiding mal-defrost. This value also aligns with the typical compulsory defrost cycle timers used in commercial ASHP controllers.

The outdoor fan employed in the present system is a brushless DC (BLDC) motor with closed-loop speed control. Under normal operation, the controller maintains a nearly constant rotational speed by adjusting the winding current in response to load torque variations. When frost accumulates on the outdoor coil, the increased airflow resistance raises the load torque on the fan. To keep the rotational speed unchanged, the BLDC controller increases the winding current; consequently, the measured fan current rises as frost builds up. For the fan current threshold (1.2 × nominal), the selection is supported by both the physical mechanisms observed in the present experiments and a recent study by Tang et al. [7], who experimentally showed that as frost accumulates on the outdoor coil, the airflow resistance increases, causing the airflow rate to drop and the fan electric current to increase abruptly, leading to fan performance deterioration and a reduction in system heating capacity. Their measurements demonstrated that a 20% increase in fan current corresponds to a substantial airflow blockage and a frost layer thickness that already causes a 10–15% COP decline under standard frosting conditions. The use of fan current as a defrost initiation parameter is further validated by the work of Xu et al. [15], who proposed a frosting state recognition method based on micro-fluctuations in evaporator fan current, achieving recognition accuracy above 94% across a temperature range of −5 to −20 °C. Additionally, the fan current threshold offers a more stable and less ambiguous signal compared to temperature-based methods, which are sensitive to sensor placement and environmental fluctuations.

**Table 6.** Time and temperature difference when 10% COP reduction for various frosting temperatures and frequencies.

| Compressor Frequency $f$ (Hz) | Ambient Temperature $t$ (°C) | Time (min) Required for 10% COP Reduction | Air-to-Coil Temperature Difference ($\Delta T$, °C) When 10% COP Reduction |
|---|---|---|---|
| 90 | 6 | 45 | 18.26 |
| 90 | 3 | 30 | 19.20 |
| 90 | 0 | 35 | 16.20 |
| 90 | −3 | 55 | 16.96 |
| 90 | −6 | 40 | 16.71 |
| 90 | −9 | 35 | 16.72 |

https://doi.org/10.3390/en19122787

**Table 6.** *Cont.*

| Compressor Frequency $f$ (Hz) | Ambient Temperature $t$ (°C) | Time (min) Required for 10% COP Reduction | Air-to-Coil Temperature Difference ($\Delta T$, °C) When 10% COP Reduction |
|---|---|---|---|
| 90 | −12 | 20 | 13.72 |
| 76 | 6 | 70 | 16.70 |
| 76 | 3 | 40 | 15.26 |
| 76 | 0 | 35 | 15.60 |
| 76 | −3 | 55 | 15.02 |
| 76 | −6 | 55 | 14.62 |
| 76 | −9 | 35 | 15.18 |
| 76 | −12 | 25 | 13.72 |
| 60 | 6 | 80 | 14.70 |
| 60 | 3 | 55 | 14.20 |
| 60 | 0 | 40 | 14.46 |
| 60 | −3 | 40 | 14.40 |
| 60 | −6 | 70 | 13.96 |
| 60 | −9 | 65 | 11.62 |
| 60 | −12 | 40 | 12.94 |
| 45 | 6 | 70 | -- |
| 45 | 3 | 60 | 12.19 |
| 45 | 0 | 45 | 12.80 |
| 45 | −3 | 60 | 12.60 |
| 45 | −6 | 60 | 10.20 |
| 45 | −9 | 60 | 10.96 |
| 45 | −12 | 45 | 11.44 |
| 30 | 6 | 30 | -- |
| 30 | 3 | 95 | 12.19 |
| 30 | 0 | 55 | 10.19 |
| 30 | −3 | 100 | 9.26 |
| 30 | −6 | 85 | 9.03 |
| 30 | −9 | 45 | 9.66 |
| 30 | −12 | 80 | 8.62 |

Figure 9 compares the measured and model-predicted values of the air-to-coil temperature difference when the unit's 10% COP reduction occurs under different frequency and ambient temperature conditions. Data analysis shows that the prediction results of the two-factor fitting model based on ambient temperature and compressor frequency are in good agreement with the measured values. The vast majority of data points are evenly distributed on both sides of the model's calculated value, indicating high prediction accuracy. Calculations show that the maximum deviation between the predicted and measured values under all operating conditions does not exceed 10%, which is acceptable for engineering applications, fully verifying the effectiveness and reliability of the fitting formula $\Delta T = f(t, f)$.

https://doi.org/10.3390/en19122787

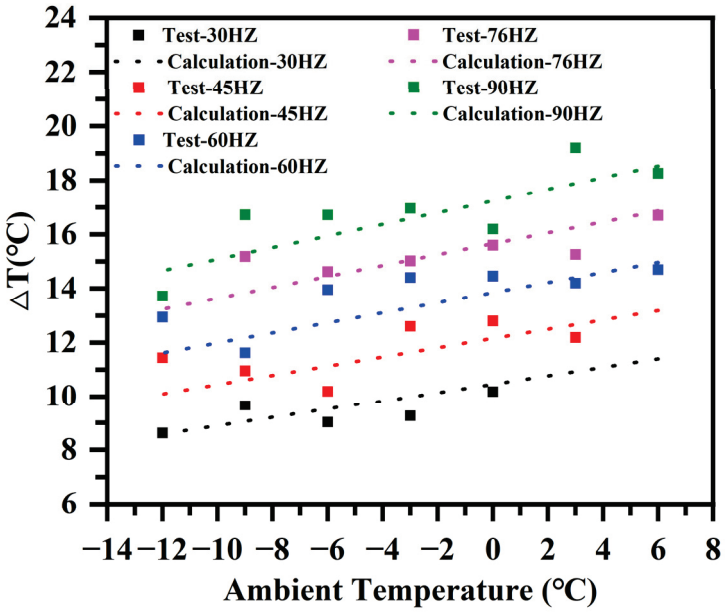



**Figure 9.** Comparison of measured and calculated values of air-to-coil temperature difference when the unit 10% COP reduction at different frequencies and ambient temperatures (6 °C, 3 °C, 0 °C, −3 °C, −6 °C, −9 °C, and −12 °C).

### *3.5. Validation of the Temperature–Frequency Two-Factor Fitting Model*

#### 3.5.1. Single-Factor Validation

Figure 10a shows the comparison between the measured and model predicted values of the air-to-coil temperature difference when the unit 10% COP reduction under a fixed ambient temperature of 0 °C, by additionally designing multiple frequency conditions such as 40, 55, 70, and 85 Hz. It can be seen that the data points at the newly added operating frequencies are evenly distributed on both sides of the reference line and fall entirely within the ±10% error band. This result clearly confirms that, under a single ambient temperature variable, the established critical air-to-coil temperature difference prediction model $\Delta T = f(f) \mid (t = 0\ ^\circ C)$ can accurately capture the influence of different frequency changes on the critical point of system performance. The verification at the added frequency points further strengthens the effectiveness and reliability of the model, providing solid data support for the accurate formulation of defrosting control strategies.

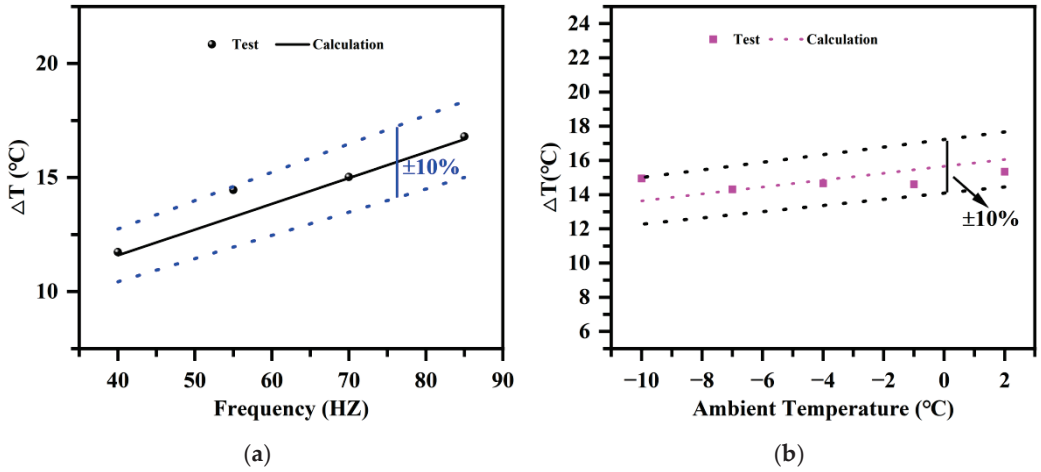



**Figure 10.** Comparison of measured and calculated values of air-to-coil temperature difference when the unit 10% COP reduction at a fixed ambient temperature of 0 °C (**a**) and at a fixed frequency of 76 Hz (**b**).

https://doi.org/10.3390/en19122787

Figure 10b shows the comparison between the measured and model-predicted values of the air-to-coil temperature difference corresponding to a 10% COP reduction when the ambient temperature changes, under the condition that the compressor frequency is fixed at 76 Hz. Test data from multiple temperature conditions, including 2 °C, −1 °C, −4 °C, −7 °C, and −10 °C, show that the measured values at all temperatures are highly consistent with the model calculations and are evenly distributed on both sides of the reference line, falling entirely within the ±10% error range. This result further confirms that, under a fixed frequency variable, the established critical temperature difference prediction model $\Delta T$= f($t$) |($f$ = 76 HZ) can accurately reflect the effect of different ambient temperatures on the critical point of system performance. The validation at the added temperature points significantly enhances the model's applicability and reliability over a wide temperature range, providing a more comprehensive theoretical basis for the accurate formulation of defrosting control strategies under complex operating conditions.

3.5.2. Two-Factor Validation

Based on the above experiments, further verification tests were conducted under coupled conditions of multiple factors (relative humidity, ambient temperature, and compressor frequency). By setting the relative humidity to 85% (Tables 7–9) and 75% (Tables 10–12), and the ambient temperature to 0 °C (Tables 7 and 10), −3 °C (Tables 8 and 11), and −6 °C (Tables 9 and 12), and allowing the heat pump to run freely in variable frequency mode (temperature fluctuation controlled within ±2 °C), the system collected measured data of the air-to-coil temperature difference under different operating conditions and compared them with the model prediction values. The results are shown in the Tables 7–12. The results show that under coupled operating conditions where ambient temperature (0 °C, −3 °C, −6 °C), relative humidity (75%, 85%), and compressor frequency (58–90 Hz) change together, the established critical air-to-coil temperature difference prediction model ($\Delta T$ = f ($t$, $f$)) exhibits good engineering applicability and prediction accuracy. Specifically, in different combinations of operating conditions, when the deviation between the measured value and the calculated value of the air-to-coil temperature difference is within 12%, the system COP decrease rate is stably maintained at around 10%. This result verifies that the model can accurately capture the critical decay point of system performance during the frosting process. Most importantly, the data comparison under the same temperature and different humidity conditions shows that the humidity change did not have a significant impact on the critical air-to-coil temperature difference, which further strengthens the reliability of the model with temperature and frequency as the core criteria and provides solid data support and theoretical basis for the formulation of intelligent defrosting control strategies under complex actual conditions.

**Table 7.** The air-to-coil temperature difference under variable frequency operating conditions with ambient temperature 0 ± 2 °C and relative humidity 85%, compared with model predictions.

| Time | Ambient Temperature (°C) | Control Value $\Delta T$ (°C) | $\Delta T$ (Converted from Measured Pressure) (°C) | Difference from Control Value | Frost Layer Thickness (mm) | COP | COP Decline |
|---|---|---|---|---|---|---|---|
| 19:33 | −0.45 | 15.56 | 10.76 | −30.87% | | 2.52 | 14.58% |
| 19:38 | −0.14 | 15.63 | 10.56 | −32.45% | micro-hang | 2.68 | 9.15% |
| 19:43 | −1.25 | 15.40 | 11.01 | −28.52% | 0.1 | 2.66 | 9.83% |
| 19:48 | −1.88 | 15.28 | 10.92 | −28.54% | 0.2 | 2.62 | 11.19% |
| 19:53 | 1.32 | 15.92 | 11.51 | −27.72% | 0.3 | 2.85 | 3.39% |
| 19:58 | 1.89 | 16.04 | 12.08 | −24.68% | 0.4 | 2.95 | 0.00% |
| 20:03 | 0.39 | 15.73 | 12.65 | −19.60% | 0.5 | 2.85 | 3.39% |
| 20:08 | −0.03 | 15.65 | 12.77 | −18.42% | 0.6 | 2.7 | 8.47% |

https://doi.org/10.3390/en19122787

**Table 7.** *Cont.*

| Time | Ambient Temperature (°C) | Control Value Δ*T* (°C) | Δ*T* (Converted from Measured Pressure) (°C) | Difference from Control Value | Frost Layer Thickness (mm) | COP | COP Decline |
|---|---|---|---|---|---|---|---|
| 20:13 | −0.22 | 15.61 | 14.24 | −8.80% | 0.7 | 2.62 | 11.19% |
| 20:18 | −0.35 | 15.58 | 15.85 | 1.68% | Full | 2.44 | 17.29% |
| 20:23 | 0.1 | 15.67 | 18.12 | 15.63% | | 2.33 | 21.02% |
| 20:28 | 0.01 | 13.85 | 13.90 | 0.40% | | 1.87 | 36.61% |

**Table 8.** The air-to-coil temperature difference under variable frequency operating conditions with ambient temperature of $-3 \pm 2$ °C and relative humidity of 85%, compared with model predictions.

| Time | Frequency | Ambient Temperature (°C) | ΔT Calculation (°C) | ΔT (Pressure Conversion) (°C) | Difference from Control Value | Frost Layer Thickness (mm) | COP | COP Decline |
|---|---|---|---|---|---|---|---|---|
| 14:20 | 76 | −3.15 | 15.02 | 10.19 | −32.15% | 0.1 | 2.4 | 13.36% |
| 14:25 | 76 | −3.19 | 15.01 | 10.70 | −28.69% | 0.25 | 2.63 | 5.05% |
| 14:30 | 76 | −4.42 | 14.76 | 10.61 | −28.16% | 0.35 | 2.6 | 6.14% |
| 14:35 | 76 | −1.9 | 15.27 | 9.83 | −35.63% | 0.4 | 2.73 | 1.44% |
| 14:40 | 76 | −2.13 | 15.23 | 11.76 | −22.73% | 0.5 | 2.77 | 0.00% |
| 14:45 | 76 | −3.14 | 15.02 | 10.75 | −28.41% | 0.6 | 2.66 | 3.97% |
| 14:50 | 76 | −2.74 | 15.10 | 12.29 | −18.64% | 0.7 | 2.69 | 2.89% |
| 14:55 | 76 | −3.09 | 15.03 | 13.11 | −12.81% | 0.75 | 2.58 | 6.86% |
| 15:00 | 76 | −2.92 | 15.07 | 14.48 | −3.86% | Full | 2.5 | 9.75% |
| 15:05 | 76 | −2.93 | 15.06 | 15.09 | 0.21% | | 2.35 | 15.16% |
| 15:10 | 76 | −2.77 | 15.10 | 18.54 | 22.79% | | 2.21 | 20.22% |

**Table 9.** The air-to-coil temperature difference under variable frequency operating conditions with ambient temperature of $-6 \pm 2$ °C and relative humidity of 85%, compared with model predictions.

| Time | Frequency | Ambient Temperature (°C) | ΔT Calculation (°C) | ΔT (Pressure Conversion) (°C) | Difference from Control Value | Frost Layer Thickness (mm) | COP | COP Decline |
|---|---|---|---|---|---|---|---|---|
| 17:05 | 70 | −6 | 13.80 | 9.61 | −30.40% | micro-hang | 2.08 | 19.69% |
| 17:10 | 76 | −6.47 | 14.35 | 9.14 | −36.34% | 0.1 | 2.33 | 10.04% |
| 17:15 | 76 | −7.39 | 14.16 | 10.01 | −29.30% | 0.2 | 2.32 | 10.42% |
| 17:20 | 76 | −5.12 | 14.62 | 8.77 | −39.99% | 0.3 | 2.53 | 2.32% |
| 17:25 | 76 | −4.87 | 14.67 | 10.74 | −26.83% | 0.4 | 2.59 | 0.00% |
| 17:30 | 76 | −6.41 | 14.36 | 10.38 | −27.70% | 0.5 | 2.49 | 3.86% |
| 17:35 | 76 | −7.17 | 14.21 | 10.23 | −27.97% | 0.6 | 2.43 | 6.18% |
| 17:40 | 76 | −5.82 | 14.48 | 10.38 | −28.35% | 0.65 | 2.5 | 3.47% |
| 17:45 | 76 | −5.98 | 14.45 | 11.42 | −20.93% | 0.7 | 2.52 | 2.70% |
| 17:50 | 76 | −6.09 | 14.43 | 11.93 | −17.27% | 0.75 | 2.5 | 3.47% |
| 17:55 | 76 | −6.06 | 14.43 | 12.60 | −12.72% | Full | 2.45 | 5.41% |
| 18:00 | 76 | −6.01 | 14.44 | 14.61 | 1.19% | | 2.4 | 7.34% |
| 18:05 | 64 | −6.04 | 13.15 | 8.99 | −31.68% | | 1.94 | 25.10% |
| 18:10 | 58 | −5.77 | 12.56 | 11.63 | −7.37% | | 1.57 | 39.38% |

https://doi.org/10.3390/en19122787

**Table 10.** The air-to-coil temperature difference under variable frequency operating conditions with ambient temperature $0 \pm 2$ °C and relative humidity 75%, compared with model predictions.

| Time | Frequency | Ambient Temperature (°C) | ΔT Calculation (°C) | ΔT (Pressure Conversion) (°C) | Difference from Control Value | Frost Layer Thickness (mm) | COP | COP Decline |
|---|---|---|---|---|---|---|---|---|
| 12:56 | 76 | −0.33 | 15.59 | 9.86 | −36.76% | | 2.57 | 13.76% |
| 13:01 | 76 | −0.1 | 15.63 | 10.60 | −32.23% | micro-hang | 2.78 | 6.71% |
| 13:06 | 76 | −0.67 | 15.52 | 11.06 | −28.73% | 0.1 | 2.79 | 6.38% |
| 13:11 | 76 | −2.02 | 15.25 | 10.78 | −29.32% | 0.2 | 2.76 | 7.38% |
| 13:16 | 76 | −1.2 | 15.41 | 11.60 | −24.76% | 0.3 | 2.78 | 6.71% |
| 13:21 | 76 | 1.54 | 15.96 | 11.23 | −29.67% | 0.4 | 2.98 | 0.00% |
| 13:26 | 76 | 1.65 | 15.99 | 12.35 | −22.78% | 0.45 | 2.93 | 1.68% |
| 13:31 | 76 | −0.09 | 15.64 | 12.71 | −18.74% | 0.5 | 2.73 | 8.39% |
| 13:36 | 76 | −0.39 | 15.58 | 12.95 | −16.85% | 0.6 | 2.71 | 9.06% |
| 13:41 | 76 | −0.18 | 15.62 | 13.71 | −12.19% | 0.7 | 2.69 | 9.73% |
| 13:46 | 76 | 0.08 | 15.67 | 15.69 | 0.10% | 0.75 | 2.65 | 11.07% |
| 13:51 | 64 | −0.26 | 14.25 | 9.93 | −30.33% | Full | 2.55 | 14.43% |
| 13:56 | 58 | 0.05 | 13.63 | 13.39 | −1.75% | | 1.62 | 45.64% |

**Table 11.** The air-to-coil temperature difference under variable frequency operating conditions with ambient temperature of $-3 \pm 2$ °C and relative humidity of 75%, compared with model predictions.

| Time | Frequency | Ambient Temperature (°C) | ΔT Calculation (°C) | ΔT (Pressure Conversion) (°C) | Difference from Control Value | Frost Layer Thickness (mm) | COP | COP Decline |
|---|---|---|---|---|---|---|---|---|
| 15:11 | 76 | −3.08 | 15.03 | 10.81 | −28.07% | | 2.47 | 12.72% |
| 15:16 | 76 | −3.54 | 14.94 | 11.49 | −23.12% | micro-hang | 2.53 | 10.60% |
| 15:21 | 76 | −4.53 | 14.74 | 11.67 | −20.87% | 0.1 | 2.62 | 7.42% |
| 15:26 | 76 | −4.89 | 14.67 | 10.72 | −26.95% | 0.15 | 2.6 | 8.13% |
| 15:31 | 76 | −4.11 | 14.83 | 10.35 | −30.22% | 0.2 | 2.67 | 5.65% |
| 15:36 | 76 | −1.56 | 15.34 | 11.24 | −26.75% | 0.25 | 2.83 | 0.00% |
| 15:41 | 76 | −1.8 | 15.29 | 11.54 | −24.53% | 0.3 | 2.78 | 1.77% |
| 15:46 | 76 | −2.82 | 15.09 | 11.64 | −22.87% | 0.4 | 2.76 | 2.47% |
| 15:51 | 76 | −3.53 | 14.94 | 11.50 | −23.06% | 0.5 | 2.68 | 5.30% |
| 16:06 | 76 | −3.66 | 14.92 | 11.37 | −23.80% | 0.55 | 2.67 | 5.65% |
| 16:01 | 76 | −4.03 | 14.84 | 11.58 | −22.01% | 0.6 | 2.61 | 7.77% |
| 16:06 | 76 | −3.07 | 15.04 | 11.39 | −24.27% | 0.7 | 2.67 | 5.65% |
| 16:11 | 76 | −2.41 | 15.17 | 13.20 | −13.00% | 0.75 | 2.69 | 4.95% |
| 16:16 | 76 | −2.99 | 15.05 | 13.21 | −12.27% | Full | 2.62 | 7.42% |
| 16:21 | 76 | −3.46 | 14.96 | 13.33 | −10.85% | | 2.57 | 9.19% |
| 16:26 | 36 | −3.14 | 10.63 | 6.55 | −38.39% | | 2.54 | 10.25% |
| 16:31 | 58 | −2.97 | 13.08 | 10.37 | −20.68% | | 2.27 | 19.79% |

**Table 12.** The air-to-coil temperature difference under variable frequency operating conditions with ambient temperature of $-6 \pm 2$ °C and relative humidity of 75%, compared with model predictions.

| Time | Frequency | Ambient Temperature (°C) | ΔT Calculation (°C) | ΔT (Pressure Conversion) (°C) | Difference from Control Value | Frost Layer Thickness (mm) | COP | COP Decline |
|---|---|---|---|---|---|---|---|---|
| 18:12 | | | | | | | | |
| 18:17 | 70 | −5.72 | 13.86 | 9.31 | −32.84% | | 2.23 | 18.32% |
| 18:22 | 76 | −6.17 | 14.41 | 10.03 | −30.43% | micro-hang | 2.28 | 16.48% |
| 18:27 | 76 | −7.42 | 14.16 | 9.98 | −29.48% | 0.1 | 2.31 | 15.38% |
| 18:32 | 76 | −7.57 | 14.13 | 10.45 | −26.00% | 0.2 | 2.35 | 13.92% |

https://doi.org/10.3390/en19122787

**Table 12.** *Cont.*

| Time | Frequency | Ambient Temperature (°C) | ΔT Calculation (°C) | ΔT (Pressure Conversion) (°C) | Difference from Control Value | Frost Layer Thickness (mm) | COP | COP Decline |
|---|---|---|---|---|---|---|---|---|
| 18:37 | 76 | −6.8 | 14.28 | 9.99 | −30.03% | 0.25 | 2.45 | 10.26% |
| 18:42 | 76 | −4.8 | 14.69 | 10.23 | −30.37% | 0.3 | 2.56 | 6.23% |
| 18:47 | 76 | −4.2 | 14.81 | 12.00 | −18.99% | 0.35 | 2.66 | 2.56% |
| 18:52 | 76 | −6.28 | 14.39 | 11.12 | −22.69% | 0.4 | 2.52 | 7.69% |
| 18:57 | 76 | −7.33 | 14.18 | 10.69 | −24.56% | 0.5 | 2.40 | 12.09% |
| 19:02 | 76 | −6.72 | 14.30 | 10.68 | −25.28% | 0.6 | 2.45 | 10.26% |
| 19:07 | 76 | −6.06 | 14.43 | 11.34 | −21.40% | 0.65 | 2.49 | 8.79% |
| 19:12 | 76 | −6.11 | 14.42 | 11.91 | −17.39% | 0.7 | 2.48 | 9.16% |
| 19:17 | 76 | −6.13 | 14.42 | 11.89 | −17.50% | 0.75 | 2.73 | 0.00% |
| 19:22 | 76 | −6.19 | 14.41 | 12.47 | −13.47% | 0.78 | 2.44 | 10.62% |
| 19:27 | 76 | −6.01 | 14.44 | 13.29 | −7.98% | Full | 2.42 | 11.36% |
| 19:32 | 76 | −6.15 | 14.41 | 14.47 | 0.41% | | 2.35 | 13.92% |
| 19:37 | 58 | −5.91 | 12.53 | 9.12 | −27.27% | | 1.99 | 27.11% |

### *3.6. Comparison with Traditional Defrost Strategies*

To further highlight the advantages of the proposed dual-factor defrosting model, a systematic comparison with representative traditional defrost strategies is provided in Table 13. These strategies include the conventional time–temperature (T-T) method [16], a pressure-based approach using differential pressure sensors [8], and two AI-based methods: deep reinforcement learning [9] and image gray recognition [11].

**Table 13.** Comparison of the proposed model with traditional defrost strategies.

| Strategy Type | Representative Study | Key Features/Input Parameters | Advantages | Limitations |
|---|---|---|---|---|
| Time-based (T-T) | Conventional method (Liu et al., 2017) [16] | Temperature threshold (−3 °C) + fixed time (60 min) | Simple, low cost | Cannot adapt to variable frosting conditions; mal-defrost rate high (68% reported) |
| Pressure-based | Chung et al. (2019) [8] | Differential pressure sensor across evaporator | Directly reflects airflow blockage | Requires additional sensor; prediction error ~5.5% but limited to specific heat exchangers |
| AI-based (deep reinforcement learning) | Klingebiel et al. (2025) [9] | Standard temperature sensors; self-optimizing | Adaptive; improves seasonal efficiency by 7.1–9.1% | Computationally intensive; requires training; black-box model |
| AI-based (image gray recognition) | Wang et al. (2024) [11] | Camera; image grayscale processing | High defrosting accuracy (93.33%); COP +36.6% | Requires camera and image processing hardware; lighting sensitivity |
| Proposed model (this work) | Dual-factor model $\Delta T = f(t, f)$ | Ambient temperature (t) and compressor frequency ($f$) | No extra sensors needed; physically transparent; captures temperature–frequency coupling; prediction error < 10%; $R^2 = 0.908$ | Limited to inverter-driven ASHPs; model constants specific to tested unit |

As shown in Table 13, the conventional T-T method is simple and low-cost, but its inability to adapt to variable frosting conditions leads to a high mal-defrost rate (up to 68% [16]). The pressure-based method offers a direct measure of airflow blockage, yet it requires an additional sensor, and its prediction error (≈5.5%) is only validated for specific heat exchanger geometries [8]. AI-based methods achieve notable performance gains-for instance, the image gray recognition equipment (IGRE) improves defrosting accuracy by 42.86% and COP by 36.60% compared to T-T control [11]. However, these methods demand extra hardware (cameras, processors) and computational resources, and their black-box nature makes physical interpretation difficult.

In contrast, the proposed dual-factor model offers several distinct advantages. First, it requires no additional sensors beyond those already present in a standard ASHP (temperature and pressure transducers). Second, the model is physically transparent: the cross-term coefficient explicitly quantifies the coupling effect between ambient temperature and compressor frequency. Third, its predictive performance is excellent, with $R^2$ = 0.908, RMSE = 0.82 °C, and a prediction error below 10% across all tested conditions. These features make the model a practical, low-cost, and accurate tool for on-demand defrosting control in inverter-driven ASHPs, especially when compared to more complex or less adaptive conventional strategies.

## 4. Conclusions

This study investigated frosting and performance degradation of air-source heat pumps (ASHPs). A controlled environmental platform was used. The coupled effects of ambient temperature and compressor frequency were revealed. Key findings are as follows: (1) Frost accumulation was most severe near 0 °C. Increased thermal resistance caused a decline in heating capacity and COP. (2) Higher compressor frequencies enhanced initial heating capacity. However, they also accelerated frosting and performance deterioration. An optimal energy efficiency balance was found at approximately 45 Hz for the tested system. (3) Relative humidity had a negligible effect on the critical ΔT at the 10% COP reduction threshold. Its variation was less than 5%. Thus, relative humidity is a secondary factor in defrosting control. (4) A dual-factor prediction model for critical defrosting ΔT was developed. The model uses ambient temperature ($t$) and compressor frequency ($f$) as independent variables. The model showed high reliability. Its prediction error was below 10% in both single-factor and multi-factor tests. Collectively, this research provides a theoretical framework and a practical engineering tool. These can help optimize intelligent defrosting strategies. They can also enhance the operational stability of variable-frequency ASHPs under complex climates.

**Author Contributions:** X.X.: conducted the experiments and wrote the original draft. Investigation. T.Z.: developed the methodology and revised the manuscript. D.L.: prepared the figures and reviewed the manuscript. W.S.: performed validation. Z.W. provided resources and curated data. Y.X.: conceived the study, supervised the project, and acquired funding. All authors have read and agreed to the published version of the manuscript.

**Funding:** This project was supported by the National Natural Science Foundation of China (No. 52506002), the Guangdong Provincial University Youth Innovation Talent Program (No. 2024KQNCX171), and the Foshan Innovation Research Project (No. 2024JNHB01).

**Data Availability Statement:** The original contributions presented in the study are included in the article, further inquiries can be directed to the corresponding author.

**Conflicts of Interest:** The authors declare no competing financial interests.

## References


1. Dong, S.; Zhao, H.; Zheng, Y.; Ni, L. Carbon reduction analysis of electric heat pumps in carbon neutrality in China. *Sustain. Cities Soc.* **2023**, *97*, 104758. [CrossRef]
2. Ma, L.; Sun, Y.; Wang, F.; Wang, M.; Zhang, S.; Wang, Z. Advancements in anti-frosting and defrosting techniques for air source heat pumps: A comprehensive review of recent progress. *Appl. Energy* **2025**, *377*, 124358. [CrossRef]
3. Qu, M.; Zhang, R.; Chen, J.; Cheng, Y.; Zhao, X.; Zhang, T.; Li, Z. Experimental analysis of heat coupling during TES based reverse cycle defrosting method for cascade air source heat pumps. *Renew. Energy* **2020**, *147*, 35–42. [CrossRef]
4. Klingebiel, J.; Höges, C.; Göbel, S.; Bannmüller, P.; Boelsen, T.; Venzik, V.; Vering, C.; Müller, D. Optimal defrost initiation for air-source heat pumps: Evaluating the improvement potential of common defrosting controllers. *Energy* **2025**, *324*, 135871. [CrossRef]
5. Liu, S.; Bai, X.; Deng, S.; Zhang, L.; Wei, M. Developing a novel control strategy for frosting suppression based on condensing-frosting performance maps for variable speed air source heat pumps. *Energy Build.* **2023**, *289*, 113049. [CrossRef]
6. Wang, S.; Wei, W.; Luo, J.; Wang, W.; Sun, Y.; Li, Z.; Huang, C.; Tang, R.; Deng, S. A prediction model of the optimal defrosting initiating time for the air source heat pumps with different configurations and operations. *Energy Build.* **2025**, *326*, 115079. [CrossRef]
7. Tang, R.; Wei, W.; Sun, P.; Zhao, J.; Wang, W.; Sun, Y.; Deng, S. A novel time-current-temperature difference (T-I-T) defrosting control method for air source heat pump based on outdoor fan operation characteristics in space heating. *Appl. Therm. Eng.* **2025**, *259*, 124850. [CrossRef]
8. Chung, Y.; Na, S.I.; Choi, J.; Kim, M.S. Feasibility and optimization of defrosting control method with differential pressure sensor for air source heat pump systems. *Appl. Therm. Eng.* **2019**, *155*, 461–469. [CrossRef]
9. Klingebiel, J.; Höges, C.; Horst, J.; Nießen, O.; Venzik, V.; Vering, C.; Müller, D. A self-optimizing defrost initiation controller for air-source heat pumps: Experimental validation of deep reinforcement learning. *Appl. Energy* **2025**, *398*, 126400. [CrossRef]
10. Guo, Y.; Shao, S.; Geng, X.; Li, H.; Wang, Z.; Akkurt, N. A data-driven evaluating method on the defrosting effect of the air source heat pump system in Beijing. *Appl. Therm. Eng.* **2023**, *235*, 121377. [CrossRef]
11. Wang, S.; Wei, W.; Xie, J.; Wang, W.; Sun, Y.; Li, Z.; Lin, Y.; Huang, C.; Deng, S. Space heating performance analysis of air source heat pump integrated with image gray recognition-based defrosting controller. *Appl. Therm. Eng.* **2024**, *236*, 121536. [CrossRef]
12. Zheng, X.; Shi, R.; You, S.; Han, Y.; Shi, K. Experimental study of defrosting control method based on image processing technology for air source heat pumps. *Sustain. Cities Soc.* **2019**, *51*, 101667. [CrossRef]
13. Wei, W.; Ni, L.; Li, S.; Wang, W.; Yao, Y.; Xu, L.; Yang, Y. A new frosting map of variable-frequency air source heat pump in severe cold region considering the variation of heating load. *Renew. Energy* **2020**, *161*, 184–199. [CrossRef]
14. Li, Z.; Wang, W.; Sun, Y.; Liang, S.; Deng, S.; Lin, Y.; Wu, X. A novel defrosting initiating method for air source heat pumps based on the optimal defrosting initiating time point. *Energy Build.* **2020**, *222*, 110064. [CrossRef]
15. Xu, Y.; Zhao, R.; Wu, K.; Jin, H.; Song, M.; Shen, X. Experimental investigation and validation on an air-source heat pump frosting state recognition method based on fan current fluctuation signal and machine learning. *Energy* **2024**, *291*, 130372. [CrossRef]
16. Liu, J.; Sun, Y.; Wang, W.; Zhu, J. Performance evaluation of air source heat pump under unnecessary defrosting phenomena for nine typical cities in China. *Int. J. Refrig.* **2017**, *74*, 385–398. [CrossRef]


**Disclaimer/Publisher's Note:** The statements, opinions and data contained in all publications are solely those of the individual author(s) and contributor(s) and not of MDPI and/or the editor(s). MDPI and/or the editor(s) disclaim responsibility for any injury to people or property resulting from any ideas, methods, instructions or products referred to in the content.

MDPI AG
Grosspeteranlage 5
4052 Basel
Switzerland
Tel.: +41 61 683 77 34

*Energies* Editorial Office
E-mail: energies@mdpi.com
www.mdpi.com/journal/energies




Disclaimer/Publisher's Note: The title and front matter of this reprint are at the discretion of the Guest Editors. The publisher is not responsible for their content or any associated concerns. The statements, opinions and data contained in all individual articles are solely those of the individual Editors and contributors and not of MDPI. MDPI disclaims responsibility for any injury to people or property resulting from any ideas, methods, instructions or products referred to in the content.





Academic Open
Access Publishing

mdpi.com

ISBN 978-3-7258-9082-8